

Multifunctional Soft Materials: Design, Development and Applications

by

Yifei Xu

A Dissertation Presented in Partial Fulfillment
of the Requirements for the Degree
Doctor of Philosophy

Approved March 2020 by the
Graduate Supervisory Committee:

Lenore L. Dai, Chair
Erica Forzani
Julianne Holloway
Hanqing Jiang
Houlong Zhuang

ARIZONA STATE UNIVERSITY

May 2020

ABSTRACT

Soft materials are matters that can easily deform from their original shapes and structures under thermal or mechanical stresses, and they range across various groups of materials including liquids, foams, gels, colloids, polymers, and biological substances. Although soft materials already have numerous applications with each of their unique characteristics, integrating materials to achieve complementary functionalities is still a growing need for designing advanced applications of complex requirements. This dissertation explores a unique approach of utilizing intermolecular interactions to accomplish not only the multifunctionality from combined materials but also their tailored properties designed for specific tasks. In this work, multifunctional soft materials are explored in two particular directions, ionic liquids (ILs)-based mixtures and interpenetrating polymer network (IPN).

First, ILs-based mixtures were studied to develop liquid electrolytes for molecular electronic transducers (MET) in planetary exploration. For space missions, it is challenging to operate any liquid electrolytes in an extremely low-temperature environment. By tuning intermolecular interactions, the results demonstrated a facile method that has successfully overcome the thermal and transport barriers of ILs-based mixtures at extremely low temperatures. Incorporation of both aqueous and organic solvents in ILs-based electrolyte systems with varying types of intermolecular interactions are investigated, respectively, to yield optimized material properties supporting not only MET sensors but also other electrochemical devices with iodide/triiodide redox couple targeting low temperatures.

Second, an environmentally responsive hydrogel was synthesized via interpenetrating two crosslinked polymer networks. The intermolecular interactions

facilitated by such an IPN structure enables not only an upper critical solution temperature (UCST) transition but also a mechanical enhancement of the hydrogel. The incorporation of functional units validates a positive swelling response to visible light and also further improves the mechanical properties. This studied IPN system can serve as a promising route in developing “smart” hydrogels utilizing visible light as a simple, inexpensive, and remotely controllable stimulus.

Over two directions across from ILs to polymeric networks, this work demonstrates an effective strategy of utilizing intermolecular interactions to not only develop multifunctional soft materials for advanced applications but also discover new properties beyond their original boundaries.

DEDICATION

To My Wife, Chen Liu

For her encouragement, support, and love

ACKNOWLEDGEMENTS

I would first like to gratefully thank my advisor, Dr. Lenore Dai, who gave me the chance to pursue my dream, a Ph.D. degree in Chemical Engineering, and has been incredibly supportive to not only my academic studies but also my overall growth as a person. I cannot be more grateful about such a dream-come-true experience, which has also helped me realize what I truly desire from myself as well as how much one can be capable to accomplish with a strong will. I cannot name a second thing in my life that allow me to feel the same level of fulfillment. I also would like to thank all members from my thesis committee, Dr. Erica Fozani, Dr. Julianna Holloway, Dr. Hanqing Jiang, and Dr. Houlong Zhuang, for guiding me in research with their valuable feedbacks and suggestions during my Ph.D. study. I would like to thank all of the former and current members from Dr. Dai's research group, especially Prithwish Chatterjee, who first showed me the synthesis of PNIPAAm and contributed to my first publication, Elizabeth Nofen, who trained me on not only the instruments in our laboratory but also having a positive spirit to embrace challenges at research, Onkar Ghag, who contributed tremendously to our exploration on the 3D tactile display hydrogel project during his master's study, Wendy Jessica Lin, who bore many of my only occasionally-good, very often-bad ideas on the ColdTech project and never complained. I would also like to take advantage of this opportunity to thank my family for their continued support and unconditional love, especially my mother, Honghong Teng, even during the time when she was going through a life-threatening surgery, all she told me was to focus on my work. That was the moment I started to realize that being able to devote to a Ph.D. study is actually a luxury, and I couldn't stop reminding myself of how lucky I am to have their support all along.

I would like to acknowledge the financial support from the National Science Foundation, award number CMMI-1462481, and the National Aeronautics and Space Administration, grant number NNX17AF70G, the Fulton Engineering Graduate Research Travel Grant, the Graduate and Professional Student Association Travel Grant, Graduate College Travel Award, and Fulton Undergraduate Research Initiative at Arizona State University. I would also like to specially acknowledge Dr. Candace Chan, Dr. Matthew Green, from the School for Engineering of Matter, Transport and Energy (SEMTE), Chemical Engineering Laboratory Manager, Fred Peña, LeRoy Eyring Center for Solid State Science, and Magnetic Resonance Research Center (MRRC), all at Arizona State University, for the instrument access.

TABLE OF CONTENTS

	Page
LIST OF TABLES	x
LIST OF FIGURES	xi
CHAPTER	
1. INTRODUCTION.....	1
2. BACKGROUND AND MOTIVATION.....	5
2.1 Ionic Liquids (ILs).....	5
2.2 Environmentally Responsive Hydrogels.....	11
2.3 Motivation of Work	21
2.3.1 Ionic Liquids Based Liquid Electrolyte Systems for Low- Temperature Molecular Electronic Transducer (MET) Sensing in Planetary Exploration	21
2.3.2 Interpenetrating Polymer Network (IPN) Based Environmentally Responsive Hydrogels for Dynamic Tactile Display	37
3. METHODOLOGY.....	44
3.1 Materials	44
3.2 Synthesis, Formulation, and Sample Preparation	44
3.2.1 Mixtures of Ionic Liquid and Solvents Based Electrolyte Solutions	44
3.2.2 Interpenetrating Polymer Network Hydrogels of Poly(acrylamide) and Poly(acrylic acid) with Incorporation of Chlorophyllin	45

CHAPTER	Page
3.3 Characterization Methods	46
3.3.1 Characterization of Mixtures Based Electrolyte Solutions	46
3.3.2 Characterization of Interpenetrating Network Hydrogels	48
4. RESULTS AND DISCUSSION	51
4.1 Dual Ionic Liquid Based Liquid Electrolyte System for Low-Temperature Planetary Exploration.....	51
4.1.1 Effects of Water and Ethylammonium Nitrate (EAN) on Thermal Behaviors of ILs/Water/LiI Mixtures Based Electrolytes	51
4.1.2 Effects of Molecular Interactions on Transport Properties of ILs/Water/LiI Mixtures at Low Temperatures	56
4.1.3 Effects of Water and [EA][N] on Ionicity of ILs/Water/LiI Mixtures via Walden Plot Analysis	67
4.1.4 Electrochemical Stability of ILs/Water/LiI Mixtures.....	70
4.1.5 Sensing Performance of Developed ILs/Water/LiI Mixtures Based Electrolyte for MET Seismometer.....	73
4.2 Ionic Liquid Based Low-Temperature Electrolyte Systems using Organic Solvents Gamma-butyrolactone (GBL) and Propylene Carbonate (PC)	82
4.2.1 Effects of Incorporating Organic Solvents on the Thermal Properties of Electrolytes.....	82
4.2.2 Probing Intermolecular Interactions between IL and Organic Solvents	86

CHAPTER	Page
4.2.3 Transport properties of [BMIM][I]/GBL/PC/LiI Mixtures Based Electrolytes	92
4.3 Mixtures of Ionic Liquid and Butyronitrile (BuCN) Based Electrolyte Systems	98
4.3.1 Effects of Incorporating BuCN on the Physical Properties of Electrolytes	98
4.3.2 Intermolecular Interactions between [BMIM][I] and BuCN	102
4.4 Visible-Light Responsive and Mechanically Enhanced “Smart” UCST Interpenetrating Polymer Network Hydrogels	105
4.4.1 Confirmation of PAAm-PAAc Interpenetrating Polymer Network (IPN) Hydrogel Synthesis	105
4.4.2 Effects of Incorporating Chlorophyllin into Interpenetrating Network Hydrogel	114
5. SUMMARY AND PROPOSED WORK	125
5.1 Summary	125
5.2 Proposed Future Work	128
5.2.1 Low-temperature Sensing Performance of MET Seismometer	128
5.2.2 Explorations of Integrating ILs and Polymeric Materials	129
REFERENCES	143

APPENDIX

A	GRAFTED CINNAMOYL-BASED MECHANOPHORES FOR SELF-SENSING AND PHOTOCHEMICAL HEALING CAPABILITIES IN EPOXY	173
B	STRESS-RESPONSIVE REINFORCED POLYMER COMPOSITES VIA FUNCTIONALIZATION OF GLASS FIBERS	204

LIST OF TABLES

Table	Page
2.3.1.1 The Molecular Structures and Physiochemical Properties of GBL and PC ...	33
4.1.2.1 Fitting Parameters from VFT Equation Based on Experimental Viscosity Data of [BMIM][I]/Water/LiI and [BMIM][I]/[EA][N]/Water/LiI Mixtures	62
4.1.2.2 Fitting Parameters from the VFT Equation Based on Experimental Conductivity Data of [BMIM][I]/Water/LiI and [BMIM][I]/[EA][N]/Water/LiI Mixtures	66

LIST OF FIGURES

Figure		Page
2.1.1	Comparison of Inorganic Salts, Ionic Liquids, and Conventional Liquid Oils: Unlike the Inorganic Salt Forms Stable Formation of Crystalline Packing Between the Cations (Yellow) and the Anions (Blue), the Ionic Liquid Shows Very Poor Coordination of the Anions and Cations, More Similar to the Randomly Orientated Molecular Structures of Conventional Oil (Purple) (Adapted from [28]).....	6
2.1.2	Current and Potential Applications of Ionic Liquid (Adapted from [77])	8
2.2.1	A Schematic Map of Most Common Classes of Hydrogels Categorized by Properties (Figure Adapted from [93])	11
2.2.2	Illustrations of (a) the Volume Transition of Environmentally Responsive Hydrogels and Examples of their Representing Applications including: (b) Actuators [113], (c) Sensors [114], (d) Drug Delivery [115], and (e) Oil Clean-up [116]	13
2.2.3	Molecular Structures of Representing (a) Synthetic and (b) Natural Temperature Responsive Polymers.....	16
2.2.4	Schematic Illustrations of the Swelling and De-swelling Process of (a) Anionic and (b) Cationic Hydrogels in Response to pH Changes in the Solution (Adapted from [97])	18
2.2.5	A Representative Example of Applying pH Responsive Hydrogels in Drug Delivery (Adapted from [127]).....	19

Figure	Page
<p>2.3.1.1 A Schematic Illustration of (a) Simplified Principle of a Mechanical Inertial Seismometer, where Damping of the Motion is in a Linear Relationship with Mass Displacement, and (b) That of an Electro-magnetic Inertial Seismometer, where the Displacement Mass is Forced to Stand Stationary within the Frame of Coils by a Current Proportional to the Displacement and a Capacitor is Used as the Displacement Transducer with Varying Capacitance Based on the Mass (Adapted from [137]); (c) Potential Challenging Conditions for Deploying a Seismometer – if a Landing Site Exceeds the Maximum Effective Landing Angle then the Lander may Fail to Perform Scientific Measurements and Compromise Mission Objectives (Adapted from NASA Europa Study 2012 Report [148])</p>	24
<p>2.3.1.2 The Molecular Electronic Transducer (MET) System: (a) A Schematic View of a MET Seismometer Cell Structure, which Consists of a Sensing Element in an Electrolyte Channel and Two Pairs of Electrodes Configured as Anode-Cathode-Cathode-Anode (ACCA), Separated by Dielectric Spacers, Span the Width of Channels Filled with an Electrolyte (Adapted from [141]); (b) Block Diagram of Power Supply and Data Acquisition Subsystems for the MET seismometer; (c) A Proposed Sensor Shell Model of the MET seismometer from the In-house Device Development at ASU, where Holes in the Electrodes and Dielectric Spacers Allow Fluid Flow Through the Channels and the Channel-Ends are Capped by Elastic Rubber Diaphragms for the Fluid to Behave Inertially</p>	25

Figure	Page
2.3.1.3 Comparison of the Conductivity (in Black Square) and the Viscosity (in Blue Circle) of [BMIM][I]/Water Binary Mixtures with Respect to the Mole Fraction of Water (X_1) (Adapted from [179]).....	28
2.3.1.4 (a) An Illustration of the Hypothesized Hydrogen Bonding between [BMIM][I] and GBL; (2) The Distance between the Alkyl Carbon Adjacent to the Oxygen on the Imidazolium Ring and the Carbonyl Oxygen of the Solvent Molecular as a Function of the Distance between the Hydrogen on the Imidazolium and the Same Carbonyl Oxygen (Adapted from [197]) ...	35
2.3.2.1 (a-b) Formation Pathway of Gold-Polymer Composite Particles with TEM Images at Varying Reaction Stages and Their Responsiveness with Respect to Temperatures [214]; (c) TEM Images of Collapsed Composite Ionic Microgels Containing Fe_3O_4 Nanoparticles and the Zeta Potentials of both Poly(NIPAAm-co-DMAPMA) Microgels and Neat Fe_3O_4 Nanoparticles at Various pH [215]; (d) Schematic Illustration of Integrating 300 nm Thick Thin Silicon Ribbon with PNIPAAm Hydrogel and Environmental SEM Images of the Buckling Pattern Based on the Silicon-PNIPAAm Integration [216]; (e) Setup of a Projection System for Fast Photo-Responsiveness of PNIPAAm Hydrogel Incorporated with Photochromic Compound Benzospiropyran Showing Visible Light Induced Features Formed on the Hydrogel Surface (Unpublished Work by Dr. Prithwish Chatterjee)	39

Figure	Page
2.3.2.2 (a) Chemical Structures of Polyacrylamide (PAAm) and Poly(acrylic acid) (PAAc); (b) A Schematic Illustration of the Synthesis Process to Interpenetrating Network Hydrogel between PAAm and PAAc.....	43
4.1.1.1 DSC Heating Curves from $-160\text{ }^{\circ}\text{C}$ to $40\text{ }^{\circ}\text{C}$ for Different Compositions of (a) [BMIM][I]/Water/LiI and (b) [BMIM][I]/[EA][N]/Water/LiI Mixture Solutions	55
4.1.2.1 Temperature Dependence of Viscosities for Comparisons between Selected Electrolyte Formulations Plotted in the Form of (a) Viscosity as a Function of Temperature and (b) VFT Equation	61
4.1.2.2 Temperature Dependence of Conductivity for Comparisons between Selected Electrolyte Formulations Plotted in the Form of (a) Conductivity as a Function of Temperature and (b) VFT Equation	65
4.1.2.1 Walden Plot for the Formulation [BMIM][I]/[EA][N]/Water/LiI-5/35/55/5 in Comparisons with Other Similar IL Systems from Literatures including [EA][N] [264], [BMIM][Br] [262], [BMIM][BF ₄] [243], and [BMIM][CH ₃ COO] [263]	69
4.1.4.1 The Identified Electrochemical Window for Selected Electrolyte Formulations of ILs/Water/LiI Mixture Solutions. All Obtained Profiles Are Steadily Reproduced for Ten Cycles with No Occurrence of Reactions from Other Species except for the I-/I ₃ - Redox Couple with Zoom-in Details Presented in the Inset	72

Figure	Page
<p>4.1.5.1 The Device Overview of a Miniature MET Seismometer That is Used for the Earthquake Detection with Selected Electrolyte Formulation [EA][N]/[BMIM][I]/Water/LiI-10/25/60/5 in this Study. (a) a Top View of the Sensor; (b) a Side View of the Sensor (via SolidWorks); (c) an Illustrative Cross-Sectional View of the Sensing Element that Consists of Two Pairs of Electrodes in a Designed Anode-Cathode-Cathode-Anode (A-C-C-A) Configuration, where the Reversible Electrochemical Redox Reaction between Iodide and Triiodide Ions Takes Place as the Key Sensing Mechanism.....</p>	74
<p>4.1.5.2 An Event Overview of the Detected Earthquake, including the Geological Information from (a) ASU Earthquake Monitoring System by Dr. Edward Garnero from School of Earth and Space Exploration and (b) The Earthquake Hazards Program by USGIS as well as (c) the Recorded Earthquake Waveform Information at the Testing Pier on ASU Tempe Campus also by Dr. Edward Garnero</p>	78
<p>4.1.5.3 Earthquake Detection Data Comparison between MET and Reference Seismometer at Frequency Ranges of (a) 0.03-0.04 Hz; (b) 0.04-0.05 Hz; (c) 0.05-0.07 Hz; (d) 0.07-0.1 Hz; (e) 0.01-0.2 Hz; and (f) 0.2-0.3 Hz</p>	81
<p>4.2.1.1 DSC Thermograms from -160 to 40 °C for Various Formulations of (a) [BMIM][I]/GBL/LiI and (b) [BMIM][I]/PC/GBL/LiI Mixture Solutions ..</p>	86

Figure	Page
4.2.2.1 FTIR Spectra of Electrolyte Formulations, [BMIM][I]/GBL/LiI-10/85/5, 5/90/5, and [BMIM][I]/PC/GBL/LiI-5/20/70/5, as well as Individual Neat Components as Controls, in the Region of (a) between 2700 and 3300 cm ⁻¹ and (b) between 1660 and 1885 cm ⁻¹	89
4.2.2.2 ¹ H-NMR Spectra of (a) Neat [BMIM][I] with the Inset Showing the Numbered Chemical Structure of [BMIM] ⁺ Cation and (b) Neat [BMIM][I], [BMIM][I]/GBL/LiI-10/85/5, 5/90/5, and [BMIM][I]/PC/GBL/LiI-5/20/70/5, Focusing on the Peaks of H-2 with the Comparison of Relative Integrated Peak Areas also Provided	91
4.2.3.1 Temperature Dependence of (a) Viscosity and (b) Ionic Conductivity Among Neat [BMIM][I], Selected Organic Solvent-Based Electrolyte Formulations from this Work, and Aqueous-Based Formulation from Previous Studied Dual Ionic Liquid System Containing both [BMIM][I] and [EA][N] [266]. In (b), the Dashed Lines and Dot-Dashed Lines Represent the VFT Fitting Result for each Formulation and their Experimentally Measured T _g , Respectively, Showing Predicted Conductivities when Temperature Approaching Glass Transition, and the Inset Provides a Zoom-in View of the Measured Conductivities between 25 °C and -75 °C	96
4.3.1.1 DSC Heating Curves with an Upward Exothermic Direction from -175 °C to 40 °C for Electrolyte Formulations Including [BMIM][I]/BuCN/LiI-5/90/5 (Purple), 10/85/5 (Green), 20/75/5 (Black), 40/55/5 (Red), and Neat [BMIM][I] (Blue).....	99

Figure	Page
4.3.1.2 Comparison of Viscosity (Blue) and Ionic Conductivity (Red) of [BMIM][I]/BuCN/LiI Mixtures with Respect to BuCN Concentration	101
4.3.2.1 Probing the Molecular Interactions in Electrolyte Formulations, [BMIM][I]/BuCN/LiI-5/90/5, 10/85/5, 20/75/5, 40/55/5 and Neat BuCN, via (a) FTIR and (b) Raman Spectroscopy	104
4.4.1.1 Conformation of PAAm-PAAc IPN Hydrogel Synthesis: (a) Comparison of ATR-FTIR Spectra between the PAAm-PAAc IPN Hydrogel (Black Solid) and Individual Network Hydrogels, Pure PAAm (Red Dash) and Pure PAAc (Blue Dot), in the Wavenumber Range from 1000 to 2000 cm ⁻¹ . (b) Representative DSC Thermograms Showing the Glass Transition of PAAm-PAAc (Black), PAAm (Red), and PAAc (Blue), with the Resulting T _g Values in the Inset on the Bottom Left. (c) SEM Image Showing the Morphology of the PAAm-PAAc IPN Hydrogel (after Freeze-Drying) with Average Pore Size of 16.0 ± 4.4 μm	106
4.4.1.2 UCST Characteristics of PAAm-PAAc IPN Hydrogel: (a) Pictorial Demonstration of the Volume and Opacity Transition of Hydrogel. (b) Swelling Ratio (W _s /W _d) at Equilibrium at 5 °C, 25 °C, and 45 °C. (c) The Change in Optical Transmittance of the Hydrogel from 15 °C to 50 °C Measured by UV-Vis Spectrophotometer Showing the Opacity Transition of the Material; Left and Right Insets are Representative Screenshots of the Hydrogel's Opacity Transition Taken at the first 15 Second after Immersion in Water at 15 °C and 50 °C from Room Temperature, Respectively	109

Figure	Page
<p>4.4.1.3 Instron E-3000 Compressive Analysis of PAAm-PAAc IPN Hydrogel (Black) in Comparison to the Single Phase of Pure PAAm (Blue) and PAAc (Red) Hydrogels, Showing the Enhanced Mechanical Properties. Left Insets: PAAm-PAAc IPN Hydrogel Being Able to Recover to Original Shape after Compressive Test; Right insets: Fractures and Material Failure of PAAm (Top) and PAAc (Bottom) after Compressive Tests.....</p>	114
<p>4.4.2.1 Incorporation of Chlorophyllin into the Interpenetrating-Network Hydrogel System: (a) UV-Vis Spectrum of Chlorophyllin Salt Aqueous Solution Between 300 and 800 nm Wavelength. Inset: Molecular Structure of Chlorophyllin Sodium Copper Salt. (b) Comparison of Representative DSC Thermograms Showing the Glass Transition Between Non-Chlorophyllin (Black Solid) and Chlorophyllin-Containing (Green Dash) Interpenetrating Network PAAm-PAAc Hydrogels with the Resulting T_g Values (as a Result of Two Runs) in the Bottom Left Inset. (c) SEM Images Showing the Morphology of PAAm-PAAc Ch IPN Hydrogel (after Freeze-Drying) $9.9 \pm 4.3 \mu\text{m}$</p>	116

4.4.2.2	UCST Swelling Behavior of PAAm-PAAc Ch IPN Hydrogel: (a) Pictorial Demonstration of the Volume and the Opacity Transition of the Hydrogel after Incorporating Chlorophyllin. (b) Comparison of the Swelling Ratio (W_s/W_d) at Equilibrium between Non-Chlorophyllin and Chlorophyllin-Containing Hydrogel at 5 °C, 25 °C, and 45 °C. (c) The Change in Optical Transmittance of PAAm-PAAc Ch IPN Hydrogel from 15 °C to 50 °C Measured by UV-Vis Spectrophotometer Showing the Opacity Transition of the Material; Bottom Left and Right Insets are Representative Screenshots of PAAm-PAAc Ch IPN Hydrogel's Opacity Transition Taken at the First 15 Second after Immersion in Water at 15 °C and 50 °C from Toom Temperature, Respectively	119
4.4.2.3	Comparison of Compressive Analysis: (a) Stress-Strain Curves of PAAm-PAAc IPN and PAAm-PAAc Ch IPN Hydrogels Obtained by Instron Showing Further Mechanical Enhancement after Incorporating Chlorophyllin. (b) Calculated Compressive Tangent Moduli of PAAm-PAAc IPN and PAAm-PAAc Ch IPN Hydrogels with Respect to Strain Ratio from 10% to 60% with an Interval of 10%. (c) The Effect of Different Strain Rates on PAAm-PAAc Ch IPN Hydrogel.....	122
4.4.2.4	The Visible-Light Responsiveness of PAAm-PAAc Ch IPN Hydrogel in Terms of Swelling Weight Increase with Respect to Exposure Time (0, 2, and 10 Minute).....	124

Figure	Page
5.2.2.1 Polymerization Reaction of (1-Vinylimidazolium) Based Ionic Liquids via Free Radical Polymerization Using AIBN as the Initiator in the Media of Dimethylformamide (Adapted from Ref [321]). In the Case of the Proposed synthesis, Anion A ⁻ is Bis(trifluoromethylsulfonyl)imide and Pendant Group R is a Butyl Functional Group	131
5.2.3.1 Mechanism for Curing of Epoxy Resin by an Imidazolium Cation (Adapted from [336]).....	138

CHAPTER

1. INTRODUCTION

Soft materials range over many different classes of materials, including liquids, foams, colloids, gels, polymers, and multifarious biological materials, and fulfill numerous critical applications throughout the modern world with each of their unique properties [1–6]. It is always a strong desire to combine the characteristics of those materials to achieve complementary functionalities. In comparison to materials with hard bodies and rigid structures, soft materials are advantageous for the integration across different materials thanks to their complexity and flexibility [7,8]. Soft matter based functional materials not only present a collective performance by each individual component but also evolve new features from their rich and intriguing interfacial interactions, inspiring broad possibilities to design and construct advanced platforms of multifunctional materials. Recent successful examples have been demonstrated in a vast variety of fields, such as flexible electronics [9–11], biomedical and tissue engineering [12–15], soft armors [16,17], soft actuators and robotics [18–22], and a great number of more.

In this work, two different systems of soft materials, ionic liquids (ILs) based mixtures and interpenetrating polymer network (IPN), are developed and investigated for two specific applications, low-temperature seismic sensing and environmentally responsive hydrogels, respectively. For each material system, a unique approach of tuning intermolecular interactions is used to obtain not only the multifunctionality from combined materials but also their tailored properties for specific tasks. In the direction on ILs-based mixtures, we developed a multi-component electrolyte system for space missions at extremely low temperatures. ILs have a wide liquid temperature range, which is a highly

favorable material characteristic in developing low-temperature electrolytes, but the ionic conductivity of ILs often suffer from high viscosities and insufficient ion-disassociations due to their commonly seen bulky cations [23] and strong electrostatic attractions between cations and anions [24]. The results from our study, including both aqueous and non-aqueous approaches, demonstrate a facile strategy to overcome such a barrier of developing liquid electrolytes for not only MET sensors but also other electrochemical devices with iodide/triiodide redox couple targeting low temperatures. In the other direction on hydrogels, an interpenetrating polymer network (IPN) system is explored to develop a visible-light responsive and mechanically enhanced “smart” hydrogel. Poor mechanical properties are known challenges for hydrogel-based materials. The formation of the interpenetrating network improves the mechanical properties of synthesized IPN hydrogels compared to hydrogels made of a single network of each polymer, and the analysis of glass transition temperature (T_g) reveals its upper critical solution temperature (UCST) responsive swelling behavior, which is in contrast to the prevalent lower critical solution temperature (LCST) transition of most currently available environmentally responsive hydrogels. The visible-light responsiveness of the IPN hydrogel was enabled by the incorporation of the functional units, which was also observed to have an effect to further enhance the mechanical properties by modifying the average pore size of the polymer networks. Such an IPN shows the potential to serve as a practical route in developing “smart” soft materials using visible light as a simple, inexpensive, and remotely controllable stimulus. Overall, this dissertation is structured as follows.

Chapter 2 provides the background and motivations for the topics discussed in this dissertation, primarily focusing on ILs and their mixtures, environmentally responsive

hydrogels, and their current limitations from available studies for the applications of our interests, which yield the main work of this presented work.

Chapter 3 explains the methodology for the preparation of ILs-based liquid electrolytes containing iodide/triiodide ions, the synthesis of IPN hydrogels and their incorporation with functional additives, as well as various tools and techniques of characterizing the soft material samples prepared in this study.

Chapter 4 provides the results and discussions that can be divided into two broad directions as stated above. Within the first direction, three iodide/triiodide-containing, ILs-based electrolyte systems are discussed in section 4.1, 4.2, and 4.3, respectively. In section 4.1, we first discussed and compared the thermal, transport, electrical, and electrochemical properties of a dual IL low-temperature electrolyte system among varying formulations, emphasizing on the effects of adding water as a co-solvent and incorporating ethylammonium nitrate ([EA][N]) as a second IL component in the mixture. Walden plot analysis was applied to compare the optimized electrolyte system with other similar IL-based electrolyte systems from literatures, followed by the electrochemical stability assessment of the electrolytes and the sensing performance validation of an in-house fabricated MET seismometer based on a real-time earthquake detection using the developed electrolyte. In section 4.2 and section 4.3, we continue to take advantage of the design strategy that is demonstrated in section 4.1 and expand the research to two different IL/organic solvent mixtures with gamma-butyrolactone (GBL)/propylene carbonate (PC) and butyronitrile (BuCN), respectively, to further extend the material limits for low-temperature liquid electrolytes. In addition, the hypothesized intermolecular interactions among certain functional group pairs between solvent molecules and ions of ILs were

characterized via several different instrumental techniques to provide insights on a microscopic level for a better understanding of the underlying physical phenomena and their potential correlations with bulk properties of electrolytes. In the second direction, section 4.4 examines the formation of an IPN hydrogel between polyacrylamide (PAAm) and poly(acrylic acid) (PAAc) as well as the incorporation of chlorophyllin with this soft composite matrix for the aimed material features in enhanced mechanical properties, UCST transition behavior, and promising responsiveness to visible-light irradiation.

Chapter 5 summarizes the experimental work conducted on the development of two multifunctional soft material systems, ILs-based low-temperature liquid electrolytes and IPN-structured hydrogels, for each of their targeted applications. Finally, future works are also proposed with regards to further advancing the maturation of MET sensing technology and integrating ILs with functional polymer networks to form new conductive composite materials.

CHAPTER

2. BACKGROUND AND MOTIVATION

2.1 Ionic Liquids (ILs)

ILs are salts in the format of liquid. They consist of entirely ions and still remain fluidic below 100 °C or even at room temperature with their low melting temperatures. This unique behavior of ILs is due to the weak coordination of their bulky and asymmetric constituent ions, which significantly resists the formation of stable crystal lattices and lowers the melting points [25,26]. Because of such conformational flexibility and the constitution of entirely ions, ionic liquids inherit the characteristics from both molecular solvents and inorganic salts [27]. A general comparison between ionic liquids and inorganic salts was given by Frost et al [28], as shown in Figure 2.1.1. ILs are also known as “designer solvents” because of their great versatility in properties by selection of cation and anion. In addition to the wide temperature range of the liquid state, ILs also possess a number of remarkable features including property tunability, ionic conductivity, electrochemical stability, negligible volatility, and non-flammability [29–31], which have extended their applications to a large variety, such as chemical synthesis and processing [32–37], facilitators for catalysis [38–41], media for separation process [42–44], lubricants [45–47], biology [48–50], electrochemistry [51–54], thermal fluids for heat storage and transfer [55,56], and nuclear waste treatment [57–59]. The industrial usage of ILs was first commercialized in the production process of alkoxyphenylphosphines, a generic photoinitiator precursor, at a multi-ton scale by a BASF site in Ludwigshafen, Germany, in 2002. Another successful example, developed by Chevron 2013 [60] and implemented by Honeywell in 2016 [60], involves a new alkylation technology in which ILs are

introduced as alternative catalysts in replace of hydrofluoric or sulfuric acids to refine cleaner-burning high-octane fuels [61].

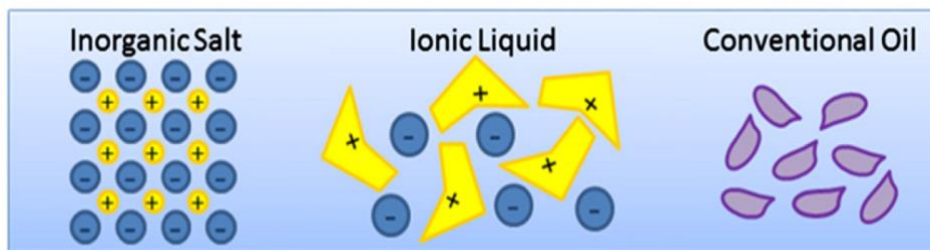


Figure 2.1.1. Comparison of inorganic salts, ionic liquids, and conventional liquid oils: unlike the inorganic salt forms stable formation of crystalline packing between the cations (yellow) and the anions (blue), the ionic liquid shows very poor coordination of the anions and cations, more similar to the randomly orientated molecular structures of conventional oil (purple) (adapted from [28]).

A map that summarizes current and potential applications of ILs is shown in Figure 2.1.2, extrapolating the development of technologies in ILs from the present progresses to the future expectations. Among diverse applications, ILs have also become an appealing family of materials in particular as electrolytes for various energy storage and electronic devices due to their advantages over conventional electrolytes based molecular liquids (MLs) as the media [62–66]. For energy storage devices such as supercapacitors, the cell voltage is constrained by the electrochemical stability window of the electrolytes. While most of aqueous electrolytes would not survive beyond a cell voltage of 1.23 V [67] and typical organic electrolytes fail to exceed 3 V [63] otherwise irreversible redox reactions begin to undermine the cell performance, ILs-based electrolytes offers the excellent

electrochemical stability to allow a much higher cell voltage and therefore improve the energy density of the devices [68]. For example, Balducci et al. reported a supercapacitor cell that can reach a maximum operating potential range of 4.5 V at 60 °C using activated microporous carbon as active material and IL *N*-butyl-*N*-methylpyrrolidinium bis(trifluoromethylsulfonyl)imide ([PYR₁₄][TFSI]) as the electrolyte, and their results showed both high cycling stability and high stable specific capacitance of the ionic liquid electrolyte [69]. Moreover, the thermal stability of ILs as electrolytes enables supercapacitors to operate at high temperatures. Borges et al. developed a composite electrolyte based on a mixture of clay and 1-butyl-2,3-dimethylimidazolium bis(trifluoromethylsulfonyl)imide ([BMIM][TFSI]) ionic liquid at an optimal weight ratio of 1:1 to facilitate a stable performance of the supercapacitor at 200 °C [70]. For processes and devices with working principles involving electrochemical reactions, on the other hand, ILs are also considered attractive materials for the development of advanced electrolytes due to their non-volatility and non-flammability. For instance, in lithium-ion batteries, current organic electrolytes that contains volatile and flammable solvents can cause serious safety concerns when encountering the accumulation of heat and pressure in the cell from the exothermic reactions in the case of thermal runaway and may eventually lead to an explosion [71–73]. ILs-based electrolyte systems have been exploited to improve the safety as well as other performances for lithium-ion batteries. A study reported by Guerfi et al. demonstrated that an addition of IL 1-ethyl-3-methyleimidazolium bis(trifluoromethylsulfonyl)imide ([EMIM][TFSI]) at an optimized concentration of 40 % in organic solvents used in commercial batteries could yield a significantly higher safety of the electrolytes with no flammability and comparable electrochemical performances up

to 2 C rate for discharge [74]. Yang et al. investigated the usage of IL *N*-propyl-*N*-methylpyrrolidinium bis(trifluoromethanesulfonyl)imide ([PYR₁₃][TFSI]) in combination with organic additives and lithium bis(trifluoromethanesulfonyl)imide (LiTFSI), and the mixed electrolyte showed no flammability when the [PYR₁₃][TFSI] is at 60 vol% as well as an increased discharge capacity with higher temperatures up to 75 °C [75]. Song et al. reported the properties of pure [PYR₁₃][TFSI] containing 1 M LiTFSI without any organic solvent as the electrolyte against silicon-based anode material with a discharge capacity of 1058–960 mA h g⁻¹ over 200 cycles at a capacity retention of 88%, and their results indicated that the products from PYR₁₃ cations and TFSI anions also contributed to forming a stable solid-electrolyte-interphase layer to effectively passivate the electrode surface for the enhanced cycling performance [76].

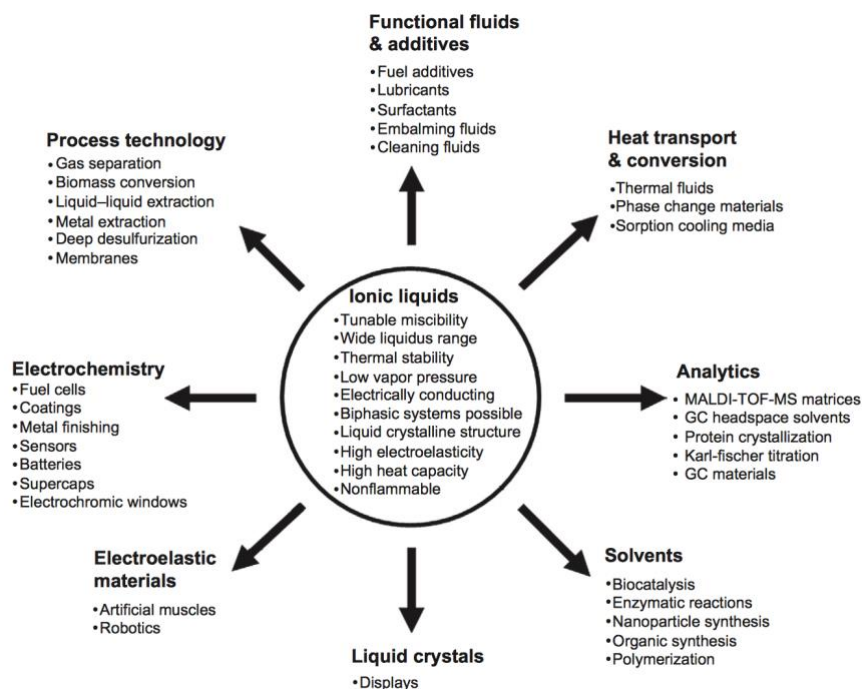


Figure 2.1.2. Current and potential applications of ionic liquid (adapted from [77]).

In addition to their applications in the energy field, ILs based electrolytes have shown their unique potentials in sensing technology and devices [52,78,79]. Very similar to their roles in energy devices, ILs electrolytes serve as media for target analytes to transport, until reaching the electrode surfaces, realizing the purposes of detection. Moreover, ILs offer their versatility to advance the performance of sensing devices in many other aspects, including high selectivity for analytes of interests [80–82], functionality as binders for electrodes [83–86], and great compatibility with analytes from a wide spectrum of material types [87–90]. For instance, Lu et al. reported an electrochemical approach of employing IL protonated-betaine bis(trifluoromethylsulfonyl)imide ([Hbet][TFSI]), not only as an electrolyte but also a selective solubilization medium, to quickly and directly detect heavy metal traces including lead oxide, cadmium oxide, and copper oxide, by anodic stripping voltammetry [82]. The concept of this sensing method is based on ability of [Hbet][TFSI] to reversibly solubilize a variety of rare earth metal oxides via the carboxylic acid group forming a coordinated metal-betaine complex with metal ions, and the electrolyte can be recycled for reuse by an aqueous acidic solution [91]. The ability of interacting with specific electrode materials hint new possibilities for ILs-based electrolytes in advanced device designs.

Although ILs exhibit excellent traits and promising advantages as electrolyte materials, they are not simple replacements of MLs yet. In comparison to MLs-based electrolytes, the ionic conductivities of ILs are limited by their relatively high viscosity, hindering the transport of ions in electrolytes and posing adverse effects at a device level in applications. For example, the performance of ILs-based electrolytes for batteries at high capacity rate are still not comparable with conventional electrolytes due to low ion mobility

[76,92]. When operating at relatively high temperatures, the transport properties of ILs-based electrolytes are not the major concerns as both conductivity and fluidity improve with elevated temperatures. At low temperatures, however, ILs-based electrolytes are often expected to encounter significant decrease in ionic conductivity, rendering unsatisfying functionalities even if they are able to remain as liquids. With increasing needs of applying energy devices and sensors under extreme environmental conditions, such a limit restrains the potential of using ILs-based electrolytes for low-temperature applications. More fundamental studies on effects of viscosity and a deeper understanding on the physiochemical properties of ILs are much needed for not only better evaluating their functionalities as electrolytes but also meeting new expectations from uprising challenges. It is also foreseeable that task-specific applications will continue to drive the research in ILs for their specialized functionalities. In our case, the development of an ILs-based multifunctional electrolyte system to support sensing operations at extreme conditions for planetary exploration will be reported with details in this dissertation.

2.2 Environmentally Responsive Hydrogels

Hydrogels are soft polymeric materials that are highly hydrophilic to contain a significant amount of water within their crosslinked networks. The chemical and physical linkages, such as ionic or covalent bonding and chain entanglement or van der Waal forces, respectively, enable hydrogels to form three-dimensional structures and possess unique swelling behaviors. The high hydrophilicity of hydrogels can be attributed to the presence of hydrophilic functions groups, such as hydroxyl, carboxyl, amines, amide, sulphonyl, and so on, and the high content of water also allow hydrogels to a certain extend of material flexibility similar to nature tissues [93]. One of popular applications of hydrogels that can be seen in daily life are soft contact lens, which were pioneered by Wichterle and Lím in 1960 using poly(2-hydroxyethyl methacrylate) (PHEMA) due to its excellent transparency, compatibility to normal biological processes, and well-balanced mechanical properties versus water content [94]. Depending the property of interest, hydrogels can be categorized into several different subgroups as schematically shown in Figure 2.2.1.

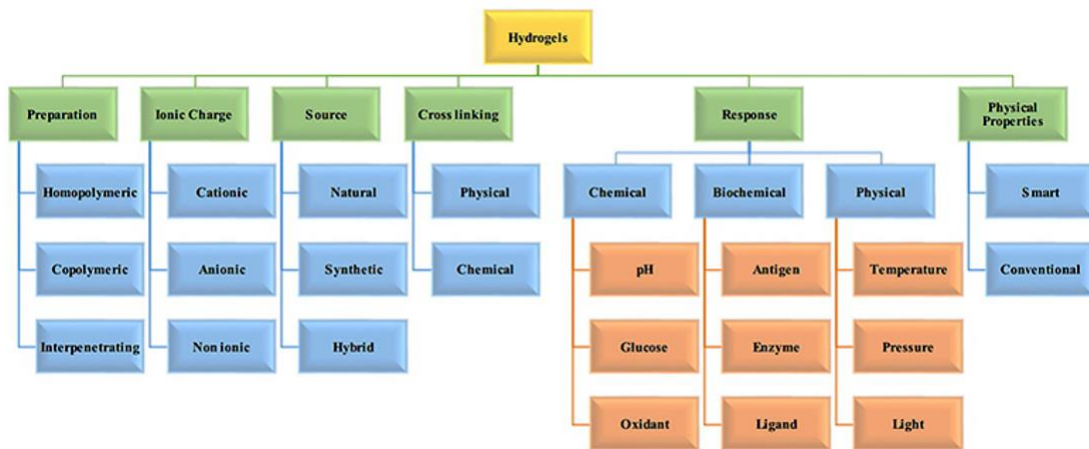


Figure 2.2.1. A schematic map of most common classes of hydrogels categorized by properties (figure adapted from [93]).

Environmentally responsive hydrogels are “smart” hydrogels that respond to external stimuli, such as temperature [95,96], pH [96,97], ions [98,99], electric field [100–102], enzymes [95,103], and light [100,104,105], with significant volume transitions. Owing to this remarkable feature, such group of hydrogels uphold a variety of important applications including sensors [106], actuators [107], drug delivery [97,100,108,109], and oil cleanup [110,111]. Very recently, environmentally responsive hydrogels have also been explored in the field of atmospheric water harvesting (AWH) with hydroscopic polymeric materials to develop a super moisture absorbent system. Such a polymeric-network-based moisture capturing system holds a unique advantage over AWH materials that use active-surface-based vapor adsorption, because it is no longer limited by the high energy barrier that is inevitably involved with the phase transition of water [112]. The switchable hydrophilicity of environmentally responsive hydrogels renders not only a synergetic route of rapid and controllable water release but also a promising cycling capability to minimize the energy consumption. Figure 2.2.2. demonstrates the volume transition of environmentally responsive hydrogels as well as some representing examples of their applications.

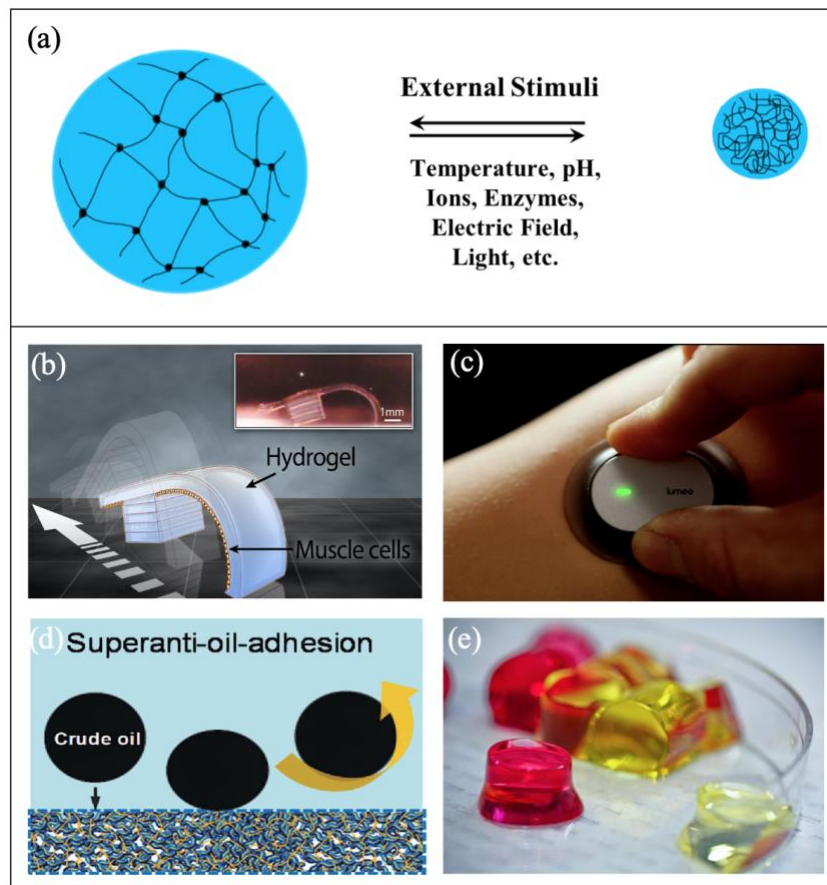


Figure 2.2.2. Illustrations of (a) the volume transition of environmentally responsive hydrogels and examples of their representing applications including: (b) actuators [113], (c) sensors [114], (d) drug delivery [115], and (e) oil clean-up [116].

One type of the most extensively studied environmentally responsive hydrogels is the temperature responsive hydrogels, due to the ease of using temperature to trigger their responses in volume transitions. Such responses to temperature stimulus can be found on hydrogels of both natural and synthetic origins, which share the feature of possessing at least one hydrophilic part and one hydrophobic part in the molecular structure. The

functional groups of the hydrophilic part are commonly found as an amide group, and the hydrophobic part can be groups such as methyl, ethyl and propyl. The molecular structures of three well-known synthetic temperature responsive polymers are shown in Figure 2.2.2 (a). The volume transition of temperature responsive hydrogels is driven by the switch between the hydrophilic and the hydrophobic characteristic of the molecules via the interplay of the dominating interaction between the functional groups of the polymers and the solvents, for example, water. According to Flory-Huggins solution theory, there are three main types of interactions when a polymer is dissolved with water, including interactions between polymer-polymer, polymer-solvent, and solvent-solvent. The relative strength of these interactions competes among each other to determine the swelling or de-swelling of a polymer network in the environment of a certain solvent. For polymers that exhibit a typical lower critical solution temperature (LCST), their network becomes more hydrophobic and shrinks due to the reduction of the polymer-solvent interaction above a specific temperature. Meanwhile, a discontinuous de-swelling of the hydrogel is also observed. There have been explanations to interpret the behavior of temperature responsive hydrogels in different angles. In the point view of Gibbs free energy of mixing, a negative free energy (ΔG) indicates a spontaneous mixing process which favors the polymer-solvent interaction. When temperature is above LCST, the water molecules around the polymer chains become significantly less ordered as hydrogen bonds are disrupted due to the rise of the kinetic energy. In this scenario, the entropy of the system increases so the term ($T\Delta S$) becomes dominant to yield a negative ΔG in the thermodynamic relation $\Delta G = \Delta H - T\Delta S$. When temperature is below LCST, the hydrogen bonds are formed so that the water

molecules around the polymer chains become more ordered, resulting in a reduced entropy and a more dominant enthalpy term (ΔH) with a positive overall ΔG .

The aforesaid behavior makes the temperature responsive hydrogels very attractive for delivering drug to targeted cells with higher functioning temperature than normal physiological temperatures, for example, cancer cells [117–119]. Additionally, the encapsulation by the hydrogel matrix can also protect and sustain the efficacy of the drug from hostile environments, for instance, the low pH condition in the stomach, until the release of the drug [120,121]. More recently, natural temperature responsive polymers based on polysaccharides, a class of polymeric carbohydrate molecules in which monosaccharide units are covalently linked by O-glycosidic bonds, have also drawn great attention because of their excellent biocompatibility and biodegradability. Representing members from this class, such as gelatin [122], dextran [123], and chitosan [124], are considered as stronger material candidates for human drug test trials in the field of pharmaceuticals and biopharmaceuticals, and their molecular structures are shown in Figure 2.2.2 (b).

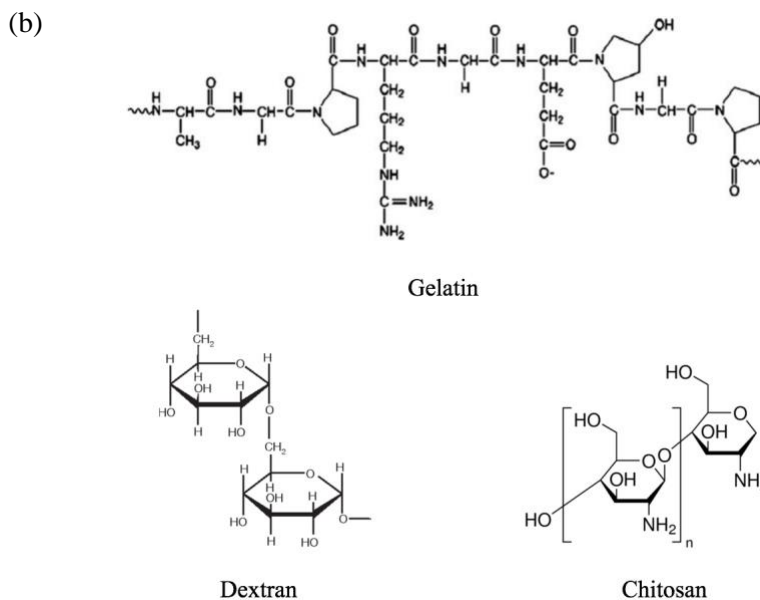
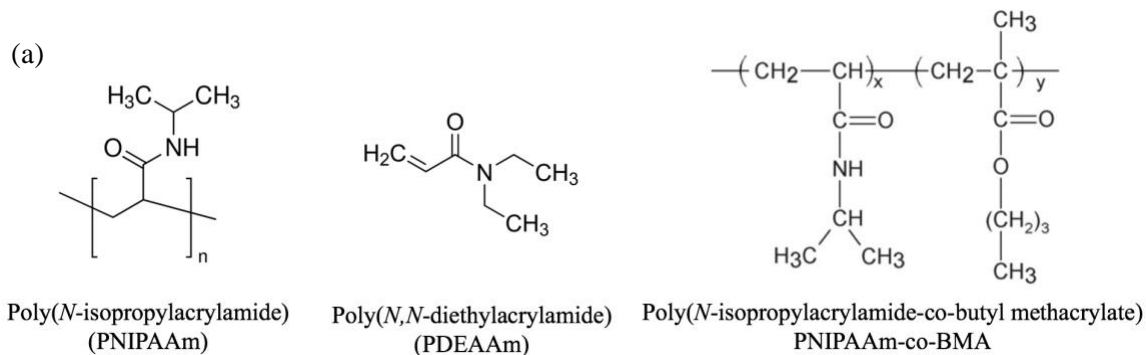


Figure 2.2.3. Molecular structures of representing (a) synthetic and (b) natural temperature responsive polymers.

Besides temperature responsive hydrogels, another extensively studied environmentally responsive hydrogel is pH responsive hydrogels, which is sensitive to changes in pH or electrolyte concentration of the solution. Those hydrogels are typically made of constituent polymers that contain ionic pendant groups, which can be either acidic

or basic functional groups, attached to their polymeric backbone. The pH responsive behavior of such hydrogels is based on the exchange of protons or hydroxyl ions present in the solution. For instance, poly(*N,N'*-dimethylaminoethyl methacrylate) hydrogel exhibits volume reduction in an environment of basic media. In contrast, poly(acrylic acid) based hydrogels demonstrate volume expansion at high pH due to the acidic nature. The transition takes place within a narrow pH range around the acid dissociation constant pK_a of the hydrogel, where the ionization level of the pendant group changes to significantly modify the water solubility of the polymer chains, resulting in a discontinuous swelling or de-swelling of the gel network [125]. A schematic presentation of the pH responsive swelling and de-swelling process for both anionic and cationic hydrogels in response to the pH changes of the environment is shown in Figure 2.2.3. When fully neutralized, pH-responsive polymers that originally contained segments of polyacid or polybase may transform to polyelectrolytes or polyampholytes. Once the ionization process is completed, a higher pH only enhances the ionic strength of the solution without causing any further swelling of the hydrogel. In addition to the concentration of the electrolyte, the swelling properties are also dependent on two other key quantities, the dissociation constant of the ionizable groups and the amount of the ionizable moieties. While the ionization of the functional pendant groups follows the similar mechanism as that of the corresponding mono-acids or mono-bases, the dissociation of the polyelectrolyte is under the influence of adjacent ionized groups and therefore subject to shifting the dissociation constant (K_a) of the hydrogel from the original dissociation constants of the respective mono-acids or mono-bases. On the other hand, the amount of the ionizable groups are dependent on the varying chemistry for the proposed synthesis routes, where the concentration of the

monomers and the degree of crosslinking can contribute to determining the actual swelling ratio of the hydrogels as well.

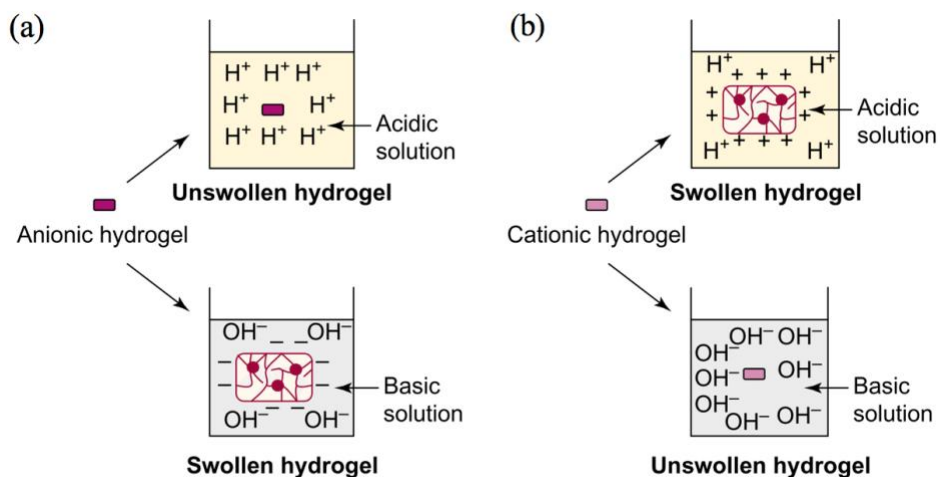


Figure 2.2.4. Schematic illustrations of the swelling and de-swelling process of (a) anionic and (b) cationic hydrogels in response to pH changes in the solution (adapted from [97]).

The pH responsive hydrogels are very attractive in many applications, especially in advanced drug delivery. The physiological environment of human body contains distinguishable pH conditions at different body sites or even within the same tract. For instance, the intestine has an almost neutral pH while the pH of the lower stomach ranges from 1.5 to 4.0. When utilizing pH responsive hydrogels for drug delivering to the target region, for example, the medicine will be encapsulated by the reduced swelling at a lower pH environment of the stomach and then released when the swelling is enhanced in the neutral environment of the intestine [97]. Lowman et al successfully demonstrated the use

of a pH responsive, poly(methacrylic-g-ethylene glycol) hydrogel as an oral delivery vehicle for localized release of insulin via rapid hydrogel swelling in the basic or neutral environment of intestine after being protected from the proteolytic activities in the acidic environment of stomach [126]. A schematic illustration of the drug delivery process is shown in Figure 2.2.4. In addition to drug delivery, applications of pH responsive hydrogels have also been widely extended to gene delivery, protein separation, coating thickeners, and biosensors where changes of external pH are needed.

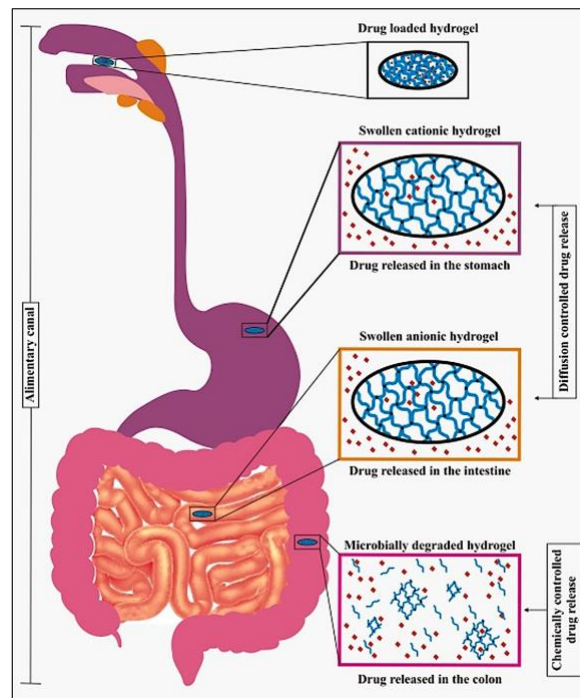


Figure 2.2.5. A representative example of applying pH responsive hydrogels in drug delivery. (Adapted from [127]).

Both temperature and pH responsive hydrogels can be synthesized through various polymerization techniques. While free radical polymerization is the most common route, other controlled polymerization methods, for example, microemulsion polymerization, can yield precisely designed block copolymers to form hydrogel particles with well-defined micro- or nanostructures [128–130]. When dispersing such microgels or nanogels in a solvent system, the pH of the solution can trigger phase separation via the swelling and deswelling of those particles. Another intriguing phenomenon, self-assembly of hydrogels from block copolymers can be observed upon environmental stimuli to form different shapes of aggregates via hydrophobic interactions [131–133]. As studies are dedicated to utilization of novel materials in synthesis, great attention has been paid to click chemistry, wherein various types of functional segments or ligands can be introduced to obtain tailored properties for specialized applications. Recently, other classes of stimuli, such as light, has also been emphasized due to their unique strength in triggering and controlling the responses of the hydrogels. In addition, one major drawback across all types of environmental responsive hydrogels, namely poor mechanical properties, demands efforts in research to tackle associated challenges without compromising the responsive sensitivity.

2.3 Motivation of Work

2.3.1 Ionic Liquids Based Liquid Electrolyte Systems for Low-Temperature Molecular Electronic Transducer (MET) Sensing in Planetary Exploration

The interest of humanity in exploring the universe is enduring and unremitting, and the remarkable properties of ionic liquids have already allowed them to play a vital role in a series of space related applications. In 2007, a hydrophilic ionic liquid, 1-ethyl-3-methylimidazolium ethylsulphate ([EMIM][EtSO₃]), which doesn't solidify until below temperature is below 175 K (−98 °C), with a layer of silver coating, has been used to form a smooth, uniform, and highly reflective surface as the basis for a lunar liquid mirror telescope, due to its negligible vapor pressure and low melting point [134]. More recently, the Laser Interferometer Space Antenna (LISA) Pathfinder spacecraft, which was launched in 2015 to test technologies for the study of gravitational waves in space, employed ionic liquids as the new propellants for its colloidal thrusters to realize more efficient and precise maneuver of the spacecraft, replacing the traditional liquid metals based propellants which are known for high surface tensions and high melting points [135,136]. Space lubricants is another critical field that is supposed to sustain the operation of mechanical systems on artificial satellites and spacecrafts while the possibility of repairing is close to none. The harsh environment in space includes high vacuum, high irradiation, and drastic change of temperature, impeding the performance of traditional lubricant materials such as silicones and mineral oils, and the non-volatility, the high thermal stability, the wide liquid temperature range of ionic liquids have also attracted special attention to their utilization as materials for space lubricants [46,47,135]. Okaniwa and Hayama reported a [TFSI] type of ionic liquids as a base oil to formulate a space lubricant with superior friction and wear

characteristics under vacuum below 10^{-4} Pa and at low temperature below -40 °C, high radiation resistance, and other satisfying performances in compliance with NASA specifications for Total Mass Loss (TML) and Collected Volatile Condensable Materials (CVCM) [46]. Fan and Wang et al also investigated the physicochemical and tribology properties of two alkyl imidazolium based ionic liquids, 1-hexyl-3-methylimidazolium tetrafluoroborate and 1-hexyl-3-methylimidazolium bis(trifluoromethylsulfonyl)imide, under simulated space environment, and the results showed excellent friction reducing and anti-wear performances against high temperature, high vacuum and various types of irradiation [47]. Despite the abovementioned advancements, the advantages of ionic liquids have not been fully taken for low-temperature electrolytes in space applications to date.

Various space missions require the electrolytes that can support electronic and energy storage devices to operate at extreme temperatures. When studying a foreign planet, a planetary seismometer provides the most direct approach to probe the composition, the interior structure, and the dynamic processes so that the planning of life detection can be informed. Conventional seismometers are based a spring-mass system, which leads to their fragile nature and the need of a strict installation angle to operate due to the inherent working principle [137]. Since the deployment often encounters a drastic deceleration and unpredictable landing conditions, such systems are very limited to serve as space-qualified planetary seismometers [138–140]. The operation mechanisms of conventional spring-mass based seismometers as well as the challenge of a tilted landing angle for deployment on an unknown surface are illustrated in Figure 2.3.1.1. These limitations can be lifted by utilizing molecular electric transducer (MET) technology in designing planetary seismometers, which uses liquid electrolytes to enable the high shock tolerance and the

independence of installation angle [141–143]. MET technology derived seismometers detect the movement of ions in a flow of liquid electrolyte between the electrodes and convert the physical motion to an output of electric current [144–147]. The device structure and the working mechanism of a MET seismometer are demonstrated in Figure 2.3.1.2. When two electrode pairs are equally biased with electrical voltage, reversible iodide/triiodide redox reactions transfer charges between anode and cathode via ions in the electrolyte. Therefore, an electrical current is established within the pair. Upon external acceleration, the inertial driving force produces movement of the electrolyte, resulting in an asymmetry in the electrical currents with a differential proportional to the ground motion. In the design of a MET seismometer, the liquid electrolyte, as the sensing body itself, is a key component that can respond to the propagations of seismic waves with signals in electric currents, disclosing the unknown information of a foreign planet to compass future life detection for planetary exploration.

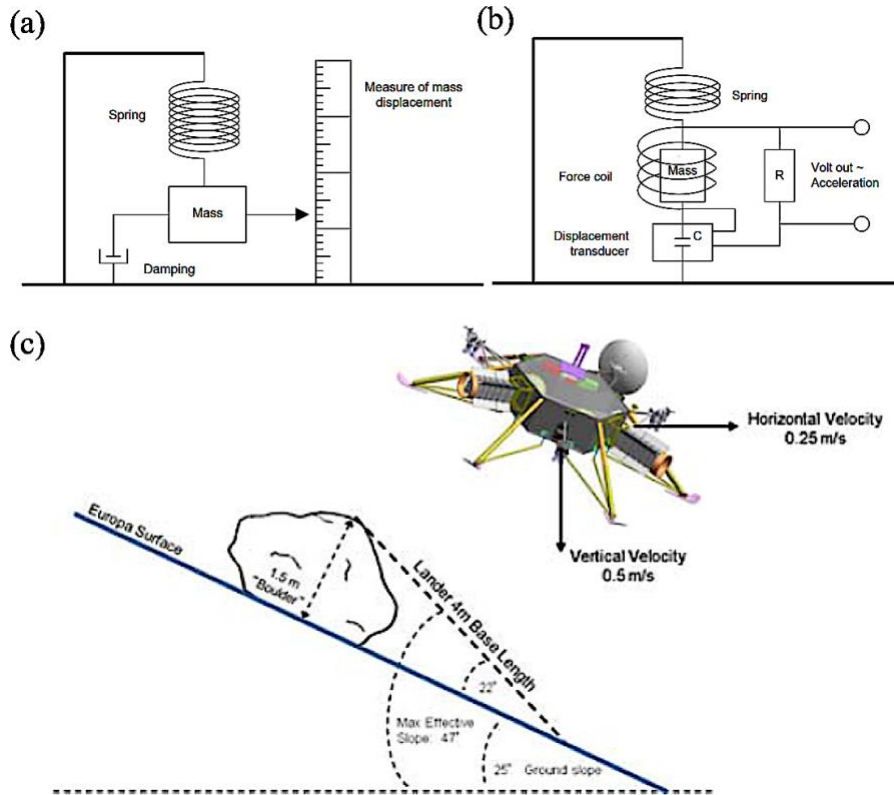


Figure 2.3.1.1. A schematic illustration of (a) simplified principle of a mechanical inertial seismometer, where damping of the motion is in a linear relationship with the mass displacement; and (b) that of an electro-magnetic inertial seismometer, where the displacement mass is forced to stand stationary within the frame of coils by a current proportional to the displacement and a capacitor is used as the displacement transducer with varying capacitance based on the mass (adapted from Havskov and Alguacil [137]; (c) potential challenging conditions for deploying a seismometer – if a landing site exceeds the maximum effective landing angle then the lander may fail to perform scientific measurements and compromise mission objectives (adapted from NASA Europa Study 2012 Report [148]).

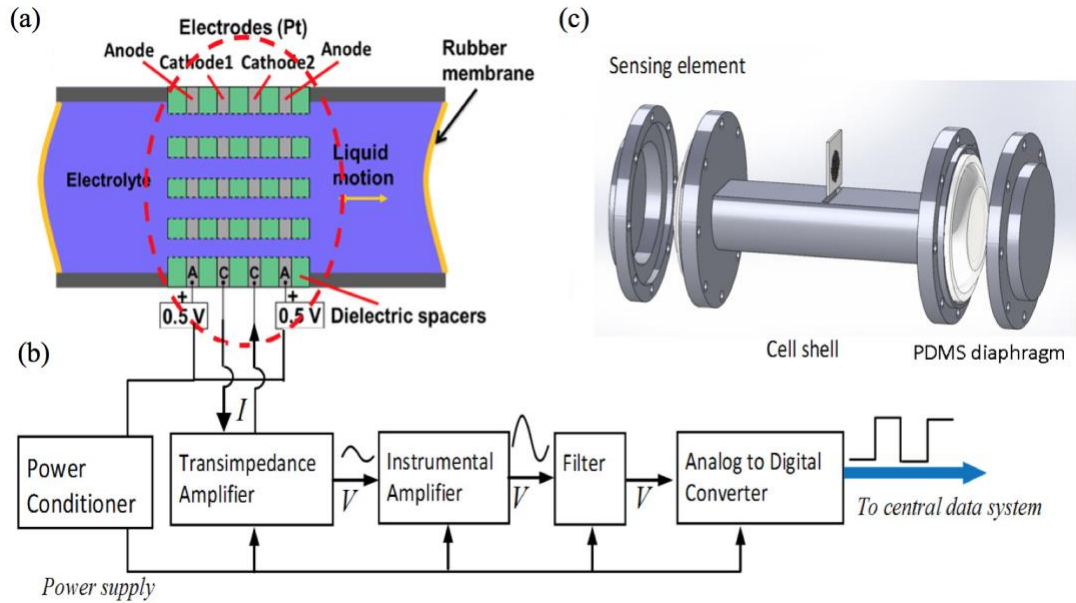


Figure 2.3.1.2. The molecular electronic transducer (MET) sensing system. (a) A schematic view of a MET seismometer cell structure, which consists of a sensing element in an electrolyte channel and two pairs of electrodes configured as anode-cathode-cathode-anode (ACCA), separated by dielectric spacers, span the width of channels filled with an electrolyte (adapted from [141]). (b) Block diagram of power supply and data acquisition subsystems for the MET seismometer. (c) A proposed sensor shell design of the MET seismometer from the in-house device development at ASU, where holes in the electrodes and dielectric spacers allow fluid flow through the channels and the channel-ends are capped by elastic rubber diaphragms for the fluid to behave inertially.

However, the liquid electrolyte used in a MET sensor is typically an aqueous solution containing potassium iodide and iodine, therefore the application is directly hindered by the working temperature range of water. In general, conventional liquid

electrolytes based on aqueous or organic solvents suffer from freezing along with lack of ionic conductivity when the environmental temperature falls below zero or melting point. The occurrence of crystallization will also cause the density change of the solution and accumulate the mechanic stress, which is a high risk of structural ss to the host device. Meanwhile, adding heating elements to the sensor is unfavored for any space mission due to the increase of the device weight and power consumption. Studies have been devoted to confronting this issue and have improved the electrolyte performance at the low temperatures typically between -20 to -40 °C [149–153]. For applications at extreme conditions, for example, at high altitude or in space, where temperature can often be lower, the challenge still remains. When the current space missions are targeting the ocean worlds where an icy shell covers the surface of the planets (e.g. Europa, Enceladus, and Titan) [154–160], the development of a liquid electrolyte that can adapt to such environments with extremely low temperatures rise up to a necessity and a priority. In order to further extend the lower temperature limit for liquid electrolytes, one of the promising approaches is to explore ionic liquids (ILs) as the material for the electrolyte development targeting low-temperature operations in planetary exploration.

As briefly discussed in Section 2.1, the main drawback of using ionic liquids as electrolyte materials is their high viscosity, which can depress the charge transport in the electrolyte, especially at low temperatures, resulting in low conductivities. While the long alkyl chains of ionic liquids resist crystalline packing, they limit the free rotation of the molecules and enhance the interactions of van der Waals forces and hydrogen bonding so that high viscosities of ionic liquids are reflected. In addition, the cohesion between cations and anions of ILs depends on electrostatic attractions, which also impacts the fluidity and

conductivity of the system [161,162]. The modification of molecular interactions can be used to improve the properties of an IL based system, where introduction of additional components such as other ILs or solvents has been applied with promising progresses [163–168]. Adding a second IL component can inhibit the lattice formation and prevent crystallization in the mixture, due to the size mismatch of ions between the primary and the second the ionic liquids [168]. Lin et al. reported an eutectic mixture of ILs from selecting the combination of different cations to increase such asymmetry of the system, which significantly widened the temperature range of operation for their energy storage devices [164]. On the other side, incorporating water or organic solvents to an IL system is another known strategy to reduce the viscosity effectively, which has been inspiring the employment of ionic liquid based binary electrolytes in batteries and dye-sensitized solar cells [169–171]. The mainstream investigation of such ILs-based electrolytes has emphasized on the operations at room temperature or higher temperatures due to the popularity of certain applications. Although there have been studies reporting the properties of ILs-based electrolytes at low temperatures [168,172–176], it is rare to find a liquid electrolyte that is designed to adapt an environment below $-40\text{ }^{\circ}\text{C}$. Fujie et al. explored 1-ethyl-3-methylimidazolium bis(trifluoromethylsulfonyl)amide ([EMIM][TFSI]) as the electrolyte incorporated with metal-organic framework nanoparticles at low temperatures down to $-45\text{ }^{\circ}\text{C}$ [177]. Aguilera et al. studied a composite electrolyte formed by a mixture of ionic liquid [PYR₁₄][TFSI], organic solvents, and lithium salt and extended the ionic conductivity measurement to $-90\text{ }^{\circ}\text{C}$ using dielectric spectroscopy, but the conductivity became almost negligible after temperature reaching $-50\text{ }^{\circ}\text{C}$ and the mass transport behavior of the electrolyte was not addressed [178]. To our knowledge, the

current developments of low-temperature electrolyte systems based on ILs focus on the platforms of supercapacitors and batteries, with little research activities in electrochemical sensors. On top of that, liquid electrolytes that contain iodide/triiodide ions for extreme low-temperature applications have also not been reported. Overall, the breakthroughs of using ILs as electrolytes for devices operating at low temperatures are very limited due to undesirable phase transitions and unsatisfying transport properties. With increasing needs for operations under extreme environmental conditions, such limits significantly restrain the potential of employing ILs-based electrolytes for applications in energy devices and sensors.

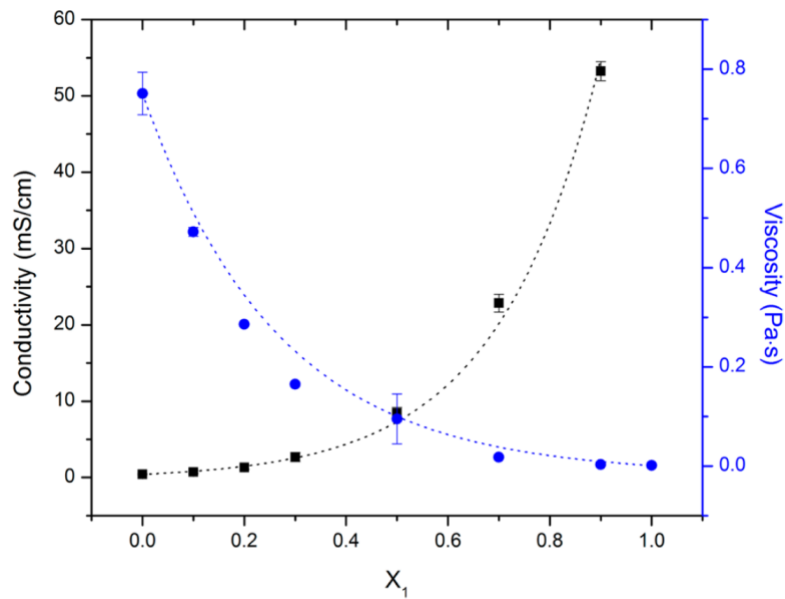


Figure 2.3.1.3. Comparison of the conductivity (in black square) and viscosity (in blue circle) of [BMIM][I]/water binary mixtures with respect to the mole fraction of water (X_1) (adapted from [179]).

In order to overcome such barriers, we herein report a strategy of utilizing intermolecular interactions to develop an ILs-based liquid electrolyte system specifically designed for the planetary application of MET seismometers at extremely low temperatures in both aqueous and non-aqueous approaches. In the aqueous approach, a multicomponent mixture that consist of a primary IL component, 1-butyl-3-methylimidazolium iodide ([BMIM][I]), water, and lithium iodide (LiI), with the incorporation of a second IL component, ethylammonium nitrate ([EA][N]) is investigated. Electrolytes that consist of [BMIM][I] have been widely studied [180,181], but their behaviors and limits of performance at low temperatures are still unrevealed. Nickerson et al. reported that the addition of water into [BMIM][I] could reduce the viscosity of the mixture and summarized the general trend between the conductivity and viscosity of the binary system, as shown in Figure 2.3.1.3, but the focus of the study was dedicated to their properties only at room temperature [179]. Furthermore, while the transport properties of IL-water mixtures have been studied with a variety of ILs, we have yet encountered results on their behaviors at temperatures below 0 °C with our best efforts. Nakata et al. reported phase diagrams of five imidazolium based ILs and water binary systems and observed ice formation before reaching the glass transition temperature (T_g) in multiple compositions [182]. The limited discussions and discoveries of ionic liquids and water mixtures at low temperatures can be attributed to early phase transitions of aqueous systems. In this work, we present an approach that, by tuning molecular interactions in the system, the designed electrolyte mixture can reach a lower operating temperature with improved transport properties. At an optimal concentration, the incorporation of [EA][N] can effectively prevent the

crystallization within the solution while successfully retaining a very low T_g below -105 °C, due to well-balanced molecular interactions. The extended liquid temperature window of the developed electrolytes by the synergy between water and [EA][N] allowed further investigations on the evolution of transport behaviors at low temperatures. The properties of viscosity and ionic conductivity of the electrolyte solutions were studied at varying temperatures from room temperature down to -75 °C, and the effects of [EA][N] were also shown to shape other properties of the electrolyte system by lowering the viscosity and enhancing the ionic conductivity. The influence was noticeable in improved ionic conductivity as well, which makes the developed electrolyte comparable with other good ionic liquids under Walden rule. The electrochemical stability of the selected candidate formulations was investigated via cyclic voltammetry, demonstrating a steady and reproducible electrochemical profile of iodide/triiodide redox reactions. A proper potential window was identified, where iodide/triiodide redox reactions were activated but electrochemical processes of other species were not induced.

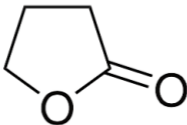
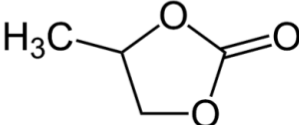
In the non-aqueous approach, we incorporated organic solvents with ([BMIM][I]) instead of using water. The success in the first aqueous approach via orchestrating the intermolecular interactions has inspired us to further take advantage of such a powerful strategy with organic solvents for new breakthroughs. Organic solvents are a strong complement to aqueous based liquid electrolytes. Recently, the binary mixtures of ILs and organic solvents have been investigated to support various electrochemical devices, such as lithium ion batteries [183] and advanced supercapacitors [184], due to the significantly improved transport properties. Moreover, such electrolyte systems have shown improved thermal stability and safety without too great compromise on the ionic conductivity,

compared to conventional organic electrolytes with higher inherent volatility [185,186]. For example, Ruiz et al. reported that electrolytes composed of pyrrolidinium-based ILs with nitrile and carbonate-based organic solvents at optimized concentrations, respectively, showed satisfying thermal stability, increased conductivity, and a wide electrochemical window, which are suitable for supercapacitors operating over a broad temperature range from -20 to 80 °C [166]. Sirisopanaporn and Scrosati reported a hybrid electrolyte containing 56 wt% *N,N*-butyl-*N*-ethylpyrrolidinium *N,N*-bis(trifluoromethane)sulfonimide – lithium *N,N*-bis(trifluoromethane)sulfonimide (Py₂₄TFSI-LiTFSI) and 14 wt% ethylene and propylene carbonate (EC-PC) in 30 wt% poly(vinylidene fluoride)-hexafluoropropylene (PVdF-HFP) copolymer matrix that demonstrated wide electrochemical stability from 1.5 V to 4.2 V, much reduced flammability, and high conductivity ranging from 3.4 to 9.4 10⁻⁴ S cm⁻¹ [187]. Aguilera et al. also observed enhancements in ionic conductivity at temperature as low as -90 °C from mixtures of two carbonate solvents (ethylene carbonate and dimethyl carbonate), 1-butyl-1-methylpyrrolidinium bis(trifluoromethanesulfonyl)imide, and lithium salt.[188] More interestingly, the mixtures of IL and carbonate solvents can introduce the electrolyte system another favorable functionality of forming a stable solid-electrolyte interface (SEI) layer on the carbon-based anode materials, which shields the ionic liquids from the electrode surface to prevent side reactions and decompositions of ionic liquids during the reduction process, while there is a moderate trade-off between the enhanced stability of the electrolytes and the mass transport of the lithium ions due to an extra diffusion step through the SEI layer [189,190].

When targeting low temperatures, as previously mentioned, the operation temperature has a major impact on the conductivity of the electrolyte and therefore the overall performance of the device. Besides the reduced conductivity at low temperatures, the freezing point or the glass transition temperature of the binary mixtures between ILs and the MLs also sets the physical limits for their applications as liquid electrolyte. Considerable efforts in research have devoted to investigations on different combinations of ILs and organic solvents to obtain desired physicochemical or electrical properties upon requirements for targeted devices. Since there is a large selection of organic solvents, their mixtures with ILs provide the flexibility to develop tailored properties for task-specific functionalities. Among various available molecular solvents, gamma-butyrolactone (GBL) and propylene carbonate (PC) have high boiling points, low melting points, making them favored candidates of components to include in the electrolytes for supporting a broad range of operation temperatures [191,192]. The chemical structures, melting points, and boiling points of GBL and PC are summarized in Table 2.3.1.1. Several studies show that the incorporation of GBL and PC not only improve the transport properties of ILs but also boost the thermal stability and electrochemical performance of the electrolytes. Wang et al. reported that a binary system of 50 wt% 1-allyl-3-methylimidazolium bis(trifluoromethanesulfonyl)imide ([AMIM][TFSI]) and 50 wt% PC improved the performance of lithium battery, in terms of high ionic conductivity and wide electrochemical window, while not compromising safety [193]. Anouti and Timperman rendered the mixtures of pyrrolidinium nitrate ([Pyr][NO₃]) and GBL as the electrolyte for low-temperature operations of carbon-based supercapacitors with a remarkable conductivity of 9 mS/cm at -40 °C [194]. Kuhnel et al. rendered a ternary electrolyte system

that are composed of containing [PYR₁₄][TFSI], PC, and LiTFSI for lithium-ion batteries, showing tunable properties by the concentration of ionic liquid and promising capacity retention of 91% after 500 cycles at room temperature [195]. More recently, Tian et al. proposed the use of the binary mixture between [EMIM][BF₄] and GBL as the electrolyte for a graphene-based capacitor with an exhibited low-temperature ionic conductivity of 0.31 mS/cm at – 70 °C, which marked the lowest temperature of measured conductivity by our best knowledge [196].

Table 2.3.1.1. The molecular structures and physicochemical properties of GBL and PC.

Molecular Solvent	γ -butyrolactone (GBL)	Propylene Carbonate (PC)
Chemical Structure		
Melting Points (°C)	– 43.5	– 49
Boiling Points (°C)	204	242

Although the past and current discoveries show encouraging results, the studies on the low-temperature properties of binary mixtures between ILs and molecular solvents are still very limited and their performances with actual electrochemical devices much less explored at low temperatures than at elevated temperatures. This gap can be attributed to the occurrence of the phase transitions before even reaching extremely low temperatures. The choice of solvents affects the electrolyte properties is also not yet well understood, despite many studies devoted to IL-solvent mixtures, and an electrolyte that can support

triiodide-iodide reactions for low-temperature applications has not been reported from the mixtures based on ILs and molecular solvents. Herein, we report an ILs/organic solvents mixture system consisting of [BMIM][I], PC, GBL, and LiI with investigations in thermal, transport, and electrochemical properties. Very recently, Zec et al quantitatively revealed the formation of hydrogen bonding between an acidic hydrogen of the alkyl group adjacent to the oxygen on the imidazolium ring and carboxylic oxygen of GBL in their molecular dynamic simulations [197], as illustrated in Figure 2.3.1.4. We hypothesize that such intermolecular interaction between GBL solvent molecule and [BMIM] cation via hydrogen bonding will disrupt the ion-pair formation between [BMIM] cation and iodide anion in the neat [BMIM][I] ionic liquid and thus reduce the cohesive energy of the mixture system to lower the T_g of the resulting solution. Moreover, while GBL has been applied as a low-temperature solvent for lithium batteries and supercapacitors, it is still expected to crystallize at extremely low temperatures when targeting the temperature of the surface environment on Europa. Since PC possess a similar molecular structure with GBL including the same carbonyl functional group, it also participates in re-configuring the intermolecular interactions when it is incorporated into the mixture solution in replace of the GBL content at optimized ratios. As a result, the thermal and the transport properties of the electrolyte can be directionally modified on the bulk scale as well. Since the molecular structure of PC resembles GBL in many ways, we anticipate the following two effects from their intermolecular interactions. First, T_g is retained at a low temperature because of the similar role PC serves as GBL in the mixture solution. Second and more importantly, the interaction between GBL and PC interferes the formation of aggregated

networks organic solvent molecules, preventing unfavorable phase transitions in the electrolyte.

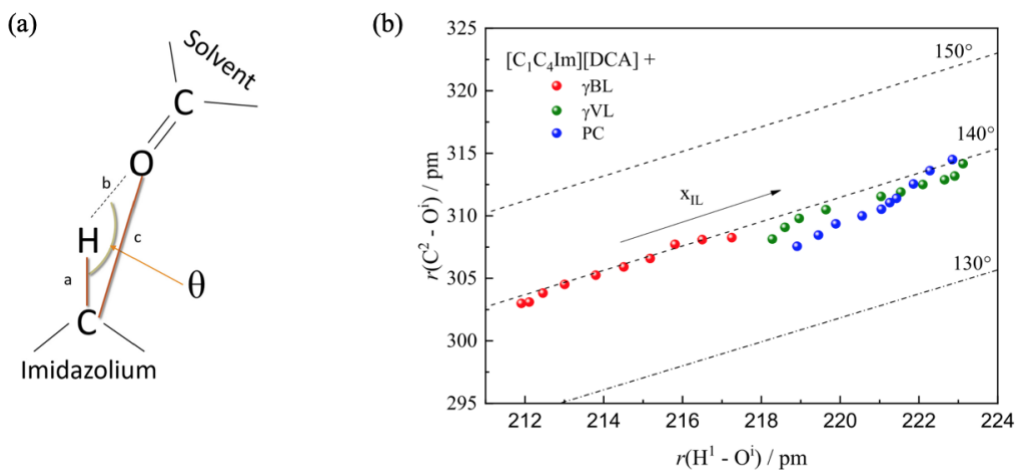


Figure 2.3.1.4. (a) An illustration of the hypothesized hydrogen bonding between [BMIM][I] and GBL; (b) The distance between the alkyl carbon adjacent to the oxygen on the imidazolium ring and the carbonyl oxygen of the solvent molecular as a function of the distance between the hydrogen on the imidazolium and the same carbonyl oxygen (adapted from reference [197]).

In addition to incorporation of GBL and PC, another organic solvent, butyronitrile (BuCN) is also studied with [BMIM][I] in the non-aqueous approach in our electrolyte development that supports the same electrochemical redox reaction between iodide and triiodide ions. BuCN is a unique solvent that possesses a high boiling point and a low melting point to allow a very wide liquid temperature window for developing electrolytes aiming the extreme operation conditions. Due to superior physical and transport properties, BuCN has been explored as a favorable solvent to form binary electrolytes with ILs for energy storage applications [198,199]. Despite its attractive potential in combining with

ILs, to our best knowledge, BuCN has not been systematically studied with ILs that contain iodide anions. We characterized the thermal, transport, and electrochemical properties of the mixture between [BMIM][I] and BuCN over a broad range of concentrations, and the underlying intermolecular interactions between the nitrile group of BuCN and [BMIM]⁺ cations are also investigated at the molecular level and connected to the macroscopic properties of the mixtures, which offers another angle to extend the tunability such mixture-based electrolyte systems towards specific tasks.

We anticipate the results from this part of the dissertation to not only provide a feasible liquid electrolyte system for the space applications of MET sensing technology at extremely low temperatures but also open up a practical design strategy to obtain tailored properties of a multi-component system via designing molecular interactions between species in a mixture system.

2.3.2 Interpenetrating Polymer Network (IPN) Based Environmentally Responsive Hydrogels for Dynamic Tactile Display

Among various temperature responsive hydrogels, crosslinked poly(N-isopropylacrylamide) (PNIPAAm) is well-known and extensively studied. The popularity of PNIPAAm hydrogel can be attributed to the substantial volume change from its famous LCST behavior at around 33 °C. As mentioned, the hydrogels of LCST nature exhibit shrinkage at above LCST due to the reduction of polymer-water interaction, showing a transition of de-swelling from a hydrophilic state to a hydrophobic state. At the hydrophobic state, the resulting polymer network of PNIPAAm separates from the water phase and collapses to a globular conformation from the structure of randomly extended coils at below LCST. With a transition temperature very near both physiological and ambient room temperatures, PNIPAAm has been able to expand the application of hydrogels into a variety of emerging fields such as flexible electronics [200,201] tissue engineering [202,203], artificial muscle [204,205], biomimetic robotics [206,207], 3D printing [208,209], and other novel devices. Depending the specific application, different architectures of PNIPAAm hydrogels can be obtained for targeted functionalities and tunable LCSTs via parameters such as chemistry of synthesis, fabrication process, and solvent environments. In addition, they have demonstrated great biocompatibility with animal cells via integration with naturally occurring polymers [210,211] and can also be modified to respond to other types or multiple types of external stimuli [212,213]. Our research group has also contributed to pioneering the synthesis and engineering of PNIPAAm in diverse directions, and some selected works are highlighted in Figure 2.3.2.1. Zhang et al. showed the formation of “smart” thermos-responsive dumbbell-structured

gold-PNIAAm/polystyrene composite particles using gold nanoparticles with controlled structures as the building blocks via seeded polymerization [214]. Chen and Dai reported a route of surfactant free precipitation polymerization to synthesize multi-stimuli responsive ionic microgel particles based on the copolymers between NIPAAm and N-[3-(dimethylamino)propyl]-methacrylamide (DMAPMA) that can effectively uptake and release rheology modifiers to alter the bulk viscosity of surrounding fluid [215]. More recently, Chatterjee et al. explored the integration between soft NIPAAm hydrogels with hard materials using thin film silicon ribbons to enable a mechanical buckling of the stiff silicon driven by the responsive transition of NIPAAm with respect to environmental stimuli [216]. The idea of a NIPAAm hydrogel based tactile display was also explored by Chatterjee in one of his later work as demonstrated in Figure 2.3.2.1 (e).

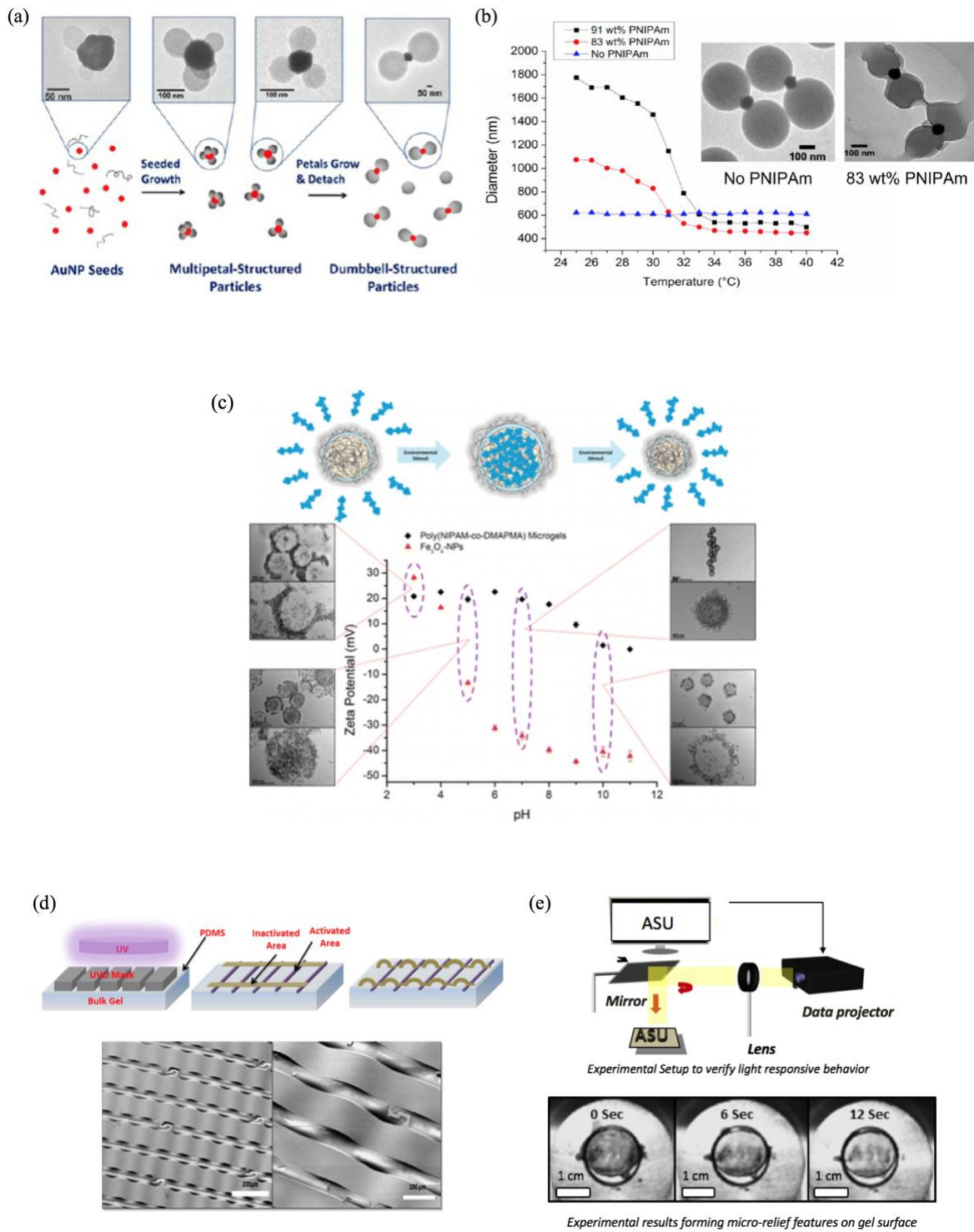


Figure 2.3.2.1. (a-b) Formation pathway of gold-polymer composite particles with TEM images at varying reaction stages and their responsiveness with respect to temperatures

[214]; (c) TEM images of collapsed composite ionic microgels containing Fe₃O₄ nanoparticles and the zeta potentials of both poly(NIPAAm-co-DMAPMA) microgels and neat Fe₃O₄ nanoparticles at various pH [215]; (d) Schematic illustration of integrating 300 nm thick thin silicon ribbon with PNIPAAm hydrogel and environmental SEM images of the buckling pattern based on the silicon-PNIPAAm integration [216]; (e) Setup of a projection system and the quick photo-responsiveness of PNIPAAm hydrogel incorporated with photochromic compound benzospiroopyran showing the light induced features formed on the hydrogel surface (unpublished work by Dr. Prithwish Chatterjee).

Although PNIPAAm may represent the current state of the art of environmentally responsive hydrogels, it confronts the following challenges. First, like typical hydrogels, PNIPAAm has weak mechanical properties due to the porous structure filled with water. The use of nanocrystalline clay as a crosslinker, such as Laponite, has been reported to increase the toughness of hydrogels by lowering crosslinking density to reduce the localized stress under deformation [217,218]. However, Laponite is highly hydrophilic and does not disperse in majority of organic solvents, which severely restricts its use to purely aqueous solvent systems [219]. Second, the response behavior of PNIPAAm in water is limited to its LCST nature. When developing materials for human-machine interfaces, a positive swelling transition where an external thermal or light stimulus drives the localized volume expansion is much more beneficial for natural sensory responses. Since a LCST governed swelling behavior only undergoes contraction upon heat or light, PNIPAAm or any other LCST-based hydrogels are not able to fulfill such a design requirement. In

contrast to LCST transition, polymers that demonstrate the property of UCST exhibit an opposition behavior where the swelling is enhanced at above a certain transition temperature and inhibited below this transition temperature. When choosing a media material outside of water, ILs as a novel type of solvents have been explored to reverse the phase transition of PNIPAAm into UCST behavior in replacement of water [220–223]. But its toxicity hinders the compatibility of hydrogels in biomedical applications. Third, it is difficult to realize certain subtle “maneuvers” in temperature responsive hydrogels, for example, localized volume transition and remote control, preventing hydrogels from being used in more sophisticated applications. Another type of stimuli, light, is less emphasized but an appealing option to overcome this shortcoming. Light can be easily focused into a beam of small size to aim at a specific area on a large hydrogel matrix and enable the more precise responses. Hydrogels have been combined with chromophore materials to realize light responsiveness [224–227]. Azobenzene, for example, has been employed to drive the volume transition of PNIPAAm based hydrogels by its reversible photo-isomerization [224,228]. However, the photo-responsive mechanism based on azobenzene groups as well as other prevailing chromophores requires the wavelength of light stimuli from either ultraviolet range (10 – 400 nm) or infra-red/near infra-red range (above 700 nm). Visible light (400 – 800 nm) responsive hydrogels are less harmful and can use more abundant sunlight so that are more demanded in designing human-machine interfaced devices, such as tactile display for visually-impaired.

In order to address the aforementioned challenges, a mechanically reinforced and visible-light responsive hydrogel with UCST characteristic was designed in this study by constructing an interpenetrating polymer network (IPN) hydrogels of polyacrylamide

(PAAm) and poly(acrylic acid) PAAc with chlorophyllin (Ch) incorporated as the chromophore. Interpenetrating network hydrogels have been known to demonstrate a greater degree of mechanical properties that traditional hydrogels fall short [229,230]. For instance, ionically crosslinked alginate network and covalently crosslinked PAAm network can form hybrid double network via the additional covalent crosslinking between the carboxyl group on alginate chains and the amine group on PAAm chains, resulting in high stretchability and toughness [231]. Both of the networks contribute to sharing the load where the unzipping of the ionic crosslinking blocks between guluronic acid and calcium in the alginate network effectively dissipates fracture energy and the covalent crosslinks in the polyacrylamide network withstands the permanent deformation [232–234]. This type of interpenetrated network, which is also called ionic-covalent entanglement (ICE), has been expanded to other novel and biocompatible choices of material systems, for example, carrageenan biopolymers and epoxy-amine systems based hydrogel [235], and calcium crosslinked gellan gum and genipin crosslinked gelatin based hydrogel [236]. Besides ionic crosslinking, physical crosslinking that has also been explored to design interpenetrating network hydrogel with biocompatible chitosan as a copolymer and showed excellent mechanical properties [237], where chitosan forms strong physical microcrystalline crosslinks that dissipates energy while the covalent crosslinked network resists the deformation [237,238]. In addition, the role of hydrogen bonding has demonstrated a significant contribution to the mechanical enhancement of interpenetrating network hydrogels as well [239]. As a weaker mode of bonding, hydrogen bonding can break before other types of bonding which facilitates the energy dissipation within the hydrogel network. We plan to utilize the interpenetrating network hydrogels to develop a

type of visible light sensitive and positive swelling environmentally responsive hydrogels. In this study, a pair of two polymers, PAAm and PAAc, is selected because of their attractive intermolecular polymer-polymer interactions allowing the complex formation by hydrogen bonding [240,241]. We anticipate the formation of an IPN network between the PAAm and PAAc polymer chains, as illustrated in Figure 2.3.2.2, and a resulting UCST swelling behavior via the formation and the dissociation of hydrogen bonding within the double network. We also hypothesize that chlorophyllin-incorporated interpenetrating network of PAAm-PAAc will present a mechanically enhanced, positive-swelling, and visible-light responsive hydrogel.

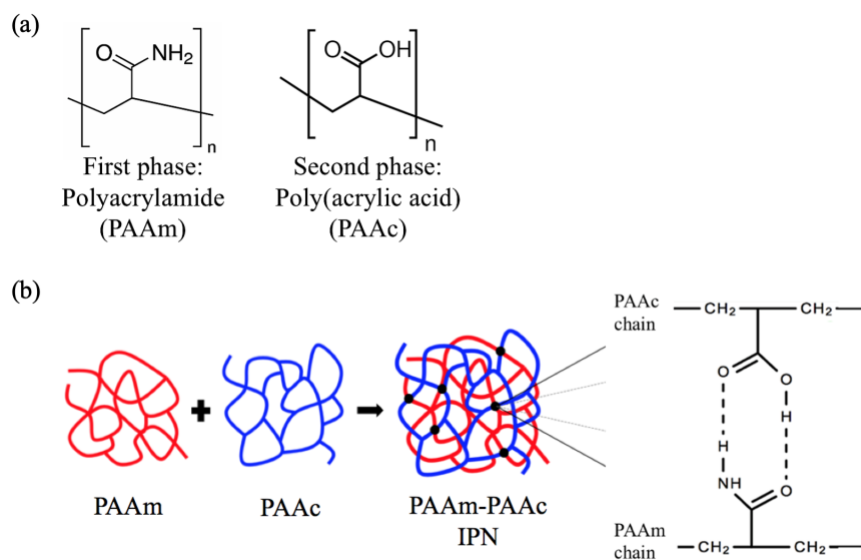


Figure 2.3.2.2. (a) Chemical structures of polyacrylamide (PAAm) and poly(acrylic acid) (PAAc); (b) A schematic illustration of the synthesis process to interpenetrating network hydrogel between PAAm and PAAc.

CHAPTER

3. METHODOLOGY

3.1 Materials

The ionic liquids, 1-butyl-3-methylimidazolium iodide ([BMIM][I]) (>98%) and ethylammonium nitrate ([EA][N]) (>97%), were purchased from Ionic Liquids Technologies Inc., and anhydrous lithium iodide (LiI) ($\geq 98\%$) was purchased from VWR International. The organic solvents, butyronitrile (BuCN) ($\geq 99\%$), gamma-butyrolactone (GBL) ($\geq 99\%$), and propylene carbonate (PC) ($\geq 99.7\%$), were purchased from Sigma-Aldrich Chemicals. Acrylamide (AAm), acrylic acid (AAc), *N,N'*-methylenebisacrylamide (MBAAm), azobisisobutyronitrile (AIBN), and chlorophyllin sodium copper salt (Ch) were also purchased from Sigma-Aldrich Chemicals. HPLC grade water was purchased from Fisher Scientific. All the chemicals were used as received without further purification.

3.2 Synthesis, Formulation, and Sample Preparation

3.2.1 Mixtures of Ionic Liquid and Solvents Based Electrolyte Solutions

The solution of ionic liquid/water/lithium salt mixtures were prepared by manual mixing and ultrasonic agitation by a Sonics VibraCell at 500W in an ice-water bath for 90 seconds. After mixing and sonicating, the solutions were visually inspected to be homogeneous and fully miscible. The incorporation of 5 mol% lithium iodide solid salt was added and dissolved to all the mixture electrolytes as a default component to increase the iodide concentration of the solution. The formulations of mixture solutions studied in this work are named by their composition in mol %, for example, a solution consist of 5

mol % [BMIM][I], 90 mol % water, and 5 mol % LiI is referred as [BMIM][I]/water/LiI-5/90/5.

The electrolyte solutions of ionic liquid/organic solvents/lithium salts mixtures were prepared following the same method mentioned above. Similarly, the formulations of such electrolyte samples are named by composition in mol%, for example, a sample electrolyte that consists of 5 mol% [BMIM][I], 20 mol% PC, 90 mol% GBL, and 5 mol% LiI is referred to as [BMIM][I]/PC/GBL/LiI – 5/20/70/5. If the solution contains only a single component that was used as received, it is referred to as “neat”.

3.2.2 Interpenetrating Polymer Network Hydrogels of Poly(acrylamide) and Poly(acrylic acid) with Incorporation of Chlorophyllin

The synthesis of the first phase PAAm chlorophyllin-containing hydrogel started with dissolving 2.35 mg AIBN as the initiator in 0.5 mL tetrahydrofuran (THF) solvent and followed by addition of 4.5 mL deionized (DI) water, 670 mg AAm, 10 mg chlorophyllin, 10 mg MBAA. After mixing and degassing, the solution was then heated at 68 °C for 8 hours to allow the polymerization reaction to proceed. Once the reaction was completed, PAAm hydrogel was rinsed with DI water several times, cut into disk-shaped geometry, and dried. The drying process included the air-drying step in the fume hood for 24 hours and then the vacuum-drying step in the oven at 40 °C for 24 hours.

The precursor solution for the second phase PAAc of PAAm-PAAc IPN hydrogel was prepared by mixing 0.345 mL (0.36 g) AAc monomer, 2.35 mg AIBN, and 10 mg MBAA in 5 mL DI water and followed by vortex mixing for 10 minutes. The previously obtained dry PAAm hydrogel was dropped into the AAc precursor solution and allowed to

soak for 24 hours at room temperature. After soaking, the above AAc solution was purged and then kept at 68 °C for 8 hours allowing the reaction to complete. During this process, AAc monomers were polymerized and crosslinked within the first phase network of PAAm gel matrix to form PAAm-PAAC chlorophyllin-containing interpenetrating network hydrogel.

3.3 Characterization Methods

3.3.1 Characterization of Mixtures Based Electrolyte Solutions

Differential Scanning Calorimetry

A differential scanning calorimeter (DSC) (TA Instruments Q-20) was used to characterize the low-temperature thermal behaviors of electrolyte sample solutions. The cooling step involved the use of liquid nitrogen via a quench cooling process from 40 °C to –160 °C, and then the heating step was performed from –160 °C to 40 °C at a controlled heating rate of 5 °C/min.

Rheology

A TA Instruments DHR-2 rheometer equipped with an Environmental Test Chamber (ETC) was used to perform a temperature sweep of samples solutions at a shear rate of 1 rad/s. Each sample solution was cooled from 25 °C down to –75 °C at a rate of 2 °C/min by liquid nitrogen and then heated up from –75 °C back to 25 °C at a rate of 10 °C/min. A TA Instruments AR-G2 rheometer was used for isothermal measurements at 25 °C on BuCN-based sample solutions at 1 rad/s and temperature was controlled by a water cooled/heated Peltier plate.

Fourier Transform Infrared Spectroscopy

The Fourier transform infrared (FTIR) spectra of electrolytes, including both neat and mixture solutions, were obtained by probing the sample under a vacuum environment using a Bruker IFS 66V/S FTIR with a deuterated lanthanum α -alanine doped triglycine sulphate (DLATGS) detector, a KBr mid-IR beam-splitter, and a Pike diamond-ATR module.

Raman Spectroscopy

The measurements were taken using a 70 mW wavelength stabilized diode laser with a wavelength of 633 nm as the excitation source, and the spectra were obtained using 1800 g mm^{-1} grating and 45 sec acquisition time.

Nuclear Magnetic Resonance Spectroscopy

A Bruker 400 MHz nuclear magnetic resonance (NMR) spectrometer was utilized to detect and confirm the intermolecular interactions among the ions in the ionic liquids and the solvent molecules in the organic carbonates, and ^1H NMR spectroscopy was performed 2 h after preparing 20 mg sample solutions in 1 mL deuterium oxide (D_2O).

Electrochemical Impedance Spectroscopy

All electrochemical experiments presented were conducted via a VMP3 multi-channel potentiostat (Bio-Logic). A customized conductivity cell was used to perform electrochemical impedance spectroscopy (EIS) for obtaining the ionic conductivities of the electrolyte sample solutions with respect to varying temperatures and chemical compositions. Platinum wire electrodes were fixed at a constant distance by customized glass tubing in the conductivity cell, and the cell constant was determined by calibration with 0.1 and 0.01 M potassium chloride solutions prior to measurements. The impedance

data of the electrolyte sample solutions were measured by an alternating voltage set to 10 mV, over frequencies sweeping from 900 kHz to 1 Hz. For low temperature measurements, the solution temperature was controlled using methanol/water mixture in a dry ice bath and monitored by an OMEGATTE HH303A thermometer/data logger (Omega). Measurements were taken after the temperature reading and the open circuit voltage stabilized for at least one minute.

Electrochemical Stability

A Dr. Bob's electrochemical cell purchased from Gamry, with a platinum disk (3 mm diameter) working electrode, a Pt wire as the counter electrode, and an Ag/AgCl (saturated KCl) reference electrode, was used to contain the prepared solution for the measurements of electrochemical window. The counter electrode and the reference electrode were separated from the solution to minimize contaminations during experiments using a glass frit and a bridge tube, respectively. The electrochemical windows of the electrolyte solutions at room temperature were determined via cyclic voltammetry at a sweep rate of 100 mV/s, where the steady profiles were reproduced for at least 10 cycles with no occurrence of undesired reactions. The potential in the presented graphs are respect to the normal hydrogen electrode (NHE).

3.3.2 Characterization of Interpenetrating Network Hydrogels

Swelling

The swelling weight of the hydrogel samples were measured gravimetrically after wiping off the excessive water from hydrogel surface. The hydrogel was incubated in water for 48 hours at room temperature prior to the weight measurement and any heat- or light-

induced swelling test. The swelling ratio of hydrogels, R , was calculated from the following equation:

$$R = \frac{W_s}{W_d} \times 100\% \quad (1)$$

where W_s and W_d stand for the swelling weight and the dry weight of hydrogel samples, respectively. The increase of the swelling weight upon stimuli, S , was calculated from the following equation:

$$S = \frac{W_t - W_0}{W_0} \times 100\% \quad (2)$$

where W_0 and W_t stand for the swelling weight of hydrogel sample before the exposure to the stimuli and after the exposure, respectively. In the visible-light induced swelling test, a commercial projector, an office computer, and a focusing lens were utilized together to irradiate visible white light to the hydrogel. A Thorlab digital optical and power energy meter was used to measure the light intensity of the projector.

Fourier Transform Infrared Spectroscopy

The attenuated total reflection Fourier transform infrared spectroscopy (ATR-FTIR) spectra were taken on the powders of ground dry interpenetrating network gel samples with a Bruker IFS 66V/S FTIR, wide-band Mercury Cadmium Telluride (MCT) detector, KBr mid-IR beamsplitter, and a Pike diamond-ATR module.

Scanning Electron Microscopy

The morphology of the synthesized interpenetrating network hydrogels was studied using a Philips FEI XL-30 Scanning Electron Microscopy (SEM). Prior to SEM, samples were dehydrated by a freeze-dryer (FreeZone1, Labconco Corporation) and glued onto the brass sample holders followed with a gold sputter coating process.

Mechanical Testing - Instron

The compressive tests were performed on synthesized hydrogels in their wet state by Instron E3000 test system at ambient room temperature. Three different strain rates, 0.5 mm/min, 0.05 mm/min, and 0.005 mm/min, were run to study the effect of ramp rate on the corresponding mechanical properties of prepared hydrogels. Prior to the test, all the samples were soaked in water for 48 h at room temperature to allow the hydrogels swelling to reach equilibrium.

Ultraviolet-Visible Spectrophotometry

The temperature dependent opacity transition of the interpenetrating network hydrogels was captured via a Cary 300 Bio UV-Vis spectrophotometer. The hydrogel sample was cut in the shape of a thin slice and was placed in the cuvette along with adequate amount of water. The temperature control function was utilized for a temperature range from 15 °C to 50 °C, and a laser wavelength of 600 nm was used.

Differential Scanning Calorimetry

The TA Instruments Q-20 DSC was also used to characterize the glass transition temperature of prepared hydrogels in their dry state. Prior to DSC measurement, the gel samples were first air dried at room temperature for 24 hours and then vacuum dried at 90 °C for 24 hours to further eliminate water retained in the network. During measurement, samples were subjected to cyclic heating and cooling with ramp rate of 10 °C/min.

CHAPTER

4. RESULTS AND DISCUSSION

4.1 Dual Ionic Liquid Based Liquid Electrolyte System for Low-Temperature Planetary Exploration

4.1.1 Effects of Water and Ethylammonium Nitrate (EAN) on Thermal Behaviors of ILs/Water/LiI Mixtures Based Electrolytes

Understandings in phase behaviors at varying temperatures are of great importance for electrolyte developments, especially when conduction mechanisms may change drastically depending on the state of matter. The differential scanning calorimetry (DSC) was employed to characterize the thermal transitions of prepared ILs/water/LiI mixture-based electrolyte formulations at low temperatures. As shown in Figure 4.1.1.1 (a), the addition of water into [BMIM][I]/LiI solution was observed to significantly shift the glass transition of the mixture solution. Pure [BMIM][I] exhibited a glass transition temperature (T_g) at -67.4 ± 1.4 °C. When the water content was increased in the mixture, the mixture solution displayed a lower T_g . With the highest water content, formulation [BMIM][I]/water/LiI-5/90/5 demonstrated the lowest T_g at -109.2 ± 0.1 °C among all the [BMIM][I]/water/LiI based mixture solutions. This phenomenon can be explained by the effect of molecular interactions that is reflected on the characteristics of the solutions at the bulk scale. Nickerson et al. reported the importance of the iodide-water hydrogen bonding present in the binary system based on [BMIM][I] and water mixtures, as two hydrogen atoms were pulled closely to the iodide ion and water molecules were able to self-arrange into the structured domain of [BMIM][I]. Their simulation via molecular dynamics uncovered that, when the water content was increased, some of the water molecules were

more surrounded by other water molecules than being drawn closer to iodide ions, resulting in a weaker iodide-water hydrogen bonding and an overall reduced intermolecular interaction in the [BMIM][I]/water binary system [179]. We hypothesize that, as the water content increases in our mixture system, water molecules can weaken the coulombic attractions between [BMIM] cations and iodide anions by forming hydrogen bonding with iodide anions, and the disrupted ion-pair formations lead to decrease in cohesive energy with a corresponding lower T_g . The glass transition is known to reflect the cohesive energy of a system, where low values of T_g indicates low cohesive energies [242,243]. Although adding water can decrease T_g of the electrolyte solution, it also presents a challenge by introducing other thermal transitions that take place over the scanning temperature range between 40 °C and -160 °C. With the highest water content, the formulation of [BMIM][I]/water/LiI-5/90/5 solution also showed a predominating endothermic peak, which could correspond to the melting of water aggregates in the solution with high water content. The formulation of [BMIM][I]/water/LiI-20/75/5 showed both exothermic and endothermic peaks, which indicated the interactions between ions and water molecules allowed the recrystallization to occur and followed by the melting process. Bernades et al. discovered similar phenomenon through their investigations of IL/water binary mixtures, concluding that distinct structural regimes in the systems are dependent on the water content in the solution [244]. Their findings showed that the system possessed a higher probability of forming water aggregates or networks at a water molar fraction of 0.8 and above, which are also in good agreement with our DSC results. While the formulations [BMIM][I]/water/LiI-5/90/5 and 20/75/5 both possess low T_g below -100 °C, their tendency to crystallize from strong water-water interaction made them an unfavorable

electrolyte candidate for low-temperature applications. On the other hand, the formulations of [BMIM][I]/water/LiI solutions, 75/20/5 and 40/55/5, demonstrated no other observable thermal behaviors than glass transition, which could be due to lower water molar fractions in the formulations; however, both formulations exhibit higher T_g as the cost. Since any solidifications caused by either glass transition or crystallization can negatively impact the transport properties of the ions and severely undermine the electrical property of the electrolyte, the identified thermal transitions above may suggest the limitations of the operating temperature for a [BMIM][I]/water mixture system.

To overcome the setback with the involvement of water as well as to retain a low T_g , a second ionic liquid component, [EA][N], was introduced to the electrolyte system. Figure 4.1.1.1 (b) showed a “smoothing” effect of incorporating [EA][N] into the solution in replacement of some portion of water. As [EA][N] was increased in place of water and [BMIM][I] was kept at 5 mol%, the peaks corresponded to crystallization of the electrolyte were significantly weakened and shifted towards lower temperatures for electrolyte formulation [BMIM][I]/[EA][N]/water/LiI-5/20/70/5 and 5/25/65/5. When [EA][N] was increased to 35 mol%, the endothermic peak of the electrolyte was no longer observed. At a different [BMIM][I] content of 10 mol%, the similar effect was also shown with formulations of [EA][N] content increased to 25 mol% or above to substitute for corresponding portions of water. Protic ionic liquids, such as [EA][N] and its alkyl derivatives, are known to demonstrate the similarity with water in forming three-dimensional donor-acceptor networks between the ammonium group on the ethylammonium and the oxygen from the nitrate via hydrogen bonding [245–247]. Therefore, we postulate that [EA][N] behaves very alike water in the system, with

ammonium groups available for constructing hydrogen bonding with iodide ions. Consequently, the addition of [EA][N] effectively substitutes the role of the replaced water in retaining T_g of the mixture system below $-105\text{ }^\circ\text{C}$ by interfering potential ion pairs. Meantime, the reduction of the water content also prevents the formation of water aggregates by lowering the possibility of water molecules surrounding one another, resulting in the absence of other undesirable thermal transitions. With [BMIM][I] and LiI both kept at 5 mol%, the magnitudes of the heat flow reflected the mitigated thermal events, as water concentrations were reduced by replacement of [EA][N], showing an observable trend between formulations [BMIM][I]/[EA][N]/water/LiI-5/20/70/5, 5/25/65/5, and 5/35/55/5. Among all the screened formulations, [BMIM][I]/[EA][N]/water/LiI-5/35/55/5, 10/30/55/5, and 10/25/60/5 demonstrated highly desirable thermal behaviors for developing low-temperature electrolyte with low glass transition temperatures all below $-105\text{ }^\circ\text{C}$, and no presence of other detectable phase transitions within the temperature range of our interest.

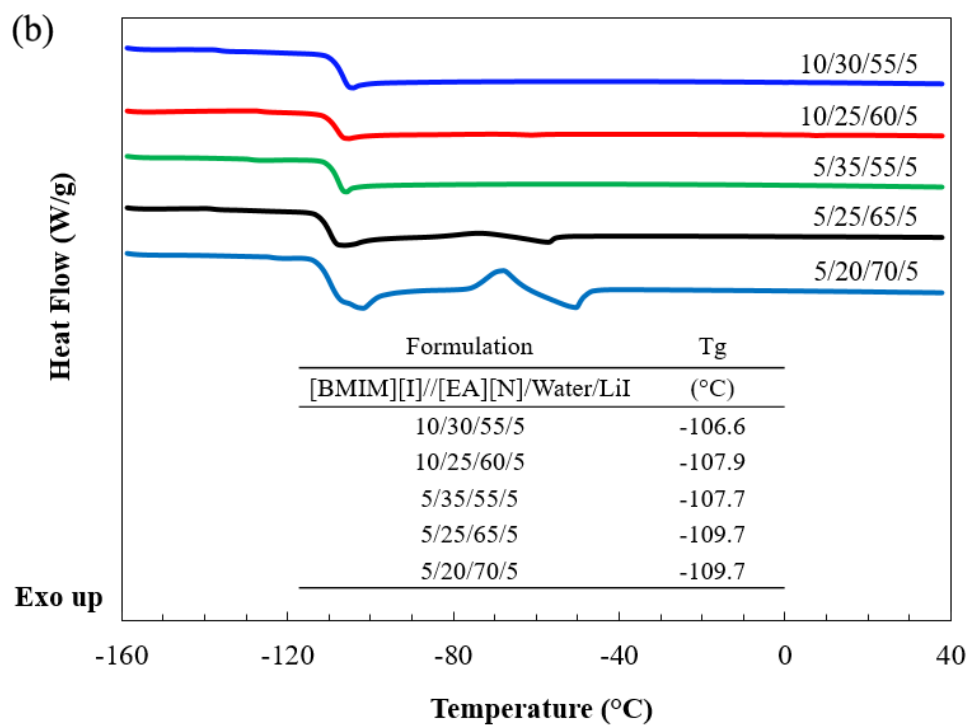
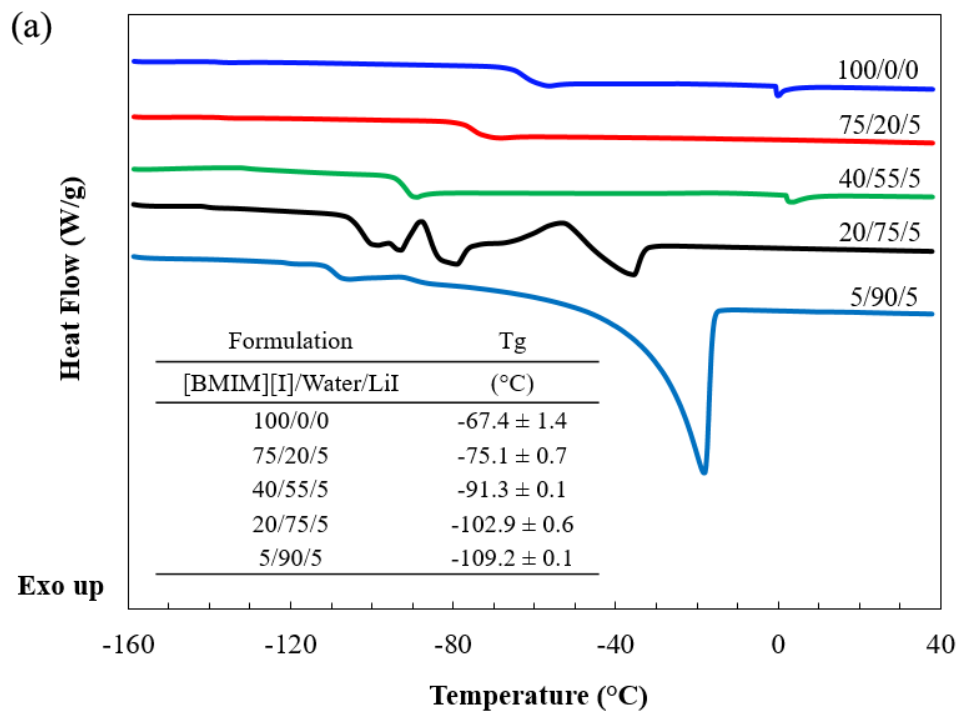


Figure 4.1.1.1. DSC heating curves from $-160\text{ }^{\circ}\text{C}$ to $40\text{ }^{\circ}\text{C}$ for different compositions of (a) [BMIM][I]/water/LiI and (b) [BMIM][I]/[EA][N]/water/LiI mixture solutions.

4.1.2 Effects of Molecular Interactions on Transport Properties of ILs/Water/LiI Mixtures at Low Temperatures

As ion transport ability of the electrolytes plays a vital role on their potential performance for electrochemical applications, the effects of optimized molecular interactions on resulting transport properties of the electrolyte systems with water and [EA][N] have also drawn our attention. In ionic liquids electrolyte systems, the movements of ions rely on self-diffusion as well as the influence from the applied electric field, with viscosities being one of the determining factors. In Figure 4.1.2.1 (a), a strong temperature dependency of the viscosity evolution was clearly shown on all the electrolyte formulations. When temperature decreased, the viscosity of the electrolyte increased exponentially because of the reduced molecular mobility and enhanced intermolecular cohesion at a lower temperature. [BMIM][I] is known for its high viscosity due to strong electrostatic attractions, so its concentration directly affects the resulting viscosity of the overall mixture solution. Due to the presence of the highest [BMIM][I] content, formulation [BMIM][I]/water/LiI-40/55/5 appeared to be the most viscous among all the measured formulations and experienced the most drastic escalation in viscosity as temperature dropped. In order to reduce the viscosity of mixtures, increasing water content to weaken interactions between [BMIM] and iodide ions becomes a viable solution, with the effect of composition on viscosity of [BMIM][I]/water binary systems reported [179]. Similarly, Seddon et al. explained the effect of water on viscosities of 1-butyl-3-methylimidazolium tetrafluoroborate at room temperature by the reduction of electrostatic attraction due to solvation and hydrogen bond formations [248]. With the least [BMIM][I] concentration and the highest water content, [BMIM][I]/water/LiI-5/90/5 solution showed the lowest

viscosity at room temperature and a very gradual growth from 25 to -25 °C, demonstrating the success of the strategy described above. At approximately -25 °C, however, [BMIM][I]/water/LiI-5/90/5 solution exhibited a sharp discontinuation with a significant viscosity increase of more than one magnitude, which could be related to the phase transition of such formulation. This unique feature could result from excess of water that were no longer hydrogen-bonded to the ions in the mixture. A similar observation was reported by Abraham and Abraham in silver/thallium nitrate and water mixtures, where the excessive water was referred as “free water” to form structures more resembling to the pure water with effects on viscosity and conductivity of the solution [249]. The viscosity evolutions of different formulations as temperature decreases display certain correlations with their respective DSC profiles, which can be potentially attributed to the impacts from the same alternation in molecular dynamics on both transport and thermal properties of the electrolytes. As previously revealed, the strong tendency of [BMIM][I]/water/LiI-5/90/5 solution to crystallize during cooling could result in an abrupt increase of viscosity for the mixture solution, where the formation of solids from water aggregates impede ion movements, making it extremely unfavorable for an electrolyte to be employed for low-temperature applications.

On the other hand, three selected [EA][N] incorporated ILs/water/LiI formulations with desired thermal behaviors, [BMIM][I]/[EA][N]/water/LiI-5/35/55/5, 10/30/55/5, and 10/25/60/5, all stood out by showcasing promising transport properties as potential electrolyte candidates. Due to reduced [BMIM][I] contents, they all demonstrated relatively low viscosities. Among them, [BMIM][I]/[EA][N]/water/LiI-5/35/55/5 showed the lowest viscosity with the least concentration of [BMIM][I] in the solution. In addition,

the viscosity profiles of [EA][N] incorporated formulations all showed smooth and continuous decreasing trends as temperature increased, confirming the results from DSC analysis that there was no presence of thermal transition within the temperature range of the rheological tests. We hypothesize that incorporations of [EA][N] provides sufficient screening effect for iodide ions, in replacement of some portions of water, to prevent the excess of water molecules from causing additional thermal transitions. A similar phenomenon was also reported by Aguilera et al. in their studied electrolyte system, where the solvation of lithium ions with the molecules of two organic solvents, ethylene carbonate and dimethyl carbonate, inhibited the formation of lithium bis-(trifluoromethanesulfonyl)imide complexes and thus effectively reduced the viscosity of the solution [248]. In our system, the viscosity curves of [EA][N] incorporated formulations shared alike features with [BMIM][I]/water/LiI-5/90/5 solution in terms of gradual slopes but without any instance of sudden interruptions, again confirming the effectiveness of [EA][N].

The temperature dependency of viscosity for liquids can be described by the well-known Arrhenius equation. For glass-forming ionic liquids or their mixtures, whose behaviors deviate from the Arrhenius equation especially at low temperatures, transport properties such as viscosity, diffusion coefficient and ionic conductivity can be better characterized by the Vogel-Fulcher-Tammann (VFT) equation. The viscosity, η , can be expressed in the modified version:

$$\eta = \eta_0 \exp [B/(T-T_0)] \quad (4)$$

where η_0 (Pa·s), B (K), and T_0 (K) are constants [250–253]. T_0 is defined as the theoretical ideal glass transition temperature, at which the flowing motions of mass transport

completely cease in the system, and B is the constant that can be related to the activation energy. The VFT equation is most extensively applied for depicting behaviors during α -relaxation, where crystallization is avoided due to the nature of supercooled liquids through a fast cooling process, with no drastic changes in transport properties until glass transition takes place [254]. Therefore, the VFT model fits well for the broad temperature window of our interest from room temperature to -75 °C and provide additional insights into the behaviors of the mixtures, allowing predictions to be extended down to glass transition temperatures. As shown in Figure 4.1.2.1 (b), the viscosities of [BMIM][I]/water/LiI and [BMIM][I]/[EA][N]/water/LiI mixture solutions followed the VFT behavior very well with all the correlation coefficients greater than 0.99. Okoturo and VanderNoot reported that the ILs having large cations with small alkyl group, for instance, methyl group, attached to the onium atom, would closely fit with the VFT model [252], which agreed with our observations on [BMIM][I] and [EA][N] based mixture solutions. The obtained values of the constants, η_0 , B, and T_0 , from the best-fit of the VFT equation are listed in Table 4.1.2.1. The B constant of the VFT equation became larger when the viscosity of the electrolyte formulation was higher, which indicated a greater activation energy was required for the diffusion of the ions in the solution. The value of the B constant for [BMIM][I]/water/LiI-40/55/5 was significantly larger than the values for [EA][N] incorporated formulations, which could be reflected by the highest viscosity and the steepest slope of its viscosity profile with respect to temperature. The trend was also seen by comparing among [EA][N] incorporated formulations, as the electrolyte formulation with a higher viscosity was associated with a larger B constant. These results hint that different transport behaviors of the mixture solutions can be related to their various activation energies, which increases

with the increasing concentration of [BMIM][I] in the solution. The higher activation energy for ion movements can imply the existence of a strong intermolecular interaction in the solution, where ions encounter more resistance to move past one another [253]. The formulation [BMIM][I]/water/LiI-40/55/5 serves as a clear evidence, where strong coulombic attractions occurred due to insufficient water molecules in separating neighbored ions, resulting in a lower fluidity. On the other hand, all the formulations showed rather close values of the T_0 constant, and no apparent correlation was found between the η_0 constant and the viscosity of tested electrolyte formulations. With all the positive effects of incorporating [EA][N] manifested, there was no obvious observation of any negative effect from adding such a second ionic liquid component in the electrolyte solution. Thus, further investigation is warranted on the dual IL system of [BMIM][I]/[EA][N]/water/LiI mixture solutions as promising candidates of low-temperature electrolytes.

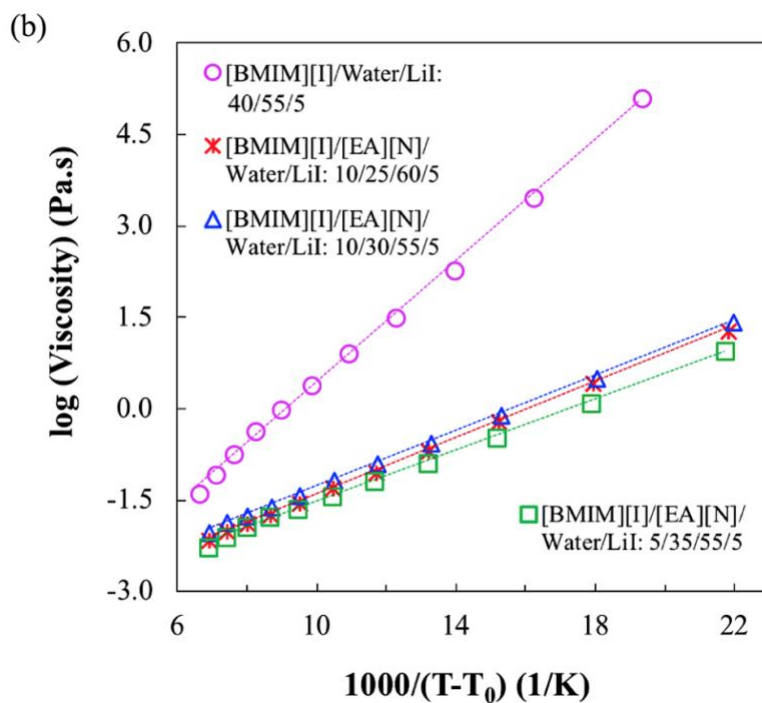
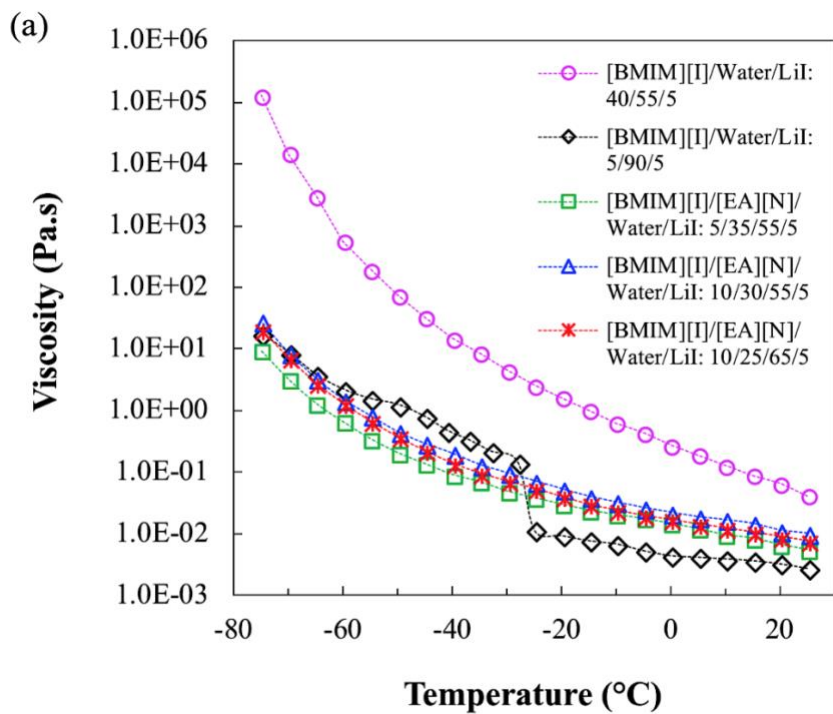


Figure. 4.1.2.1. Temperature dependence of viscosities for comparisons between selected electrolyte formulations plotted in the form of (a) viscosity as a function of temperature; (b) VFT equation.

Table. 4.1.2.1. Fitting parameters from VFT equation based on experimental viscosity data of [BMIM][I]/water/LiI and [BMIM][I]/[EA][N]/water/LiI mixtures.

Formulation	$\eta_0 \cdot 10^5$ (Pa.s)	B (K)	T₀ (K)	R²
[BMIM][I]/Water/LiI 40/55/5	3.0	1141.5	146.3	> 0.99
[BMIM][I]/[EA][N]/Water/LiI 10/30/55/5	25.0	549.1	150.6	> 0.99
[BMIM][I]/[EA][N]/Water/LiI 10/25/60/5	20.6	531.3	152.1	> 0.99
[BMIM][I]/[EA][N]/Water/LiI 5/35/55/5	24.5	483.5	152.1	> 0.99

The ionic conductivity is directly relevant to the device performance for the potential applications of using ILs-based electrolytes, especially at low temperatures when charge transport in the solution heavily relies on motions of cations and anions. According to previous analyses, we selected the formulations with favorable thermal and transport properties, [BMIM][I]/[EA][N]/water/LiI-5/35/55/5, 10/30/55/5, and 10/25/60/5, for characterization in conductivity via EIS. The other formulations that displayed high viscosity, which would impede the ion movements in the solution, or underwent undesired thermal transitions before reaching target operation temperature during cooling, which would contribute to dramatic increase of viscosity, were not extended to the low-temperature conductivity measurements. The results in Figure 4.1.2.2 (a) showed that the ionic conductivity of the ILs/water/LiI mixture solutions decreased exponentially as temperature decreased, confirming the inverse relation between conductivity and viscosity

over a wide temperature window. The formulation of [BMIM][I]/[EA][N]/water/LiI-5/35/55/5 exhibited the highest conductivity, due to its lowest viscosity, followed by [BMIM][I]/[EA][N]/water/LiI-10/30/55/5 and 10/25/60/5 with the second and third highest conductivity, respectively, in correspondence to their viscosities. At approximately $-75\text{ }^{\circ}\text{C}$, which was the lower limit of our measurement temperature, the electrolyte solutions from all abovementioned formulations remained fluidic.

In addition to viscosity, other factors can also impact the conductivity of a mixture electrolyte system based on ILs. The intrinsic nature of ILs can further complicate the relationship between viscosity and ionic conductivity with their unique molecular interaction. Jarosik et al. investigated the conductivity of ionic liquids in different mixtures and considered the effect of ion-ion interactions on the charge transports of ILs. In their study, for example, the binary system of 1-ethyl-3-methylimidazolium tetrafluoroborate ([EMIM][BF₄]) and water displayed a maximum conductivity with a molar fraction of [EMIM][BF₄] at approximate 0.1, while the viscosity kept decreasing with increasing water content. Their interpretation concluded that formations of stable ion aggregates, which could no longer behave as charge carriers, was the underlying reason why the highest conductivity can be obtained by an optimal composition to maximize the disruption of ion-pairs by intermolecular forces between [EMIM][BF₄] and water [255]. Ruiz et al. also reported the similar type of parabolic relationships between the conductivities and the compositions of n-butyl-n-methylpyrrolidinium bis(trifluoromethanesulfonyl)imide mixing with a variety of molecular solvents [166]. Although such a factor can often be overlooked among relatively simple systems of conventional electrolytes, where ions are mostly 100% dissociated, it becomes incredibly crucial in ILs-based electrolytes because

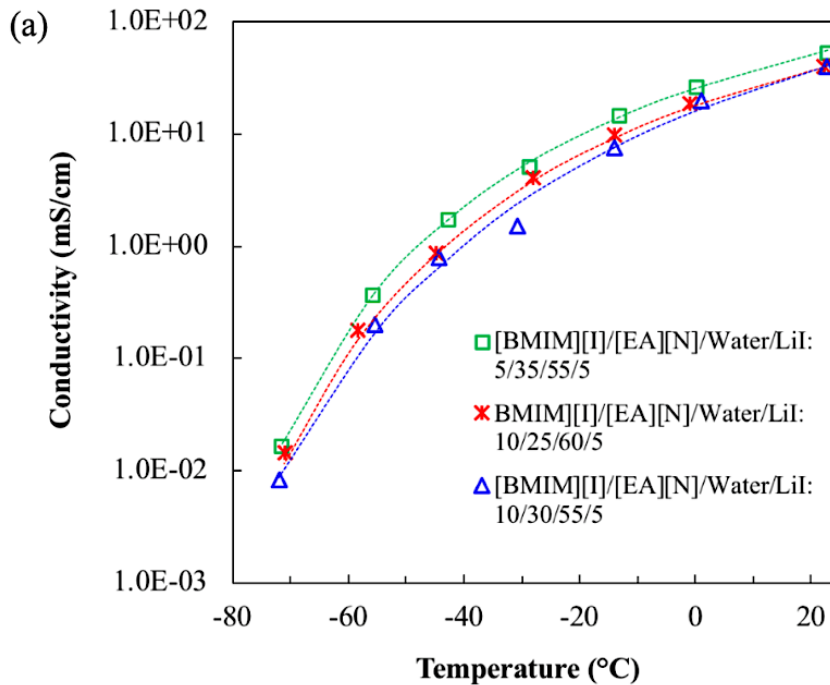
the involvement of several ion-ion interactions between different charged species can potentially cap the conductivity performance despite the reduction of the viscosity. For all the formulations presented in Figure 4.1.2.2 (a), however, it did not appear to be the case as the viscosity remained to be the dominant factor of our electrolyte systems over the tested temperature range. Since their compositions were tuned for desirable thermal properties, the existence of ion clusters was minimized. The negative impact of ion-ion interactions, which could be alarming in other ILs based electrolytes, was not observed in our dual IL system due to the strategy of incorporating [EA][N] and water to enhance the conductivity at low temperatures.

Resembling the previous discussion on viscosity, the temperature dependence of the ionic conductivity, σ , for the electrolyte solutions in this study can also be depicted by the VFT behavior in the following expression:

$$\sigma = \sigma_0 \exp [-B/(T-T_0)] \quad (5)$$

where constant σ_0 is the limiting conductivity at indefinite high temperature[256,257]. As shown in Figure 4.1.2.2 (b), the measured conductivities of selected [BMIM][I]/[EA][N]/water/LiI mixture solutions can be fitted by the VFT equation very well with all correlation coefficients greater than 0.99. The fitting results for each tested formulation are summarized in Table 4.1.2.2. The formulation with a higher conductivity is associated with a smaller value of the constant B, indicating a lower activation energy barrier for ions to overcome in such a solution system. This finding is consistent with the previous results from viscosity analyses, where a smaller value of the constant B also reflects a lower viscosity as viscosity is inversely proportional to ionic conductivity. In addition, the VFT behavior can be useful to predict the conductivity of ILs/water/LiI

mixture solutions outside the temperature range of measurements. For example, we experimentally observed that among all three tested formulations [BMIM][I]/[EA][N]/water/LiI-10/30/55/5 with its largest B constant suffered the most conductivity drop as temperature decreased, but it also presented the largest value of constant σ_0 which hinted that it could potentially have the highest limiting conductivity at a much more elevated temperature when diffusion is no longer the dominating limitation to ionic charge transfer in such solution systems. For the focus of this project in developing a low-temperature electrolyte solution, the formulation of [BMIM][I]/[EA][N]/water/LiI-5/35/55/5 thus far demonstrated the highest conductivity as well as the most desirable thermal properties. As the best candidate, it is further assessed by the Walden plot analysis in the next section for comparisons with other reported electrolyte systems based on different ILs.



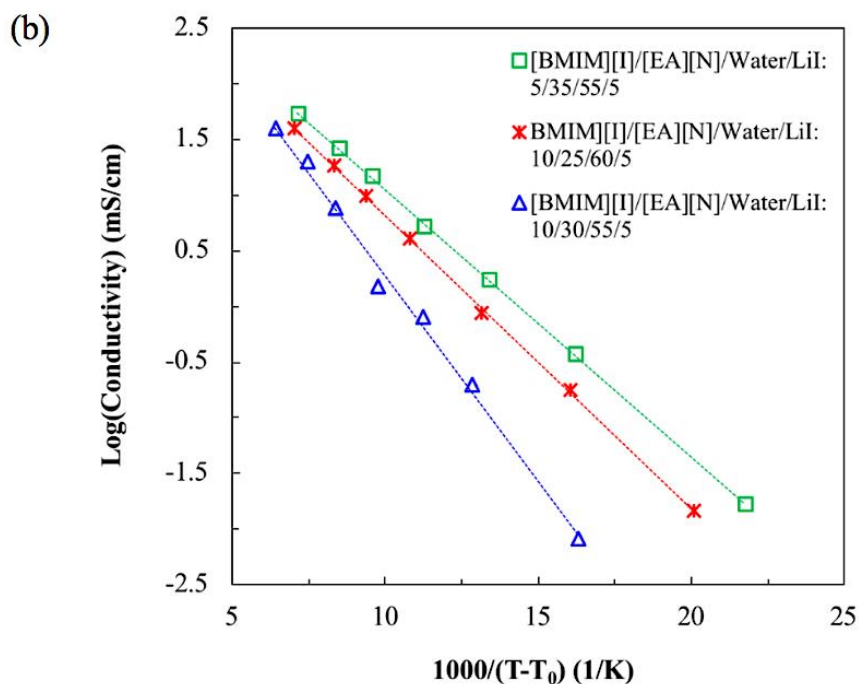


Figure. 4.1.2.2. Temperature dependence of conductivity for comparisons between selected electrolyte formulations plotted in the form of (a) conductivity as a function of temperature; (b) VFT equation.

Table 4.1.2.2. Fitting parameters from the VFT equation based on experimental conductivity data.

Formulation	σ_0 (mS/cm)	B (K)	T ₀ (K)	R ²
[BMIM][I]/[EA][N]/Water/LiI 10-30-55-5	9540.7	852.5	139.8	> 0.99
[BMIM][I]/[EA][N]/Water/LiI 10-25-60-5	3077.9	622.4	152.3	> 0.99
[BMIM][I]/[EA][N]/Water/LiI 5-35-55-5	2830.2	552.9	155.6	> 0.99

4.1.3 Effects of Water and [EA][N] on Ionicity of ILs/Water/LiI Mixtures via Walden Plot Analysis

In addition to respective discussion on viscosity and ionic conductivity, here we correlate these two properties and analyze their evolutions simultaneously. The conductivity of ILs based electrolytes does not solely depend on viscosity, thus the other influential component, namely the ionicity, is worth further investigation. Ionicity represents the extent of ion disassociation, which also shows strong dependence on molecular interactions of the system. The relationship between the viscosity and the molar ionic conductivity of ionic liquids can be quantitatively illustrated by the Walden rule [258–260]:

$$\Lambda\eta = \text{constant} \quad (6)$$

where Λ is the molar conductivity and the constant is material dependent. As previously discussed, the consideration of ion-ion interactions highlights the concepts of ionicity for studying transport properties of the ILs based electrolytes. The Walden plot allows us to evaluate the transport behavior of the ILs/water/LiI electrolyte system from our development and compare it to similar systems of ionic liquids reported in the literatures containing at least one of the same cations or anions. As shown in Figure 4.1.3.1, the plot is constructed by the molar conductivities versus the reciprocal of viscosities. The diagonal line across the plot with a slope that equals to 1 represents the ideal Walden line, which is derived from 0.01 M aqueous KCl solution, indicating the complete dissociation of the ions in the dilute solution. The departure of the data points deviating above or below from the ideal line can suggest the decoupling or clustering of the ions, respectively, which provides an approach to characterize the ionicity of the solution. If the values are close to the ideal

line, they advise good ionicity of the solution. Otherwise poor ionicity is informed for systems far below the line. Ueno et al. classified the dependency of ionicity on structures and combinations of cations and anions based on their Lewis acidity and Lewis basicity, and their work summarized that higher Lewis acidity or basicity of cations and anions, respectively, suggests stronger ion-ion interactions, resulting in ion aggregates and therefore a lower ionicity [261]. The primary ionic liquid of our systems, [BMIM][I], consists of an imidazolium cation with moderate Lewis acidity and an halide anion with high Lewis basicity. According to the definitions established by Ueno et al., such a combination indicates poor ionicity. However, when water and [EA][N] are incorporated at a designed concentration, the mixture system demonstrates molar conductivities comparable with typical ILs that have good ionicity at room temperature. Figure 4.1.3.1 showed comparable ionicity of the formulation [BMIM][I]/[EA][N]/water/LiI-5/35/55/5 with other electrolyte systems that are commonly categorized as good ionic liquids. On the other hand, 1-butyl-3-methylimidazolium bromide ([BMIM][Br]) [262], which has similar combinations of cation and anion with [BMIM][I], exhibits the feature of poor ionicity with its profile significantly deviating from the ideal line even at room temperature. This remarkable improvement can again be attributed to effects of incorporating water and [EA][N], which validates the success in minimizing formations of ion clusters discussed in the previous section. As temperature decreases, the deviation from the ideal line becomes larger for our formulation, implying a weaker dissociation of ions due to the presence of stronger hydrogen bonding at lower temperatures. The weakened dissociation of ions can also be seen on 1-butyl-3-methylimidazolium acetate ([BMIM][CH₃OO]) [263] in response to the temperature drop, while the enhanced dissociation of ions appears on [EA][N] [264],

1-butyl-3-methylimidazolium tetrafluoroborate ([BMIM][BF₄]) [243] and [BMIM][Br] [262] at varying degrees. Despite the descending ionicity, the highly linear relation between conductivity and viscosity showed that the ionic conduction of the dual ionic liquids system in our formulation still obeys the Walden rule well over the temperature range of our investigation. Moreover, the studies of other similar systems from literatures were not extended into such a low temperature region as this work did. To our best knowledge, it is the first time that the ionic conductivities and viscosities of any [BMIM][I] based electrolyte were reported below $-70\text{ }^{\circ}\text{C}$.

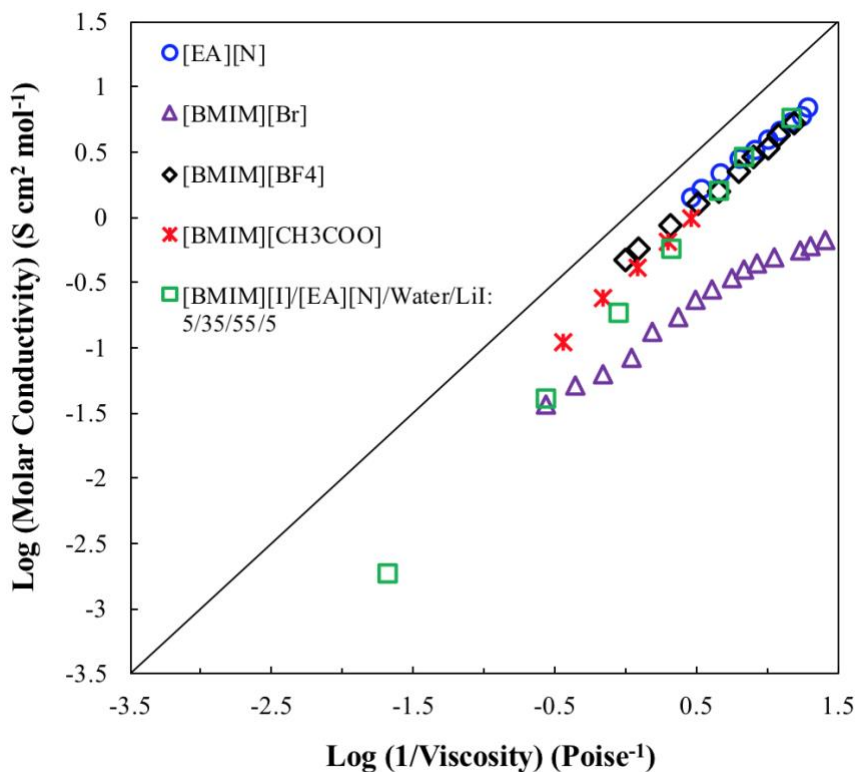


Figure. 4.1.3.1. Walden plot of the formulation [BMIM][I]/[EA][N]/water/LiI-5/35/55/5 in comparisons with other similar IL systems from literatures including [EA][N] [264], [BMIM][Br] [262], [BMIM][BF₄] [243], and [BMIM][CH₃COO] [263].

4.1.4 Electrochemical Stability of ILs/Water/LiI Mixtures

The electrochemical stability is another important property of electrolytes because the electrochemical window (EW) determines the proper range of potential that can be applied to a specific electrolyte system, especially as the sensing mechanism of a MET seismometer relies on the electrochemical reactions of the I-/I₃⁻ redox couple. Cyclic voltammetry (CV) analyses were conducted to identify the EW for the proposed best candidate of the electrolyte formulation, [BMIM][I]/[EA][N]/water/LiI-5/35/55/5, targeting I-/I₃⁻ redox reactions. In addition, two other formulations, [BMIM][I]/water/LiI-5/90-5 and [BMIM][I]/[EA][N]/water/LiI-10/30/55/5, were also measured to investigate the effects of the [EA][N] involvement and the iodide ion concentration, respectively. Figure 4.1.4.1. illustrated the CV profiles of the above three electrolyte systems, scanned from -0.6 V to 0.4 V and then reversed. The formulation [BMIM][I]/[EA][N]/water/LiI-5/35/55/5 showed no apparent current at the beginning until reaching approximately 0.32 V, indicating that I- oxidations were electrochemically activated at the anode. The reverse scan exhibited a cathodic current as an evidence of I₃⁻ reductions, which peaked at 0.305 V, marking a depletion of I₃⁻ at the surface of the electrode. The other two formulations behaved similarly, with slight shifts in the starting potentials of anodic reactions and the peaked potentials of cathodic currents, depending on the specific compositions. After I₃⁻ reductions, no other measurable electrochemical events were noticed. It was observed that I- never encountered depletions throughout anodic polarization, while I₃⁻ were mostly consumed during reductions right after generated from oxidations, disclosing that when freshly prepared the majority of iodide element from [BMIM][I] and LiI remained as I-. The involvement of [EA][N], which is crucial for optimizing the physicochemical

properties of the electrolyte system, did not introduce undesired reactions nor affect the behaviors of I-/I₃- redox couple, as evidenced by the high similarity between the profiles of the [BMIM][I]/water/LiI-5/90/5 and [BMIM][I]/[EA][N]/water/LiI-5/35/55/5 formulations. Interestingly, when comparing the three systems, [BMIM][I]/[EA][N]/water/LiI-10/30/55/5 did not generate a higher current despite containing up to 5 mol% more I- than the other two formulations. Because I- never depleted, the magnitude of the produced current is presumably determined by the ion mobility and kinetics but not the concentration. Applying potentials outside the identified EW may result in water reductions and I- oxidations, leading to electrode poisoning and irreversible composition changes, which would interfere with the working principle and eventually disable sensing operations. When operating within the controlled EW from -0.6 to 0.4 V, I-/I₃- redox reactions were successfully activated with no unexpected event from other species, which indicates good electrolyte stability and also provides a guidance of proper operating parameters for electrochemical devices.

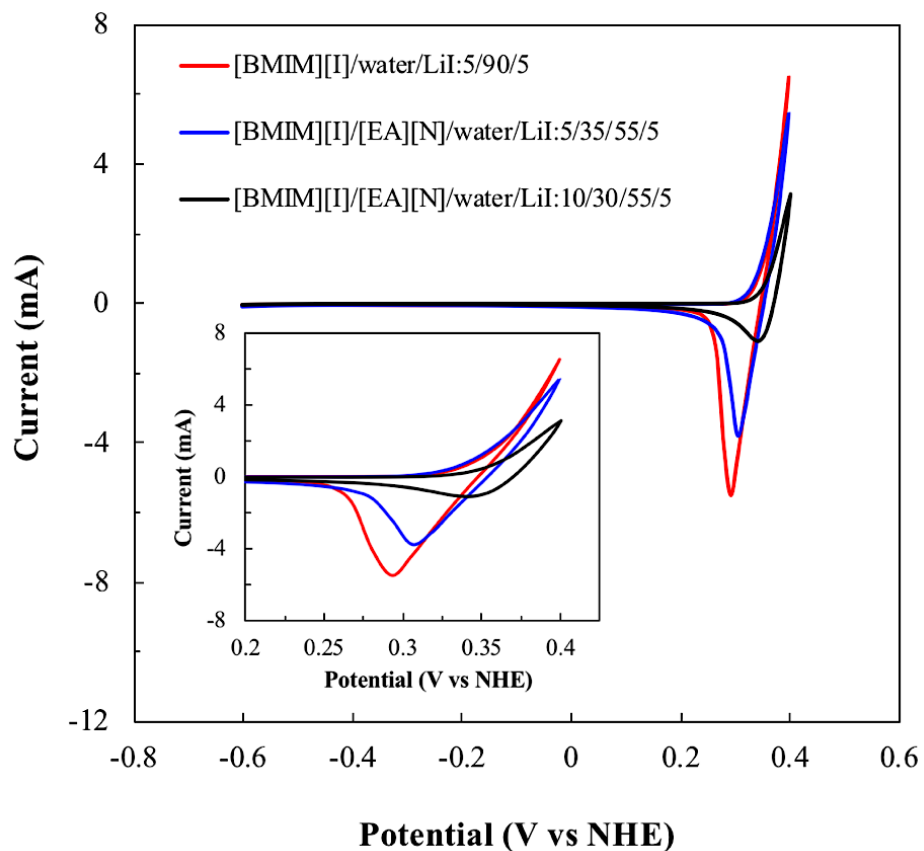


Figure 4.1.4.1. The identified EW for selected electrolyte formulations of ILs/water/LiI mixture solutions. All obtained profiles are steadily reproduced for ten cycles with no occurrence of reactions from other species except for the I-/I₃⁻ redox couple with zoom-in details presented in the inset.

4.1.5 Sensing Performance of Developed ILs/Water/LiI Mixtures Based Electrolyte for MET Seismometer

The sensing performance of developed dual IL electrolyte formulation was tested by an in-house built MET seismometer at Arizona State University. The device overview of a MET seismometer is shown in Figure 4.1.5.1. The targeted electrochemical redox reactions between iodide and triiodide ions take place at the surface of the electrode, which are the inner cross-sectional areas of micro-channels on the sensing element. There are two different approaches to fabricate the sensing element for a MET device. One approach is a micro-electromechanical system (MEMS) approach, which utilizes microfabrication techniques (photolithography, wet etch, reactive-ion etch, etc.) to create precisely controlled microstructures on the base of a silicon wafer and yield a better symmetry of the electrode geometry to potentially reduce the noise floor of the sensor. The other approach is a mechanical approach, which is applied to make the sensing element that is used in the MET seismometer to characterize and validate the electrolyte formulation in this work. In the mechanical route, the sensing element is made of four thin platinum metal layers configured in a designed order of anode-cathode-cathode-anode (A-C-C-A) and placed perpendicular to the direction of the liquid flow in the device, and each layer was separated by an insulation coating while those inner cross-sectional areas of micro-channels are exposed to the electrolyte body. After the sensing element is fabricated, it is inserted into the sensor shell via a slit opening along with a 3D-printed sensing element holder, which provides structural support and mechanical protection to the sensing element. Once the sensing element is put in place, epoxy is applied to seal the opening and left still for curing. Polydimethylsiloxane (PDMS) diaphragms are also used to not only seal both sides of the

sensor shell to contain the electrolyte body but also provide elastic boundaries to allow the flow of the liquid in response to external motions. A small injection hole on the inner side of the sensor shell is kept open by designing for transferring the liquid electrolyte into the sensor body.

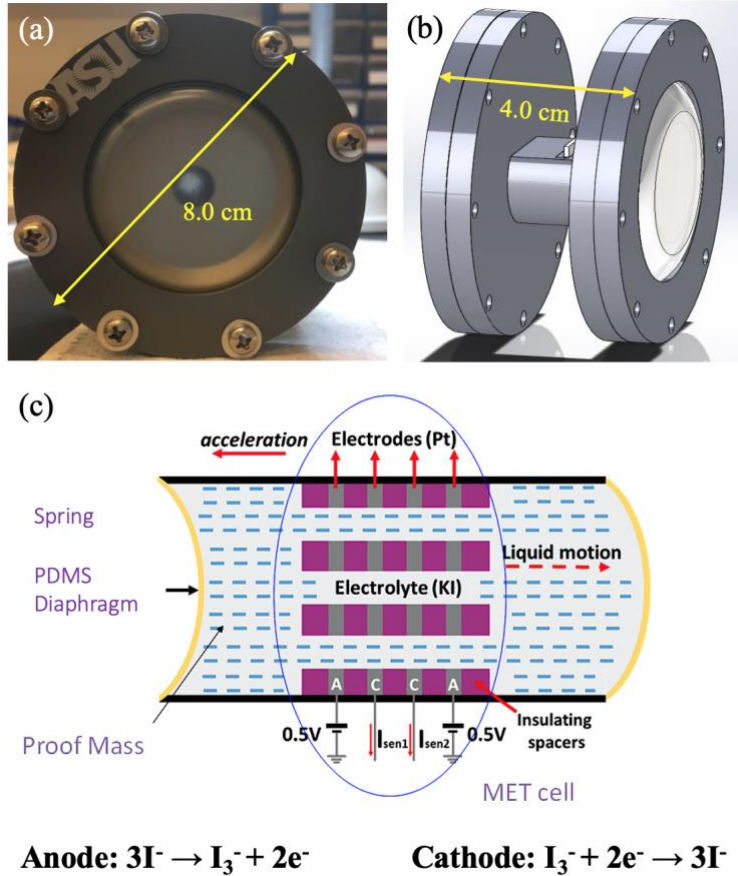


Figure 4.1.5.1. A device overview of a miniature MET seismometer that is used for the earthquake detection with selected electrolyte formulation [EA][N]/[BMIM][I]/water/LiI-10/25/60/5 in this study. (a) a top view of the sensor; (b) a side view of the sensor (via SolidWorks); (c) an illustrative cross-sectional view of the sensing element that consists of two pairs of electrodes in a designed anode-cathode-cathode-anode (A-C-C-A)

configuration, where the reversible electrochemical redox reaction between iodide and triiodide ions takes place as the key sensing mechanism.

The electrolyte formulation selected for the MET seismometer sensing performance testing is [EA][N]/[BMIM][I]/water/LiI-10/25/60/5 after considering its overall thermal, transport, and electrochemical properties. Upon completion of the hardware assembling, a desired volume of electrolyte is manually prepared using the method described in the previous chapter. Prior to filling, a degassing procedure is carried out for three cycles to eliminate the air dissolved in the electrolyte during preparation at an ambient environment, using liquid nitrogen and vacuum pump. The filling process is manually operated in a controlled helium environment to minimize the exposure to air and carefully observed to avoid overflow or any gas bubble trapped inside of the device. The shape of PDMS diaphragms can serve as an indicator for the filling process, where a neutral position of the diaphragms is preferred to ensure no additional stress is induced by any excessive volume of the liquid electrolyte body. After filling the electrolyte, both MET and a commercial force-feedback, broadband reference seismometer (Guralp CMG-3T) were placed on a specialized, concert-based testing pier in advance and stayed connected to the readout circuit and the power source during the entire testing period, standing by for monitoring and detecting earthquakes.

The detected earthquake reported in this study occurred at 04:27:05 (UTC) on November 20th, 2019, and the location is 124 kilometers southwest of Puerto Madero, Mexico (13.892°N, 93.209°W). It had a magnitude of 6.3 and a depth of 14.6 kilometer,

according to United States Geological Survey (USGS). Figure 4.1.5.2 discloses the geographical information of this detected earthquake as well as the earthquake wave profile recorded by the reference sensor upon its arrival at testing location in Tempe, Arizona. The comparison of the pier testing results for such an earthquake detection between the reference and MET seismometer filled with electrolyte formulation [EA][N]/[BMIM][I]/water/LiI-10/25/60/5 is shown in Figure 4.1.5.3. The overall detected signals from both sensors are filtered by different frequency ranges to analyze the sensing results with respect to frequencies. In the snapshot of each respective frequency range across from 0.03 Hz to 0.3 Hz, the green and blue lines represent the signals from MET seismometer and the reference sensor, respectively, while the overlay of the two (after scaling) displayed in the bottom. In the electrolyte that contains iodide ions, triiodide ions also exist at a very low concentration via the redox reaction equilibrium between iodide and triiodide ions. When a MET seismometer is at its standby state, the triiodide ions react instantly at the electrode surface of cathode and stay locally depleted, creating and retaining its concentration gradient as a function of the distance from the electrode through the volume of the electrolyte body. When the earthquake wave traveled to the testing pier, the motion was able to trigger the flow of the electrolyte in the MET seismometer. As the chemical equilibrium was disturbed, the cathode was supplied by a suddenly increased amount of triiodide ions from the flow within a short period and generate an electrical signal in the format of current that can reflect the external motion. In the reported frequencies, MET seismometer was able to pick up the earthquake signals and rendered the resemblance with the signals from the reference seismometer within the same time window. The similarity of the waveforms between MET and the reference is compared in

the overlay of their signals, and the best waveform match (83%) is observed at the frequency range between 0.05 Hz and 0.07 Hz with a minor delay of 0.32 second. It is also noticeable that MET has a higher noise floor than the reference seismometer, although their sensing principles are fundamentally different.

The results from this recorded event showed that MET seismometer using the formulation [EA][N]/[BMIM][I]/water/LiI-10/25/60/5 successfully detected the earthquake with a good signal match in comparison with a commercial seismometer, validating not only the material development for a task-specific electrolyte containing iodide and triiodide redox couple but also the hardware development of fabricating a MET-based, miniature seismometer. Such obtained testing results also warrant our future work, including low-temperature pier-testing, field testing, and other flight qualifications in collaboration with (NASA). Meanwhile, we also see room for continuous development to potentially improve the sensitivity and lower the noise floor of MET seismometer. From a materials perspective, one of the approaches is to introduce iodine into the electrolyte. Because iodine at a low concentration has an effect to reduce back-electron transfer reactions [265], further optimization in the liquid electrolyte materials can be performed to enhance the sensitivity of MET seismometer.

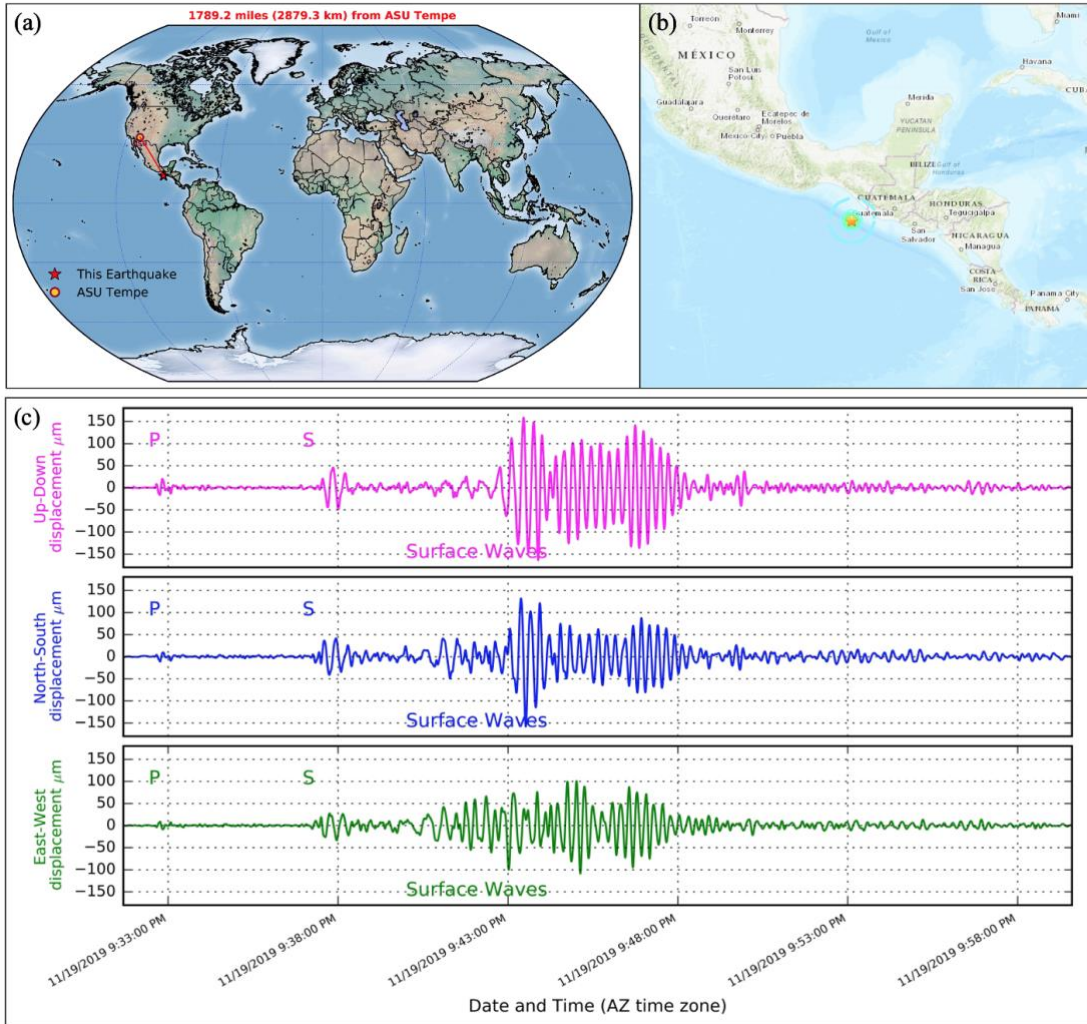
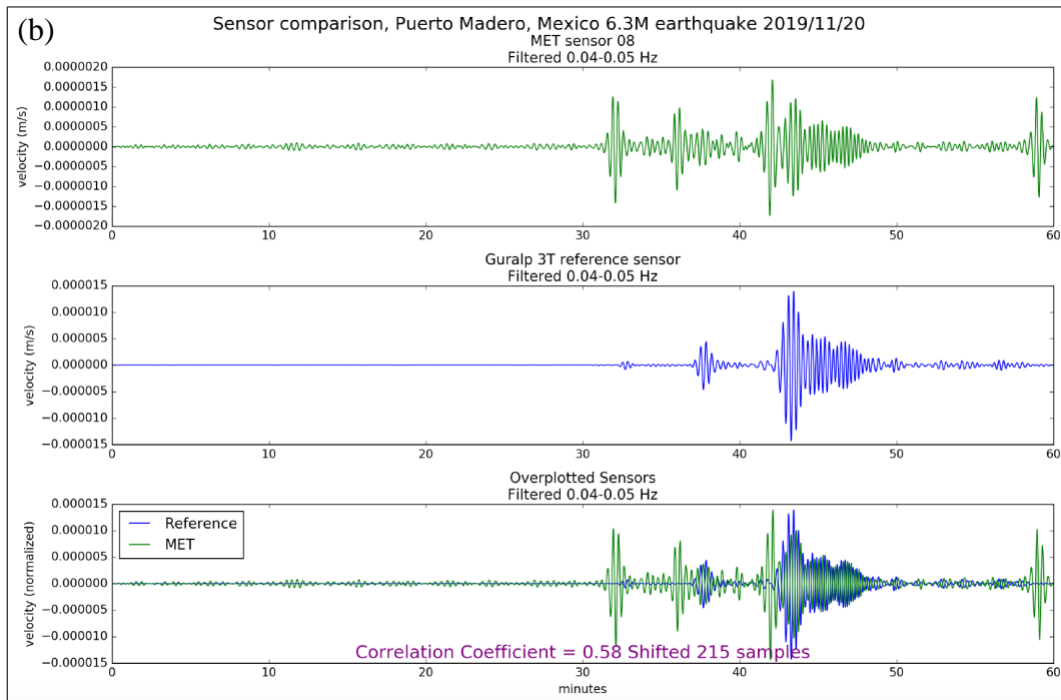
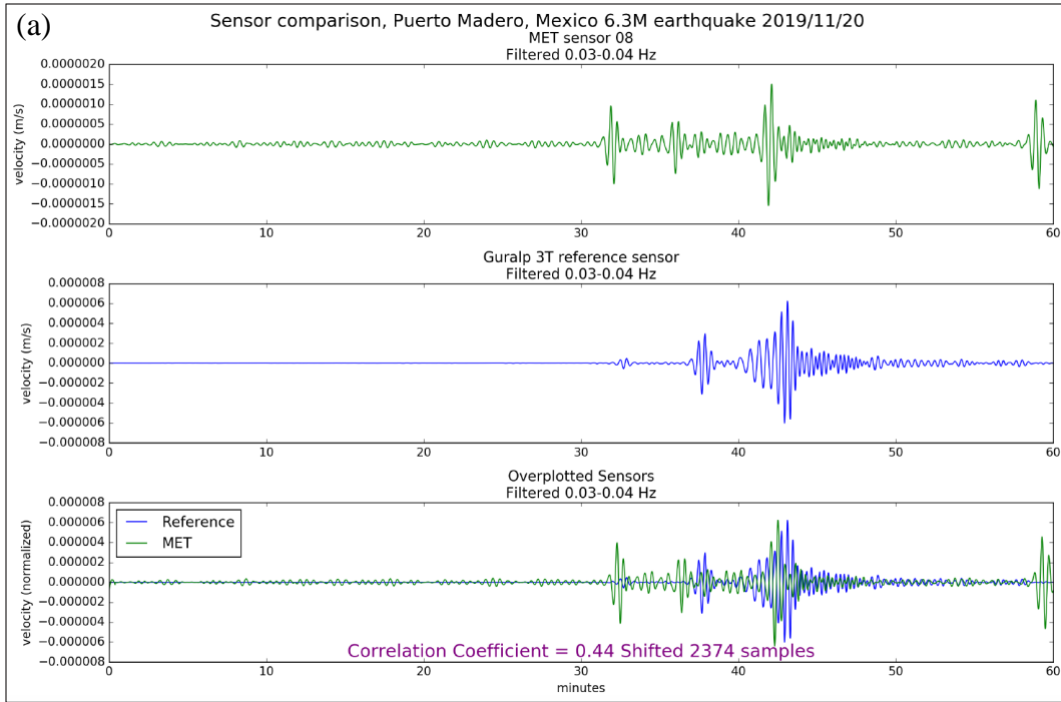
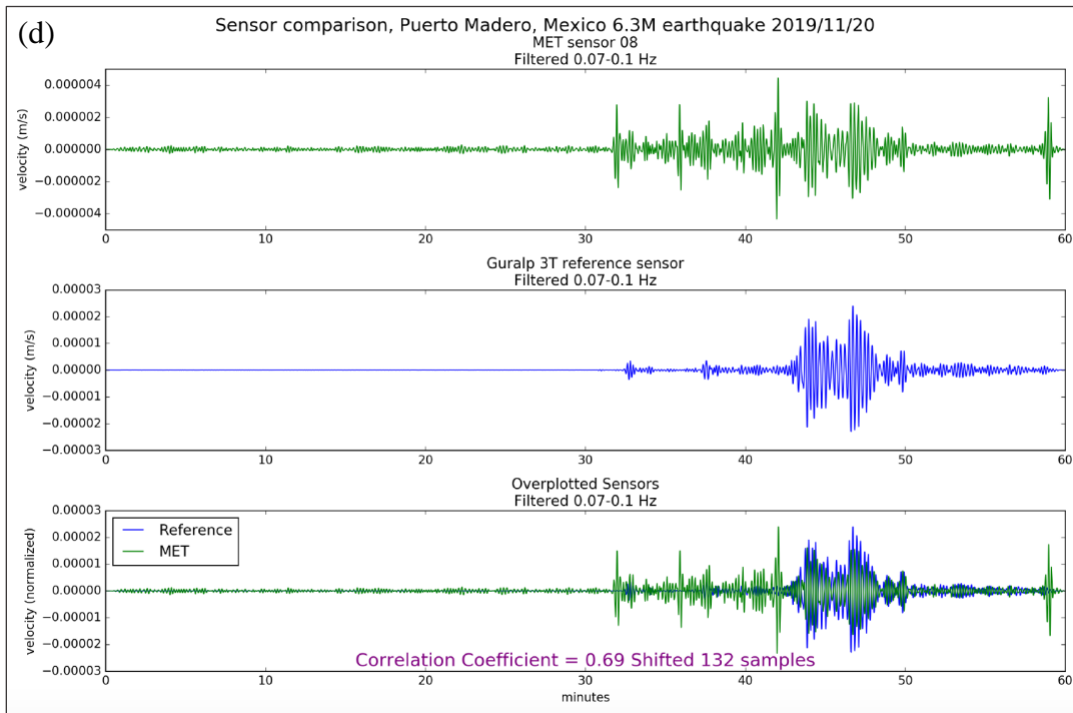
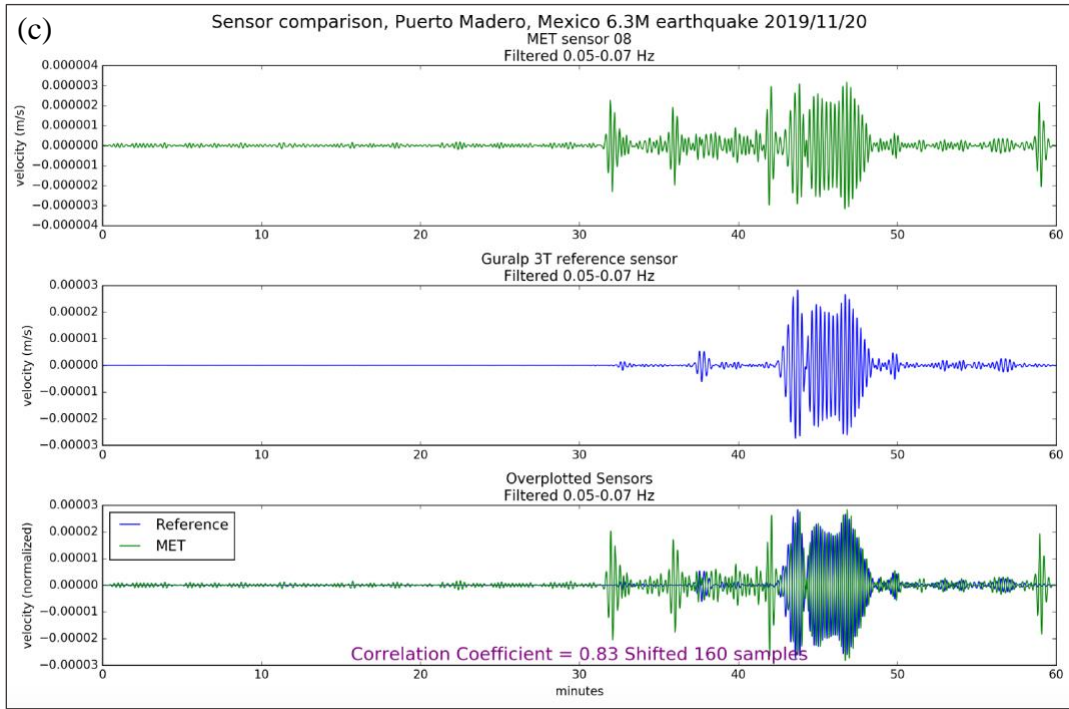


Figure 4.1.5.2. An event overview of the detected earthquake, including the geological information from (a) ASU earthquake monitoring system by Dr. Edward Garnero from School of Earth and Space Exploration and (b) The Earthquake Hazards Program by USGIS as well as (c) the recorded earthquake waveform information at the testing pier on ASU Tempe Campus also by Dr. Edward Garnero.





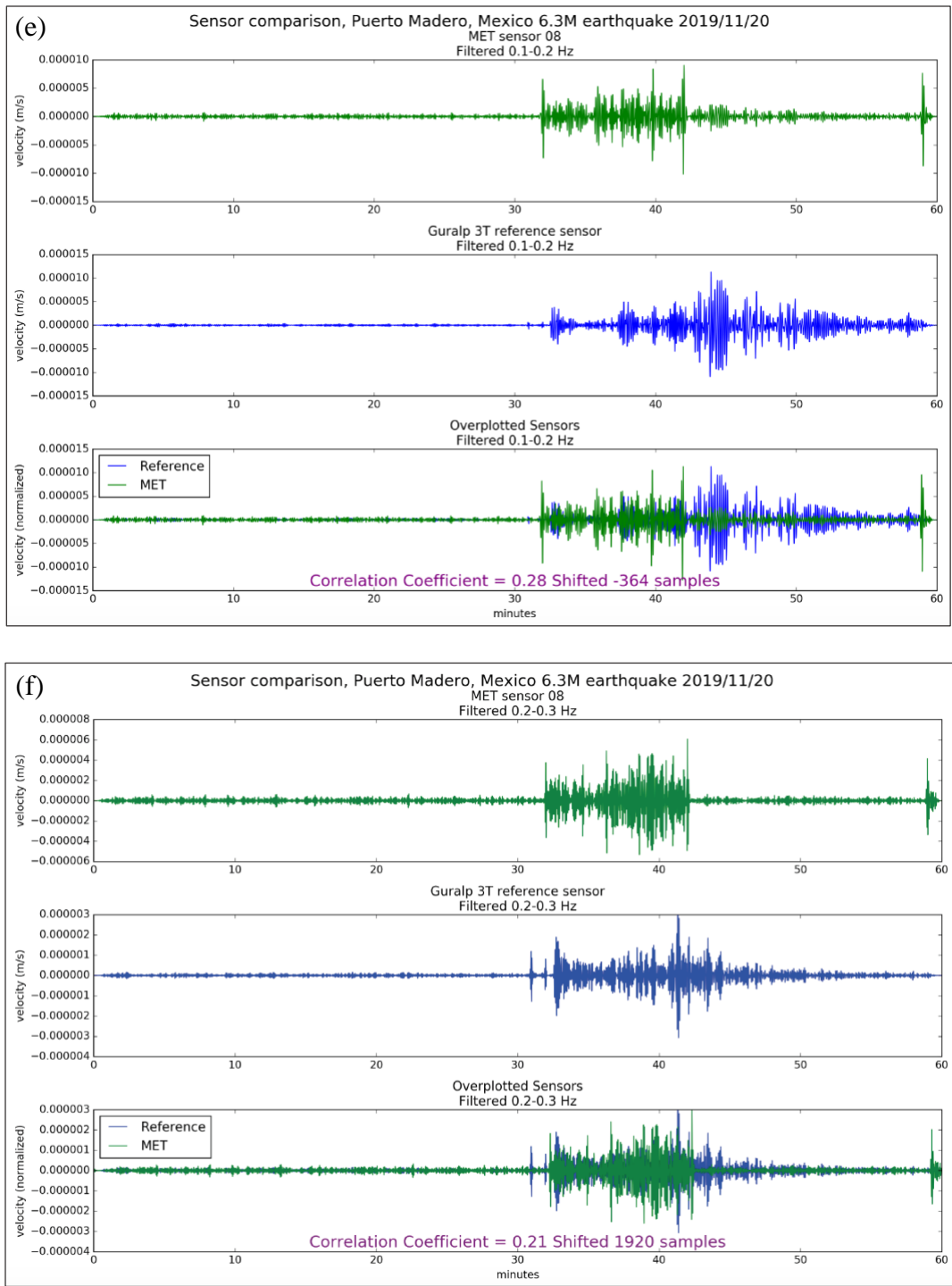


Figure 4.1.5.3. Earthquake detection data comparison between MET and reference seismometer at frequency ranges of (a) 0.03-0.04 Hz; (b) 0.04-0.05 Hz; (c) 0.05-0.07 Hz; (d) 0.07-0.1 Hz; (e) 0.01-0.2 Hz; and (f) 0.2-0.3 Hz.

4.2 Ionic Liquid Based Low-Temperature Electrolyte Systems using Organic Solvents Gamma-butyrolactone (GBL) and Propylene Carbonate (PC)

4.2.1 Effects of Incorporating Organic Solvents on the Thermal Properties of Electrolytes

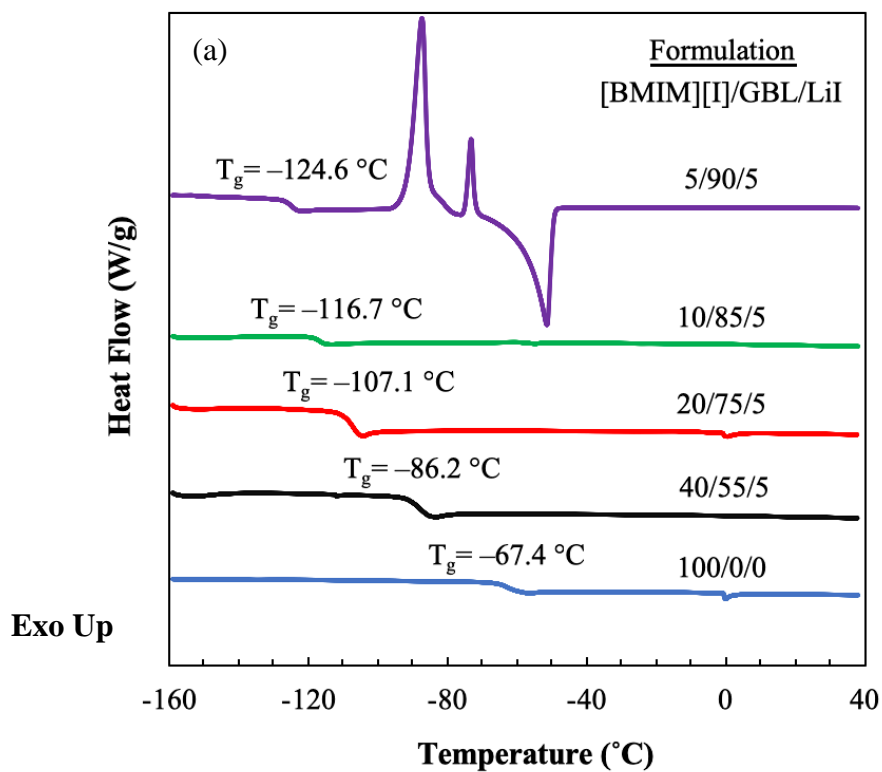
When designing an electrolyte system for low-temperature operations, the phase behaviors of the materials, such as freezing and glass transition, set the physical limit of the liquid electrolytes for their applications. Differential scanning calorimetry (DSC) was used to characterize the thermal transitions of prepared electrolyte formulations, revealing the interplay between ILs and organic solvents in their mixture solution at various formulations over the temperature range from 40 °C to -160 °C. As shown in Figure 4.2.1.1 (a), the effect of GBL can be clearly seen by DSC analysis. Neat [BMIM][I] demonstrated a T_g at -67.4 °C and did not appear to have any additional thermal transitions. GBL was employed to host IL as the primary organic solvent for formulating the mixture-based electrolyte due to its potential in designing molecular interactions. When GBL was added to [BMIM][I], T_g of the mixture system was effectively reduced and furthermore, as the concentration of GBL increased, a decreased T_g of the mixture solution was observed. When the concentration of GBL was at 90 mol%, the formulation [BMIM][I]/GBL/LiI-5/90/5 showed the most reduced T_g at -124.6 °C. This strong effect of shifting T_g towards a lower temperature by introducing GBL into the electrolyte can be interpreted by the interactions in the mixture solution at the molecular level. Vranes et al. also observed the similar effect of suppressing phase transition temperatures of IL when mixing 1-butyl-3-methylimidazolium bis(trifluoromethylsulfonyl)imide ([BMIM][NTf₂]) with a variety of lactone solvents, including GBL.[170] The ionic liquids and molecular liquids are able to

establish notable intermolecular interactions through multiple routes. [BMIM][I], for example, has exhibited to form hydrogen bonding via the iodide anions with surrounding water molecules in their binary mixtures.[179,266] On the other hand, the cations of imidazolium-based ILs have been observed, both computationally and experimentally, to interact with various organic molecular solvents via the formation of hydrogen bonding between the most acidic hydrogen on the imidazolium ring and the lone electron pair of the solvent molecules.[197,267–269] Papović et al studied the binary systems of GBL and various imidazolium-based ionic liquids and discovered that longer alkyl side chains on the imidazolium cation leads to stronger interactions between GBL and ILs.[269,270] In our developed mixture system that consists of [BMIM][I] and GBL, we hypothesized that a similar intermolecular interaction between the imidazolium moiety of [BMIM]⁺ cations and the carbonyl group of solvent molecules through hydrogen bonding disrupts the ion-pair formation between [BMIM]⁺ cations and iodide anions within [BMIM][I] network. Consequently, the cohesive energy of the system is significantly reduced and reflected on a lower T_g of the resulting mixture solution. The existence of such intermolecular interaction will be further revealed experimentally in later sections.

Although the addition of GBL shifted T_g of the mixtures towards a favorable lower temperature, it had a negative impact by introducing undesirable thermal transitions to the electrolyte. Despite that the formulation [BMIM][I]/GBL/LiI-5/90/5 displayed the lowest T_g among all the solutions, it showed a critical drawback that a series of undesirable thermal transitions were observed above T_g . The predominating endothermic peaks at approximately -87 °C and -73 °C indicates the occurrence of crystallization, which will not only fail the function of liquid electrolyte owing to insufficient motion of flow but also

cause high risks of structural damage to the device by volume change of the solution and accumulation of mechanical stresses. While the low T_g promised a wider liquidus window for low-temperature sensing operations of MET sensor, the phase transitions associated with this formulation were not suitable for our targeting liquid electrolyte system. Thus, another co-solvent component, PC, was introduced into the mixture to further optimize the properties of the electrolyte. Figure 4.2.1.1 (b) demonstrates the effects of incorporating PC on the thermal behaviors of the multicomponent system. As PC was used to replace a varying fraction of GBL in the solution, the tendency of the mixture to crystallize responds to this composition change. With an increasing concentration of PC, the corresponding endothermic heat flow of crystallization decreased. When the concentration of PC was at 15 mol%, the phase transition of formulation [BMIM][I]/PC/GBL/LiI-5/15/75/5 was significantly mitigated. After increasing PC concentration to 20 mol% or higher, we no longer observed any phase transitions other than the glass transition from these formulations. In contrast to formulation [BMIM][I]/GBL/LiI-5/90/5, very smooth DSC curves were presented by formulations [BMIM][I]/GBL/LiI-5/20/70/5 and 5/30/60/5. Meanwhile, their T_g values, in despite of a slightly rise, were still retained at a very low temperature. Formulation [BMIM][I]/GBL/LiI-5/20/70/5 showed a T_g at approximately -120 °C. To the best knowledge of the authors, this is the lowest T_g that has been reported for a liquid electrolyte system. The effects of incorporating PC on retaining T_g at low temperatures and tuning the thermal behaviors of the electrolyte can also be interpreted by modified intermolecular interactions. It can be viewed that the similar carbonyl functional groups shared by both PC and GBL can interact with [BMIM]⁺ cation to keep the glass transition from happening at higher temperatures, while the existence of PC in the mixture

also interferes with GBL to prevent its crystallization. This low T_g , free-crystallization, IL-organic solvent mixture system exhibits great potentials as liquid electrolytes for low-temperature applications. As we attribute desired thermal behaviors to effects of optimized molecular interactions, further studies were intrigued on those interactions between IL and organic solvents.



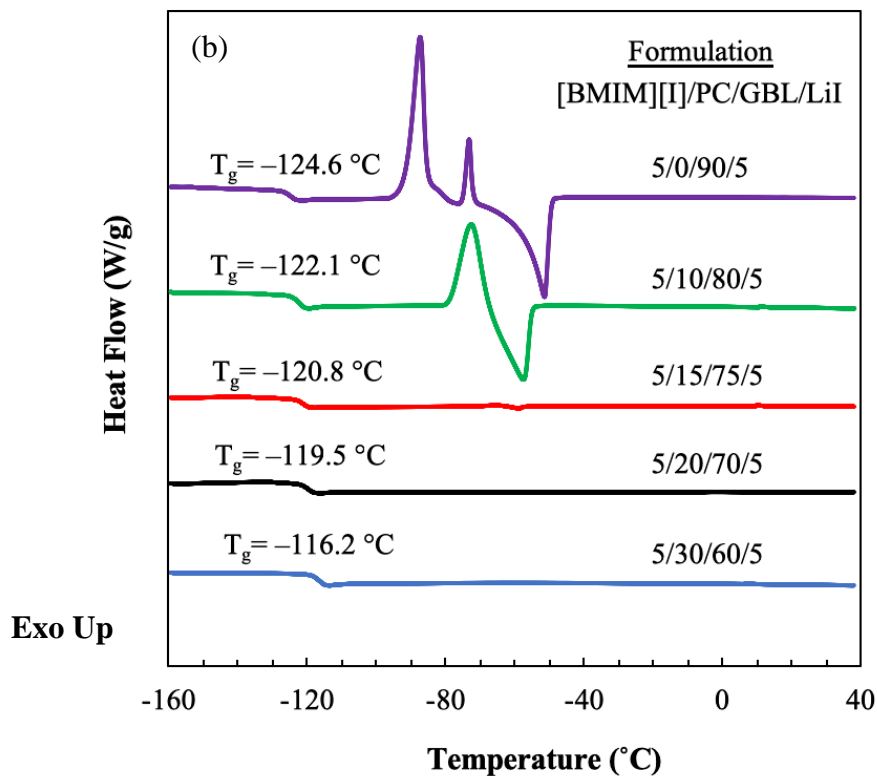


Figure 4.2.1.1. DSC thermograms from -160 to 40 °C for various formulations of (a) [BMIM][I]/GBL/LiI mixture solutions and (b) [BMIM][I]/PC/GBL/LiI mixture solutions.

4.2.2 Probing Intermolecular Interactions between IL and Organic Solvents

In order to reveal the hypothesized molecular interactions, FTIR was first employed to investigate the modification of the bonding structures in the developed IL-organic solvents electrolytes. As shown in Figure 4.2.2.1 (a), FTIR spectra confirmed the signature peaks from the functional groups of each main chemical in the multicomponent system. For example, neat [BMIM][I] displayed the vibrations of C–H stretching from both the alkenyl group and the carbon-hydrogen bond in between two adjacent nitrogen atoms on

the imidazolium ring at 3136 cm^{-1} and 3070 cm^{-1} , respectively.[271] The former peaks from the alkenyl group were still observed in the electrolyte formulations, [BMIM][I]/GBL/LiI-10/85/5 and 5/90/5, and [BMIM][I]/PC/GBL/LiI-5/20/70/5, but at a much smaller magnitude (with wavenumber shifts between 9 and 18 cm^{-1}). However, the latter peak was no longer significant in those formulations, indicating the disruption of the bonding configuration due to the interaction between cation and organic solvent molecules. This emerged interaction can be further disclosed by the IR response of the carbonyl group, which is the same functional group shared by both solvent molecules. Each of neat GBL and PC showed a peak of C=O stretching at 1760 and 1780 cm^{-1} , respectively. It is known that the carbonyl stretching is sensitive to formation of hydrogen bonding.[272,273] When the total number of present carbonyl groups is excessive to that of the available donor groups in the system, a partial number of the carbonyl groups will exhibit a peak shift on the spectra because their intrinsic vibrations are altered as they accept the protons from the most acidic hydrogen of [BMIM]⁺ cations, while rest of the carbonyl groups that are not hydrogen-bonded remain uninfluenced.[273,274]

When GBL was incorporated with [BMIM][I], the hydrogen bonding formation between a faction of the carbonyl groups from GBL as acceptors and [BMIM]⁺ cations as donors was clearly captured by an arisen “shoulder” off the original carbonyl peak at approximately 1742 cm^{-1} on the spectra for formulations [BMIM][I]/GBL/LiI-10/85/5 and 5/90/5, as shown in Figure 4.2.2.1 (b), indicating the emergence of a new peak from those carbonyl groups that strongly interact with [BMIM][I] via hydrogen bonding. This observation serves as a direct manifestation of the hypothesized GBL-[BMIM]⁺ interaction in the electrolyte solutions. When the mixture was incorporated with both GBL and PC,

the similar effect from the interaction between GBL and [BMIM]⁺ was also seen on the spectrum of formulation [BMIM][I]/PC/GBL/LiI-5/20/70/5, however, much less significant on PC. Instead of “splitting” into two peaks, the carbonyl stretching of PC only displayed a minor shift from 1780 cm⁻¹ to 1784 cm⁻¹ without showing any “shoulder” peak from the original peak, suggesting that its ability to form hydrogen bonding with [BMIM]⁺ cations is weaker when competing against GBL for limited number of donors and therefore the interaction was not as predominant. This trend is consistent with the mixture system reported by Tian et al, where [EMIM]⁺ cations showed stronger interactions with GBL than PC, and this difference was also reflected on bulk properties of the studied formulations.[275] Furthermore, we also noticed that such a minor shift from PC is identified as a blue shift. Although blue shifts for hydrogen bonds can exist in various cases, red shifts are more often expected.[276] In comparison to GBL, which can be viewed as the primary source to form hydrogen bonding with imidazolium cation in our developed system, the hydrogen bonding associated with PC could be much weaker and more subtle, and such moderate blue shift that was observed on the carbonyl group of PC could be caused by a more complex scenario. PC is a special solvent that has a high dielectric constant and has been reported to demonstrate strong molecular interactions (i.e. dipole-dipole interactions) via its carbonyl groups and form local structures among themselves.[277,278] When PC is incorporated in the mixture, we hypothesized that the overall electronegativity environment of its carbonyl groups was altered by more than a single factor of hydrogen bonding and therefore caused a minor blue shift. Via FTIR results, we were able to validate the modified molecular interactions in the mixture system and further details of the targeted ion-solvent interactions were unveiled by NMR next.

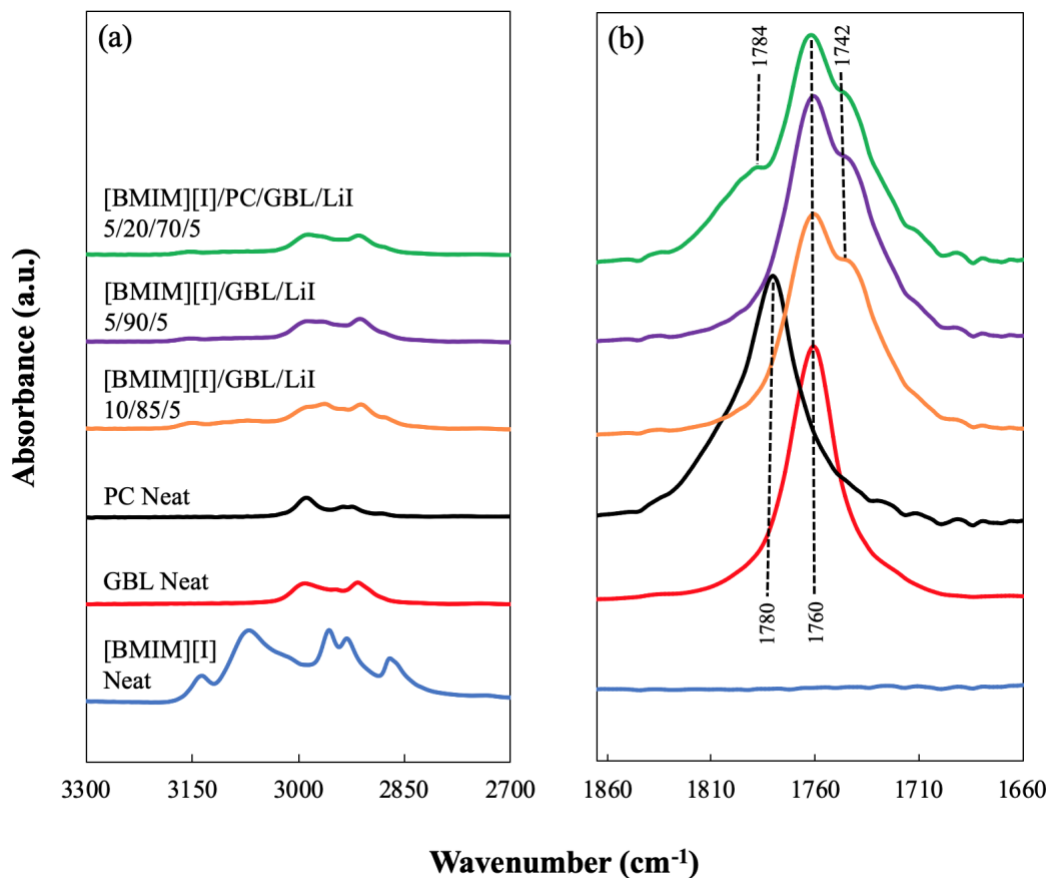


Figure 4.2.2.1. FTIR spectra of electrolyte formulations, [BMIM][I]/GBL/LiI-10/85/5, 5/90/5, and [BMIM][I]/PC/GBL/LiI-5/20/70/5, as well as individual neat components as controls, in the region of (a) between 2700 and 3300 cm⁻¹ and (b) between 1660 and 1885 cm⁻¹.

The ¹H NMR spectrum of neat [BMIM][I] is shown in Figure 4.2.2.2 (a), and the chemical shifts for all the protons at each position of the molecular structure are in agreement with reported literature values.[279–281] In addition, an effect of hydrogen-deuterium exchange was also detected. The numbering of each carbon on the imidazolium cation are schematically depicted in the inset of Figure 4.2.2.2 (a), and it is noticed that the

peak of the proton at H-2 position was significantly weaker than its corresponding stoichiometric ratio among all the proton at other positions. Such a feature can be explained by a dynamic process of equilibrium, where the labile protons on the [BMIM]⁺ cations are replaced by the deuterons in the solvent when they are dilute in D₂O.[282] The hydrogen at H-2 position is known to be more acidic, so its lower surrounding electron density makes the proton tend to exchange with deuterons from the solution, while the rest of protons from other positions of the cation are able to remain stable.[283–285] This phenomenon has also been observed in other chemical systems that contain imidazole groups such as histidine.[286,287] When [BMIM][I] was incorporated with organic solvents to form a mixture solution, more interestingly, an evolvement of the hydrogen-deuterium exchange was observed with ¹H NMR. All the electrolyte formulations shown in Figure 4.2.2.2 (b) demonstrated a significantly larger integrated peak area for the hydrogen at H-2 position than neat [BMIM][I], which indicates a mitigated extent of hydrogen-deuterium exchange with the presence of carbonyl groups in the solution. The integrated peak area for the hydrogen at H-1 position was set as a baseline value of 3.00, given there are three hydrogens possessed by the alkyl group at this position. Accordingly, the hydrogen at H-8 position demonstrated a matching integrated peak area of 3.06, approximately, validating the quantitative results from ¹H NMR based on the stoichiometric ratio between H-1 and H-8. At the position of H-2, in comparison, the neat [BMIM][I] and mixture solutions showed the integrated peak areas of 0.33 and an approximate range between 0.82 and 0.85, respectively, which again confirmed the additional molecular interactions between the [BMIM]⁺ cations and the solvent molecules. In the mixture solution, the carbonyl groups from the organic solvents become acceptors to form hydrogen bonding with the hydrogens

at H-2 position of [BMIM]⁺ cation as donors and modifies the surrounding electron density accordingly. Thus, the hydrogen at this position is more stabilized and its exchange with the deuterium from the solution is significantly reduced, reflecting a higher integrated peak area of H-2 protons than neat [BMIM][I] in ¹H NMR.

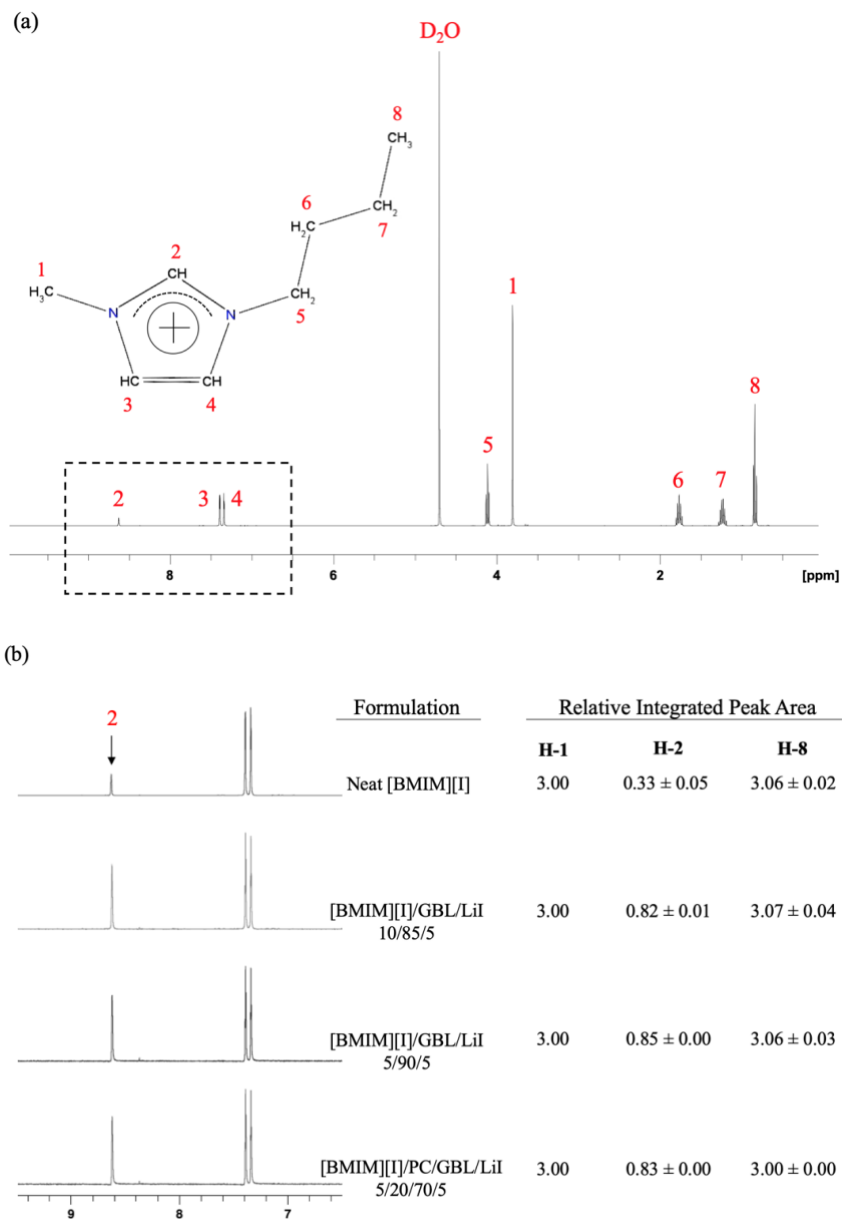


Figure 4.2.2.2. ¹H-NMR spectra of (a) neat [BMIM][I] with the inset showing the numbered chemical structure of [BMIM]⁺ cation and (b) neat [BMIM][I],

[BMIM][I]/GBL/LiI-10/85/5, 5/90/5, and [BMIM][I]/PC/GBL/LiI-5/20/70/5, focusing on the peaks of H-2 with the comparison of relative integrated peak areas also provided.

4.2.3 Transport properties of [BMIM][I]/GBL/PC/LiI Mixtures Based Electrolytes

Besides thermal properties, interactions between ILs and organic solvents also affect transport properties of electrolytes, which are critical for their electrochemical applications. ILs typically possess high viscosities, due to various intermolecular forces such as the prominent coulombic attractions, van der Waals forces, and hydrogen bonding.[24,288] Neat [BMIM][I] solution, as shown in Figure 4.2.3.1 (a), displayed high viscosities with a strong temperature dependence, increasing by approximately six orders of magnitude from 25 °C to -75 °C. While the temperature dependence was observed across all the formulations, the ones that were incorporated with molecular solvents demonstrated not only much less drastic viscosity increases as temperature decreased but also significantly lower viscosities over the entire temperature range of testing. At room temperature, two selected electrolyte formulations from this study, [BMIM][I]/GBL/LiI-10/85/5 and [BMIM][I]/PC/GBL/LiI-5/20/70/5, whose thermal profiles showed low T_g and free of crystallization, exhibited similar magnitude of viscosities between 0.002 and 0.005 Pa·s with minor differences. As temperature decreased to -75 °C, [BMIM][I]/GBL/LiI-10/85/5 evolved to a significantly higher viscosity of 1.29 Pa·s, presumably due to its higher concentration of [BMIM][I]. In contrast, [BMIM][I]/GBL/PC/LiI-5/20/70/5 yielded a much lower viscosity of 0.31 Pa·s at -75 °C, indicating that the addition of PC did not compromise the fluidity of the solution yet effectively prevent undesired phase transition

of the electrolyte system. If comparing to an aqueous-based ILs electrolyte formulation previously developed by our group [266], [BMIM][I]/[EA][N]/water/LiI-5/35/55/5 showed a comparable viscosity to [BMIM][I]/PC/GBL/LiI-5/35/55/5 at room temperature but a significantly higher viscosity by more than 30 times at -75 °C, owing to a stronger temperature dependence of the employed solvents. The effectiveness of reducing viscosity by incorporating organic solvents into the systems can be attributed to the intrinsic superior fluidity of GBL and PC at low temperatures, which is consistent with observations on other IL-based electrolyte systems [193,275,289].

While viscosity depicts overall fluidity of liquid-state electrolytes, ionic conductivity is another key transport property that directly reflects the mobility of charge carriers in a system. As shown in Figure 4.2.3.1 (b), the ionic conductivities of all the electrolyte formulations reduced significantly as temperature decreased. The behavior of such an exponential correlation between ionic conductivity and temperature can also be well described by the Vogel–Fulcher–Tammann (VFT) equation [65]. For each formulation, the dashed line was plotted based on the VFT fitting results, showing the ionic conductivity evolution over the testing temperature range and prediction extended down to its respective experimental T_g as marked by the dotted line. Figure 4.2.3.1 (b) inset provides ionic conductivity data collected via EIS from 25 to -75 °C. Starting from 25 °C, [BMIM][I]/GBL/LiI-10/85/5 and [BMIM][I]/PC/GBL/LiI-5/20/70/5 showed comparable ionic conductivities, which were approximately 5 times lower than [BMIM][I]/[EA][N]/water/LiI-5/35/55/5. Although the aqueous-based electrolyte began with a higher ionic conductivity, the gap was narrowed gradually with decreasing temperature. At around -70 °C, [BMIM][I]/PC/GBL/LiI-5/20/70/5 reached a similar ionic

conductivity as the aqueous-based electrolyte. Moreover, following the trajectory of the VFT fitting curves in Figure 4.2.3.1 (b), the two organic solvent-based electrolytes will eventually possess higher ionic conductivities than the aqueous-based electrolyte at around -80 °C. Formulations [BMIM][I]/GBL/LiI-10/85/5 and [BMIM][I]/PC/GBL/LiI-5/20/70/5 are expected to retain better ionic conductivities until their ideal glass transition temperatures, where the VFT model no longer provides adequate predictions for supercooled liquids.

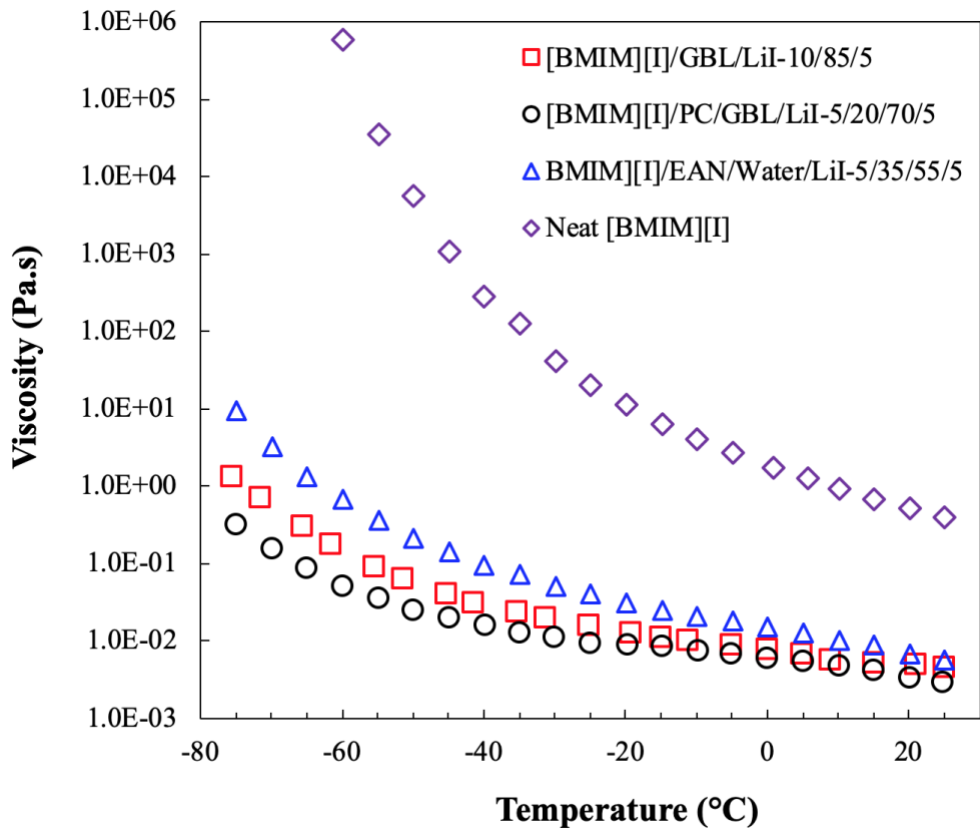
Ionic conductivities of IL-based mixtures can be determined by several factors simultaneously. In general, we often focus on two tunable properties from the electrolyte design standpoint, naming the viscosity and the ionicity (the degree of ion disassociation). The former affects the mobility of existing species while the later corresponds to number of charge carriers available for the conduction mechanism, both contributing to the overall bulk ionic conductivity [65]. Experimental results showcase that over the testing temperature range, the aqueous-based electrolyte provided the highest ionic conductivity despite the highest viscosity, indicating the impact from available charge carriers. The aqueous-based electrolyte was incorporated with [EA][N], another ionic liquid, as an approach to inhibit predominant crystallization. Consequently, [BMIM][I]/[EA][N]/water/LiI-5/35/55/5 possessed the highest theoretical ion concentration among the three electrolyte formulations. On top of that, in reality the actual number of ions available for conduction also depends on the extent of ion disassociation. For pure ILs where the sole media is formed by ions with strong coulombic attractions, considerable ions exist in forms of pairs or aggregates that are not accountable for charge transport [24]. It is known that selections of molecular solvents and ionic liquids have great

impacts on optimizing ionicity of the electrolytes, attributed to the structures and properties of existing species that result in different degrees of interactions [290,291]. For instance, Li et al. performed a comprehensive discussion on transport properties of binary mixtures by incorporating imidazolium ionic liquids with water and several organic solvents [292]. Particularly, water appeared to be the most effective in weakening coulombic attractions between ions, due to both the high dielectric constant and the ability of forming hydrogen bonds with the anions. Therefore, we hypothesize that the higher ionic conductivity of the aqueous-based electrolyte at higher temperatures can be explained by the highest number of available ions owing to a potentially higher extent of ion disassociation.

However, when temperature decreases to $-70\text{ }^{\circ}\text{C}$ or below, the ionic conductivities of both organic solvent-based electrolytes are predicted to be comparable and even exceeding the aqueous-based electrolyte, according to the trends based on the VFT fitting. Such results suggest potential changes in viscosity and ionicity, which are both known to be temperature dependent and can also be correlated to intermolecular interactions. Our comparison showed that the differences in viscosity between the aqueous-based electrolyte and the organic solvent-based electrolytes has become more prominent as temperature decreased. While the viscosity difference at higher temperatures might be insignificant when comparing to the ionicity, we speculate it to be more influential on the ionic conductivity at low temperatures as the differences evolved to over an order of magnitude. Papović et al. also discussed the combined impact of viscosity and ionicity on conductivity of [BMIM][NTf₂]/GBL binary mixtures, concluding that improvements in electrochemical properties are more likely due to the significant reduction of viscosity when increasing GBL fraction in the system [270]. Therefore, despite the lower effectiveness in solvation,

incorporation of GBL and PC successfully reduced viscosity and presents itself as a more viable strategy on designing electrolytes for the promoted low-temperature applications than the aqueous-based approach from the perspective of optimizing transport properties.

(a)



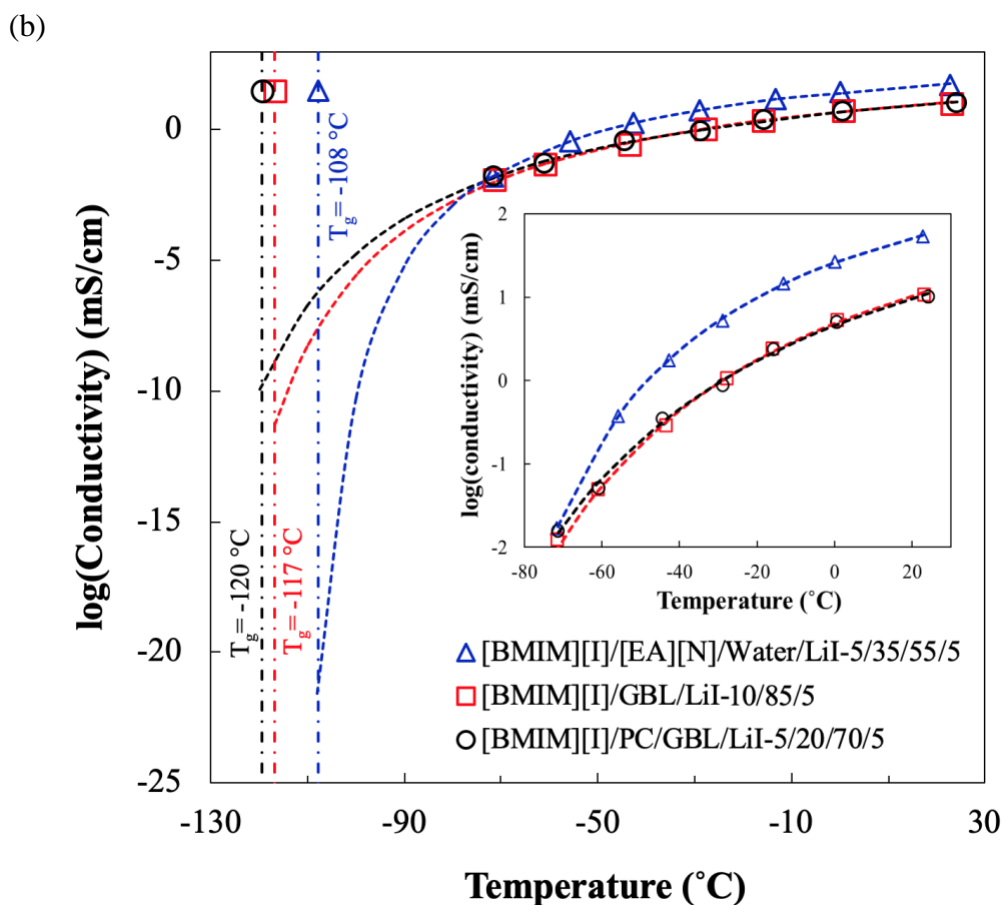


Figure 4.2.3.1. Temperature dependence of (a) viscosity and (b) ionic conductivity among neat [BMIM][I], selected organic solvent-based electrolyte formulations from this work, and aqueous-based formulation from previous studied dual ionic liquid system containing both [BMIM][I] and [EA][N] [266]. In (b), the dashed lines and dot-dashed lines represent the VFT fitting result for each formulation and their experimentally measured T_g , respectively, showing predicted conductivities when approaching glass transition, and the inset provides a zoom-in view of the measured conductivities between 25 °C and -75 °C.

4.3 Mixtures of Ionic Liquid and Butyronitrile (BuCN) Based Electrolyte Systems

4.3.1 Effects of Incorporating BuCN on the Physical Properties of Electrolytes

The previous success with both [BMIM][I]/[EA][N]/water/LiI and [BMIM][I]/GBL/PC/LiI mixtures has encouraged us to continue the design philosophy of utilizing intermolecular interactions on new co-solvents for further pushing the physical limits of electrolyte materials. Due to a favorable thermal profile and superior transport properties, BuCN is also employed to host [BMIM][I] for formulating a new mixture-based electrolyte. The effects of BuCN incorporation on the physical properties of electrolytes are disclosed by experimental results. In Figure 4.3.1.1, DSC analysis clearly revealed that the T_g of the mixture was shifted with respect to the concentration of BuCN. As BuCN content increased in the mixture, the T_g was effectively reduced to a lower temperature. When BuCN was at 95 mol%, the formulation [BMIM][I]/BuCN/LiI-5/90/5 displayed the lowest T_g at -152.3 °C, which is also a new record low T_g among three studied mixture electrolyte systems so far. This strong effect of T_g reduction can be due to not only the intrinsically low freezing point of BuCN (-111.9 °C) but also the presence of intermolecular interactions between BuCN and [BMIM][I]. We hypothesize that the lone pair of electrons of nitrile functional group from BuCN could interact with the proton at the H2 position of the imidazolium group from [BMIM]⁺ cation via hydrogen bonding, which will be further demonstrated with characterization details in section 4.3.2. Similar to the interactions between the carbonyl group and imidazolium group that was discussed previously, such hydrogen bonding between BuCN and IL interfere the ion-pair formation between the cations and anions of [BMIM][I] in the mixture, reducing the cohesive energy of the system and therefore shifting T_g towards a lower temperature. It is also worth

noticing that no crystallization or any other phase transition other than the glass transition was observed on any formulation of [BMIM][I]/BCN/LiI mixtures, which is distinguishable from two previous electrolyte systems. This phenomenon could be due to the intrinsic physicochemical properties of BuCN.

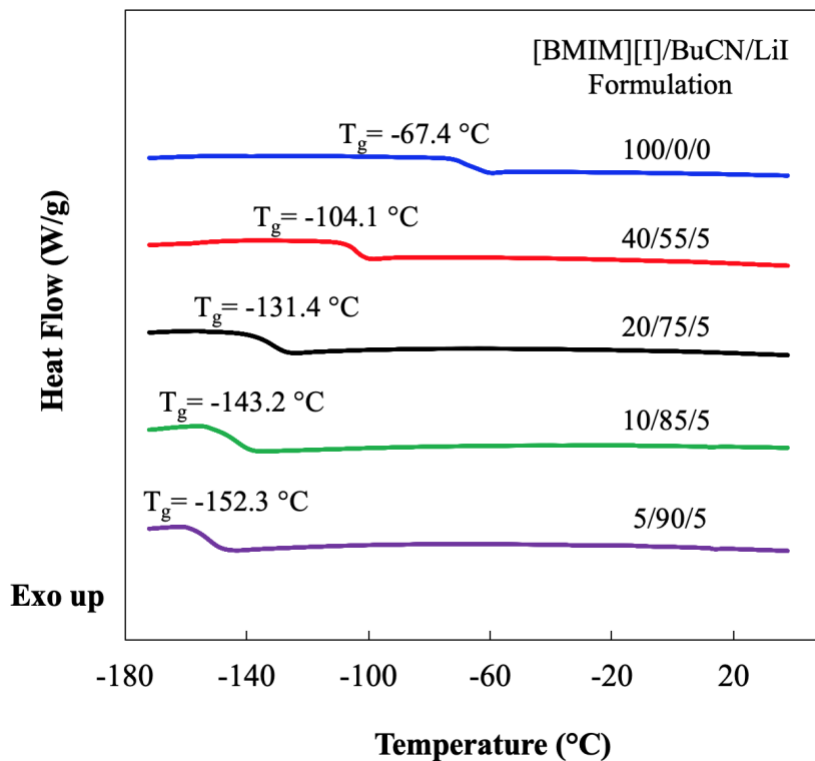


Figure 4.3.1.1. DSC heating curves with an upward exothermic direction from -175 °C to 40 °C for electrolyte formulations including [BMIM][I]/BuCN/LiI-5/90/5 (purple), 10/85/5 (green), 20/75/5 (black), 40/55/5 (red), and neat [BMIM][I] (blue).

The effects of BuCN on the transport properties of [BMIM][I]/BCN/LiI mixtures are also examined at room temperature. Figure 4.3.1.2 shows a comparison of viscosity and ionic conductivity with respect to varying BuCN concentrations. Effects of molecular

solvents on transport properties of molecular solvents/ILs mixtures have been well studied, where incorporation of molecular solvents in ILs results in rearrangement of the originally closely packed ions and lead to significant decrease in viscosities of the mixtures [293,294]. As expected, viscosities of the mixtures decreased exponentially with increasing BuCN concentration. In particular, differences in viscosities between formulations [BMIM][I]/BuCN/LiI-40/55/5 and 5/90/5 was more than one order of magnitude. Again, we hypothesize that interactions between BuCN molecules and imidazolium cations, as evidenced by FTIR and Raman spectroscopy in the following section, have altered arrangement of existing species on a microscopic level that significantly reduces the bulk viscosity. Similar observations were also reported in various mixtures between acetonitrile and imidazolium based ILs [295–297]. In correspondence to the trend of viscosity, an increasing BuCN content leads to a higher ionic conductivity. Since ion mobility for the conduction mechanism is dependent on fluidity of the solution, such an inverse relationship between these two transport properties agree with each other to some extent. However, unlike viscosity which decreases exponentially with increasing BuCN, the increase in ionic conductivity is more in a linear fashion, indicating that other factors could also play a role besides viscosity. In addition to fluidity, Galiński et al. further disclose the contribution of ionicity, the extent of ion disassociation, on the bulk ionic conductivity in IL-based mixtures [65]. In pure ILs, strong attractions between cations and anions often result in neutral ion-pairs and ion-aggregates that do not serve functionalities of charge carries. By introducing co-solvents into ILs, a higher ionicity is achieved via a solvation effect of solvent molecules around ions and thus an improved ionic conductivity [248,298,299]. Similarly, such an enhancement on ionic conductivity in acetonitrile/IL systems were

observed through various experimental and computational researches [300–303]. However, studies on effects of other nitrile solvents such as propionitrile and BuCN in ILs are still very limited. In addition to the hydrogen bond between the nitrile group and imidazolium ring, the longer alkyl chain of BuCN can lead to other intermolecular forces such as the van der Waal force that can affect transport properties considerably [162]. For instance, Ruiz et al. observed viscosity reduction and ionic conductivity improvement in [PYR₁₄][TFSI] based mixtures with acetonitrile and BuCN, respectively, but correlations with resulting mixture properties were drawn more on the intrinsic characteristics of materials rather than a thorough understanding of the complex interplays between IL and co-solvents [199].

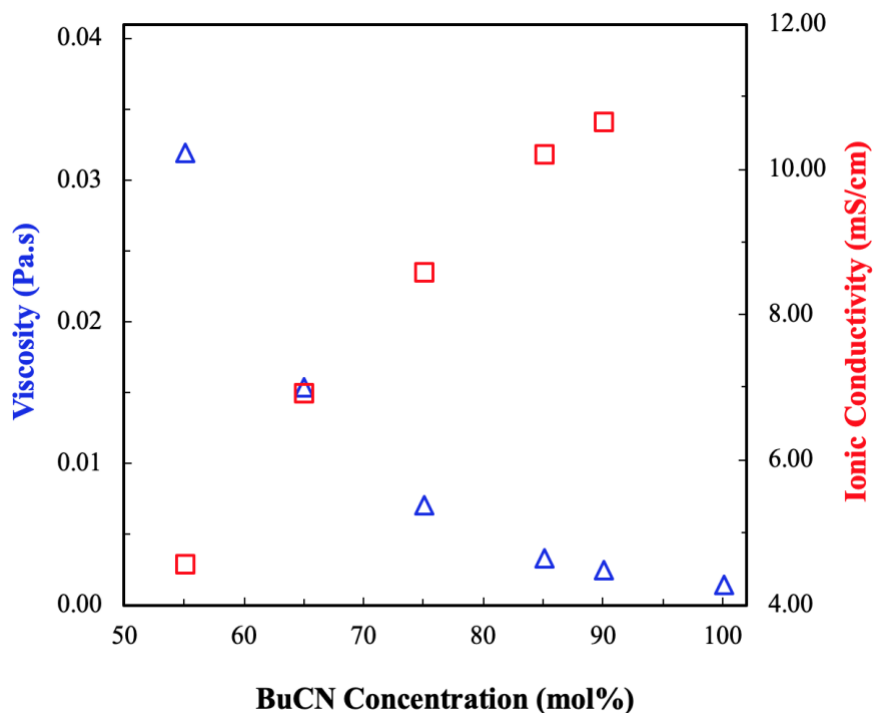


Figure 4.3.1.2. Comparison of viscosity (blue) and ionic conductivity (red) of [BMIM][I]/BuCN/LiI mixtures with respect to BuCN concentration.

4.3.2 Intermolecular Interactions between [BMIM][I] and BuCN

FTIR was used to provide experimental evidence for the hypothesized intermolecular interactions by characterizing the bonding structures in the electrolyte mixtures. The FTIR spectra of all the mixture formulations and neat BuCN solvent were shown in Figure 4.3.2.1 (a), where their signature peaks from the wavenumber range between 2000 and 3600 cm^{-1} from were revealed with the inset showing a closer look at the range between 2100 and 2400 cm^{-1} . For [BMIM][I]/BuCN/LiI-based formulations, the peaks between 3000 and 3200 cm^{-1} are attributed to the vibrations of C–H stretching on the imidazolium ring of [BMIM]⁺ cations [271,275], which is not observed on the spectrum of neat BuCN. On the other hand, the peaks from symmetric and asymmetric stretching of alkyl groups between 2800 and 3000 cm^{-1} were observed on all the spectra [271,304]. More importantly, neat BuCN spectrum clearly showed a single peak for its the signature vibration of C≡N stretching from the nitrile groups at a wavenumber of 2249 cm^{-1} [304]. On the spectra of other mixture formulations, the vibration of C≡N stretching is observed as well but in a modified fashion. In addition to its original peak position, a secondary peak, to a varying extent on each mixture formulation, is also detected at a wavenumber of approximately 2270 cm^{-1} . This can be attributed to the presence of a unique format of intermolecular interactions between [BMIM][I] and BuCN. Similar to the interactions with the carbonyl group of GBL in the earlier discussion, the hydrogen bonding can form between the proton at C-2 position on imidazolium ring as a donor and the lone pair of electrons of the nitrile group on BuCN as an acceptor. This effect was shown to be stronger on the formulations [BMIM][I]/BCN/LiI-5/90/5 and 10/85/5, where the nitrile groups under the influence of such a hydrogen bonding were shaped into a full peak on the spectra,

and the formulations [BMIM][I]/BCN/LiI-20/75/5 and 40/55/5 yielded a weaker reflection with the emerging secondary peak appearing as only “shoulders” off the original peak position.

Raman spectroscopy was also employed to validate such findings. As shown in Figure 4.3.2.1 (b), vibrational peaks of the nitrile group were observed across all the formulations in the range of 2100 – 2400 cm^{-1} . Without any influence of hydrogen bonding with the imidazolium group from IL, neat BuCN expectedly showed a strong single peak at 2251 cm^{-1} . When forming a mixture, the primary nitrile peak was also exhibited on each electrolyte formulation with a minor shift at 2248 cm^{-1} and the secondary nitrile peaks were also subtly displayed as shoulder-like features at a wavenumber position of approximately 2272 cm^{-1} . Those features were more distinguishable on formulations [BMIM][I]/BCN/LiI-5/90/5 and 10/85/5 but much weaker to an extent of almost disappearing on [BMIM][I]/BCN/LiI-20/75/5 and 40/55/5. Such a difference in the vibrational intensity is consistent with the observations from FTIR earlier, where [BMIM][I]/BCN/LiI-5/90/5 and 10/85/5 both demonstrate a stronger influence of hydrogen bonding on their nitrile groups.

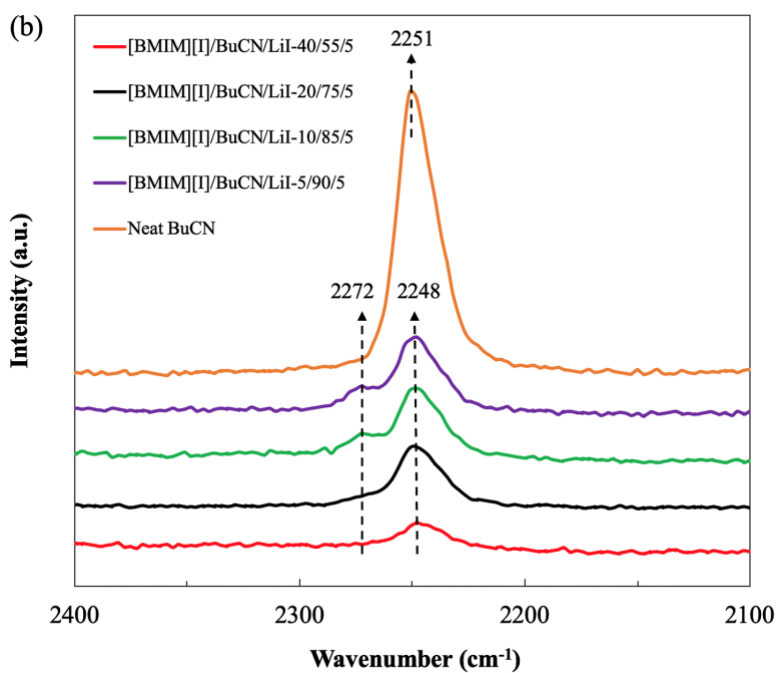
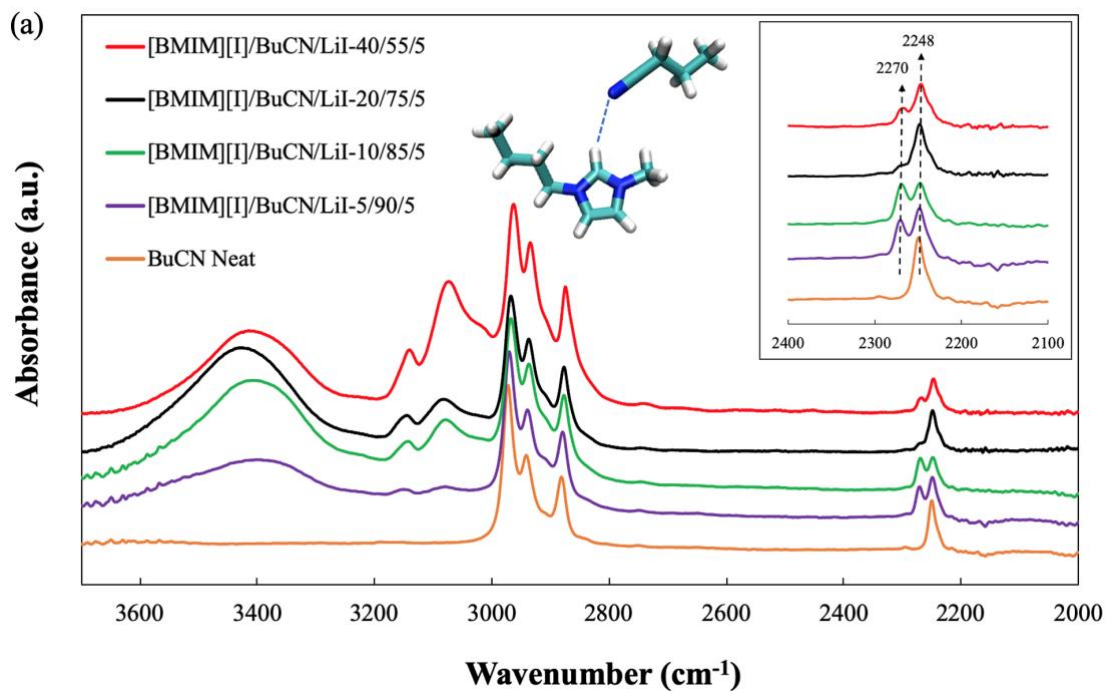


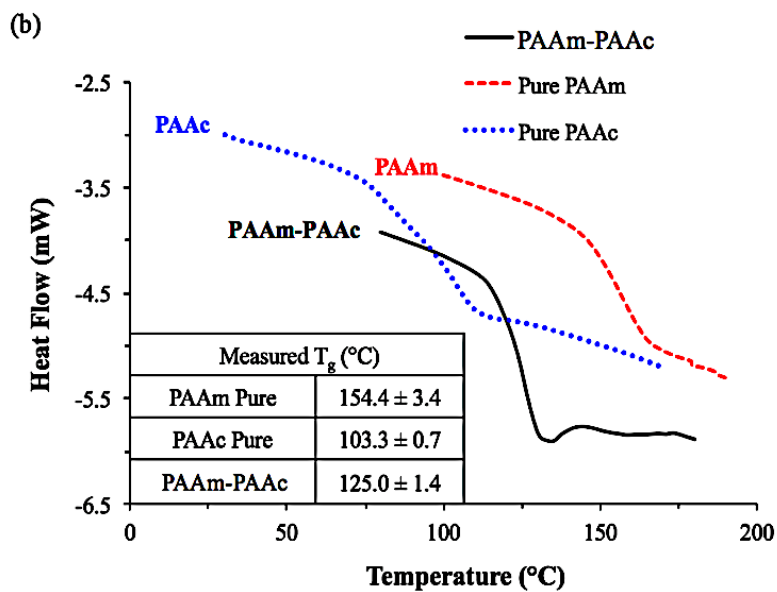
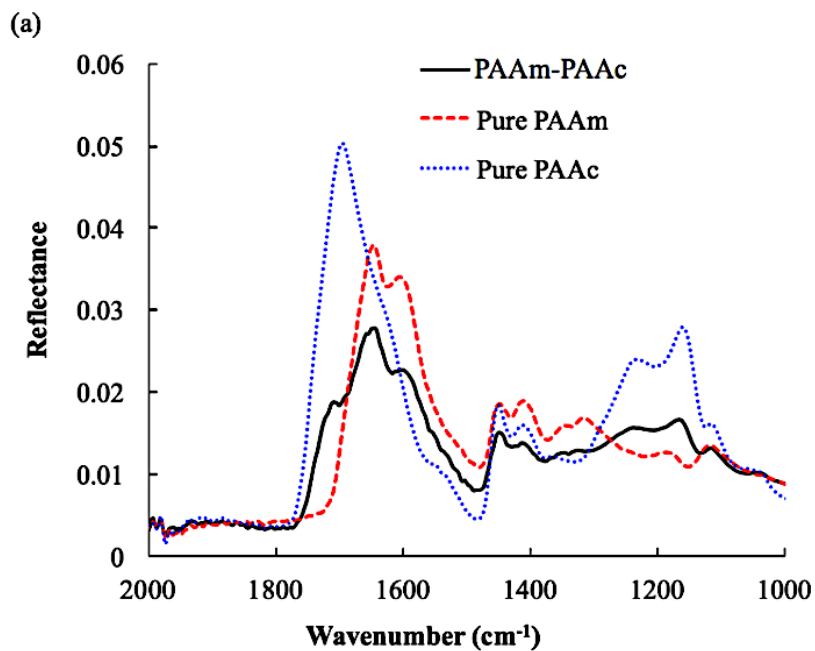
Figure 4.3.2.1. Probing the molecular interactions in electrolyte formulations, [BMIM][I]/BuCN/LiI-5/90/5, 10/85/5, 20/75/5, 40/55/5 and neat BuCN, via (a) FTIR and (b) Raman spectroscopy.

4.4 Visible-Light Responsive and Mechanically Enhanced “Smart” UCST Interpenetrating Polymer Network Hydrogels

4.4.1 Confirmation of PAAm-PAAc Interpenetrating Polymer Network (IPN) Hydrogel Synthesis

The formation of interpenetrating network hydrogel was validated by experimental results from ATR-FTIR, DSC, and compressive tests. The functional groups of PAAm and PAAc were characterized by ATR-FTIR to confirm the synthesis. As shown in Figure 4.4.1.1 (a), the FTIR spectra demonstrates the amide functional group of PAAm with N-H bending and the C=O stretch which are indicated by the peaks at 1605 cm^{-1} and 1645 cm^{-1} , respectively. Similarly, the presence of PAAc group is proven by the C-O stretch and the C=O stretch with the unsaturated carboxylic acid group are indicated by the peaks at 1240 cm^{-1} and 1695 cm^{-1} , respectively. In the spectrum of PAAm-PAAc interpenetrating polymer network (PAAm-PAAc IPN), the above signature peaks are all observed at 1238 cm^{-1} , 1601 cm^{-1} , 1645 cm^{-1} and 1708 cm^{-1} , respectively, with minimal shifts compared to the individual spectrum of PAAm and PAAc polymer networks. The FTIR results demonstrate that the synthesis of interpenetrating network hydrogel was able to successfully include both PAAm and PAAc polymer networks. The peaks of N-H stretch with the amide group of PAAm and the O-H stretch with the carboxylic acid group of PAAc are broad and overlapping at the adjacent wavelengths, so they cannot be used to distinguish the functional groups of PAAm and PAAc. The PAAm and PAAc form the structure of the interpenetrating network hydrogel due to their intermolecular polymer-polymer interactions. PAAm and PAAc serve the first phase and the second phase of the interpenetrating network, respectively. The intermolecular interaction is based on the

dynamic mechanism of hydrogen bonding formation and dissociation between the amide group of PAAm and the carboxylic acid group of PAAc [241].



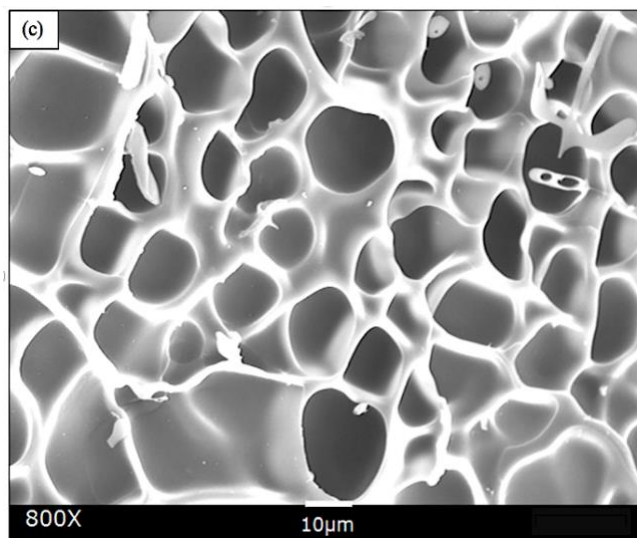


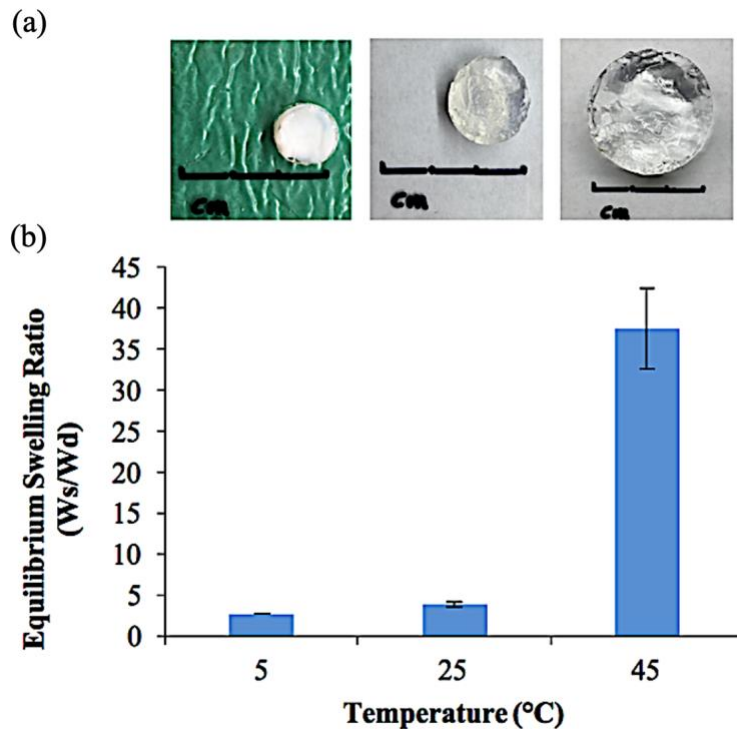
Figure 4.4.1.1. Conformation of PAAM-PAAc IPN hydrogel synthesis: (a) comparison of ATR-FTIR spectra between the PAAM-PAAc IPN hydrogel (black solid) and individual network hydrogels, pure PAAM (red dash) and pure PAAc (blue dot), in the wavenumber range from 1000 to 2000 cm^{-1} . (b) Representative DSC thermograms showing the glass transition of PAAM-PAAc (black), PAAM (red), and PAAc (blue), with the resulting T_g values in the inset on the bottom left. (c) SEM image showing the morphology of the PAAM-PAAc IPN hydrogel (after freeze-drying) with average pore size of $16.0 \pm 4.4 \mu\text{m}$.

The formation of PAAM-PAAc interpenetrating network was also confirmed by thermal evidence from DSC analysis. Previously, Ribellies et al [305] suggested that a well-mixed, highly cross-linked IPN is expected to have one single glass transition temperature (T_g) due to the close interaction between two polymer networks that cannot express themselves independently. On the contrary, when the two polymer networks fail to interpenetrate or are only loosely cross-linked, two separate glass transitions should be

observed in correspondence to a phase-separated system [305,306]. As shown in Figure 4.4.1.1 (b), the single polymer network of pure PAAm and PAAc show their individual glass transitions at 154.4 ± 3.4 °C and 103.3 ± 0.7 °C, respectively. The interpenetrating network of PAAm-PAAc demonstrates a clear single glass transition at 125.0 ± 1.4 °C between the T_g values of pure PAAm and PAAc networks, which is evident of the successful formation of the interpenetrating network between the PAAm and the PAAc. The morphological features of the PAAm-PAAc interpenetrating network after freeze-drying are shown by the SEM image in Figure 4.4.1.1 (c), and the macro-porous structures of the interpenetrating network hydrogel was revealed. The average pore size of the porous structures was calculated as 16.0 ± 4.4 μm based on 20 measurements randomly selected in the image using ImageJ.

The intermolecular interaction between PAAm and PAAc within the interpenetrating network structure also facilitated a unique UCST swelling behavior of the synthesized PAAm-PAAc IPN hydrogel. Figure 4.4.1.2 (a) shows a pictorial depiction of the UCST characteristic of synthesized PAAm-PAAc IPN hydrogel. At 5 °C, the PAAm-PAAc IPN hydrogel exhibited the most shrinkage. At both 25 °C and 45 °C, the PAAm-PAAc IPN hydrogel exhibited continuous volume expansion with the positive temperature dependence. In Figure 4.4.1.2 (b), the swelling ratios of the synthesized PAAm-PAAc IPN hydrogel were experimented at three different temperatures, 5 °C, 25 °C and 45 °C, and a strong temperature dependence could be seen. As the media temperature rose from 5 °C to 45 °C, the swelling ratio increased over 13.6 ± 1.8 times. The volume transition of the PAAm-PAAc IPN hydrogel was much more dramatic over the tested temperature range between 25 °C and 45 °C than between 5 °C and 25 °C, which was visually observable by

the increasing volume of the gel dimensions. Katono et al. [307] also reported the similar positive swelling behavior on the poly(acrylamide-co-butyl methacrylate)-poly(acrylic acid) IPN system for the application of drug delivery and attributed the phenomenon to the formation and the dissociation of the intermolecular complex. On a bulk scale, the overall interpenetrating network hydrogel exhibits de-swelling due to a more “tightly” held intermolecular complex by the stable formation of hydrogen bonding at a lower temperature. At a higher temperature, the hydrogel then shows enhanced swelling due to the dissociation of the intermolecular complex by the breakage of hydrogen bonding. However, Katono et al.’s work was focused on the swelling aspect and did not evaluate the formation of the interpenetrating network from other valuable angles, such as thermal and mechanical approaches, which will be discussed in the following sections.



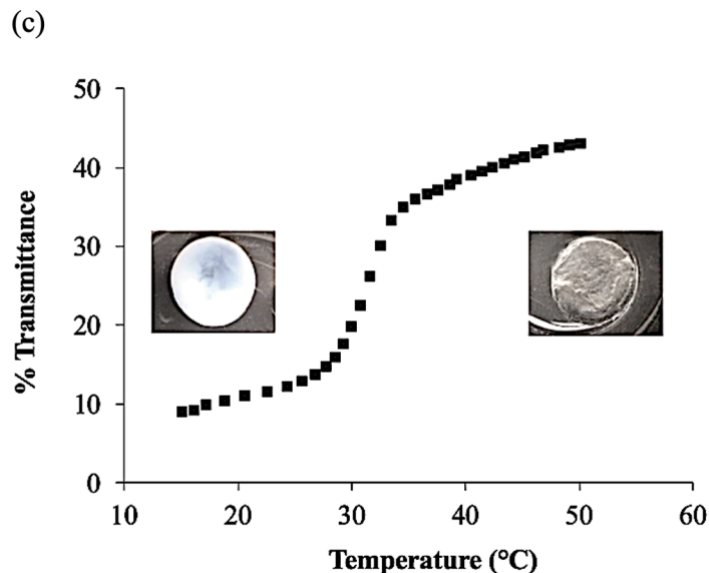


Figure 4.4.1.2. UCST characteristics of PAAm-PAAc IPN hydrogel: (a) pictorial demonstration of the volume and opacity transition of hydrogel. (b) swelling ratio (W_s/W_d) at equilibrium at 5 °C, 25 °C, and 45 °C. (c) The change in optical transmittance of the hydrogel from 15 °C to 50 °C measured by UV-Vis spectrophotometer showing the opacity transition of the material; Left and right insets are representative screenshots of the hydrogel’s opacity transition taken at the first 15 second after immersion in water at 15 °C and 50 °C from room temperature, respectively.

In addition to the swelling behavior, the interpenetrating network hydrogel also demonstrates a temperature dependent opacity transition. As also shown in Figure 4.4.1.2 (a), the color of PAAm-PAAc IPN hydrogel appears as opaque at 5 °C and becomes clearly transparent at 45 °C. In order to further investigate this phenomenon, UV-vis analysis is employed to quantify the opacity change of the PAAm-PAAc IPN hydrogel with respect to temperature. As shown in Figure 4.4.1.2 (c), the hydrogel has a low transmittance of

only 8.9% with a white opaque color at 15 °C. As the temperature ramps up, the hydrogel responds to this environmental change by exhibiting a reduced opacity with transmittance increasing to 43.0% measured at 50 °C. At this point, the hydrogel displays as almost transparent in the media instead of opaque. The most dramatic change of the percentage transmittance is observed to take place at approximately 32 °C while a more gradual transition occurs below 29 °C and above 35 °C. Unlike the volume transition described earlier, the opacity transition of hydrogel is rather fast. When placing the hydrogel that is equilibrated in the media from a higher temperature (e.g. 50 °C) to a lower temperature (e.g. 15°C), the opaqueness starts to form within the gel body immediately. Also, this opacity transition is observed as a reversible process. Zhang et al [308] reported a similar reversible opaque-transparent phase transition on a physically cross-linked poly(sulfobetaine methacrylate) double network hydrogel, and their work showed that intramolecular and intermolecular associations were strong enough to drive a phase transition with sufficient water content. In our case, we hypothesize that the PAAm-PAAc IPN hydrogel at temperatures lower than UCST can be viewed as a collapsed coil structure due to intermolecular attractive forces between the acid and amide group. Under this status, the interaction between the polymer chains was strong enough by the predominant presence of hydrogen bonding formation so that water was prevented from entering the polymer chain system. As a result, the separation of phases was pronounced, and the solvent was minimized, giving the interpenetrating network hydrogel its opacity. At temperatures above UCST, the intermolecular forces subsided while the electrostatic bonding between water and polymer chains became more dominant. The hydrophilicity of the network was then increased, which drove the transition from opaque to transparent. Overall, both of the

volume transition and the opacity transition contributed to the UCST characteristics of the PAAm-PAAc IPN hydrogel.

Another result of the formation of the PAAm-PAAc interpenetrating network was that the mechanical property of the PAAm-PAAc IPN hydrogel was enhanced. As shown in Figure 4.4.1.3, the compressive tests by Instron E3000 provided the quantitative comparison of stress-strain profiles between the PAAm-PAAc IPN hydrogel and the hydrogels based on its individual polymer components. At a strain at 65%, for example, PAAm-PAAc IPN hydrogel demonstrates a stress of approximate 57,300 Pa while pure PAAm and PAAc hydrogel only show a stress of 14,700 Pa and 6,900 Pa, respectively. When comparing to PNIPAAm hydrogel, one of the most commonly studied environmentally responsive hydrogels, which was reported to show a stress response lower than 2,000 Pa at approximately 25% strain [309], PAAm-PAAc IPN gel showed a higher stress response of 3,000 Pa under the same strain. Furthermore, PAAm-PAAc IPN hydrogel can fully and repetitively recover to its original shape after being compressed up to above 65 % strain without any observable fracture or material failure. In contrast, the pure PAAm hydrogel began to form fractures before reaching 35% strain and the pure PAAc hydrogel also failed to preserve the material integrity from the compressive test. The inset images in Figure 4.4.1.3 vividly demonstrate the PAAm-PAAc IPN hydrogel can withstand the large extent of compression while pure PAAm and PAAc hydrogels suffer from severe deformation and permanent fractures from compression. Both, PAAm and PAAc hydrogels, are very fragile in nature by their individual polymer network alone due to the high content of water. By forming the interpenetrated polymer network, the PAAm-PAAc IPN gel displays enhancement with a much greater toughness and a much better

ability to stretch than pure PAAm and PAAc hydrogels when the weight ratio of monomer and the crosslinker are remained the same. The enhanced mechanical properties of PAAm-PAAc IPN hydrogel can be ascribed to the presence of hydrogen bonding between amide groups of PAAm and carboxylic acid groups of PAAc. Such hydrogen bonding serves to reinforce the intermolecular interaction and offer additional crosslinking between polymer chains to strengthen the interpenetrated polymer networks. When subjected to an external mechanical load, some of the hydrogen bonds dissociate first and hence dissipate the energy, preventing further compromise of the material integrity. Upon the removal of the load, the hydrogen bonds can re-form, allowing the hydrogel to be applied in frequently operated devices. Similar mechanical enhancements through hydrogen bonding have also been observed on several other polymeric systems. Myung et al [310] reported the strain-hardening behavior of a poly(ethylene glycol)-poly(acrylic acid) IPN system with a significantly improved fracture strength and more than two times of modulus enhancement. Wang et al [311] also reported the role of hydrogen bonding in increasing the material strength in a *n*-acryloyl glycinamide-*co*-2-vinyl-4,6-diamino-1,3,5-triazine copolymer system. Over the change of pH, such strengthening effect can be weakened and resumed reversibly based on the dissociation and re-construction of hydrogen bonding.

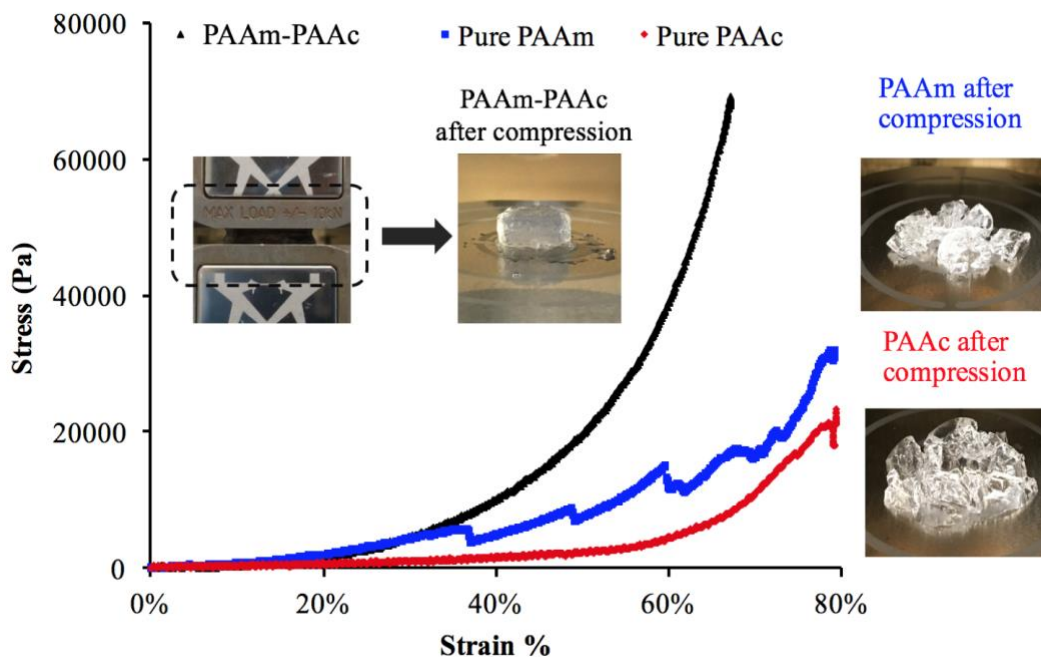


Figure 4.4.1.3. Intron E-3000 compressive analysis of PAAm-PAAc IPN hydrogel (black) in comparison to the single phase of pure PAAm (blue) and PAAc (red) hydrogels, showing the enhanced mechanical properties. Left insets: PAAm-PAAc IPN hydrogel being able to recover to original shape after compressive test; Right insets: fractures and material failure of PAAm (top) and PAAc (bottom) after compressive tests.

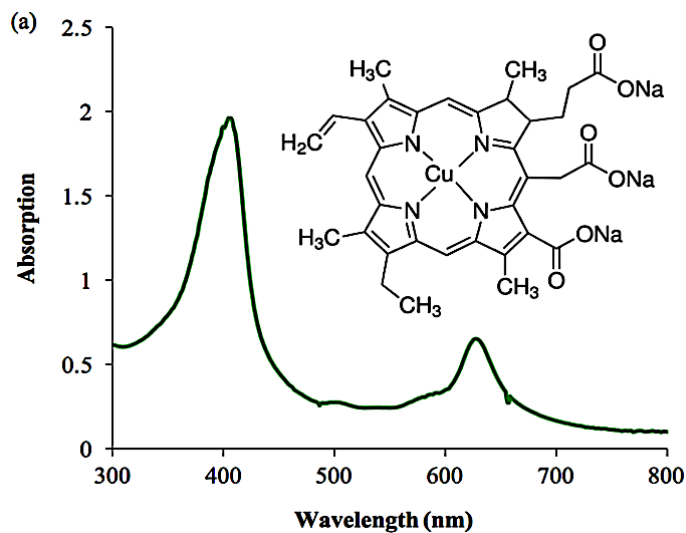
4.4.2 Effects of Incorporating Chlorophyllin into Interpenetrating Network Hydrogel

Chlorophyllin sodium copper salt (Ch) was selected as a suitable chromophore for the purpose of this study because its light responsiveness lies well within the wavelength range of visible light. In Figure 4.4.2.1 (a), the UV-Vis spectroscopy of chlorophyllin salt aqueous solution indicates the absorption peaks at the wavelengths of approximate 404 nm

and 625 nm. Farag also reported the very similar absorption ranges between 350 – 480 nm and 620 – 670 nm for chlorophyllin based thin films [312]. As the molecular structure shown in the inset image of Figure 4.4.2.1 (a), chlorophyllin has delocalized electrons that can be easily excited to orbitals at higher energy level by light irradiation of appropriate wavelength. Those electrons quickly fall back to their original state, releasing energy in the form of heat, which can induce the positive volume transition of PAAc-PAAm interpenetrating network system. In addition, the excellent water solubility of chlorophyllin salt also allowed a facile process of its incorporation in the synthesis via simply well-mixing in the pre-cursor solution prior to polymerization.

After incorporation, as shown in Figure 4.4.2.1 (b), the DSC measurement detected a glass transition of the PAAm-PAAc chlorophyllin-containing interpenetrating polymer network (PAAm-PAAc Ch IPN) hydrogel to occur at 126.6 ± 1.6 °C. It was very close to the glass transition of PAAm-PAAc IPN gel at 125.0 ± 1.4 °C, which suggested that the incorporation of chlorophyllin didn't significantly affect the thermal property of the PAAm-PAAc interpenetrating network system. Figure 4.4.2.1 (c) shows the SEM image of the PAAm-PAAc Ch IPN hydrogel sample after freeze-drying. Very similar to PAAm-PAAc IPN hydrogel, macro-porous structures were also observed with no phase separation in the image. As the DSC analysis only reported T_g , the morphology of the PAAm-PAAc Ch IPN hydrogel additionally confirmed that the chlorophyllin as the chromophore was successfully incorporated in the matrix. Theoretically, the vinyl group on the chlorophyllin molecule can react with the free radical in the solution allowing the chlorophyllin to chemically bond onto the propagating polymer chain during polymerization [313–315]. It is also worth noting that the average pore size of PAAm-PAAc Ch IPN hydrogel is

calculated as $9.92 \pm 4.31 \mu\text{m}$ by ImageJ, which is 0.6 times smaller than the pore size of PAAm-PAAc IPN hydrogel. Zhang et al [316] reported the use of different carbonyl group content in the precursor solution to control the pore sizes of synthesized hydrogel. In their work, the hydrogel was crosslinked by the carbonyl group of dialdehyde microfibrillated cellulose and the amino group of gelatin with a comparable range of pore sizes from 10 to 50 μm . The increase in the carbonyl group content of dialdehyde microfibrillated cellulose leads to a higher crosslinking degree between dialdehyde microfibrillated cellulose and gelatin, and therefore a decrease of the average pore sizes of the hydrogel. In our system, the multiple carbonyl groups on the chlorophyllin molecule can have the similar effect to increase the degree of crosslinking via hydrogen bonding, where the carbonyl group serves as the hydrogen bond acceptor with the amine group of the acrylamide as the donor. This enriched intermolecular interaction between PAAm chains after the incorporation of chlorophyllin then causes a more compact porous structure of the polymeric matrix in the hydrogel with the reduction of the pore dimensions.



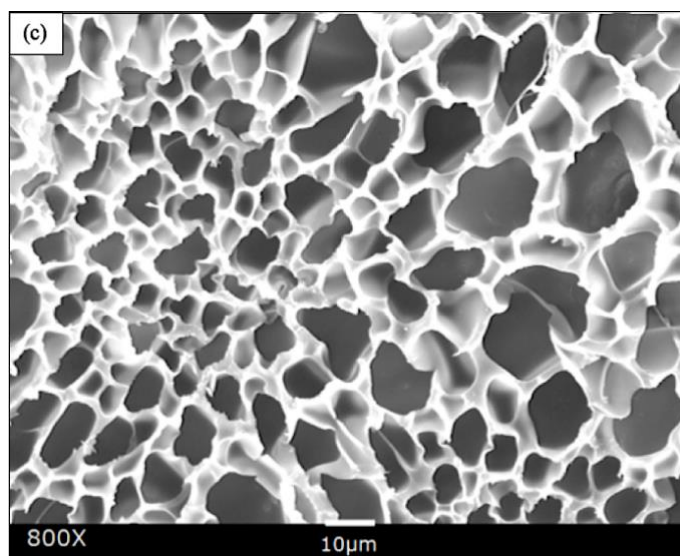
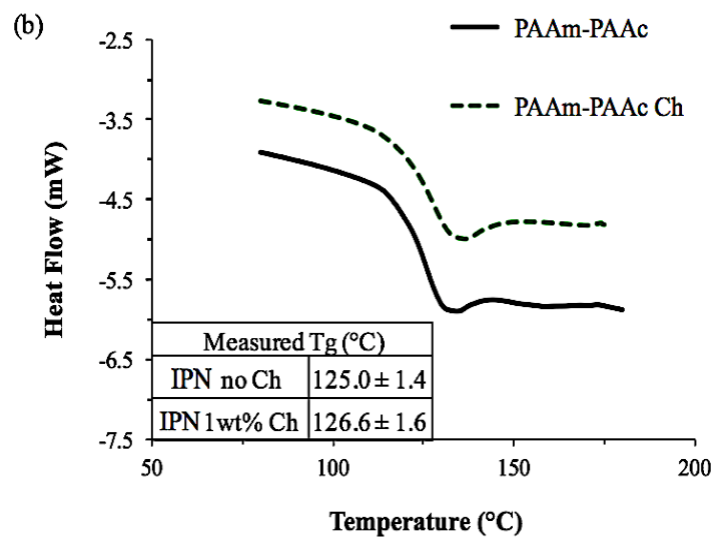
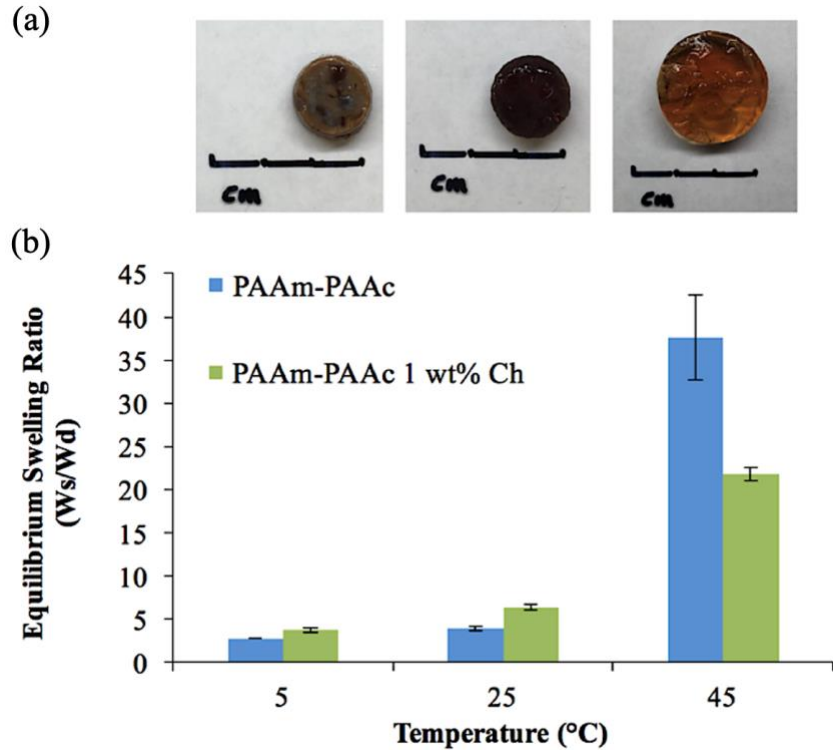


Figure 4.4.2.1. Incorporation of chlorophyllin into the interpenetrating-network hydrogel system: (a) UV-Vis spectrum of chlorophyllin salt aqueous solution between 300 and 800 nm wavelength. Inset: the molecular structure of chlorophyllin sodium copper salt. (b) Comparison of representative DSC thermograms showing the glass transition between non-chlorophyllin (black solid) and chlorophyllin-containing (green dash) interpenetrating network PAAm-PAAc hydrogels with the resulting T_g values (as a result of two runs) in

the bottom left inset. (c) SEM images showing the morphology of PAAm-PAAc Ch IPN hydrogel (after freeze-drying) $9.9 \pm 4.3 \mu\text{m}$.

After introducing chlorophyllin, PAAm-PAAc Ch IPN hydrogel still held a clear UCST characteristic by an increasing swelling ratio as temperature increases. A pictorial depiction of the UCST swelling behavior of PAAm-PAAc Ch IPN hydrogel is shown in Figure 4.4.2.2 (a). Similar to PAAm-PAA IPN hydrogel, a comparable positive volume expansion of the PAAm-PAAc Ch IPN hydrogel was observed as the media temperature was increased. In addition to the volume transition, the opacity transition of PAAm-PAAc Ch IPN hydrogel was also observable as the color of the gel changed from opaque brown to transparent dark brown over the change of environmental temperature from $5\text{ }^{\circ}\text{C}$ to $25\text{ }^{\circ}\text{C}$ and above. Figure 4.4.2.2 (b) shows the comparison of the temperature dependent swelling ratio between PAAm-PAAc IPN and PAAm-PAAc Ch IPN hydrogels. PAAm-PAAc Ch IPN hydrogel displays a slightly higher swelling ratio at both $5\text{ }^{\circ}\text{C}$ and $25\text{ }^{\circ}\text{C}$ yet a notably lower swelling ratio at $45\text{ }^{\circ}\text{C}$ than PAAm-PAAc IPN hydrogel. The total increase of the swelling ratio over the change of temperature for PAAm-PAAc Ch IPN hydrogel, 5.70 ± 0.42 times, was considerably smaller than that for PAAm-PAAc IPN hydrogel, 13.62 ± 1.75 times. It suggests that the incorporation of chlorophyllin may have an inhibition effect on the swelling of PAAm-PAAc Ch IPN hydrogel, which can be related to its smaller pore dimensions. The more compact porous structure can not only hold the polymer network more “tightly” together but also hinder the water diffusion through the network, resulting in less extent of expansion. A mimicking but much weaker behavior of opacity transition

is also observed on the PAAm-PAAc Ch IPN hydrogel via UV-vis analysis. As shown in Figure 4.4.2.2 (c), the opacity transition of the PAAm-PAAc Ch IPN hydrogel is captured increasing from only 0.6% increasing to 4.3% transmittance over the range of the temperature increase. Since the PAAm-PAAc Ch IPN hydrogel has a dark color from the incorporation of chlorophyllin, the transmittance of the material is significantly lower than the PAAm-PAAc IPN hydrogel. The visual color of PAAm-PAAc Ch IPN hydrogel also changes from an opaque brown to a transparent brown over the transition, and the most dramatic transition takes place at approximately 36 °C. This similar opacity transition behavior of PAAm-PAAc Ch IPN hydrogel confirms that the temperature dependent intramolecular and intermolecular interaction in the interpenetrating network is well sustained after the incorporation of chlorophyllin.



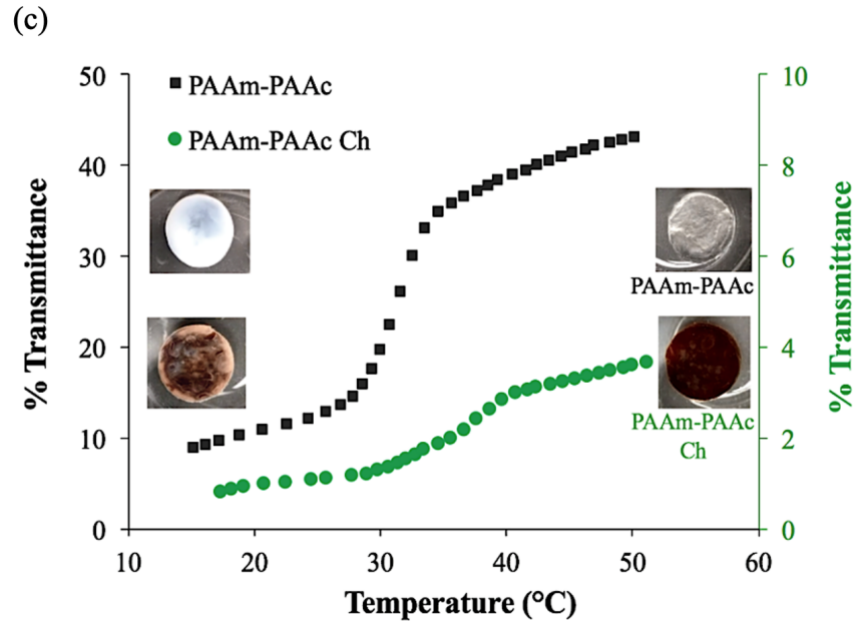
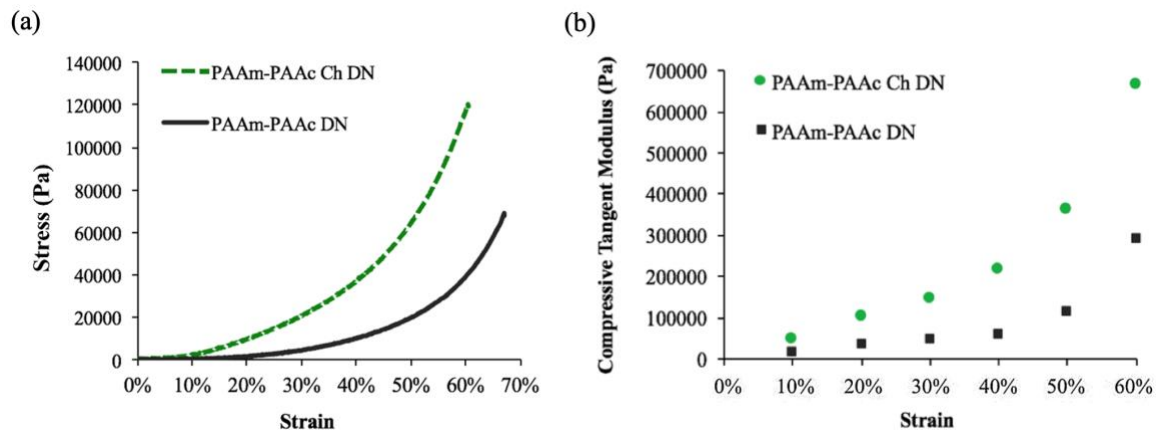


Figure 4.4.2.2. UCST swelling behavior of PAAm-PAAc Ch IPN hydrogel: (a) pictorial demonstration of the volume and the opacity transition of the hydrogel after incorporating chlorophyllin. (b) comparison of the swelling ratio (W_s/W_d) at equilibrium between non-chlorophyllin and chlorophyllin-containing hydrogel at 5 °C, 25 °C, and 45 °C. (c) The change in optical transmittance of PAAm-PAAc Ch IPN hydrogel from 15 °C to 50 °C measured by UV-Vis spectrophotometer showing the opacity transition of the material; bottom left and bottom right insets are representative screenshots of PAAm-PAAc Ch IPN hydrogel's opacity transition taken at the first 15 second after immersion in water at 15 °C and 50 °C from room temperature, respectively.

Apart from the differences in swelling ratio, the incorporation of chlorophyllin also has an effect on the mechanical property of the interpenetrating network hydrogel system. The mechanical property of PAAm-PAAc Ch IPN hydrogel was also examined by compressive test using Instron and compared to PAAm-PAAc IPN hydrogel in Figure 4.4.2.3 (a). PAAm-PAAc Ch IPN hydrogel demonstrates a significantly higher stress than PAAm-PAAc IPN hydrogel at a given strain. For example, PAAm-PAAc Ch IPN hydrogel shows a stress of approximately 120,000 Pa at 60% strain in comparison to PAAm-PAAc IPN hydrogel with a stress at approximately 38,800 Pa. It suggests that the enhancement of mechanical property on the PAAm-PAAc interpenetrating network is further improved by incorporating chlorophyllin. This improvement can be related to the morphology of PAAm-PAAc Ch IPN hydrogel again. The mechanical property of hydrogels can be substantially affected by their porous structures. As discussed earlier, the smaller pore size, induced by the incorporation of chlorophyllin, can form a more compact packing of the polymer network which displays a stronger stress response toward increasing strain and an overall greater mechanical property of the hydrogel at the bulk scale. A previous study by Chiu et al [317] reported a similar observation of the increase of compressive modulus with decreasing pore size on poly(ethylene glycol)-*co*-(L-lactic acid) hydrogel. This consistent trend can be explained that the smaller pore size decreases of water-to-hydrogel contact and hence reduces the plasticizing effect of water in the polymer network [318]. Figure 4.4.2.3 (b) shows the changing trend of the compressive tangent modulus of PAAm-PAAc IPN and PAAm-PAAc Ch IPN hydrogels calculated using the method described by Li and et al [319]. As the compression strain increases, the compressive tangent moduli of both hydrogels demonstrate an exponential increase. Due to the incorporation of chlorophyllin,

the PAAm-PAAc Ch IPN hydrogel has a higher and more rapidly increasing modulus than the PAAm-PAAm IPN hydrogel as expected from the previous stress-strain comparison. Over the rise of the compression strain from 10% to 60%, the modulus of PAAm-PAAc Ch IPN significantly increases from 0.05 MPa to 0.67 MPa. When the applied strain is at a low level, the hydrogels display lower moduli because of the large amount of free water content contained in highly three-dimensional porous structures in the network. At a high strain level, a strain-hardening effect on the hydrogels become more pronounced due to the release of free water from the hydrogel and the intensified physical entanglement from the re-orientation of the polymer network [310,319]. The effect of strain rate on the responding mechanical property of the PAAm-PAAc Ch IPN hydrogel is also studied. As shown in Figure 4.4.2.3 (c), the stress-strain curves can be clearly differentiated by three different strain rates of 0.5 mm/min, 0.05 mm/min, and 0.005 mm/min. At a given strain, the stress under a faster strain rate is found to be larger than a slower strain rate. This phenomenon is due to the fact that under a faster strain rate less relaxation is allowed to occur in the polymer network and thus a faster increasing stress takes place to respond the strain.



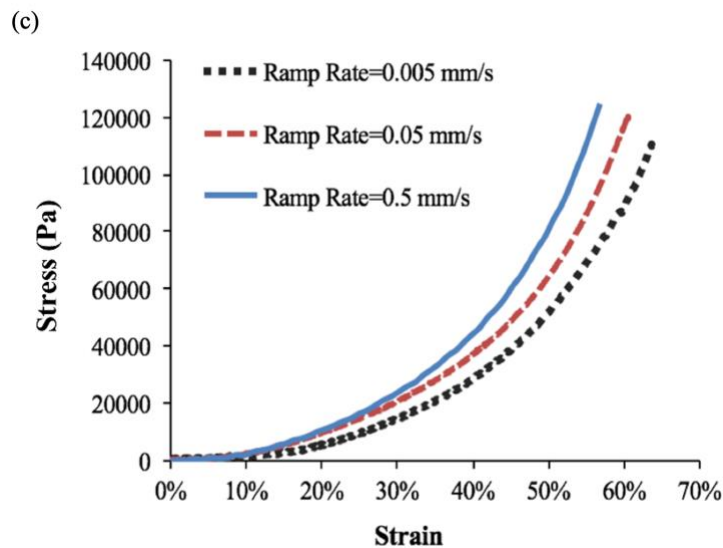


Figure 4.4.2.3. Comparison of compressive analysis: (a) stress-strain curves of PAAm-PAAc IPN and PAAm-PAAc Ch IPN hydrogels obtained by Instron showing further mechanical enhancement after incorporating chlorophyllin. (b) calculated compressive tangent moduli of PAAm-PAAc IPN and PAAm-PAAc Ch IPN hydrogels with respect to strain ratio from 10% to 60% with an interval of 10%. (c) The effect of different strain rates on PAAm-PAAc Ch IPN hydrogel.

Figure 4.4.2.4 demonstrates the visible-light responsiveness of PAAm-PAAc Ch IPN hydrogel. The visible-light that comes from the LED lamp of a commercial projector (Epson) is used to mimic the illumination of the display screen from commonly used electronic devices, and white light is selected to maximize the optical output from the region of visible-light. All the light responsiveness tests were performed with the light intensity at 42.5 mW cm^{-2} , which was measured at the height of the upper water surface. Upon the irradiation of the incident visible-light, PAAm-PAAc Ch IPN hydrogel responds

with a swelling weight increase of $18.3 \pm 3.0\%$ and $20.8 \pm 4.5\%$, after 2 minutes and 10 minutes of exposure, respectively. This trend can be explained through local heat effect which is caused by the light-heat conversion by chlorophyllin to equilibrate. Additionally, a more thorough diffusion process for water to transport from solution to polymer network will enhance the swelling weight increase of chlorophyllin-containing hydrogel. PAAm-PAAc IPN hydrogel as control shows negligible responsiveness to visible light in despite of the exposure time, which is expected due to the inert nature PAAm-PAAc IPN hydrogel towards the stimulus without chlorophyllin converting light to heat. Due to that the intensity of light irradiation from the projector was not sufficient to raise up the water temperature, the media remained at room temperature throughout each test.

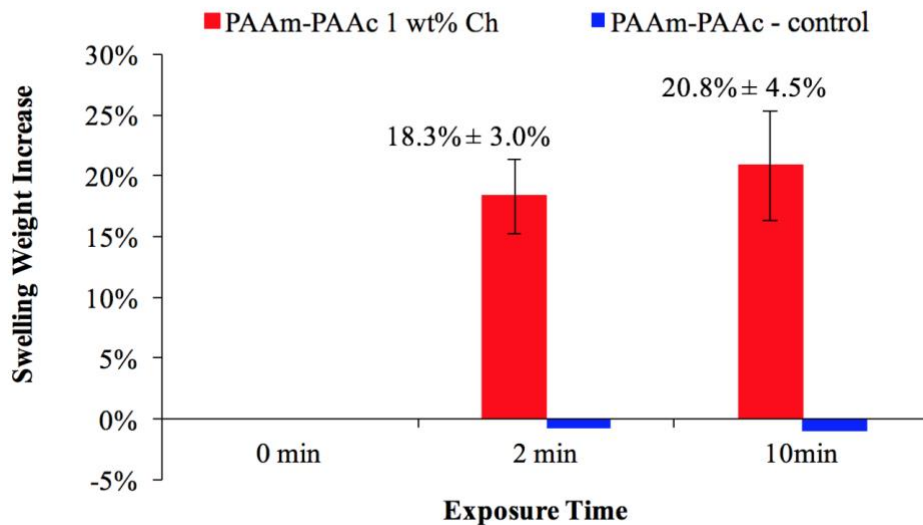


Figure 4.4.2.4. The visible-light responsiveness of PAAm-PAAc Ch IPN hydrogel in terms of swelling weight increase with respect to exposure time (0, 2, and 10 minute).

CHAPTER

5. SUMMARY AND PROPOSED WORK

5.1 Summary

In summary, we have elucidated the utilization of tailoring molecular interactions to design multifunctional soft materials with desired properties in two directions, IL-based mixtures and interpenetrating polymeric network systems, for developing low-temperature electrolytes and environmentally responsive hydrogels, respectively.

First, our work covers two different approaches including aqueous and non-aqueous systems. The first approach is focused on an aqueous dual IL system of [BMIM][I]/[EA][N]/water/LiI mixtures. We demonstrate that with careful considerations of molecular interactions, the designed IL based electrolyte system can obtain tailored thermal and transport properties for applications at extremely low temperatures. In the developed electrolyte system, we discover that water and [EA][N] can both potentially interact with iodide via hydrogen bonding, as both components are hydrogen bond donors and can construct donor-acceptor networks. As the result, in contrast to [BMIM][I]/water/LiI 5/90/5 formulation which showed a low T_g , but accompanied with undesirable thermal transitions, the incorporation of [EA][N] at a designed concentration was able to effectively prevent the crystallization within the mixture and successfully sustain T_g of the solution below -107 °C. Furthermore, significant improvements in transport properties of the electrolyte systems were observed, and the evolution of properties with respect to decreasing temperatures followed the VFT behavior well. In particular, the ionic conductivity and the viscosity of ionic liquid-based electrolyte were reported for the first time below -70 °C. The formulation [BMIM][I]/[EA][N]/water/LiI-

5/35/55/5 showed the highest conductivity at low temperatures as well as the most desirable thermal properties and was therefore proposed as the best electrolyte candidate. The Walden plot analysis revealed an improved ionicity of the developed electrolyte system, which was comparable with other reported good ionic liquids. The electrochemical stability of such formulation was also confirmed within the identified electrochemical window between -0.6 V and 0.4 V. By controlling the proposed potential range properly, targeted iodide/triiodide redox reactions were activated successfully and steadily, without electrochemical reactions of other present species in the system.

The second approach take advantages of organic solvents, including GBL, PC, and BuCN, instead of water, to further extend the physical limits of low-temperature electrolyte materials. By incorporating PC and GBL with [BMIM][I] at an optimal ratio, the designed intermolecular interactions via hydrogen bonding between the carbonyl groups of the organic solvents and the imidazolium cations of the IL, which were confirmed via FTIR and ^1H NMR, successfully modified and optimized the properties of the electrolytes. Consequently, formulation [BMIM][I]/PC/GBL/LiI – 5/20/70/5 showcased remarkable improvement in thermal property with an extended liquidus range down to -120 °C. Furthermore, it also possessed the highest fluidity over a wide temperature range from 25 to 75 C among the tested formulations, leading to the highest ionic conductivity at temperatures lower than -70 °C based on the predictions from the VFT fitting. Besides the combination of GBL and PC, the incorporation of BuCN with [BMIM][I] is also explored. The physicochemical properties of BuCN and [BMIM][I] mixtures are experimentally studied over a wide range of concentrations, and the underlying intermolecular interactions between BuCN and [BMIM][I] are also examined by FTIR and Raman spectroscopy in

correspondence to their macroscopic behaviors. The results from this first direction of the work will not only directly support MET sensing technology in planetary exploration but also inspire new insights to develop IL-based electrolyte materials for other low-temperature applications.

Second, we focus on the soft polymer materials to develop an environmentally responsive hydrogel via interpenetrating polymer network. The synthesized composite hydrogel exhibits the following features: enhanced mechanical property, upper critical solution temperature (UCST) swelling behavior, and promising visible-light responsiveness. The formation of the interpenetrating network between the pair of selected polymeric networks, PAAm and PAAc, was experimentally confirmed by the observation of an UCST swelling behavior and the occurrence of a new T_g in between the T_g values of pure PAAm and PAAc single network. By forming the interpenetrated network, the mechanical properties of PAAm-PAAc IPN hydrogels were significantly improved compared to those made of the single network of each polymer. The visible-light responsiveness of the synthesized hydrogel also demonstrated a positive swelling behavior, and the effect of incorporating chlorophyllin as the chromophore unit was observed to reduce the average pore sizes and further enhance the mechanical properties of the hydrogel. This interpenetrating network system showed a new potential to not only overcome the aforementioned challenges in developing “smart” hydrogels but also explore a new route of using visible light as a simple, inexpensive, and remotely controllable stimulus.

5.2 Proposed Future Work

5.2.1 Low-temperature Sensing Performance of MET Seismometer

We have demonstrated the capability of performing earthquake detections on MET seismometer at room temperature using our developed electrolyte formulation of [BMIM][I]/[EA][N]/water/LiI-10/25/60/5. Two other electrolyte systems, [BMIM][I]/GBL/PC/LiI and [BMIM][I]/BuCN/LiI have also shown even stronger low-temperature sensing potentials with their promising thermal and transport profiles. In order to further meet the mission requirements for planetary seismic sensing, low-temperature sensor performance measurements, including both sensitivity calibration and pier testing, are highly desired. When conducting low-temperature experiments, one of the predictable challenges is to provide a precise environmental control for the testing apparatus. While liquid nitrogen, dry-ice, and their mixtures with various organic solvents are immediate options as a cooling source with some room of temperature tunability for specimens with small sizes, not only the large volume required for cooling and sustaining the entire testing setup at a very low temperature but also the addition noise sources that could be brought by the environmental control processes are both needed to be taken into considerations. In addition, when the temperature decreases, it is expected that the ion mobility in the electrolytes will decrease. This inevitable trend from materials will lead an overall performance compromise at the device level, for example, a reduced sensitivity and a weakened noise tolerance. Therefore, one of future works should be emphasized on the maturation of the MET technology, including the following aspects: (a) further understand and quantify the correlation from the key physical properties from both materials and hardware design (e.g., electrolyte viscosity, applied potential, dimensions of electrode

channels, position of PDMS diaphragms, etc.) to the final outcome of sensor performances, providing fundamental insights for device optimization; (b) improve and standardize the fabrication processes of key sensor components, increasing fabrication and testing reproducibility; (3) potential field testing under environmental and geographical conditions that mimics the target planetary destinations and flight qualifications, upgrading the technology readiness level for a MET-based seismometers.

5.2.2 Explorations of Integrating ILs and Polymeric Materials

We have demonstrated that the versatile functionalities from the “smart” responsive transitions of the environmentally responsive hydrogels and the remarkable conductive and thermally stable characteristics of the ILs. Although both of those two classes show strong potential for various applications, their applicability is still limited in practical situations by the intrinsic material properties. For example, one of the fatal drawbacks for using ionic liquids as electrolytes is leakage related issues in energy storage devices due to the disadvantage of its liquid nature, which is the concern not only for ILs-based electrolytes but also other organic electrolytes. On the other hand, hydrogels are soft with large water volume contained in the network of polymer chains, so they lack good mechanical strength and not thermally resilient to environments with large temperature fluctuations. From a material design perspective, it will be very attractive if we could combine the advantageous properties from both of ILs and polymeric materials to expand the boundaries for developing advanced multifunctional soft materials. Thus, I proposed two following directions of integrating ILs and polymeric materials.

The first direction is through development of IPN between poly(ionic liquids) (PILs) and Poly(*N*-isopropylacrylamide) to achieve environmentally responsive conductivity, mechanical flexibility, and thermal stability in one system. PILs can be viewed as a subclass of polyelectrolytes that contain at least one of the ions from ionic liquid as the repeating units of the polymer chains [320,321]. PILs naturally inherit almost all the superior features of ionic liquids. In addition, PILs also have macromolecular properties, including flexible mechanical architecture and tunable functions, by designing the polymer backbone and the outer ions. In recent years, PILs based gels have drawn significant interest due to their broad applications in flexible electronics, such as wearable electronics, roll-up mobile devices and displays, and implantable biosensors [322]. As an alternative to traditional polyelectrolytes, PILs have not only a higher ionic conductivity but also a better thermal and electrochemical stability. These properties allow PILs to serve as flexible scaffold that allows the charged counter-ions to transport along the polymer chains within the solid matrix and also provides the physical barrier between electrodes to prevent short circuits between two electrodes.

Despite the encouraging research progresses in both polymerized ionic liquids and environmentally responsive hydrogels, the integration between those two classes of materials has not been explored. In order fully exploit their unique advantages, we propose a hybrid environmentally responsive PIL-polymer hydrogel using poly(1-Butyl-3-vinylimidazolium bis(trifluoromethylsulfonyl)imide) (poly[BVIM][TFSI]) and poly(*N*-isopropylacrylamide) (PNIPAAm) via interpenetrating polymer network (IPN) for “smart” soft electrolyte. The designed the IPN poly[BVIM][TFSI]-PNIPAAm gel will consist of two phases. The first phase of the proposed IPN gel is a temperature responsive hydrogel

that is comprised of crosslinked PNIPAAm network, and the synthesis will follow a similar procedure that has been illustrated in a previous work by our group [323]. After synthesis, the PNIPAAm hydrogel will be rinsed and dried for the use of next step. Then second phase of the IPN gel will be prepared within the first phase of the IPN gel by soaking the dried PNIPAAm gel in the precursor solution of [BVIM][TFSI] monomers and other suitable reaction reagents, allowing the free radical polymerization to proceed at either an elevated temperature or under UV exposure. Figure 5.2.2.1 illustrates the synthesis of vinylimidazolium based ionic liquids via free radical polymerization at elevated temperature using azobisisobutyronitrile (AIBN) as the initiator in the media of dimethylformamide [321].

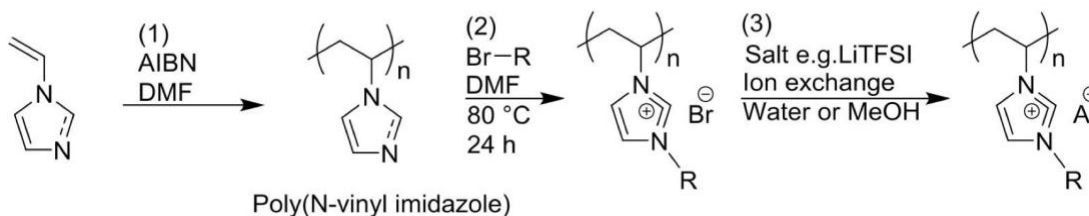


Figure 5.2.2.1. Polymerization reaction of (1-vinylimidazolium) based ionic liquids via free radical polymerization using AIBN as the initiator in the media of dimethylformamide (adapted from Ref [321]). In the case of the proposed synthesis, anion A⁻ is bis(trifluoromethylsulfonyl)imide and pendant group R is a butyl functional group.

In such a design, the thermal responsiveness of IPN poly[BVIM][TFSI]-PNIPAAm gel will facilitate switchable conductivities of the material between on and off (or high and low) states via its volume transition. Upon change of the environmental temperature, PNIPAAm network will undergo volume transitions following its lower critical solution temperature (LCST) behavior. When the PNIPAAm network exhibits shrinking at above its LCST, the overall network of the IPN gel will contract with reduced pore sizes, which can decrease the mobility of the ions along the second PIL network and thus hinder the charge transport. In contrast, the expansion of the PNIPAAm network from reswelling below the LCST will drive the volume increase of the IPN gel, enlarging the pore sizes to boost the transport of charged ions. Such a dynamic phenomenon at the molecular level can be simultaneously translated into a change in the bulk property of the material with a conductivity drop. Reversely, when the PNIPAAm network expands, the transport of ions will be enhanced due to increased transport of ions within the enlarged pore sizes of the overall network and a boost of conductivity is expected. This “smart” gel with switchable conductivity has potential to be applied for wearable sensors and flexible electronics. Moreover, some recent studies have shown that the mechanical enhancement of PILs can also be achieved by the ionic bonding/interactions between the organic cations and the anions in ionic liquids as well as the structural properties of counterions and the side-chain ions [324,325], but the enhancing mechanism was vaguely described in those studies lacking a systematic understanding. The development of a PIL-based tough and multifunctional soft gel can be another sub-task under this proposed direction to not only deliver a practical trait of the material for its potential applications but also a deeper understanding of the mechanical behaviors on PILs.

Several characterization methods will be utilized to confirm the synthesis and quantitatively analyze the core properties of the proposed “smart” IPN poly[BVIM][TFSI]-PNIPAAm gel. Differential scanning calorimetry (DSC) will help us verify the interpenetrating network formation by detecting T_g of the prepared IPN gel sample and comparing to T_g of the individual PNIPAAm and poly[BVIM][TFSI] phase. If the interpenetrating network formation is successful, a single T_g will be expected because of the close interaction and the entanglement between both of the polymer networks so that each individual network cannot thermally express themselves independently. Otherwise, two different T_g values will be observed due to a phase separated system. Swelling test will be performed at various temperatures to reveal the degree of the volume transition of the IPN gel, where the additionally incorporated poly[BVIM][TFSI] network could alter the LCST behavior of PNIPAAm in terms of the transition temperature and the degree of swelling. Electrochemical impedance spectroscopy (EIS) will be used to measure the conductivities of the poly[BVIM][TFSI]-PNIPAAm IPN gel with respect to temperature, capturing the response in conductivity of the system that is driven by the volume transition. Since the ionic conductivity of PILs in general can also be temperature dependent, three potential sets of control experiments will be conducted to further differentiate the effects from temperature change and volume transition, including the conductivity measurements of neat PNIPAAm in DI water, PNIPAAm in [BVIM][TFSI] (soaking after drying), and neat poly[BVIM][TFSI] gel. On the other hand, compressive tests by Instron E3000 will provide insights to disclose the evolution of the mechanical properties from the individual gel networks to the interpenetrated network.

Potential challenges that could also be associated with the exploration of the integration between PILs and environmentally responsive hydrogel are also summarized as follow. A non-aqueous media is more favored for the synthesis of poly[BVIM][TFSI], whereas the LCST behavior of PNIPAAm is typically associated with an aqueous environment. Although the thermal transition of PNIPAAm has been studied with various solvent systems other than pure water, even including ionic liquids and ionic liquid-water mixtures [326–329], the swelling behavior of the first phase PNIPAAm can still deviate from its most expected characteristics to an unknown extent in the soaking process prior to the polymerization of [BVIM][TFSI] monomers as well as in any thermal process to induce the responsive transition of the IPN gel after the overall preparation. It would be very interesting to investigate how phase transitions and responsive properties can be modified by non-aqueous solvent systems and the formation of IPN network with polymerized ionic liquids. The proposed work will offer not only a new route to integrate functional materials across different classes for practical applications but also a very beneficial approach to fundamentally understand the ionic conduction process within a thermally responsive polymeric network that can change the dimension of its porous structures.

The second direction is to utilize imidazolium based ILs as crosslinking agents to develop conductive composites. Epoxies are extensively applied as a versatile material in part due to their wide applications from composites to adhesives and coatings. However, while traditional epoxies may excel in properties such as thermal stability, toughness, and scratch resistance, a notable weakness of epoxies lies in its conductivity. Recent work has shown that opposed to a traditional amine-based hardener for curing of an epoxy matrix, ionic liquids can also serve as a hardener substitute with its own unique crosslinking

mechanism [330–332]. Of the many available ionic liquids, the two most notable classifications capable of forming such a crosslink are the imidazolium and phosphonium based ionic liquids. Due to the catalytic anionic nature of imidazolium and phosphonium moieties present in ionic liquids, high crosslink density can be achieved with relatively low loading [331,333]. In addition, the ionic conductive properties of ionic liquids allow for some of these properties to be inherited by the cured epoxy/IL system. Current solid-state electrolytes generally rely on highly conductive crystalline/ceramic materials or electrolyte-doped soft gel polymers, and common issues found with these solid electrolytes are their mechanical properties as well as electrochemical and thermal stability [334]. The development of a thermally and electrochemically stable solid electrolyte with high toughness would be revolutionary to current solid electrolyte technology.

Since the idea to employ ionic liquids as crosslinkers within an epoxy matrix is still in its infancy, much work regarding exploring different types of ionic liquids as well as fully understanding their capabilities as crosslinkers and conductivity enhancers is limited. Most of the existing work has been pioneered by Soares et al [335,336], who have experimented with several types of imidazolium and phosphonium ionic liquids in diglycidyl ether of bisphenol A (DGEBA)/Jeffamine epoxy systems. These Epoxy/IL systems show a large improvement in both thermal and mechanical properties over Epoxy/DETA systems with relatively low loading of IL (2.5-20 parts per hundred resin). While the thermal and mechanical performance of these epoxy using IL crosslinkers were not as high as epoxies with Jeffamine D230 and MCDEA crosslinkers, it has been found that as a general trend ionic conductivity increases at higher frequencies and temperature, especially above the T_g of the system. This is most likely due to increased flexibility of

the crosslinks above T_g , allowing ions to more freely move throughout the system. However, these studies have only scratched the surface of comprehending how the ionic conductivities of these systems behave. The ionic liquids used in these studies are reported to have relatively low conductivity between 2 and 8 mS/cm [330–333,335,336], compared to that of other ionic liquids commercially available. For example, 1-ethyl-3-methylimidazolium dicyanamide, [EMIM][DCA], has a high ionic conductivity of 27 mS/cm [337], much higher than the ionic liquids used in the above study. Additionally, no study has been done on the electrochemical stability changes due to incorporation of these ILs in an epoxy matrix. A better understanding of how the electrochemical stability of these solid epoxy electrolytes changes with respect to crosslink density and type of ionic liquids could also provide new contribution to breakthroughs regarding electrochemical stability issues with current solid-state electrolytes.

The proposed work of this section will be focused on a systematic investigation of epoxy with ionic liquid based crosslinkers with the following objective in two folds. First, an epoxy-ionic liquid system will be synthesized to improve the ionic conductivity. Second, the chain length, functionality, and the weight loading of the ionic liquids on the electrochemical stability will be studied and examined to develop a better understanding of the chemistry as well as the interplay between the structures and the material properties. We will synthesize an Epoxy/IL system by crosslinking imidazolium and/or phosphonium cation with diglycidyl ether bisphenol F, a constituent resin monomer that is widely used in epoxy based thermosetting products. Ionic Liquids considered for use in this crosslinking mechanism include triethyl(2-ethoxymethyl)phosphonium bis(fluorosulfonyl)amide, [P₂₂₂₍₁₀₁₎][FSA], and 1-ethyl-3-methylimidazolium dicyanamide [EMIM][DCA]. While

phosphonium-based ionic liquids may not offer as high of conductivity as imidazolium, they do offer increased mechanical properties of the resulting crosslinked epoxy [332,333]. The ionic liquid [P₂₂₂₍₁₀₁₎][FSA] offers excellent conductivity from the phosphonium category, which can offer vital insight into controlling the ionic conductivity in epoxy/IL systems. As stated previously, [EMIM][DCA] offers one of the highest ionic conductivity in ILs commercially available at 27 mS/cm but lacks the electrochemical stability that phosphonium ILs offer. The crosslinking of the unconjugated, insulating epoxy resin backbone with the imidazolium ring may help localize the charge, allowing for increased charge stability and increasing the electrochemical stability window. Figure 5.2.3.1 shows a schematic of the chemical crosslinking between the imidazolium ring and epoxide groups found on the epoxy resin. It has been found that both the imidazolium and phosphonium groups can actively form covalent bonds with epoxide groups at temperatures above 150 °C. Soares et al contributes this reaction mechanism at high heat to the decomposition of the initial imidazolium-based ionic liquid [336]. Above certain temperatures, the imidazolium ionic liquid decomposes into an imidazolium ring (pictured in Stage 1 of Figure 5.2.3.1) and small hydrocarbon chains dependent on the initial ionic liquid. The imidazole ring can then freely react with the epoxide ring of an epoxy resin molecule on each nitrogen in the imidazole ring. This serves to isolate the charge of the imidazole ring within the epoxy matrix, which may lead to increased electrochemical stability. Epoxy/IL systems containing [P₂₂₂₍₁₀₁₎][FSA] and [EMIM][DCA] will then be cured at various stages from 150 °C – 200 °C until the system is fully crosslinked. After fully curing, the epoxy/IL system will be characterized via mechanical properties, thermal properties, and ionic conductivity. In addition, targeted additional functionalities could be characterized such

depending on the type of ionic liquid chosen. Previous epoxy/IL systems using imidazolium based ILs reported glass transition temperatures ranging from 84 – 150 °C and tensile strengths ranging from 22 – 44 MPa depending on concentration and chain length [338].

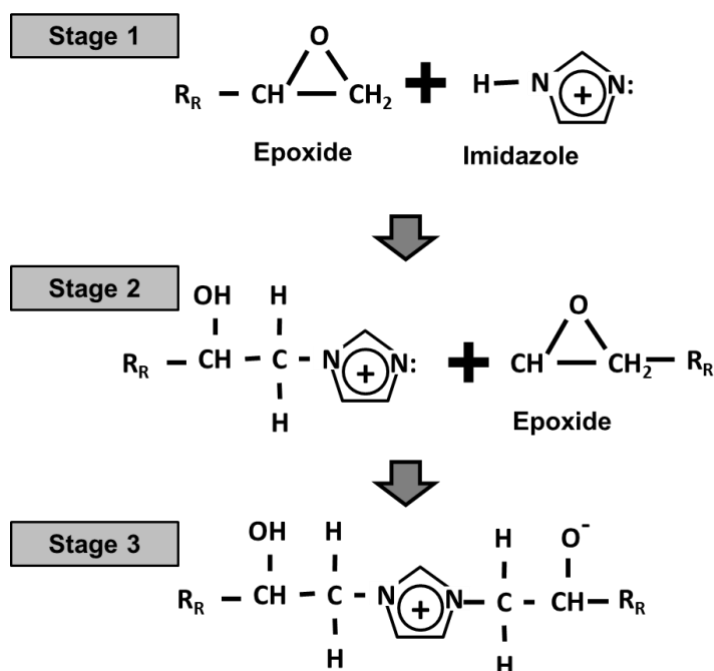


Figure 5.2.3.1. Mechanism for curing of epoxy resin by an imidazolium cation (adapted from [336]).

As stated previously, studies done by Soares et al discovered that the ionic conductivity could be increased with the addition of more ionic liquid per resin in their synthesized epoxy/IL systems, with a notable increase in ionic conductivity above 20 parts per hundred resin [335,336]. However, the ionic conductivity of the ionic liquids used in their systems was relatively low. We hypothesize that the ionic conductivity of the resulting epoxy/IL system may be improved with the use of ionic liquids with higher conductivity.

For example, the [EMIM] cation provides excellent conductivity, and the anion can be altered to examine effects of anion types on the resulting conductivity. Recently, [EMIM][DCA]/Epoxy systems have been reported by Maka et al as having exceptionally high T_g , thermal stability, and storage moduli [338]. However, their conductivity measurements only consisted of electrical conductivity, as they did not examine ionic conductivity at all. Epoxy/IL systems will be prepared with various combinations of cations and anions as well as weight loadings of ionic liquid to maximize the ionic conductivity as well as the thermal and mechanical performance. For ionic liquids containing the [EMIM] cation, anions such as dicyanamide [DCA], thiocyanate [SCN], tetrafluoroborate [BF₄], and trifluoromethylsulfonate [OTf] all offer excellent conductivity and are worth examining for their electrochemical, thermal, and mechanical effects on the resulting epoxy/IL systems.

Ionic conductivity will be measured via two separate methods for our proposed electrolytes: electrochemical impedance spectroscopy (EIS) and dielectric spectroscopy. As previously demonstrated, EIS is a very powerful tool when examining electrical properties of electrolytes in both solid and liquid phase. In a typical complex impedance plot, the intercept of the impedance semicircle with the real impedance axis (Z') gives the value of the bulk resistance (R_b). From this bulk resistance value, the ionic conductivity of the electrolyte can then be calculated via the equation, $\sigma=L/(R_bA)$, where σ is the ionic conductivity in S/cm, L is the film thickness, and A is the area of the electrode [339]. Dielectric spectroscopy is another alternative to EIS that can provide additional information on relevant properties in addition to ionic conductivity, such as permittivity and dielectric modulus. Measurements involve placing a sample between two parallel plate

capacitors and controlling both temperature and frequency. By subjecting this capacitor and electrolyte to an AC current, permittivity (both real, ϵ' , and imaginary, ϵ'') can be measured from total relaxation time of ions between the parallel plates with respect to scanning AC frequency (ω). Based on this dielectric constant profile, the conductivity can be obtained from the imaginary component of the permittivity, ϵ'' , via the known relationship $\epsilon''(\omega)_{dc} = \sigma_{dc}/(\epsilon_0\omega)$ [340], where ϵ_0 is the permittivity in free space and ω is the angular frequency, $\omega=2\pi\nu$. Lastly, mechanical properties will also be examined via in house analytical equipment. Glass transition temperature will be measured using a TA Instruments Q20 differential scanning calorimetry (DSC), glass transition temperature/moduli/crosslink density using dynamic mechanical analyzer (DMA), and Young's modulus/yield point via an Instron E3000.

While the ionic conductivity of the Epoxy/IL systems reported in literature have been examined with respect to temperature and frequency dependence, none have examined the electrochemical stability of these new materials. We propose to examine the effects of incorporation of the ionic liquid as an epoxy hardener on the electrochemical stability window (ESW) of these systems. Several systems with differing types of ionic liquid crosslinkers as describe in previous sections will be measured. It is anticipated that the polymer backbone of the epoxy resin will provide much needed stability due to its natural insulating properties and ability to localize charge on the ionic liquid cation group. However, too low of a concentration of ionic liquid crosslinker could cause for too weak of a signal, leading to a poor electrolyte. Therefore, it is important to find an optimal loading as well as optimal ionic liquid that provides good mechanical and thermal properties, while also providing sufficient electrochemical stability to be used in common

solid electrolyte applications. While electrochemical stability can be measured several ways, the most notable of these methods is through cyclic voltammetry. It is important to note that cyclic voltammetry does not measure the long-term effects on the stability of the electrolyte, only the potential window for electrolyte operation. One particular mode of cyclic voltammetry, Linear Sweep Voltammetry (LSV), can be performed to observe the effects of voltage applied on the direction of the current. From this plot, the electrochemical stability window (ESW) can be determined by the region of the LSV plot which no reduction or oxidation occurs. Typical electrolytes for current lithium ion batteries target voltage windows of approximately 4-5 V [340]. However, no group has currently reported the ESW of epoxy/IL systems. It is hypothesized that the unconjugated epoxy resin backbone will help stabilize the electrochemical properties of the electrolyte and prevent voltage window loss over multiple cycles. It is well documented that conjugation within a charged ionic liquid cation decreases the electrochemical stability window due to resonance and charge delocalization [341]. The unconjugated backbone of an epoxy resin bonding with a phosphonium or imidazolium cation allows for the charge to be localized, increasing the electrochemical stability window. Another important factor to examine with respect to electrochemical stability is the cation-anion pairing of the ionic liquid. For example, while the [EMIM][DCA] ionic liquid may offer high conductivity, it lacks electrochemical stability. One approach to improve the electrochemical stability is by altering the anion associated with the [EMIM] cation. While this may sacrifice some of the conductivity offered, the stability benefits may outweigh the loss of the [DCA] anion. Some studies report the ability of ionic liquid anions such as bis(trifluoromethylsulfonyl)imide (TFSI) expand the electrochemical stability window

(ESW) of polymer electrolyte systems [342]. IL crosslinkers such as [EMIM][TFSI] and its effect on the ESW of the epoxy/IL electrolyte will be compared to the other ILs such as [EMIM][DCA] and [P₂₂₂(101)][FSA] with high conductivity.

REFERENCES

- [1] Bauer S, Bauer-Gogonea S, Graz I, Kaltenbrunner M, Keplinger C, Schwödiauer R. 25th anniversary article: A soft future: From robots and sensor skin to energy harvesters. *Adv Mater* 2014;26:149–62. doi:10.1002/adma.201303349.
- [2] Nagel SR. Experimental soft-matter science. *Rev Mod Phys* 2017;89. doi:10.1103/RevModPhys.89.025002.
- [3] Nayak S, Andrew Lyon L. Soft nanotechnology with soft nanoparticles. *Angew Chemie - Int Ed* 2005;44:7686–708. doi:10.1002/anie.200501321.
- [4] Peppas NA, Langer R, Peppas NA, Langer R. *New Challenges in Biomaterials* 2016;263:1715–20.
- [5] Quake, Scherer. From micro-to nanofabrication with soft materials. *Science (80-)* 2000;290:1536. doi:10.1126/science.290.5496.1536.
- [6] Meeker SP, Poon WCK, Crain J, Terentjev EM. Colloid–liquid-crystal composites: An unusual soft solid. *Phys Rev E - Stat Physics, Plasmas, Fluids, Relat Interdiscip Top* 2000;61:6083–6. doi:10.1103/PhysRevE.61.R6083.
- [7] Morehead, S., Oliver, R., O’Connor, N., Stevenson-Keating, P., Toomey, A., & Wallace J. The Power of ‘Soft.’ *MRS Adv* 2016:1. doi:10.1557/adv.2016.
- [8] P.G. de Gennes. *Soft Matter*. *Rev Mod Phys* 1992;64. doi:10.1039/c7sm00977a.
- [9] Kazem N, Hellebrekers T, Majidi C. Soft Multifunctional Composites and Emulsions with Liquid Metals. *Adv Mater* 2017;29:1–14. doi:10.1002/adma.201605985.
- [10] Gong S, Cheng W. One-Dimensional Nanomaterials for Soft Electronics. *Adv Electron Mater* 2017;3. doi:10.1002/aelm.201600314.
- [11] Tsao CW, Guo XC, Hu WW. Highly stretchable conductive polypyrrole film on a three dimensional porous polydimethylsiloxane surface fabricated by a simple soft lithography process. *RSC Adv* 2016;6:113344–51. doi:10.1039/c6ra24521h.
- [12] Kamel S. Nanotechnology and its applications in lignocellulosic composites, a mini review. *Express Polym Lett* 2007;1:546–75. doi:10.3144/expresspolymlett.2007.78.
- [13] Ho Y-C, Huang F-M, Chang Y-C. Cytotoxicity of formaldehyde on human osteoblastic cells is related to intracellular glutathione levels. *J Biomed Mater Res B Appl Biomater* 2007;83:340–4. doi:10.1002/jbmb.

- [14] Jang KI, Chung HU, Xu S, Lee CH, Luan H, Jeong J, et al. Soft network composite materials with deterministic and bio-inspired designs. *Nat Commun* 2015;6:1–11. doi:10.1038/ncomms7566.
- [15] Meyers MA, Chen PY, Lin AYM, Seki Y. Biological materials: Structure and mechanical properties. *Prog Mater Sci* 2008;53:1–206. doi:10.1016/j.pmatsci.2007.05.002.
- [16] Majumdar A, Butola BS, Srivastava A. Development of soft composite materials with improved impact resistance using Kevlar fabric and nano-silica based shear thickening fluid. *Mater Des* 2014;54:295–300. doi:10.1016/j.matdes.2013.07.086.
- [17] Guo C, Zhou L, Lv J. Effects of expandable graphite and modified ammonium polyphosphate on the flame-retardant and mechanical properties of wood flour-polypropylene composites. *Polym Polym Compos* 2013;21:449–56. doi:10.1002/app.
- [18] Miriyev A, Stack K, Lipson H. Soft material for soft actuators. *Nat Commun* 2017;8:1–8. doi:10.1038/s41467-017-00685-3.
- [19] Mosadegh B, Polygerinos P, Keplinger C, Wennstedt S, Shepherd RF, Gupta U, et al. Pneumatic networks for soft robotics that actuate rapidly. *Adv Funct Mater* 2014;24:2163–70. doi:10.1002/adfm.201303288.
- [20] Martinez R V., Glavan AC, Keplinger C, Oyetibo AI, Whitesides GM. Soft actuators and robots that are resistant to mechanical damage. *Adv Funct Mater* 2014;24:3003–10. doi:10.1002/adfm.201303676.
- [21] Calvert P. Hydrogels for soft machines. *Adv Mater* 2009;21:743–56. doi:10.1002/adma.200800534.
- [22] Hua D, Zhang X, Ji Z, Yan C, Yu B, Li Y, et al. 3D printing of shape changing composites for constructing flexible paper-based photothermal bilayer actuators. *J Mater Chem C* 2018;6:2123–31. doi:10.1039/c7tc05710e.
- [23] Rocha MAA, Neves CMSS, Freire MG, Russina O, Triolo A, Coutinho JAP, et al. Alkylimidazolium based ionic liquids: Impact of cation symmetry on their nanoscale structural organization. *J Phys Chem B* 2013;117:10889–97. doi:10.1021/jp406374a.
- [24] Ohno H. *Electrochemical Aspects of Ionic Liquids*. 2nd ed. John Wiley & Sons, Inc., Hoboken, New Jersey; 2011.
- [25] Krossing I, Slattery JM, Dagueuet C, Dyson PJ, Oleinikova A, Weingärtner H. Why are ionic liquids liquid? A simple explanation based on lattice and solvation

- energies. *J Am Chem Soc* 2006;128:13427–34. doi:10.1021/ja0619612.
- [26] Palacio M, Bhushan B. A review of ionic liquids for green molecular lubrication in nanotechnology. *Tribol Lett* 2010;40:247–68. doi:10.1007/s11249-010-9671-8.
- [27] Shi R, Wang Y. Dual Ionic and Organic Nature of Ionic Liquids. *Sci Rep* 2016;6:1–12. doi:10.1038/srep19644.
- [28] Frost DS, Nofen EM, Dai LL. Particle self-assembly at ionic liquid-based interfaces. *Adv Colloid Interface Sci* 2014;206:92–105. doi:10.1016/j.cis.2013.09.004.
- [29] Ueno K, Hiroyuki T, Masayoshi W. Physical chemistry of ionic liquids: correlation with ionic structure and physicochemical properties. *Phys Chem Chem Phys* 2010;12:1648–1648. doi:10.1039/c001176m.
- [30] Austen Angell C, Ansari Y, Zhao Z. Ionic Liquids: Past, present and future. *Faraday Discuss* 2012;154:9–27. doi:10.1039/c1fd00112d.
- [31] Welton T. Ionic liquids: a brief history. *Biophys Rev* 2018;10:691–706. doi:10.1007/s12551-018-0419-2.
- [32] Plechkova N V., Seddon KR. Applications of ionic liquids in the chemical industry. *Chem Soc Rev* 2008;37:123–50. doi:10.1039/b006677j.
- [33] Goharshadi EK, Ding Y, Nancarrow P. Green synthesis of ZnO nanoparticles in a room-temperature ionic liquid 1-ethyl-3-methylimidazolium bis(trifluoromethylsulfonyl)imide. *J Phys Chem Solids* 2008;69:2057–60. doi:10.1016/j.jpcs.2008.03.002.
- [34] Kubisa P. Application of ionic liquids as solvents for polymerization processes. *Prog Polym Sci* 2004;29:3–12. doi:10.1016/j.progpolymsci.2003.10.002.
- [35] Vallette H, Ferron L, Coquerel G, Gaumont AC, Plaquevent JC. Peptide synthesis in room temperature ionic liquids. *Tetrahedron Lett* 2004;45:1617–9. doi:10.1016/j.tetlet.2003.12.124.
- [36] Brennecke JF, Maginn EJ. Ionic liquids: Innovative fluids for chemical processing. *AIChE J* 2001;47:2384–9. doi:10.1002/aic.690471102.
- [37] Welton T. Room-Temperature Ionic Liquids. Solvents for Synthesis and Catalysis. *Chem Rev* 1999;99:2071–84. doi:10.1021/cr980032t.
- [38] Wasserscheid P, Keim W. Ionic Liquids—New “Solutions” for Transition Metal Catalysis. *Angew Chemie* 2000;39:3772–89. doi:10.1002/1521-

3773(20001103)39:21<3772::AID-ANIE3772>3.0.CO;2-5.

- [39] Zhao D, Wu M, Kou Y, Min E. Ionic liquids: Applications in catalysis. *Catal Today* 2002;74:157–89. doi:10.1016/S0920-5861(01)00541-7.
- [40] Olivier-Bourbigou H, Magna L, Morvan D. Ionic liquids and catalysis: Recent progress from knowledge to applications. *Appl Catal A Gen* 2010;373:1–56. doi:10.1016/j.apcata.2009.10.008.
- [41] Gordon CM. New developments in catalysis using ionic liquids. *Appl Catal A Gen* 2001;222:101–17. doi:10.1016/S0926-860X(01)00834-1.
- [42] Zhao H, Xia S, Ma P. Use of ionic liquids as “green” solvents for extractions. *J Chem Technol Biotechnol* 2005;80:1089–96. doi:10.1002/jctb.1333.
- [43] Bara JE, Carlisle TK, Gabriel CJ, Finotello A, Gin DL, Noble RD, et al. Guide to CO Separations in Imidazolium-Based Room-Temperature Ionic Liquids Guide to CO 2 Separations in Imidazolium-Based Room-Temperature Ionic Liquids. *Ind* 2009:2739–51. doi:10.1021/ie8016237.
- [44] Berthod A, Ruiz-Ángel MJ, Carda-Broch S. Ionic liquids in separation techniques. *J Chromatogr A* 2008;1184:6–18. doi:10.1016/j.chroma.2007.11.109.
- [45] Ye C, Liu W, Chen Y, Yu L. Room-temperature ionic liquids: A novel versatile lubricant. *Chem Commun* 2001;21:2244–5. doi:10.1039/b106935g.
- [46] Okaniwa T, Hayama M. The application of ionic liquids into space lubricants 2013:25–7.
- [47] Fan X, Wang L. Highly conductive ionic liquids toward high-performance space-lubricating greases. *ACS Appl Mater Interfaces* 2014;6:14660–71. doi:10.1021/am503941e.
- [48] Moniruzzaman M, Kamiya N, Goto M. Activation and stabilization of enzymes in ionic liquids. *Org Biomol Chem* 2010;8:2887–99. doi:10.1039/b926130c.
- [49] Egorova KS, Gordeev EG, Ananikov VP. Biological Activity of Ionic Liquids and Their Application in Pharmaceuticals and Medicine. *Chem Rev* 2017;117:7132–89. doi:10.1021/acs.chemrev.6b00562.
- [50] Van Rantwijk F, Lau RM, Sheldon RA. Biocatalytic transformations in ionic liquids. *Trends Biotechnol* 2003;21:131–8. doi:10.1016/S0167-7799(03)00008-8.
- [51] Armand M, Endres F, MacFarlane DR, Ohno H, Scrosati B. Ionic-liquid materials for the electrochemical challenges of the future. *Nat Mater* 2009;8:621–9.

doi:10.1038/nmat2448.

- [52] Wei D, Ivaska A. Applications of ionic liquids in electrochemical sensors. *Anal Chim Acta* 2008;607:126–35. doi:10.1016/j.aca.2007.12.011.
- [53] Macfarlane DR, Forsyth M, Howlett PC, Jennifer M, Sun J, Annat G, et al. Ionic Liquids in Electrochemical Devices and Processes : Managing Interfacial Electrochemistry *Ionic Liquids in Electrochemical Devices and Processes : Managing Interfacial Electrochemistry* 2007;40:1165–73. doi:10.1021/ar7000952.
- [54] Fujita K, Murata K, Masuda M, Nakamura N, Ohno H. Ionic liquids designed for advanced applications in bioelectrochemistry. *RSC Adv* 2012;2:4018–30. doi:10.1039/c2ra01045c.
- [55] Valkenburg MEV, Vaughn RL, Williams M, Wilkes JS. Thermochemistry of ionic liquid heat-transfer fluids. *Thermochim Acta* 2005;425:181–8. doi:10.1016/j.tca.2004.11.013.
- [56] Liu J, Wang F, Zhang L, Fang X, Zhang Z. Thermodynamic properties and thermal stability of ionic liquid-based nanofluids containing graphene as advanced heat transfer fluids for medium-to-high-temperature applications. *Renew Energy* 2014;63:519–23. doi:10.1016/j.renene.2013.10.002.
- [57] Ha SH, Menchavez RN, Koo Y-M. Reprocessing of spent nuclear waste using ionic liquids. *Korean J Chem Eng* 2010;27:1360–5. doi:10.1007/s11814-010-0386-1.
- [58] Sengupta A, Mohapatra PK, Kadam RM, Manna D, Ghanty TK, Iqbal M, et al. Diglycolamide-functionalized task specific ionic liquids for nuclear waste remediation: Extraction, luminescence, theoretical and EPR investigations. *RSC Adv* 2014;4:46613–23. doi:10.1039/c4ra05798h.
- [59] Yan C, Mu T. Investigation of ionic liquids for efficient removal and reliable storage of radioactive iodine: A halogen-bonding case. *Phys Chem Chem Phys* 2014;16:5071–5. doi:10.1039/c4cp00279b.
- [60] Luo HL, Ahmed M. IONIC LIQUID CATALYZED ALKYLATION PROCESSES & SYSTEMS, 2013. doi:10.1037/t24245-000.
- [61] Timken HK. Isoalky ™ Technology : Next Generation Alkylate Gasoline Manufacturing Process Technology. 2017.
- [62] Sakaebe H, Matsumoto H. N-methyl-N-propylpiperidinium bis(trifluoromethanesulfonyl)imide (PP13-TFSI) - Novel electrolyte base for Li battery. *Electrochem Commun* 2003;5:594–8. doi:10.1016/S1388-2481(03)00137-

1.

- [63] MacFarlane DR, Tachikawa N, Forsyth M, Pringle JM, Howlett PC, Elliott GD, et al. Energy applications of ionic liquids. *Energy Environ Sci* 2014;7:232–50. doi:10.1039/C3EE42099J.
- [64] Lewandowski A, Świdarska-Mocek A. Ionic liquids as electrolytes for Li-ion batteries-An overview of electrochemical studies. *J Power Sources* 2009;194:601–9. doi:10.1016/j.jpowsour.2009.06.089.
- [65] Galiński M, Lewandowski A, Stepniak I. Ionic liquids as electrolytes. *Electrochim Acta* 2006;51:5567–80. doi:10.1016/j.electacta.2006.03.016.
- [66] Simon P, Gogotsi Y. Materials for electrochemical capacitors. *Nat Mater* 2008;7:845–54. doi:10.1038/nmat2297.
- [67] Tsai WY, Lin R, Murali S, Zhang LL, McDonough JK, Ruoff RS, et al. Outstanding performance of activated graphene based supercapacitors in ionic liquid electrolyte from -50 to 80°C. *Nano Energy* 2013;2:403–11. doi:10.1016/j.nanoen.2012.11.006.
- [68] Brandt A, Pohlmann S, Varzi A, Balducci A, Passerini S. Ionic liquids in supercapacitors. *MRS Bull* 2013;38:554–9. doi:10.1557/mrs.2013.151.
- [69] Balducci A, Dugas R, Taberna PL, Simon P, Plée D, Mastragostino M, et al. High temperature carbon-carbon supercapacitor using ionic liquid as electrolyte. *J Power Sources* 2007;165:922–7. doi:10.1016/j.jpowsour.2006.12.048.
- [70] Borges RS, Reddy ALM, Rodrigues MTF, Gullapalli H, Balakrishnan K, Silva GG, et al. Supercapacitor Operating at 200 Degrees Celsius. *Sci Rep* 2013;3:1–6. doi:10.1038/srep02572.
- [71] Elia GA, Ulissi U, Jeong S, Passerini S, Hassoun J. Exceptional long-life performance of lithium-ion batteries using ionic liquid-based electrolytes. *Energy Environ Sci* 2016;9:3210–20. doi:10.1039/C6EE01295G.
- [72] Hammami A, Raymond N AM. Lithium-ion batteries: Runaway risk of forming toxic compounds. *Nature* 2003;424:635–636. doi:10.1126/science.1086743.
- [73] Liu K, Liu Y, Lin D, Pei A, Cui Y. Materials for lithium-ion battery safety. *Sci Adv* 2018;4. doi:10.1126/sciadv.aas9820.
- [74] Guerfi A, Dontigny M, Charest P, Petitclerc M, Lagacé M, Vijn A, et al. Improved electrolytes for Li-ion batteries: Mixtures of ionic liquid and organic electrolyte with enhanced safety and electrochemical performance. *J Power Sources*

- 2010;195:845–52. doi:10.1016/j.jpowsour.2009.08.056.
- [75] Yang B, Li C, Zhou J, Liu J, Zhang Q. Pyrrolidinium-based ionic liquid electrolyte with organic additive and LiTFSI for high-safety lithium-ion batteries. *Electrochim Acta* 2014;148:39–45. doi:10.1016/j.electacta.2014.10.001.
- [76] Song JW, Nguyen CC, Song SW. Stabilized cycling performance of silicon oxide anode in ionic liquid electrolyte for rechargeable lithium batteries. *RSC Adv* 2012;2:2003–9. doi:10.1039/c2ra01183b.
- [77] Kohli R. *Removal of Surface Contaminants Using Ionic Liquids*. vol. 6. Elsevier; 2013. doi:10.1016/B978-1-4377-7879-3.00001-7.
- [78] Rehman A, Zeng X. Ionic liquids as green solvents and electrolytes for robust chemical sensor development. *Acc Chem Res* 2012;45:1667–77. doi:10.1021/ar200330v.
- [79] Silvester DS. Recent advances in the use of ionic liquids for electrochemical sensing. *Analyst* 2011;136:4871–82. doi:10.1039/c1an15699c.
- [80] Aguilar AD, Forzani ES, Leright M, Tsow F, Cagan A, Iglesias RA, et al. A hybrid nanosensor for TNT vapor detection. *Nano Lett* 2010;10:380–4. doi:10.1021/nl902382s.
- [81] Wadhawan JD, Schroder U, Neudeck A, Wilkins SJ, Compton RG, Marken F, et al. Ionic liquid modified electrodes. Unusual partitioning and diffusion effects of Fe(CN)₆(4-/3-) in droplet and thin layer deposits of 1-methyl-3-(2, 6-(S)-dimethylocten-2-yl)-imidazolium tetrafluoroborate. *J Electroanal Chem* 2000;493:75–83. doi:10.1016/s0022-0728(00)00308-9.
- [82] Lu D, Shomali N, Shen A. Task specific ionic liquid for direct electrochemistry of metal oxides. *Electrochem Commun* 2010;12:1214–7. doi:10.1016/j.elecom.2010.06.022.
- [83] Kim K Il, Kang HY, Lee JC, Choi SH. Fabrication of a multi-walled nanotube (MWNT) ionic liquid electrode and its application for sensing phenolics in red wines. *Sensors* 2009;9:6701–14. doi:10.3390/s90906701.
- [84] Opallo M, Lesniewski A. A review on electrodes modified with ionic liquids. *J Electroanal Chem* 2011;656:2–16. doi:10.1016/j.jelechem.2011.01.008.
- [85] Sanati AL, Karimi-Maleh H, Badiei A, Biparva P, Ensafi AA. A voltammetric sensor based on NiO/CNTs ionic liquid carbon paste electrode for determination of morphine in the presence of diclofenac. *Mater Sci Eng C* 2014;35:379–85. doi:10.1016/j.msec.2013.11.031.

- [86] Musameh M, Wang J. Sensitive and stable amperometric measurements at ionic liquid-carbon paste microelectrodes. *Anal Chim Acta* 2008;606:45–9. doi:10.1016/j.aca.2007.11.012.
- [87] Shiddiky MJA, Torriero AAJ. Application of ionic liquids in electrochemical sensing systems. *Biosens Bioelectron* 2011;26:1775–87. doi:10.1016/j.bios.2010.08.064.
- [88] Rogers EI, Mahony AMO, Aldous L, Compton RG. No Title 2010;33:473–502.
- [89] Peng B, Zhu J, Liu X, Qin Y. Potentiometric response of ion-selective membranes with ionic liquids as ion-exchanger and plasticizer. *Sensors Actuators, B Chem* 2008;133:308–14. doi:10.1016/j.snb.2008.02.027.
- [90] Huang J-F, Lin B-T. Application of a nanoporous gold electrode for the sensitive detection of copper via mercury-free anodic stripping voltammetry. *Analyst* 2009;134:2306. doi:10.1039/b910282e.
- [91] Nockemann P, Thijs B, Pittois S, Thoen J, Glorieux C, Van Hecke K, et al. Task-specific ionic liquid for solubilizing metal oxides. *J Phys Chem B* 2006;110:20978–92. doi:10.1021/jp0642995.
- [92] Balducci A. Ionic Liquids in Lithium-Ion Batteries. *Top Curr Chem* 2017;375:1–27. doi:10.1007/s41061-017-0109-8.
- [93] Bahram M, Mohseni N, Moghtader M. An Introduction to Hydrogels and Some Recent Applications. *Emerg. Concepts Anal. Appl. Hydrogels*, 2016. doi:10.5772/64301.
- [94] Wichterle O, Lím D. Hydrophilic Gels for Biological Use. *Nature* 1960;185:117–8. doi:10.1038/185117a0.
- [95] Bawa P, Pillay V, Choonara YE, Toit LC du. Stimuli-responsive polymers and their applications in drug delivery. *Biomed Mater* 2009;4:22001. doi:10.1088/1748-6041/4/2/022001.
- [96] Richter A, Paschew G, Klatt S, Lienig J, Arndt K-F, Adler H-JP. Review on Hydrogel-based pH Sensors and Microsensors. *Sensors* 2008;8:561–81. doi:10.3390/s8010561.
- [97] Gupta P, Vermani K, Garg S. Hydrogels: From controlled release to pH-responsive drug delivery. *Drug Discov Today* 2002;7:569–79. doi:10.1016/S1359-6446(02)02255-9.
- [98] Gong JP, Nitta T, Osada Y. Electrokinetic modeling of the contractile phenomena

- of polyelectrolyte gels. One-dimensional capillary model. *J Chem Inf Model* 2013;53:1689–99. doi:10.1017/CBO9781107415324.004.
- [99] Luo R, Li H, Lam KY. Modeling and simulation of chemo-electro-mechanical behavior of pH-electric-sensitive hydrogel. *Anal Bioanal Chem* 2007;389:863–73. doi:10.1007/s00216-007-1483-9.
- [100] Qiu Y, Park K. Environment-sensitive hydrogels for drug delivery. *Adv Drug Deliv Rev* 2012;64:49–60. doi:10.1016/j.addr.2012.09.024.
- [101] Wallmersperger T, Ballhause D, Kroplin B, Gunther M, Gerlach G. Coupled Multi-field Formulation in Space and Time for the Simulation of Intelligent Hydrogels. *J Intell Mater Syst Struct* 2009;20:1483–92. doi:10.1177/1045389X09105236.
- [102] Tanaka T, Izumi N, Sun S-T, Ueno-Nishio S. Collapse of Gels in an Electric Field. *Science* (80-) 1982;218:467–9. doi:10.1126/science.218.4571.467.
- [103] Miyata T, Uragami T, Nakamae K. Biomolecule-sensitive hydrogels. *Adv Drug Deliv Rev* 2002;54:79–98. doi:10.1016/S0169-409X(01)00241-1.
- [104] Suzuki a, Ishii T, Maruyama Y. Optical switching in polymer gels. *J Appl Phys* 1996;80:131. doi:10.1063/1.362768.
- [105] Suzuki A, Tanaka T. Phase transition in polymer gels induced by visible light. *Nature* 1990;346:345–7. doi:10.1038/346345a0.
- [106] Gerlach G, Guenther M, Sorber J, Suchaneck G, Arndt KF, Richter A. Chemical and pH sensors based on the swelling behavior of hydrogels. *Sensors Actuators, B Chem* 2005;111–112:555–61. doi:10.1016/j.snb.2005.03.040.
- [107] Hoffmann J, Plötner M, Kuckling D, Fischer WJ. Photopatterning of thermally sensitive hydrogels useful for microactuators. *Sensors Actuators, A Phys* 1999;77:139–44. doi:10.1016/S0924-4247(99)00080-1.
- [108] Hoare TR, Kohane DS. Hydrogels in drug delivery: Progress and challenges. *Polymer (Guildf)* 2008;49:1993–2007. doi:10.1016/j.polymer.2008.01.027.
- [109] Peppas NA. Hydrogels and drug delivery. *Curr Opin Colloid Interface Sci* 1997;2:531–7. doi:10.1016/S1359-0294(97)80103-3.
- [110] Atta AM, El-Ghazawy RAM, Farag RK, Abdel-Azim AAA. Crosslinked reactive macromonomers based on polyisobutylene and octadecyl acrylate copolymers as crude oil sorbers. *React Funct Polym* 2006;66:931–43. doi:10.1016/j.reactfunctpolym.2006.01.001.

- [111] Ummadisingu A, Gupta S. Characteristics and kinetic study of chitosan prepared from seafood industry waste for oil spills cleanup. *Desalin Water Treat* 2012;44:44–51. doi:10.1080/19443994.2012.691742.
- [112] Zhao F, Zhou X, Liu Y, Shi Y, Dai Y, Yu G. Super Moisture-Absorbent Gels for All-Weather Atmospheric Water Harvesting. *Adv Mater* 2019;31:1–7. doi:10.1002/adma.201806446.
- [113] Chan V, Park K, Collens MB, Kong H, Saif T a, Bashir R. Development of miniaturized walking biological machines. *Sci Rep* 2012;2:857. doi:10.1038/srep00857.
- [114] Montero-Baker MF, Au-Yeung KY, Wisniewski NA, Gamsey S, Morelli-Alvarez L, Mills JL, et al. The First-in-Man “si Se Puede” Study for the use of micro-oxygen sensors (MOXYs) to determine dynamic relative oxygen indices in the feet of patients with limb-threatening ischemia during endovascular therapy. *J Vasc Surg* 2015;61:1501-1510.e1. doi:10.1016/j.jvs.2014.12.060.
- [115] Phadke A, Zhang C, Arman B, Hsu C-C, Mashelkar RA, Lele AK, et al. Rapid self-healing hydrogels. *Proc Natl Acad Sci U S A* 2012;109:4383–8. doi:10.1073/pnas.1201122109.
- [116] Gao S, Sun J, Liu P, Zhang F, Zhang W, Yuan S, et al. A Robust Polyionized Hydrogel with an Unprecedented Underwater Anti-Crude-Oil-Adhesion Property. *Adv Mater* 2016;28:5307–14. doi:10.1002/adma.201600417.
- [117] Vishnubhaktula S, Elupula R, Durán-Lara EF. Recent Advances in Hydrogel-Based Drug Delivery for Melanoma Cancer Therapy: A Mini Review. *J Drug Deliv* 2017;2017:1–9. doi:10.1155/2017/7275985.
- [118] Sanyal S, Huang H-C, Rege K, Dai LL. Thermo-Responsive Core-Shell Composite Nanoparticles Synthesized via One-Step Pickering Emulsion Polymerization for Controlled Drug Delivery. *J Nanomed Nanotechnol* 2011;02. doi:10.4172/2157-7439.1000126.
- [119] Wang F, Wang YC, Dou S, Xiong MH, Sun TM, Wang J. Doxorubicin-tethered responsive gold nanoparticles facilitate intracellular drug delivery for overcoming multidrug resistance in cancer cells. *ACS Nano* 2011;5:3679–92. doi:10.1021/nn200007z.
- [120] Zhang H, Tian Y, Zhu Z, Xu H, Li X, Zheng D, et al. Efficient antitumor effect of co-drug-loaded nanoparticles with gelatin hydrogel by local implantation. *Sci Rep* 2016;6:1–14. doi:10.1038/srep26546.
- [121] Senapati S, Mahanta AK, Kumar S, Maiti P. Controlled drug delivery vehicles for

- cancer treatment and their performance. *Signal Transduct Target Ther* 2018;3:7. doi:10.1038/s41392-017-0004-3.
- [122] Klouda L, Mikos AG. Thermoresponsive hydrogels in biomedical applications - a review. *Eur J Pharm Biopharm* 2011;68:34–45. doi:10.1016/j.ejpb.2007.02.025.Thermoresponsive.
- [123] Hennink WE, Franssen O, Van Dijk-Wolthuis WNE, Talsma H. Dextran hydrogels for the controlled release of proteins. *J Control Release* 1997;48:107–14. doi:10.1016/S0168-3659(97)00047-3.
- [124] Fang JY, Chen JP, Leu YL, Hu JW. Temperature-sensitive hydrogels composed of chitosan and hyaluronic acid as injectable carriers for drug delivery. *Eur J Pharm Biopharm* 2008;68:626–36. doi:10.1016/j.ejpb.2007.08.012.
- [125] Mano JF. Stimuli-responsive polymeric systems for biomedical applications. *Adv Eng Mater* 2008;10:515–27. doi:10.1002/adem.200700355.
- [126] Lowman AM, Morishita M, Kajita M, Nagai T, Peppas NA. Oral delivery of insulin using pH-responsive complexation gels. *J Pharm Sci* 1999. doi:10.1021/js980337n.
- [127] Rizwan M, Yahya R, Hassan A, Yar M, Azzahari AD, Selvanathan V, et al. pH sensitive hydrogels in drug delivery: Brief history, properties, swelling, and release mechanism, material selection and applications. *Polymers (Basel)* 2017;9. doi:10.3390/polym9040137.
- [128] Sugihara S, Blanz A, Armes SP, Ryan AJ, Lewis AL. Aqueous dispersion polymerization: A new paradigm for in situ block copolymer self-assembly in concentrated solution. *J Am Chem Soc* 2011;133:15707–13. doi:10.1021/ja205887v.
- [129] Dai S, Ravi P, Tam KC. pH-Responsive polymers: Synthesis, properties and applications. *Soft Matter* 2008;4:435–49. doi:10.1039/b714741d.
- [130] Xiong W, Gao X, Zhao Y, Xu H, Yang X. The dual temperature/pH-sensitive multiphase behavior of poly(N-isopropylacrylamide-co-acrylic acid) microgels for potential application in in situ gelling system. *Colloids Surfaces B Biointerfaces* 2011;84:103–10. doi:10.1016/j.colsurfb.2010.12.017.
- [131] Matsumura S, Hlil AR, Lepiller C, Gaudet J, Guay D, Shi Z, et al. Ionomers for proton exchange membrane fuel cells with sulfonic acid groups on the end-groups: Novel branched poly(ether-ketone)s. *Am Chem Soc Polym Prepr Div Polym Chem* 2008;49:511–2. doi:10.1002/pola.

- [132] Glassman MJ, Chan J, Olsen BD. Reinforcement of shear thinning protein hydrogels by responsive block copolymer self-assembly. *Adv Funct Mater* 2013;23:1182–93. doi:10.1002/adfm.201202034.
- [133] Oh JK. Polylactide (PLA)-based amphiphilic block copolymers: Synthesis, self-assembly, and biomedical applications. *Soft Matter* 2011;7:5096–108. doi:10.1039/c0sm01539c.
- [134] Borra EF, Seddiki O, Angel R, Eisenstein D, Hickson P, Seddon KR, et al. Deposition of metal films on an ionic liquid as a basis for a lunar telescope. *Nature* 2007;447:979–81. doi:10.1038/nature05909.
- [135] Nancarrow P, Mohammed H. Ionic Liquids in Space Technology - Current and Future Trends. *ChemBioEng Rev* 2017;4:106–19. doi:10.1002/cben.201600021.
- [136] Anderson J, Plett G, Anderson M, Ziemer J. Testing Fundamental Properties of Ionic Liquids for Colloid Microthruster Applications. 42nd AIAA/ASME/SAE/ASEE Jt Propuls Conf Exhib 2006:1–9. doi:10.2514/6.2006-4646.
- [137] Havskov J, Alguacil G. Instrumentation in earthquake seismology. 2015. doi:10.1007/978-3-319-21314-9.
- [138] Lognonné P, Johnson C. Planetary Seismology. *Treatise Geophys* 2007;10:69–122. doi:10.1016/B978-044452748-6.00154-1.
- [139] Lognonné P, Giardini D, Banerdt B, Gagnepain-Beyneix J, Mocquet a, Spohn T, et al. The NetLander very broad band seismometer. *Planet Space Sci* 2000;48:1289–302. doi:10.1016/S0032-0633(00)00110-0.
- [140] Hopf T, Kumar S, Karl WJ, Pike WT. Shock protection of penetrator-based instrumentation via a sublimation approach. *Adv Sp Res* 2010;45:460–7. doi:10.1016/j.asr.2009.08.015.
- [141] Huang H, Carande B, Tang R, Oiler J, Dmitriy Z, Vadim A, et al. Development of a micro seismometer based on molecular electronic transducer technology for planetary exploration. *Appl Phys Lett* 2013;102:193512. doi:10.1109/MEMSYS.2013.6474320.
- [142] Mengbing Liang, Hai Huang, Vadim Agafonov, Rui Tang, Ruirui Han HY. Molecular electronic transducer based planetary seismometer with new fabrication process. *Micro Electro Mech Syst 2016 IEEE 29th Int Conf* 2016;5:986–9.
- [143] Huang H, Carande B, Tang R, Oiler J, Dmitriy Z, Vadim A. Development of a micro seismometer based on molecular electronic transducer technology for

planetary exploration. *Micro Electro Mech Syst 2013 IEEE 26th Int Conf* 2013:629–32.

- [144] Antonov A, Shabalina A, Razin A, Avdyukhina S, Egorov I, Agafonov V. Low-frequency seismic node based on molecular-electronic transfer sensors for marine and transition zone exploration. *J Atmos Ocean Technol* 2017;34:1743–8. doi:10.1175/JTECH-D-16-0254.1.
- [145] Huang H, Agafonov V, Yu H. Molecular electric transducers as motion sensors: A review. *Sensors (Switzerland)* 2013;13:4581–97. doi:10.3390/s130404581.
- [146] Zhelonkin AI. DESIGN METHODS AND BASIC CHARACTERISTICS FOR MOLECULAR ELECTRONIC TRANSDUCERS. *Meas Tech* 2008;51:13–6.
- [147] Zaitsev DL, Dudkin P V, Krishtop T V, Neeshpapa A V, Popov VG, Uskov V V, et al. Experimental Studies of Temperature Dependence of Transfer Function of Molecular Electronic Transducers at High Frequencies. *IEEE Sens J* 2016;16:7864–9. doi:10.1109/JSEN.2016.2606517.
- [148] Europa Study Team. Europa Study 2012 Report. *Natl Aeronaut Sp Adm* 2012:2–707. doi:JPL D-71990.
- [149] Smart MC. Electrolytes for Low-Temperature Lithium Batteries Based on Ternary Mixtures of Aliphatic Carbonates. *J Electrochem Soc* 1999;146:486. doi:10.1149/1.1391633.
- [150] Hamenu L, Lee HS, Latifatu M, Kim KM, Park J, Baek YG, et al. Lithium-silica nanosalt as a low-temperature electrolyte additive for lithium-ion batteries. *Curr Appl Phys* 2016;16:611–7. doi:10.1016/j.cap.2016.03.012.
- [151] Zhu G, Wen K, Lv W, Zhou X, Liang Y, Yang F, et al. Materials insights into low-temperature performances of lithium-ion batteries. *J Power Sources* 2015;300:29–40. doi:10.1016/j.jpowsour.2015.09.056.
- [152] Plichta EJ, Behl WK. Low-temperature electrolyte for lithium and lithium-ion batteries. *J Power Sources* 2000;88:192–6. doi:10.1016/S0378-7753(00)00367-0.
- [153] Kasprzyk M, Zalewska A, Niedzicki L, Bitner A, Marcinek M, Wiczorek W. Non-crystallizing solvent mixtures and lithium electrolytes for low temperatures. *Solid State Ionics* 2017;308:22–6. doi:10.1016/j.ssi.2017.05.014.
- [154] Waite JH, Glein CR, Perryman RS, Teolis BD, Magee BA, Miller G, et al. Cassini finds molecular hydrogen in the Enceladus plume: Evidence for hydrothermal processes. *Science (80-)* 2017;356:155–9. doi:10.1126/science.aai8703.

- [155] McKay CP. The search for life in our Solar System and the implications for science and society. *Philos Trans R Soc A Math Phys Eng Sci* 2011;369:594–606. doi:10.1098/rsta.2010.0247.
- [156] Lam T, Buffington B, Campagnola S. A Robust Mission Tour for NASA's Planned Europa Clipper Mission. 2018 Sp. Flight Mech. Meet., 2018. doi:10.2514/6.2018-0202.
- [157] Jia X, Kivelson MG, Khurana KK, Kurth WS. Evidence of a plume on Europa from Galileo magnetic and plasma wave signatures. *Nat Astron* 2018;2. doi:10.1038/s41550-018-0450-z.
- [158] Witze A. Plate tectonics found on Europa. *Nature* 2014;513:153–4. doi:10.1038/513153a.
- [159] Mann A. Inner Workings: Icy ocean worlds offer chances to find life. *Proc Natl Acad Sci* 2017;114:4566–8. doi:10.1073/pnas.1703361114.
- [160] Hiscox JA. Outer solar system, Europa, Titan and the possibility of life. *Astron Geophys* 2000;41:5.23.
- [161] Ohno H, Yoshizawa M, Fujita K, Fukaya Y, Ogihara W, Mizumo T, et al. *Electrochemical Aspects Of Ionic Liquids*. 2011. doi:10.1002/9781118003350.
- [162] Zhang S, Wang J. *Structures and Interactions of Ionic Liquids*. vol. 151. Springer Berlin Heidelberg; 2014. doi:10.1007/978-3-642-38619-0.
- [163] Osti NC, Gallegos A, Dyatkin B, Wu J, Gogotsi Y, Mamontov E. Mixed Ionic Liquid Improves Electrolyte Dynamics in Supercapacitors. *J Phys Chem C* 2018;122:10476–81. doi:10.1021/acs.jpcc.8b02521.
- [164] Lin R, Taberna P-L, Fantini S, Presser V, Pérez CR, Malbosc F, et al. Capacitive Energy Storage from –50 to 100 °C Using an Ionic Liquid Electrolyte. *J Phys Chem Lett* 2011;2:2396–401. doi:10.1021/jz201065t.
- [165] Fox ET, Paillard E, Borodin O, Henderson WA. Physicochemical properties of binary ionic liquid-aprotic solvent electrolyte mixtures. *J Phys Chem C* 2013;117:78–84. doi:10.1021/jp3089403.
- [166] Ruiz V, Huynh T, Sivakkumar SR, Pandolfo AG. Ionic liquid-solvent mixtures as supercapacitor electrolytes for extreme temperature operation. *RSC Adv* 2012;2:5591–8. doi:10.1007/978-94-007-7802-3_10.
- [167] Chaban V V., Voroshylova I V., Kalugin ON, Prezhdo O V. Acetonitrile boosts conductivity of imidazolium ionic liquids. *J Phys Chem B* 2012;116:7719–27.

doi:10.1021/jp3034825.

- [168] Kunze M, Jeong S, Appetecchi GB, Schönhoff M, Winter M, Passerini S. Mixtures of ionic liquids for low temperature electrolytes. *Electrochim Acta* 2012;82:69–74. doi:10.1016/j.electacta.2012.02.035.
- [169] Sankarasubramanian S, Seo J, Mizuno F, Singh N, Takechi K, Prakash J. Enhancement of oxygen reduction reaction rate by addition of water to an oxidatively stable ionic liquid electrolyte for lithium-air cells. *Electrochem Commun* 2016;73:55–8. doi:10.1016/j.elecom.2016.11.001.
- [170] Vraneš M, Cvjetičanin N, Papović S, Šarac B, Prislani I, Megušar P, et al. Electrical, electrochemical and thermal properties of the ionic liquid + lactone binary mixtures as the potential electrolytes for lithium-ion batteries. *J Mol Liq* 2017;243:52–60. doi:10.1016/j.molliq.2017.07.129.
- [171] Lau GPS, Décoppet J-D, Moehl T, Zakeeruddin SM, Grätzel M, Dyson PJ. Robust High-performance Dye-sensitized Solar Cells Based on Ionic Liquid-sulfolane Composite Electrolytes. *Sci Rep* 2016;5:18158. doi:10.1038/srep18158.
- [172] Moreno M, Simonetti E, Appetecchi GB, Carewska M, Montanino M, Kim G-T, et al. Ionic Liquid Electrolytes for Safer Lithium Batteries. *J Electrochem Soc* 2017;164:A6026–31. doi:10.1149/2.0051701jes.
- [173] Platek A, Piwek J, Fic K, Schubert T, Gentile P, Bidan G, et al. Electrochemical performance of silicon nanostructures in low-temperature ionic liquids for microelectronic applications. *J Mater Chem A* 2017;5:22708–16. doi:10.1039/C7TA08175H.
- [174] Zhang S, Xu K, Jow T. Low-temperature performance of Li-ion cells with a LiBF₄-based electrolyte. *J Solid State Electrochem* 2003;7:147–51. doi:10.1007/s10008-002-0300-9.
- [175] Mandal BK, Padhi AK, Shi Z, Chakraborty S, Filler R. New low temperature electrolytes with thermal runaway inhibition for lithium-ion rechargeable batteries. *J Power Sources* 2006;162:690–5. doi:10.1016/j.jpowsour.2006.06.053.
- [176] Anouti M, Timperman L. A pyrrolidinium nitrate protic ionic liquid-based electrolyte for very low-temperature electrical double-layer capacitors. *Phys Chem Chem Phys* 2013;15:6539. doi:10.1039/c3cp44680h.
- [177] Fujie K, Otsubo K, Ikeda R, Yamada T, Kitagawa H. Low temperature ionic conductor: ionic liquid incorporated within a metal–organic framework. *Chem Sci* 2015;6:4306–10. doi:10.1039/C5SC01398D.

- [178] Aguilera L, Scheers J, Matic A. Enhanced low-temperature ionic conductivity via different Li⁺ solvated clusters in organic solvent/ionic liquid mixed electrolytes. *Phys Chem Chem Phys* 2016;18:25458–64. doi:10.1039/C6CP04766A.
- [179] Nickerson SD, Nofen EM, Chen H, Ngan M, Shindel B, Yu H, et al. A Combined Experimental and Molecular Dynamics Study of Iodide-Based Ionic Liquid and Water Mixtures. *J Phys Chem B* 2015;119:8764–72. doi:10.1021/acs.jpcc.5b04020.
- [180] Farhana NK, Khanmirzaei MH, Omar FS, Ramesh S, Ramesh K. Ionic conductivity improvement in poly (propylene) carbonate-based gel polymer electrolytes using 1-butyl-3-methylimidazolium iodide (BmimI) ionic liquid for dye-sensitized solar cell application. *Ionics (Kiel)* 2017;23:1601–5. doi:10.1007/s11581-017-1979-z.
- [181] Gorlov M, Kloo L. Ionic liquid electrolytes for dye-sensitized solar cells. *Dalt Trans* 2008:2655. doi:10.1039/b716419j.
- [182] Nakata Y, Kohara K, Matsumoto K, Hagiwara R. Thermal Properties of Ionic Liquid þ Water Binary Systems Applied to Heat Pipes 2011:1840–6.
- [183] MacFarlane DR, Chong AL, Forsyth M, Kar M, Vijayaraghavan R, Somers A, et al. New dimensions in salt-solvent mixtures: A 4th evolution of ionic liquids. *Faraday Discuss* 2018;206:9–28. doi:10.1039/c7fd00189d.
- [184] Macfarlane DR, Tachikawa N, Forsyth M, Pringle JM, Howlett PC, Elliott GD, et al. Energy applications of ionic liquids. *Energy Environ Sci* 2014;7:232–50. doi:10.1039/c3ee42099j.
- [185] Goodenough JB, Kim Y. Challenges for rechargeable Li batteries. *Chem Mater* 2010;22:587–603. doi:10.1021/cm901452z.
- [186] Zhong C, Deng Y, Hu W, Qiao J, Zhang L, Zhang J. A review of electrolyte materials and compositions for electrochemical supercapacitors. *Chem Soc Rev* 2015;44:7484–539. doi:10.1039/c5cs00303b.
- [187] Sirisopanaporn C, Fericola A, Scrosati B. New, ionic liquid-based membranes for lithium battery application. *J Power Sources* 2009;186:490–5. doi:10.1016/j.jpowsour.2008.10.036.
- [188] Aguilera L, Scheers J, Matic A. Enhanced low-temperature ionic conductivity via different Li⁺-solvated clusters in organic solvent/ionic liquid mixed electrolytes. *Phys Chem Chem Phys* 2016;18:25458–64. doi:10.1039/c6cp04766a.
- [189] Lane GH, Best AS, MacFarlane DR, Forsyth M, Bayley PM, Hollenkamp AF. The

- electrochemistry of lithium in ionic liquid/organic diluent mixtures. *Electrochim Acta* 2010;55:8947–52. doi:10.1016/j.electacta.2010.08.023.
- [190] Navarra MA. Ionic liquids as safe electrolyte components for Li-metal and Li-ion batteries. *MRS Bull* 2013;38:548–53. doi:10.1557/mrs.2013.152.
- [191] Xu L, Cui X, Zhang Y, Feng T, Lin R, Li X, et al. Measurement and correlation of electrical conductivity of ionic liquid [EMIM][DCA] in propylene carbonate and γ -butyrolactone. *Electrochim Acta* 2015;174:900–7. doi:10.1016/j.electacta.2015.06.053.
- [192] Yu Z, Xu T, Xing T, Fan LZ, Lian F, Qiu W. A Raman spectroscopy investigation of the interactions of LiBOB with γ -BL as electrolyte for advanced lithium batteries. *J Power Sources* 2010;195:4285–9. doi:10.1016/j.jpowsour.2010.01.052.
- [193] Wang M, Shan Z, Tian J, Yang K, Liu X, Liu H, et al. Mixtures of unsaturated imidazolium based ionic liquid and organic carbonate as electrolyte for Li-ion batteries. *Electrochim Acta* 2013;95:301–7. doi:10.1016/j.electacta.2013.02.032.
- [194] Anouti M, Timperman L. A pyrrolidinium nitrate protic ionic liquid-based electrolyte for very low-temperature electrical double-layer capacitors. *Phys Chem Chem Phys* 2013;15:6539–48. doi:10.1039/c3cp44680h.
- [195] Kühnel RS, Böckenfeld N, Passerini S, Winter M, Balducci A. Mixtures of ionic liquid and organic carbonate as electrolyte with improved safety and performance for rechargeable lithium batteries. *Electrochim Acta* 2011;56:4092–9. doi:10.1016/j.electacta.2011.01.116.
- [196] Tian J, Cui C, Xie Q, Qian W, Xue C, Miao Y, et al. EMIMBF₄–GBL binary electrolyte working at –70 °C and 3.7 V for a high performance graphene-based capacitor. *J Mater Chem A* 2018;6:3593–601. doi:10.1039/C7TA10474J.
- [197] Zec N, Idrissi A, Bešter-Rogač M, Vraneš M, Gadžurić S. Insights into interactions between 1-butyl-3-methylimidazolium dicyanamide and molecular solvents: γ -valerolactone, γ -butyrolactone and propylene carbonate. Volumetric properties and MD simulations. *J Mol Liq* 2018;268:481–9. doi:10.1016/j.molliq.2018.07.079.
- [198] Neale AR, Schütter C, Wilde P, Goodrich P, Hardacre C, Passerini S, et al. Physical-Chemical Characterization of Binary Mixtures of 1-Butyl-1-methylpyrrolidinium Bis{(trifluoromethyl)sulfonyl}imide and Aliphatic Nitrile Solvents as Potential Electrolytes for Electrochemical Energy Storage Applications. *J Chem Eng Data* 2017;62:376–90. doi:10.1021/acs.jced.6b00718.
- [199] Ruiz V, Huynh T, Sivakkumar SR, Pandolfo AG. Ionic liquid-solvent mixtures as

supercapacitor electrolytes for extreme temperature operation. *RSC Adv* 2012;2:5591–8. doi:10.1039/c2ra20177a.

- [200] Ko H, Kapadia R, Takei K, Takahashi T, Zhang X, Javey A. Multifunctional, flexible electronic systems based on engineered nanostructured materials. *Nanotechnology* 2012;23:344001. doi:10.1088/0957-4484/23/34/344001.
- [201] Tran VT, Zhou H, Hong S, Youn J, Chen H, Koh K, et al. Thermal behavior of surface plasmon resonance in dynamic suprastructure multilayer. *Curr Appl Phys* 2013;13:940–4. doi:10.1016/j.cap.2013.01.048.
- [202] Klouda L. Thermoresponsive hydrogels in biomedical applications A seven-year update. *Eur J Pharm Biopharm* 2015;97:338–49. doi:10.1016/j.ejpb.2015.05.017.
- [203] Shimizu T, Yamato M, Isoi Y, Akutsu T, Setomaru T, Abe K, et al. Fabrication of Pulsatile Cardiac Tissue Grafts Using a Novel 3-Dimensional Cell Sheet Manipulation Technique and Temperature-Responsive Cell Culture Surfaces. *Circ Res* 2002;90:40–8. doi:10.1161/hh0302.105722.
- [204] Fujimoto KL, Ma Z, Nelson DM, Hashizume R, Guan J, Tobita K, et al. Synthesis, characterization and therapeutic efficacy of a biodegradable, thermoresponsive hydrogel designed for application in chronic infarcted myocardium. *Biomaterials* 2009;30:4357–68. doi:10.1016/j.biomaterials.2009.04.055.
- [205] Lee S-H, Kim TH, Lima MD, Baughman RH, Kim SJ. Biothermal sensing of a torsional artificial muscle. *Nanoscale* 2016:3248–53. doi:10.1039/C5NR07195J.
- [206] Zheng WJ, An N, Yang JH, Zhou J, Chen YM. Tough Al-alginate/Poly(N - isopropylacrylamide) hydrogel with tunable LCST for soft robotics. *ACS Appl Mater Interfaces* 2015;7:1758–64. doi:10.1021/am507339r.
- [207] Zhu Y, Wood NA, Fok K, Yoshizumi T, Park DW, Jiang H, et al. Design of a Coupled Thermoresponsive Hydrogel and Robotic System for Postinfarct Biomaterial Injection Therapy. *Ann Thorac Surg* 2016;102:780–6. doi:10.1016/j.athoracsur.2016.02.082.
- [208] Hydrogel UT, Akashi M, Ph D, Yatani H, Ph D. Fabrication of Three-Dimensional Cell Constructs 2010;16. doi:10.1089/ten.tea.2009.0523.
- [209] Wang X, Sun Y, Peng C, Luo H, Wang R, Zhang D. Transitional Suspensions Containing Thermosensitive Dispersant for Three-Dimensional Printing 2015. doi:10.1021/acsami.5b07913.
- [210] Cho JH, Kim SH, Park KD, Jung MC, Yang WI, Han SW, et al. Chondrogenic differentiation of human mesenchymal stem cells using a thermosensitive poly(N-

- isopropylacrylamide) and water-soluble chitosan copolymer. *Biomaterials* 2004;25:5743–51. doi:10.1016/j.biomaterials.2004.01.051.
- [211] Ohya S, Nakayama Y, Matsuda T. In vivo evaluation of poly(N-isopropylacrylamide) (PNIPAM)-grafted gelatin as an in situ-formable scaffold. *J Artif Organs* 2004;7:181–6. doi:10.1007/s10047-004-0265-9.
- [212] Jochum FD, Theato P. Temperature- and light-responsive smart polymer materials. *Chem Soc Rev* 2013;42:7468–83. doi:10.1039/c2cs35191a.
- [213] Kim J, Nayak S, Lyon LA. Bioresponsive hydrogel microlenses. *J Am Chem Soc* 2005;127:9588–92. doi:10.1021/ja0519076.
- [214] Zhang M, Otanicar TP, Phelan PE, Dai LL. Multipetal-Structured and Dumbbell-Structured Gold-Polymer Composite Particles with Self-Modulated Catalytic Activity. *Langmuir* 2015;31:13191–200. doi:10.1021/acs.langmuir.5b02333.
- [215] Chen H, Dai LL. Adsorption and release of active species into and from multifunctional ionic microgel particles. *Langmuir* 2013;29:11227–35. doi:10.1021/la401297b.
- [216] Chatterjee P, Pan Y, Stevens EC, Ma T, Jiang H, Dai LL. Controlled morphology of thin film silicon integrated with environmentally responsive hydrogels. *Langmuir* 2013. doi:10.1021/la401267u.
- [217] Schexnailder P, Schmidt G. Nanocomposite polymer hydrogels. *Colloid Polym Sci* 2009;287:1–11. doi:10.1007/s00396-008-1949-0.
- [218] Wu CJ, Gaharwar AK, Chan BK, Schmidt G. Mechanically tough Pluronic F127/Laponite nanocomposite hydrogels from covalently and physically cross-linked networks. *Macromolecules* 2011;44:8215–24. doi:10.1021/ma200562k.
- [219] Park M, Shim IK, Jung EY, Choy JH. Modification of external surface of laponite by silane grafting. *J. Phys. Chem. Solids*, vol. 65, 2004, p. 499–501. doi:10.1016/j.jpcs.2003.10.031.
- [220] Ueki T. Stimuli-responsive polymers in ionic liquids. *Polym J* 2014;46:1–10. doi:10.1038/pj.2014.37.
- [221] Ueki T, Nakamura Y, Yamaguchi A, Niitsuma K, Lodge TP, Watanabe M. UCST phase transition of azobenzene-containing random copolymer in an ionic liquid. *Macromolecules* 2011;44:6908–14. doi:10.1021/ma2014244.
- [222] Byrne R, Ventura C, Benito Lopez F, Walther A, Heise A, Diamond D. Characterisation and analytical potential of a photo-responsive polymeric material

based on spiropyran. *Biosens Bioelectron* 2010;26:1392–8.
doi:10.1016/j.bios.2010.07.059.

- [223] Takeshi Ueki MW. Upper Critical Solution Temperature Behavior of Poly(N-isopropylacrylamide) in an Ionic Liquid and Preparation of Thermo-sensitive Nonvolatile Gels. *Chem Lett* 2006;35:964–5.
- [224] Alvarez-Lorenzo C, Bromberg L, Concheiro A. Light-sensitive intelligent drug delivery systems. *Photochem Photobiol* 2009;85:848–60. doi:10.1111/j.1751-1097.2008.00530.x.
- [225] Lo C-W, Zhu D, Jiang H. An infrared-light responsive graphene-oxide incorporated poly(N-isopropylacrylamide) hydrogel nanocomposite. *Soft Matter* 2011;7:5604. doi:10.1039/c1sm00011j.
- [226] Peng L, You M, Yuan Q, Wu C, Han D, Chen Y, et al. Macroscopic volume change of dynamic hydrogels induced by reversible DNA hybridization. *J Am Chem Soc* 2012;134:12302–7. doi:10.1021/ja305109n.
- [227] Yan B, Boyer J, Habault D, Branda NR, Zhao Y. Near Infrared Light Triggered Release of Biomacromolecules from Hydrogels Loaded with Upconversion Nanoparticles Near Infrared Light Triggered Release of Biomacromolecules from Hydrogels Loaded with Upconversion Nanoparticles 2012.
- [228] Li L, Lu B, Zhang Y, Xing X, Wu X, Liu Z. Multi-sensitive copolymer hydrogels of N-isopropylacrylamide with several polymerizable azobenzene-containing monomers. *J Polym Res* 2015;22. doi:10.1007/s10965-015-0787-2.
- [229] Nakajima T, Furukawa H, Tanaka Y, Kurokawa T, Osada Y, Gong JP. True chemical structure of double network hydrogels. *Macromolecules* 2009;42:2184–9. doi:10.1021/ma802148p.
- [230] Webber RE, Creton C, Brown HR, Gong JP. Large strain hysteresis and Mullins effect of tough double-network hydrogels. *Macromolecules* 2007;40:2919–27. doi:10.1021/ma062924y.
- [231] Sun J, Zhao X, Illeperuma WRK, Chaudhuri O, Oh KH, Mooney DJ, et al. Highly stretchable and tough hydrogels. *Nature* 2012;489:133–6. doi:10.1038/nature11409.
- [232] Baumberger T, Ronsin O. From thermally activated to viscosity controlled fracture of biopolymer hydrogels. *J Chem Phys* 2009;130. doi:10.1063/1.3078267.
- [233] Sun JY, Zhao X, Illeperuma WRK, Chaudhuri O, Oh KH, Mooney DJ, et al. Highly stretchable and tough hydrogels. *Nature* 2012;489:133–6.

doi:10.1038/nature11409.

- [234] Kong HJ, Wong E, Mooney DJ. Independent Control of Rigidity and Toughness of Polymeric Hydrogels 2003;4582–8.
- [235] Stevens L, Calvert P, Wallace GG, Panhuis M in Het. Ionic-covalent entanglement hydrogels from gellan gum, carrageenan and an epoxy-amine. *Soft Matter* 2013;9:3009. doi:10.1039/c3sm27413f.
- [236] Kirchmayer DM, Panhuis M in het. Robust biopolymer based ionic-covalent entanglement hydrogels with reversible mechanical behaviour. *J Mater Chem B* 2014;2:4694–702. doi:10.1039/C4TB00258J.
- [237] Yang Y, Wang X, Yang F, Shen H, Wu D. A Universal Soaking Strategy to Convert Composite Hydrogels into Extremely Tough and Rapidly Recoverable Double-Network Hydrogels. *Adv Mater* 2016;2959:7178–84. doi:10.1002/adma.201601742.
- [238] Duan J, Liang X, Cao Y, Wang S, Zhang L. High strength chitosan hydrogels with biocompatibility via new avenue based on constructing nanofibrous architecture. *Macromolecules* 2015;48:2706–14. doi:10.1021/acs.macromol.5b00117.
- [239] Low ZW, Chee PL, Kai D, Loh XJ. The role of hydrogen bonding in alginate/poly(acrylamide-co-dimethylacrylamide) and alginate/poly(ethylene glycol) methyl ether methacrylate-based tough hybrid hydrogels. *RSC Adv* 2015;5:57678–85. doi:10.1039/C5RA09926A.
- [240] Xiao XC, Chu LY, Chen WM, Wang S, Li Y. Positively Thermo-Sensitive Monodisperse Core-Shell Microspheres. *Adv Funct Mater* 2003;13:847–52. doi:10.1002/adfm.200304513.
- [241] Ilmain F, Tanaka T, Kokufuta E. Volume transition in a gel driven by hydrogen bonding. *Nature* 1991;349:400–1. doi:10.1038/349400a0.
- [242] Greaves TL, Weerawardena A, Fong C, Krodkiewska I, Drummond CJ. Protic ionic liquids: Solvents with tunable phase behavior and physicochemical properties. *J Phys Chem B* 2006;110:22479–87. doi:10.1021/jp0634048.
- [243] Xu W, Cooper EI, Angell CA. Ionic Liquids: Ion Mobilities, Glass Temperatures, and Fragilities. *J Phys Chem B* 2003;107:6170–8. doi:10.1021/jp0275894.
- [244] Bernardes CES, Minas Da Piedade ME, Canongia Lopes JN. The structure of aqueous solutions of a hydrophilic ionic liquid: The full concentration range of 1-ethyl-3-methylimidazolium ethylsulfate and water. *J Phys Chem B* 2011;115:2067–74. doi:10.1021/jp1113202.

- [245] Evans DF, Kaler EW, Benton WJ. Liquid crystals in a fused salt: β , γ -distearoylphosphatidylcholine in N-ethylammonium nitrate. *J Phys Chem* 1983;87:533–5. doi:10.1021/j100227a003.
- [246] Evans DF, Chen SH, Schriver GW, Arnett EM. Thermodynamics of Solution of Nonpolar Gases in a Fused Salt. “Hydrophobic Bonding” Behavior in a Nonaqueous System. *J Am Chem Soc* 1981;103:481–2. doi:10.1021/ja00392a049.
- [247] Fumino K, Wulf A, Ludwig R. Hydrogen Bonding in Protic Ionic Liquids: Reminiscent of Water. *Angew Chemie Int Ed* 2009;48:3184–6. doi:10.1002/anie.200806224.
- [248] Seddon KR, Stark A, Torres M-J. Influence of chloride, water, and organic solvents on the physical properties of ionic liquids. *Pure Appl Chem* 2000;72:2275–87.
- [249] Abraham M, Abraham M, Abraham M. Electrolytic Conductance and Viscosity of Some Mixed Nitrate-Water Systems from Fused Salts to Dilute Solutions. *Electrochim Acta* 1985;31:821–9.
- [250] Angell CA. Formation of Glasses from Liquids and Biopolymers. *Science (80-)* 1995;267:1924–35. doi:10.1126/science.267.5206.1924.
- [251] Rodríguez H, Brennecke JF. Temperature and composition dependence of the density and viscosity of binary mixtures of water + ionic liquid. *J Chem Eng Data* 2006;51:2145–55. doi:10.1021/je0602824.
- [252] Okoturo OO, VanderNoot TJ. Temperature dependence of viscosity for room temperature ionic liquids. *J Electroanal Chem* 2004;568:167–81. doi:10.1016/j.jelechem.2003.12.050.
- [253] Zheng H, Zhang H, Fu Y, Abe T, Ogumi Z. Temperature Effects on the Electrochemical Behavior of Spinel LiMn_2O_4 in Quaternary Ammonium-Based Ionic Liquid Electrolyte. *J Phys Chem B* 2005;109:13676–84. doi:10.1021/jp051238i.
- [254] Ikeda M, Aniya M. Understanding the Vogel – Fulcher – Tammann law in terms of the bond strength – coordination number fluctuation model. *J Non Cryst Solids* 2013;371–372:53–7. doi:10.1016/j.jnoncrysol.2013.04.034.
- [255] Jarosik A, Krajewski SR, Lewandowski A, Radzinski P. Conductivity of ionic liquids in mixtures. *J Mol Liq* 2006;123:43–50. doi:10.1016/j.molliq.2005.06.001.
- [256] Leys J, Rajesh RN, Menon PC, Glorieux C, Longuemart S, Nockemann P, et al. Influence of the anion on the electrical conductivity and glass formation of 1-

- butyl-3-methylimidazolium ionic liquids. *J Chem Phys* 2010;133:1–10. doi:10.1063/1.3455892.
- [257] McFarlane DR, Sun J, Golding J, Meakin P, Forsyth M. High conductivity molten salts based on the imide ion. *Electrochim Acta* 2000;45:1271–8. doi:10.1016/S0013-4686(99)00331-X.
- [258] MacFarlane DR, Forsyth M, Izgorodina EI, Abbott AP, Annat G, Fraser K. On the concept of ionicity in ionic liquids. *Phys Chem Chem Phys* 2009;11:4962. doi:10.1039/b900201d.
- [259] Austen Angell C, Ansari Y, Zhao Z. Ionic Liquids: Past, present and future. *Faraday Discuss* 2012;154:9–27. doi:10.1039/C1FD00112D.
- [260] Hagiwara R, Lee JS. Ionic liquids for electrochemical devices. *Electrochemistry* 2007;75:23–34. doi:10.5796/electrochemistry.75.23.
- [261] Ueno K, Tokuda H, Watanabe M. Physical chemistry of ionic liquids. *Phys Chem Chem Phys* 2010;12:1648–1648. doi:10.1039/c001176m.
- [262] Tshibangu PN, Ndwandwe SN, Dikio ED. Density , Viscosity and Conductivity Study of 1-Butyl-3- Methylimidazolium Bromide. *Int J Electrochem Sci* 2011;6:2201–13.
- [263] Xu A, Zhang Y, Li Z, Wang J. Viscosities and conductivities of 1-butyl-3-methylimidazolium carboxylates ionic liquids at different temperatures. *J Chem Eng Data* 2012;57:3102–8. doi:10.1021/je300507h.
- [264] Fraser KJ, Izgorodina EI, Forsyth M, Scott JL, MacFarlane DR. Liquids intermediate between “molecular” and “ionic” liquids: Liquid Ion Pairs? *Chem Commun* 2007:3817. doi:10.1039/b710014k.
- [265] Bella F, Galliano S, Falco M, Viscardi G, Barolo C, Grätzel M, et al. Unveiling iodine-based electrolytes chemistry in aqueous dye-sensitized solar cells. *Chem Sci* 2016;7:4880–90. doi:10.1039/c6sc01145d.
- [266] Xu Y, Lin WJ, Gliege M, Gunckel R, Zhao Z, Yu H, et al. A Dual Ionic Liquid Based Low-Temperature Electrolyte System. *J Phys Chem B* 2018;122:12077–86. doi:10.1021/acs.jpcc.8b08815.
- [267] Ali A, Ali M, Malik NA, Uzair S, Khan AB. Solvatochromic absorbance probe behavior within mixtures of the ionic liquid 1-butyl-3-methylimidazolium bis(trifluoromethylsulfonyl)imide + molecular organic solvents. *J Chem Eng Data* 2014;59:1755–65. doi:10.1021/je400908z.

- [268] Mellein BR, Aki SNVK, Ladewski RL, Brennecke JF. Solvatochromic studies of ionic liquid/organic mixtures. *J Phys Chem B* 2007;111:131–8. doi:10.1021/jp0653353.
- [269] Papović S, Cvjetičanin N, Gadžurić S, Bešter-Rogač M, Vraneš M. Physicochemical and electrochemical characterisation of imidazolium based IL + GBL mixtures as electrolytes for lithium-ion batteries. *Phys Chem Chem Phys* 2017;19:28139–52. doi:10.1039/c7cp04478j.
- [270] Papović S, Gadžurić S, Bešter-Rogač M, Jović B, Vraneš M. A systematic study on physicochemical and transport properties of imidazolium-based ionic liquids with Γ -butyrolactone. *J Chem Thermodyn* 2018;116:330–40. doi:10.1016/j.jct.2017.10.004.
- [271] Zhang QG, Wang NN, Yu ZW. The hydrogen bonding interactions between the ionic liquid 1-Ethyl-3-methylimidazolium ethyl sulfate and water. *J Phys Chem B* 2010;114:4747–54. doi:10.1021/jp1009498.
- [272] Modro AM, Modro TA. The phosphoryl and the carbonyl group as hydrogen bond acceptors. *Can J Chem* 1999;77:890–4. doi:10.1080/10426500213336.
- [273] Ryu IS, Liu X, Jin Y, Sun J, Lee YJ. Stoichiometric analysis of competing intermolecular hydrogen bonds using infrared spectroscopy. *RSC Adv* 2018;8:23481–8. doi:10.1039/c8ra02919a.
- [274] Kuo SW, Huang CF, Chang FC. Study of hydrogen-bonding strength in poly(ϵ -caprolactone) blends by DSC and FTIR. *J Polym Sci Part B Polym Phys* 2001;39:1348–59. doi:10.1002/polb.1107.
- [275] Tian J, Cui C, Xie Q, Qian W, Xue C, Miao Y, et al. EMIMBF₄-GBL binary electrolyte working at -70 °c and 3.7 v for a high performance graphene-based capacitor. *J Mater Chem A* 2018;6:3593–601. doi:10.1039/c7ta10474j.
- [276] Hermansson K. Blue-shifting hydrogen bonds. *J Phys Chem A* 2002;106:4695–702. doi:10.1021/jp0143948.
- [277] Tagawa A, Numata T, Shikata T. Anti-parallel dimer and tetramer formation of propylene carbonate. *AIP Adv* 2017;7. doi:10.1063/1.5002118.
- [278] Koverga VA, Voroshylova I V., Smortsova Y, Miannay FA, Cordeiro MNDS, Idrissi A, et al. Local structure and hydrogen bonding in liquid γ -butyrolactone and propylene carbonate: A molecular dynamics simulation. *J Mol Liq* 2019;287. doi:10.1016/j.molliq.2019.110912.
- [279] Salazar PF, Chan KJ, Stephens ST, Cola BA. Enhanced Electrical Conductivity of

Imidazolium-Based Ionic Liquids Mixed with Carbon Nanotubes: A Spectroscopic Study. *J Electrochem Soc* 2014;161:H481–6. doi:10.1149/2.0401409jes.

- [280] Li Q, Liu D, Song L, Hou X, Wu C, Yan Z. Efficient hydro-liquefaction of woody biomass over ionic liquid nickel based catalyst. *Ind Crops Prod* 2018;113:157–66. doi:10.1016/j.indcrop.2018.01.033.
- [281] Saihara K, Yoshimura Y, Ohta S, Shimizu A. Properties of water confined in ionic liquids. *Sci Rep* 2015;5:10619. doi:10.1038/srep10619.
- [282] Avent AG, Chaloner PA, Day MP, Seddon KR, Welton T. Evidence for Hydrogen Bonding in Solutions of 1-Ethyl-3-methylimidazolium Halides, and its Implications for Room-temperature Halogenoaluminate(III) Ionic Liquids. *Dalt Trans* 1994:3405–13.
- [283] Cha S, Ao M, Sung W, Moon B, Ahlström B, Johansson P, et al. Structures of ionic liquid-water mixtures investigated by IR and NMR spectroscopy. *Phys Chem Chem Phys* 2014;16:9591–601. doi:10.1039/c4cp00589a.
- [284] Handy ST, Okello M. The 2-position of imidazolium ionic liquids: Substitution and exchange. *J Org Chem* 2005;70:1915–8. doi:10.1021/jo0480850.
- [285] Ohta S, Shimizu A, Ima Y, Abe H, Hatano N, Yoshimura Y. Peculiar Concentration Dependence of H/D Exchange Reaction in 1-Butyl-3-methylimidazolium Tetrafluoroborate-D₂O Mixtures. *Open J Phys Chem* 2011;01:70–6. doi:10.4236/ojpc.2011.13010.
- [286] Hayashi N, Kuyama H, Nakajima C, Kawahara K, Miyagi M, Nishimura O, et al. Imidazole C-2 hydrogen/deuterium exchange reaction at histidine for probing protein structure and function with matrix-assisted laser desorption ionization mass spectrometry. *Biochemistry* 2014;53:1818–26. doi:10.1021/bi401260f.
- [287] Cebo M, Kielmas M, Adamczyk J, Cebrat M, Szewczuk Z, Stefanowicz P. Hydrogen-deuterium exchange in imidazole as a tool for studying histidine phosphorylation. *Anal Bioanal Chem* 2014;406:8013–20. doi:10.1007/s00216-014-8218-5.
- [288] Zhang S, Wang J, Lu X, Zhou Q. Structures and Interactions of Ionic Liquids. Berlin, Heidelberg: Springer-Verlag; 2014. doi:10.1007/978-3-642-38619-0.
- [289] Anouti M, Timperman L. A pyrrolidinium nitrate protic ionic liquid-based electrolyte for very low-temperature electrical double-layer capacitors. *Phys Chem Chem Phys* 2013;15:6539–48. doi:10.1039/c3cp44680h.
- [290] Ueno K, Tokuda H, Watanabe M. Ionicity in ionic liquids: correlation with ionic

- structure and physicochemical properties. *Phys Chem Chem Phys* 2010;12:1649–58. doi:10.1039/c001176m.
- [291] Ye YS, Rick J, Hwang BJ. Ionic liquid polymer electrolytes. *J Mater Chem A* 2013;1:2719–43. doi:10.1039/c2ta00126h.
- [292] Li W, Zhang Z, Han B, Hu S, Xie Y, Yang G. Effect of water and organic solvents on-the ionic dissociation of ionic liquids. *J Phys Chem B* 2007;111:6452–6. doi:10.1021/jp071051m.
- [293] Rodríguez H, Brennecke JF. Temperature and composition dependence of the density and viscosity of binary mixtures of water + ionic liquid. *J Chem Eng Data* 2006;51:2145–55. doi:10.1021/je0602824.
- [294] Zafarani-Moattar MT, Majdan-Cegincara R. Viscosity, density, speed of sound, and refractive index of binary mixtures of organic solvent + Ionic liquid, 1-Butyl-3-methylimidazolium hexafluorophosphate at 298.15 K. *J Chem Eng Data* 2007;52:2359–64. doi:10.1021/je700338t.
- [295] Wu JY, Chen YP, Su CS. Density and viscosity of ionic liquid binary mixtures of 1-n-butyl-3-methylimidazolium tetrafluoroborate with acetonitrile, N,N-dimethylacetamide, methanol, and N-methyl-2-pyrrolidone. *J Solution Chem* 2015;44:395–412. doi:10.1007/s10953-014-0273-1.
- [296] Wang J, Tian Y, Zhao Y, Zhuo K. A volumetric and viscosity study for the mixtures of 1-n-butyl-3- methylimidazolium tetrafluoroborate ionic liquid with acetonitrile, dichloromethane, 2-butanone and N, N-dimethylformamide. *Green Chem* 2003;5:618–22. doi:10.1039/b303735e.
- [297] Ciocirlan O, Croitoru O, Iulian O. Viscosity of binary mixtures of 1-ethyl-3-methylimidazolium tetrafluoroborate ionic liquid with four organic solvents. *J Chem Thermodyn* 2016;101:285–92. doi:10.1016/j.jct.2016.06.015.
- [298] Zhang XX, Liang M, Ernsting NP, Maroncelli M. Conductivity and solvation dynamics in ionic liquids. *J Phys Chem Lett* 2013;4:1205–10. doi:10.1021/jz400359r.
- [299] Marekha BA, Kalugin ON, Bria M, Idrissi A. Probing structural patterns of ion association and solvation in mixtures of imidazolium ionic liquids with acetonitrile by means of relative ¹H and ¹³C NMR chemical shifts. *Phys Chem Chem Phys* 2015;17:23183–94. doi:10.1039/c5cp02748a.
- [300] Stoppa A, Hunger J, Buchner R. Conductivities of binary mixtures of ionic liquids with polar solvents. *J Chem Eng Data* 2009;54:472–9. doi:10.1021/je800468h.

- [301] Liang M, Zhang XX, Kaintz A, Ernsting NP, Maroncelli M. Solvation dynamics in a prototypical ionic liquid + dipolar aprotic liquid mixture: 1-butyl-3-methylimidazolium tetrafluoroborate + acetonitrile. *J Phys Chem B* 2014;118:1340–52. doi:10.1021/jp412086t.
- [302] Conway B, Uitvlugt C, Maroncelli M. Simulations of 1-Butyl-3-methylimidazolium Tetrafluoroborate + Acetonitrile Mixtures: Force-Field Validation and Frictional Characteristics. *J Phys Chem B* 2018;122:7385–93. doi:10.1021/acs.jpcc.8b04341.
- [303] Chaban V V., Voroshylova I V., Kalugin ON, Prezhdo O V. Acetonitrile boosts conductivity of imidazolium ionic liquids. *J Phys Chem B* 2012;116:7719–27. doi:10.1021/jp3034825.
- [304] Karthick NK, Arivazhagan G, Kumbharkhane AC, Joshi YS, Kannan PP. Time Domain Reflectometric and spectroscopic studies on toluene + butyronitrile solution. *J Mol Struct* 2016;1108:203–8. doi:10.1016/j.molstruc.2015.12.009.
- [305] Gómez Ribelles JL, Monleón Pradas M, Meseguer Dueas JM, Torregrosa Cabanilles C. Glass transition in homogeneous and heterogeneous interpenetrating polymer networks and its relation to concentration fluctuations. *J Non Cryst Solids* 2002;307–310:731–7. doi:10.1016/S0022-3093(02)01554-5.
- [306] Bobo E, Bobo E. Development of a controllable polymer system using interpenetrating networks By 2013.
- [307] Katono H, Maruyama A, Sanui K, Ogata N, Okano T, Sakurai Y. Thermo-responsive swelling and drug release switching of interpenetrating polymer networks composed of poly (acrylamide-co-butyl methacrylate) and poly (acrylic acid). *J Control Release* 1991;16:215–28.
- [308] Zhang Z, Chao T, Jiang S. Physical, chemical, and chemical-physical double network of zwitterionic hydrogels. *J Phys Chem B* 2008;112:5327–32. doi:10.1021/jp710683w.
- [309] Rivero RE, Alustiza F, RodriGuez N, Bosch P, Miras MC, Rivarola CR, et al. Effect of functional groups on physicochemical and mechanical behavior of biocompatible macroporous hydrogels. *React Funct Polym* 2015;97:77–85. doi:10.1016/j.reactfunctpolym.2015.10.011.
- [310] Myung D, Koh W, Ko J, Hu Y, Carrasco M, Noolandi J, et al. Biomimetic strain hardening in interpenetrating polymer network hydrogels. *Polymer (Guildf)* 2007;48:5376–87. doi:10.1016/j.polymer.2007.06.070.
- [311] Wang Q, Zhang YY, Dai XY, Shi XH, Liu WG. A high strength pH responsive

- supramolecular copolymer hydrogel. *Sci China Technol Sci* 2017;60:78–83. doi:10.1007/s11431-016-0698-0.
- [312] Farag AAM. Optical absorption of sodium copper chlorophyllin thin films in UV-vis-NIR region. *Spectrochim Acta - Part A Mol Biomol Spectrosc* 2006;65:667–72. doi:10.1016/j.saa.2005.12.026.
- [313] Yuan L, Kusuda T. Adsorption of ammonium and nitrate ions by poly(N-isopropylacrylamide) gel and poly(N-isopropylacrylamide-co-chlorophyllin) gel in different states. *J Appl Polym Sci* 2005;96:2367–72. doi:10.1002/app.21683.
- [314] Chen J, Miao S, Wan J, Xia J, Cao X. Synthesis and application of two light-sensitive copolymers forming recyclable aqueous two-phase systems. *Process Biochem* 2010;45:1928–36. doi:10.1016/j.procbio.2010.05.028.
- [315] Yuan L, Kusuda T, Satoh H. Response of NIPAAm-Ch Gel to Temperature Changes and Its Effectiveness on Nitrification as Medium for Immobilization. *J Appl Polym Sci* 2007;103:681–6. doi:10.1002/app.
- [316] Zheng X, Zhang Q, Liu J, Pei Y, Tang K. A unique high mechanical strength dialdehyde microfibrillated cellulose/gelatin composite hydrogel with a giant network structure. *RSC Adv* 2016;6:71999–2007. doi:10.1039/C6RA12517D.
- [317] Chiu Y-C, Kocagöz S, Larson JC, Brey EM. Evaluation of physical and mechanical properties of porous poly (ethylene glycol)-co-(L-lactic acid) hydrogels during degradation. *PLoS One* 2013;8:e60728. doi:10.1371/journal.pone.0060728.
- [318] Carrow JK, Kerativitayanan P, Jaiswal MK, Lokhande G, Gaharwar AK. *Polymers for bioprinting*. Elsevier Inc.; 2015. doi:10.1016/B978-0-12-800972-7.00013-X.
- [319] Li W, Wang D, Yang W, Song Y. Compressive mechanical properties and microstructure of PVA–HA hydrogels for cartilage repair. *RSC Adv* 2016;6:20166–72. doi:10.1039/C6RA02166B.
- [320] Yuan J, Antonietti M. Poly(ionic liquid)s: Polymers expanding classical property profiles. *Polymer (Guildf)* 2011;52:1469–82. doi:10.1016/j.polymer.2011.01.043.
- [321] Eftekhari A, Saito T. Synthesis and properties of polymerized ionic liquids. *Eur Polym J* 2017;90:245–72. doi:10.1016/j.eurpolymj.2017.03.033.
- [322] Taghavikish M, Subianto S, Gu Y, Sun X, Zhao XS, Choudhury NR. A Poly(ionic liquid) Gel Electrolyte for Efficient all Solid Electrochemical Double-Layer Capacitor. *Sci Rep* 2018;8:1–10. doi:10.1038/s41598-018-29028-y.

- [323] Chatterjee P, Dai A, Yu H, Jiang H, Dai LL. Thermal and mechanical properties of poly(*N*-isopropylacrylamide)-based hydrogels as a function of porosity and medium change. *J Appl Polym Sci* 2015;132:n/a-n/a. doi:10.1002/app.42776.
- [324] Matsumoto A, Iacob C, Noda T, Urakawa O, Runt J, Inoue T. Introducing Large Counteranions Enhances the Elastic Modulus of Imidazolium-Based Polymerized Ionic Liquids. *Macromolecules* 2018;51:4129–42. doi:10.1021/acs.macromol.8b00312.
- [325] Zhou T, Gao X, Dong B, Sun N, Zheng L. Poly(ionic liquid) hydrogels exhibiting superior mechanical and electrochemical properties as flexible electrolytes. *J Mater Chem A* 2016;4:1112–8. doi:10.1039/c5ta08166a.
- [326] Umaphathi R, Kumar A, Narang P, Venkatesu P. How Does a Smart Polymer Respond to Imidazolium-Based Ionic Liquids? *ACS Sustain Chem Eng* 2018;6:1400–10. doi:10.1021/acssuschemeng.7b03790.
- [327] Ziöłkowski B, Ates Z, Gallagher S, Byrne R, Heise A, Fraser KJ, et al. Mechanical properties and UV curing behavior of poly(*N*-Isopropylacrylamide) in phosphonium-based ionic liquids. *Macromol Chem Phys* 2013;214:787–96. doi:10.1002/macp.201200616.
- [328] Renamayor CS, Pastoriza A, Usma CL, Pierola IF. Ionic liquid-water mixtures as solvents for poly(*N*-vinylimidazole). *Colloid Polym Sci* 2013;291:2439–46. doi:10.1007/s00396-013-2963-4.
- [329] Li Q, Tang Q, He B, Yang P. Full-ionic liquid gel electrolytes: Enhanced photovoltaic performances in dye-sensitized solar cells. *J Power Sources* 2014;264:83–91. doi:10.1016/j.jpowsour.2014.04.095.
- [330] Ly Nguyen TK, Obadia MM, Serghei A, Livi S, Duchet-Rumeau J, Drockenmuller E. 1,2,3-Triazolium-Based Epoxy-Amine Networks: Ion-Conducting Polymer Electrolytes. *Macromol Rapid Commun* 2016;37:1168–74. doi:10.1002/marc.201600018.
- [331] Nguyen TKL, Livi S, Soares BG, Barra GMO, Gérard JF, Duchet-Rumeau J. Development of Sustainable Thermosets from Cardanol-based Epoxy Prepolymer and Ionic Liquids. *ACS Sustain Chem Eng* 2017;5:8429–38. doi:10.1021/acssuschemeng.7b02292.
- [332] Nguyen TKL, Livi S, Soares BG, Pruvost S, Duchet-Rumeau J, Gérard JF. Ionic liquids: A New Route for the Design of Epoxy Networks. *ACS Sustain Chem Eng* 2016;4:481–90. doi:10.1021/acssuschemeng.5b00953.
- [333] Nguyen TKL, Livi S, Soares BG, Benes H, Gérard JF, Duchet-Rumeau J.

Toughening of Epoxy/Ionic Liquid Networks with Thermoplastics Based on Poly(2,6-dimethyl-1,4-phenylene ether) (PPE). *ACS Sustain Chem Eng* 2017;5:1153–64. doi:10.1021/acssuschemeng.6b02479.

- [334] Sun C, Liu J, Gong Y, Wilkinson DP, Zhang J. Recent advances in all-solid-state rechargeable lithium batteries. *Nano Energy* 2017;33:363–86. doi:10.1016/j.nanoen.2017.01.028.
- [335] Soares BG, Silva AA, Pereira J, Livi S. Preparation of epoxy/jeffamine networks modified with phosphonium based ionic liquids. *Macromol Mater Eng* 2015;300:312–9. doi:10.1002/mame.201400293.
- [336] Soares BG, Livi S, Duchet-Rumeau J, Gerard JF. Synthesis and characterization of epoxy/MCDEA networks modified with imidazolium-based ionic liquids. *Macromol Mater Eng* 2011;296:826–34. doi:10.1002/mame.201000388.
- [337] Stenger-Smith J, Irvin J. Ionic Liquids for Energy Storage Applications. *Mater Matters* 2009;4:103.
- [338] Mąka H, Spychaj T, Kowalczyk K. Imidazolium and deep eutectic ionic liquids as epoxy resin crosslinkers and graphite nanoplatelets dispersants. *J Appl Polym Sci* 2014;131:1–7. doi:10.1002/app.40401.
- [339] Deshmukh K, Ahamed MB, Polu AR, Sadasivuni KK, Pasha SKK, Ponnamma D, et al. Impedance spectroscopy, ionic conductivity and dielectric studies of new Li⁺-ion conducting polymer blend electrolytes based on biodegradable polymers for solid state battery applications. *J Mater Sci Mater Electron* 2016;27:11410–24. doi:10.1007/s10854-016-5267-x.
- [340] Geirhos K, Lunkenheimer P, Michl M, Reuter D, Loidl A. Communication: Conductivity enhancement in plastic-crystalline solid-state electrolytes. *J Chem Phys* 2015;143. doi:10.1063/1.4929554.
- [341] DeVos N, Maton C, Stevens C V. Electrochemical Stability of Ionic Liquids: General Influences and Degradation Mechanisms. *ChemElectroChem* 2014;1:1258–70. doi:10.1002/celc.201402086.
- [342] Bai J, Lu H, Cao Y, Li X, Wang J. A novel ionic liquid polymer electrolyte for quasi-solid state lithium air batteries. *RSC Adv* 2017;7:30603–9. doi:10.1039/c7ra05035f.

APPENDIX A

GRAFTED CINNAMOYL-BASED MECHANOPHORES FOR SELF-SENSING AND PHOTOCHEMICAL HEALING CAPABILITIES IN EPOXY

Introduction

As polymeric materials prevail in numerous structural applications, stimuli responsive polymeric materials have become a large focus of materials development and research in recent decades. The nature of such responsive materials can be suited to the needs of their applications with various formats of property transitions, such as volume, heat, conductivity, fluorescence, and phosphorescence, and a variety of stimuli have been effectively utilized from light, temperature, pH, redox potential, and force.¹⁻⁹ Among different stimuli, an external or applied mechanical force can activate a reaction within certain moieties, often called ‘mechanophores,’ to induce bond breakage.¹⁰ These mechanophores have been incorporated in thermoplastics, crosslinked polymers, and block copolymers and used to study the mechanical responsiveness under stress at the molecular level by detecting chain breakage within these polymer networks.¹¹⁻¹³ There are two main routes to tailor polymeric materials and composites for stress-responsiveness utilizing mechanophores: incorporating of stimuli responsive additives and creating mechanophore stress-responsiveness intrinsic properties of the polymer itself. This polymer with intrinsic mechanophore properties can be created through covalently grafting a stimuli responsive moiety into the backbone of a polymer chain or matrix.¹⁴⁻²²

While mechanophores have proven their ability to respond to a stress, there are also drawbacks to their incorporation as particulate additives. For example, when dianthracene 9-carboxylic acid (DiAC) mechanophore particles were blended in a polyurethane network, the glass transition temperature (T_g) of the composite material was decreased by 16 °C and the crosslinking density was halved, resulting in a 30% decrease in Young’s modulus and yield strength.²³ In order to overcome the thermal and mechanical property loss, a solution

that can maintain the structural integrity of the polymer is needed. More recently, a shift towards chemical grafting of these mechanophores into the backbone of a thermoset matrix has shown a moderate success in achieving similar stress-responsive properties while limiting this property loss. Moore et al. examined the process of chemically incorporating colorless spiropyran molecules into the linear backbone of a poly(methyl acrylate) (PMA) thermoset, where an electrocyclic ring-opening reaction took place to form a red-colored merocyanine when straining the sample to large strains under tensile loading.⁷ However, this color-change as a form of signal for damage detection was not generated until after significant and permanent mechanical damage had been applied. Nofen et. al. demonstrated that cinnamamide moieties can react with epoxide groups on an epoxy resin to form a hybrid (or grafted) resin unit with force-responsive properties.²⁴ However, glass transitions decreased by approximately 6 °C when compared to neat epoxy, as well as a drop in Young's modulus and yield strain by approximately 0.32 GPa (14.5%) and 18.17 MPa (19%), respectively. Although those progresses can be considered a critical step in the right direction for use of these materials in structural applications without compromising the majority of their performance, it is also highly desirable to actively prevent the subsequent failure of the materials after an early strain is detected.

Studies have shown that mechanophores can be incorporated in the backbone of linear polymers to provide signal detection in the presence of mechanical force.^{25, 26} For example, a study undergone by Davis et al. examined the process in which colorless spiropyran undergoes a ring-opening reaction when applied with a tensile force to form a red-colored merocyanine.¹⁹ In this study, spiropyran molecules were chemically bonded into the linear backbone of a poly(methyl acrylate) (PMA) thermoset. After straining the

sample to large strains under tensile loading, the spiropyran grafted into the backbone of the PMA underwent electrocyclic ring opening to form a red-colored merocyanine. However, this color-change as a form of signal for damage detection was not generated until after significant and permanent mechanical damage had been applied. This force-sensitive bond formed by the reversible dimerization in the cinnamoyl or anthracene moieties can be dimerized using ultraviolet light to form a reversible force-sensitive and highly strained bond that can be severed by the external application of a mechanical force.^{14, 27-28} When severed, these bonds become fluorescent with an emission at 500-550 nm and 365-415 nm, respectively. This fluorescence enables the ability to generate signals within the material. It is also suggested that the fluorescent response intensity within the region of 6% to 15% strain seems to be linear with respect to the applied strain on the sample.^{14, 29} Previous work has incorporated cinnamoyl groups into an epoxy thermoset by mixing 1,1,1-tris(cinnamoyloxymethyl) ethane (TCE).¹⁴ In addition, the anthracene moiety has been applied using dimeric anthracene carboxylic acid (DiAC) as a mechanophore particle distributed throughout an epoxy matrix.²³ These samples each underwent compressive forces with varying strains and mechanophore loadings to examine the signal generation abilities of the embedded mechanophore. DiAC samples were capable of generating stress-response signal as early as 4% strain, while TCE samples generated signals at approximately 6% strain.^{1, 23}

Mechanophores include various types of mechanisms for activation among different subgroups.²¹ For instance, hemolytic and heterolytic cleavage take place when simple dissociation of weak bonds occurs.²¹ Dative bond scission typically happens when selective and specialized weak bonds with inorganic intermediates are severed.²¹

Electrocyclic ring opening can also arise when ring opening occurs without separation into multiple molecules.²¹ Lastly, cycloreversion is the process in which ring opening creates two separate molecular structures.²¹ In addition to different mechanisms for activation, the mechanical loading that is applied to the mechanophores is also very important in its activation. Compression, tension, shear, impact, and any potential combination of these types of damage directly correlate to the amount of energy directed towards the specific mechanically active bond. For example, a mechanophore that responds well to a compressive force may not activate well in a tensile loading environment, as it is likely any signal observed within the experiment would be due to the perpendicular compressive force during necking. Additionally, packing and chain orientation on a molecular level is also important for energy to be transferred properly to the correct bonds. Mechanophores incorporated into backbone of a linear polymer rely heavily on the tensile strain applied to the ends of the polymer chain.¹⁹ While load direction may not be entirely important in amorphous polymers, crystalline regions containing mechanophore would show little to no activation if applied perpendicular to the crystalline orientation. The types of signals generated from mechanophores can also be very broad depending on the chemistry and the requirement of specific applications, including mechanochromic reaction, fluorescence response, reactivity, conductivity, heat generation, and so on.³⁰⁻³⁴ For example, the benzocyclobutene mechanophore is relatively well known mechanophore which undergoes a ring opening reaction within its cyclobutene component, creating a conjugated reactive site.^{16,35} Such a reactive site has the unique advantage that it can be bonded by a free reactive group and therefore produces a chemical signal. Craig et al. has shown that a chemical crosslinker can be introduced to cause gelation upon the mechanophore activation

of benzocyclobutene.^{16,35} Mechanophores such as the cinnamoyl and anthracene group, which are fluorescent in their initial monomeric state, can undergo [2+2] and [4+4] cycloaddition, respectively, in the presence of UV light to yield a non-fluorescent, force-responsive dimer.

Grafting of reversible UV-curable mechanophores also opens up new functionalities for functional polymers containing anthracene and cinnamoyl groups which are capable, to some extent, of healing.³⁶ Due to the proximity remained by the monomer pairs of the mechanophores after activation, they can be re-dimerized with UV light. However, their intrinsic photochemical healing capabilities are usually limited to soft polymers that generally consist of linear chains or flexible networks. Damage in thermosets must be small volume due to needing direct contact between active healing functional groups.³⁷ Very little progress had been made with respect to photochemical healing of these mechanophores within a thermoset matrix such as epoxy. Coope et al. have shown that a reversible heating/cooling mechanism for a Diels-Alder process is capable of photochemical healing within an epoxy matrix, utilizing a Diels-Alder based crosslinker instead of the traditional amine-based hardener.³⁸ Anthracene based mechanophores have shown similar behavior to these Diels-Alder crosslinkers.³⁷ In addition, cinnamoyl groups incorporated in thermoplastic materials have shown similar healing behavior but rely on the flexibility of these polymer chains to promote functional group proximity and re-dimerize.³⁹

In this work, we propose to graft the cinnamoyl mechanophore into the backbone of an epoxy matrix through a new approach of modifying a cinnamic acid molecule that not only improves mechanical properties but also allows for force-responsive properties

with amine hardener functionality. For the epoxy system used in this manuscript, diglycidylether of bisphenol F was chosen as the resin component, while diethylenetriamine (DETA) was chosen as the hardener (crosslinker), referred to in this paper as Hardener 1 or H1. The cinnamoyl mechanophore will be functionalized with DETA to produce a mechanophore functionalized hardener, referred to in this paper as Hardener 2 or H2. The anticipated results will be two-fold. First, this approach will not only limit the property loss from these cinnamoyl mechanophores but also improve upon their sensitivity to detect stresses compared to other cinnamoyl mechanophore approaches. Second, we demonstrate a feasibility study on the photochemical healing properties of the resulting matrix. Our results will provide a fundamental understanding of how mechanophores behave after chemical alteration as well as how these mechanophores can be applied to heal damaged thermoset materials under pre-failure conditions.

Methodology

Materials

Cinnamic acid, dichloromethane, methylchloroformate, triethylamine (TEA), and tris(2-aminoethyl)amine (TAA) were used as received from Sigma-Aldrich. Epoxy resin FS-A23 (diglycidyl ether bisphenol F, DGE BPF) and epoxy hardener FS-B412 (diethylenetriamine, DETA) were purchased from Epoxy Systems Inc. and used as received.

Synthesis of N-[2-bis(2-aminoethyl)aminoethyl]cinnamamide

Hardener (H2) grafting was achieved via bonding of the cinnamoyl group with a tris(2-aminoethyl)amine (TAA) molecule. To create the composite, the functionalized

hardener (H2) first needed to be synthesized separately. 7.408 grams of cinnamic acid, 14.0 mL of triethylamine, and 40 mL of dichloromethane were added into a round bottom flask and put in an ice bath under reflux. 7.7 mL of methyl chloroformate was added dropwise slowly to ensure no excess heat was generated during the addition process and let stir for 2 hours. After completion, 15.0 mL of tris(2-aminoethyl)amine was added to the mixture dropwise slowly, as to not introduce too much precipitate into the reaction vessel at once. Once fully added, the mixture was allowed to set overnight (minimum 8 hours). The precipitate was filtered from the mixture and washed with dichloromethane twice before being set to dry in a vacuum oven.

Synthesis of 10 wt% Functionalized Mechanophore Epoxy Composite

Once dry, 0.92 g of solid H2 was added to 0.65 g of diethylenetriamine (DETA) and heated to 110 °C under mechanical stirring until a homogenous liquid mixture was formed. 3.43 g of DGEbPF was quickly added and stirred at 200 rpms for 2 mins before being poured into molds. Samples were cured initially at 110 °C for 1 hour and 50 °C for at least 16 hours. After fully curing, samples were placed under a UV lamp and irradiated at 302 nm for 4 hours.

Attenuated Total Reflectance Fourier Transform Infrared Spectroscopy

Characterization of the functionalized composite was performed using Fourier Transform Infrared Spectroscopy (FTIR) under vacuum with a Bruker IFS 6v/S FTIR spectrometer and Pike Diamond Attenuated Total Reflectance (ATR) module.

2.5 Differential Scanning Calorimetry

Glass transition temperature (T_g) was measured via a Q20 Differential Scanning Calorimeter (DSC) with aluminum pans, nitrogen purge, and an empty pan as a reference.

The DSC procedure followed a standard heat/cool/heat method with initial heating to 70 °C, cooling to -20 °C, and second heating to 120 °C at 10 °C min⁻¹.

Thermogravimetric Analysis

Decomposition temperature (T_d) was measured via a Q500 Thermogravimetric Analyzer (TGA) under nitrogen purge and aluminum pan. The heating profile consisted of a 10 °C min⁻¹ ramp from 25 to 500 °C. The peak of the derivative weight profile was used to calculate T_d .

Dynamic Mechanical Analysis

Storage modulus, loss modulus, and tan delta were measured via a Q800 TA Instruments Dynamic Mechanical Analyzer (DMA). A multi-frequency/strain method was used with a single cantilever clamp at a frequency of 1 Hz and 25 μm amplitude. The temperature profile consisted of a 5 °C min⁻¹ ramp from 25 to 120 °C. Crosslink density was calculated using the theory of rubber elasticity.³¹

Compression Testing and In-situ Fluorescence Measurements

Compression tests were performed using a TestResources 800L Compression Test System at a rate of 1 mm per minute. Fluorescent images and video were taken in-situ with a Thorlabs DCU223 UV Camera. External noise was reduced with a bandpass filter (450 ± 20 nm) so that only the fluorescent emission was captured. The sample was excited using a Thorlabs M365LP1 UV Lamp with emission at 365 nm. Images taken during sample testing were plotted using an in-house MATLAB program to calculate the integrated density, or the sum of the intensity values for all pixels across an image. One image was captured per second, and this integrated density value was plotted as a function of strain

and used to compare fluorescent intensity differences between samples. Figure 1 shows a schematic of the load frame in conjunction with the UV camera and UV light source.

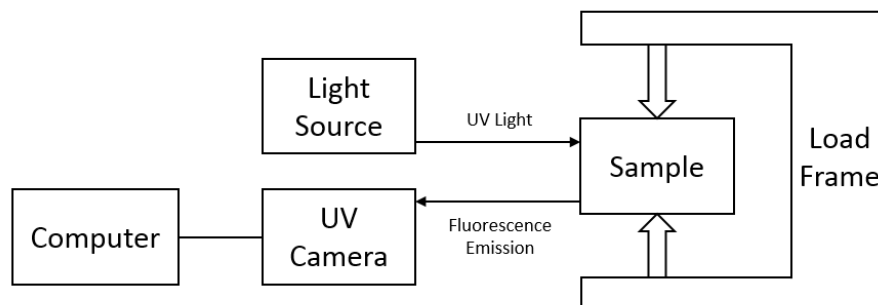


Figure A1. Schematic for in-situ measurements of cinnamoyl grafted epoxy composites with a TestResources 800L Compression System, UV camera, and UV light source.

Results and Discussion

Confirmation of N-[2-bis(2-aminoethyl)aminoethyl]cinnamamide Synthesis

Hardeners possess a strong effect on the mechanical and thermal properties of the resulting thermoset. The T_g for DGEbPF-based epoxies can be dramatically varied based on the hardener chosen. Therefore, the H2 grafted composites are expected to demonstrate very different behaviors when compared to neat epoxy. To begin this approach, the cinnamoyl mechanophore was first dimerized by UV irradiating cinnamic acid with 302 nm light in a suspension of hexanes for 48 hours. As shown in Figure 2, the comparison of FTIR spectra between cinnamic acid and the resulting dimer, truxillic acid, confirmed the successful dimerization reaction, where the dominating adsorption peak consist of the C=O shifting from 1668 cm^{-1} to 1685 cm^{-1} due to the changes in conjugation of the molecule, as well as the disappearance of the trans C=C band at 1623 cm^{-1} due to the formation of the cyclobutane.

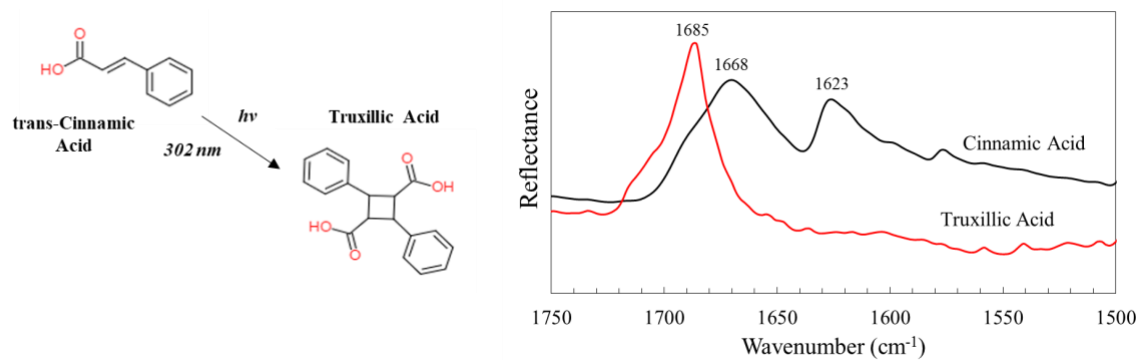


Figure A2. (Left) Chemical structure of cinnamic acid and resulting dimer, truxillic acid, after UV exposure for 48 hours. (Right) ATR-FTIR spectra results of initial cinnamic acid monomer and purified product truxillic acid after dimerization.

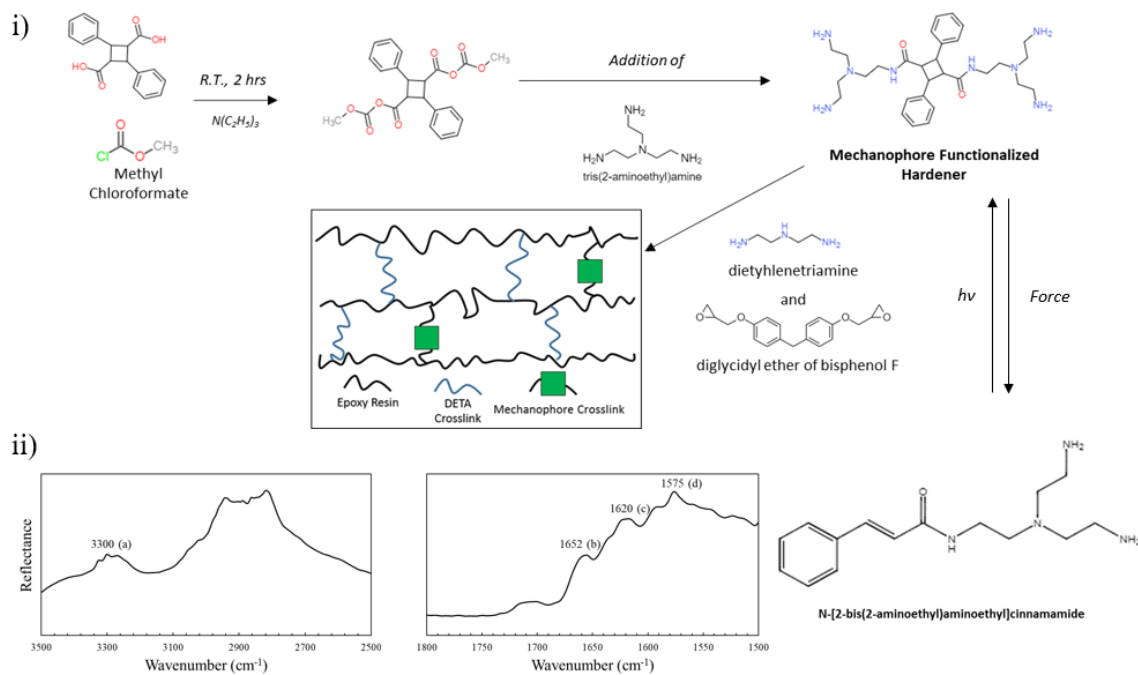


Figure A3. i) Illustration of the hypothetical reaction mechanism to produce mechanophore functionalized hardener (H2) and cartoon of subsequent matrix. ii) FTIR spectra for synthesized mechanophore N-[2-bis(2-aminoethyl)aminoethyl]cinnamide,

where notable peaks include (a) primary N-H vibrations at approximately 3300 cm^{-1} , (b) amide C=O vibrations at 1652 cm^{-1} , (c) cis C=C vibrations at 1620 cm^{-1} , and (d) trans C=C vibrations at 1575 cm^{-1} .

In order to graft the mechanophore into the backbone of an epoxy matrix, a reactive site needs to be created on the mechanophore to allow bonding into the matrix. Due to ease of reactivity and relative strength of resulting matrices, amine-based hardeners were chosen as a suitable approach. Tris(2-aminoethyl)amine (TAA) was selected as the most optimal hardener due to its three sets of primary amines, allowing for increased incorporation of the grafted mechanophore into the epoxy matrix. DETA and *m*-phenylenediamine (MPD) are robust hardeners that are commercially available, but were ultimately not adequate due to limited amine reactivity and difficult curing conditions.^{40,41} After truxillic acid was successfully synthesized, a two-step substitution reaction was utilized to graft the hardener molecule tris(2-aminoethyl)amine to the mechanophore molecule with the proposed reaction mechanism illustrated in Figure A3 (i). First the creation of an anhydride leaving group on the cinnamoyl functionality was accomplished through addition of methyl chloroformate. Subsequently, the second step substituted this anhydride into an amide through the addition of an aliphatic amine functionality – in this particular case, TAA – to produce the desired product. Figure A3 (ii) shows the ATR-FTIR spectra of the synthesized H2, N-[2-bis(2-aminoethyl)aminoethyl]cinnamamide, at its force-activated, monomeric form. Notable functional group changes in this reaction are reflected by the disappearance of the carboxylic acid C=O peak at 1700 cm^{-1} from truxillic acid and amide C=O peaks at 1652 cm^{-1} , indicating the successful bonding of primary amines. To the best of the author's

knowledge, this is the first time a mechanophore with amine-based hardener functional moieties has been synthesized for incorporation into an epoxy matrix.

Effect of Functionalized Hardener (H2) on Thermal and Mechanical Properties

After the new H2 was synthesized, a two-stage curing process was carried out to incorporate the hardener into an epoxy-based composite at 100 °C and 50 °C, respectively. Due to the relatively high melting point, approximately 95 °C, of the H2, the first step of curing consists of 100 °C for 1 hour in order to fully cure the functionalized mechanophore within the matrix. The second step, 50 °C for 16 hours, is to cure the H1 crosslinks and further increase the degree of crosslinking throughout the entire matrix. The effect of incorporating the H2 on the properties of the composite were studied by mechanical and thermal characterization methods. Figure A4 shows the comparison of the stress-strain curve between neat and 10 wt% functionalized epoxies, where Young's modulus and yield stress were manually calculated from the linear slope of the elastic deformation region and peak of the curve. It is noticeable that there was an increase of approximately 15 °C in T_g after incorporation of mechanophores as well as an improvement in both Young's modulus and yield stress under compression loading. Figure A5 shows the comparison between neat and 10 wt% functionalized epoxies T_g when measured by DSC. T_g values were calculated using a 5-point step transition analysis with TA instrument software. A rather significant increase in T_g is seen with the functionalized epoxies, increasing from 69 °C to 84 °C. These improvements in both mechanical and thermal properties can be attributed to a high loading of a H2 component. Additionally, DMA results confirm that this H2 increases crosslink density over neat epoxy, seen in Figure A7.

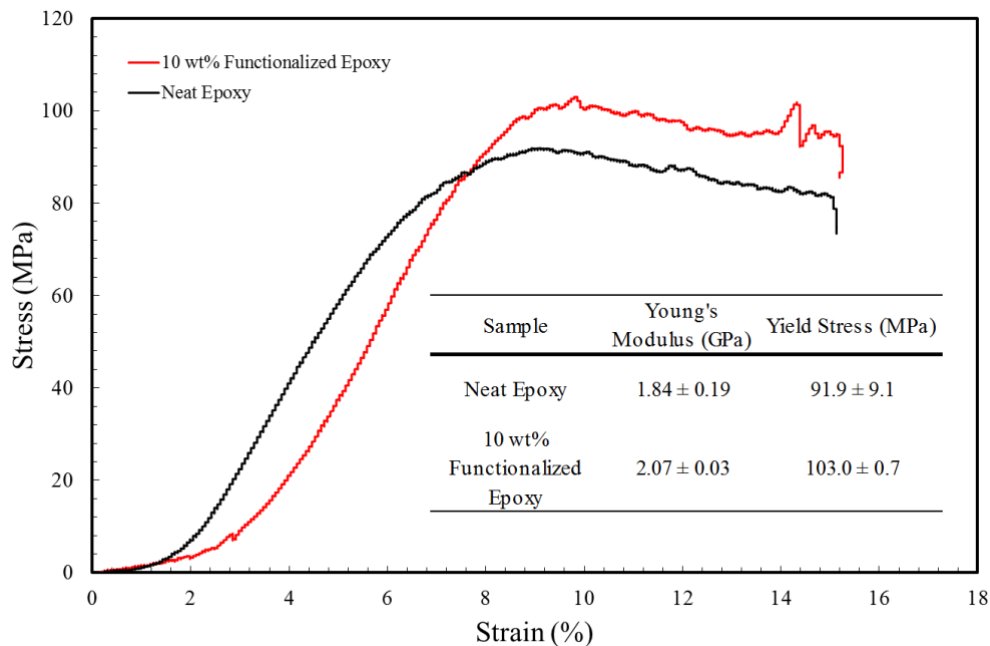


Figure A4. Mechanical properties of grafted hardener (H2) epoxy composites compared to neat epoxy. Inset shows calculated Young's modulus and yield stress.

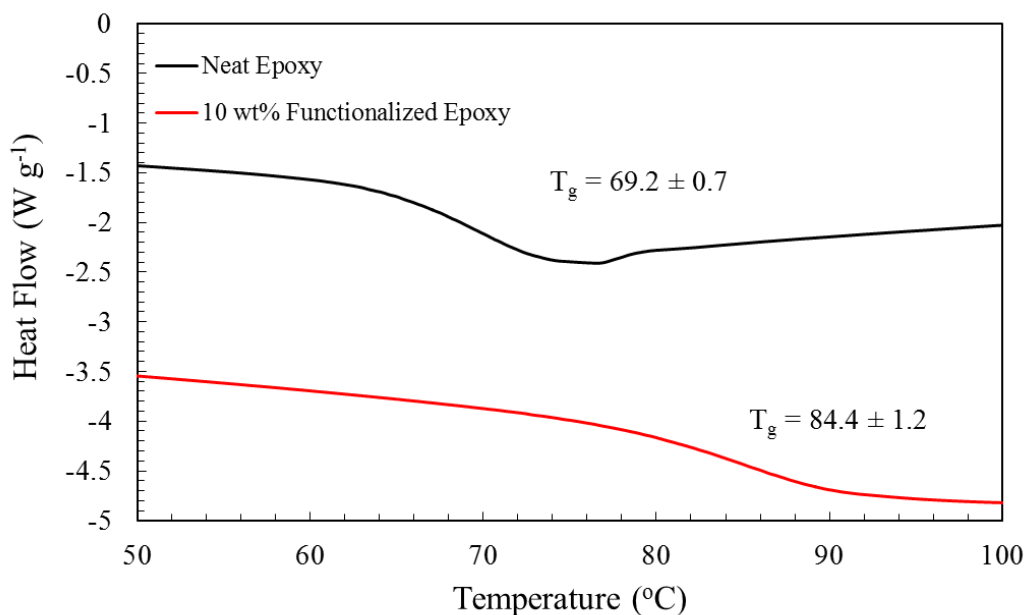


Figure A5. DSC results for neat epoxy (H1) and grafted mechanophore hardener (H2) epoxy composites. Inset shows glass transitions for both samples.

To further study the thermal stability of the 10 wt% functionalized epoxy system, thermogravimetric analysis (TGA) was performed in comparison with a neat epoxy control. Results from this experiment can be seen in Figure 6. In contrast to the thermal and mechanical property improvements measured with DSC and compression loading, 10 wt% functionalized epoxies showed a slight decrease in decomposition temperature (T_d) from 353 °C to 335 °C. This suggests that while the new crosslinks introduced by the mechanophore do enhance the mechanical properties and glass transition, they negatively affect the bulk decomposition of the polymer when compared to the neat counterpart. Nofen et. al. found that grafting mechanophore onto the resin component of the epoxy also lowered the T_d , but in a different manner. It was reported that two modes of decomposition for resin-based grafting occurred – one as early as 120 °C, attributed to the decomposition of the mechanophore bonds, while the main bulk of the epoxy network decomposed at the same temperature as the neat epoxy control. Rather than an early decomposition before the bulk decomposition step as seen in resin-based mechanophore grafted composites, the 10 wt% H2 epoxy contained a singular decomposition step. It is hypothesized that a higher degree of incorporation and crosslinking with hardener-based grafting created a more homogenized system than resin-based grafting, preventing the less thermally stable mechanophore bonds from decomposing early. As a consequence, the bulk T_d was lowered rather than remaining on par with neat epoxy.

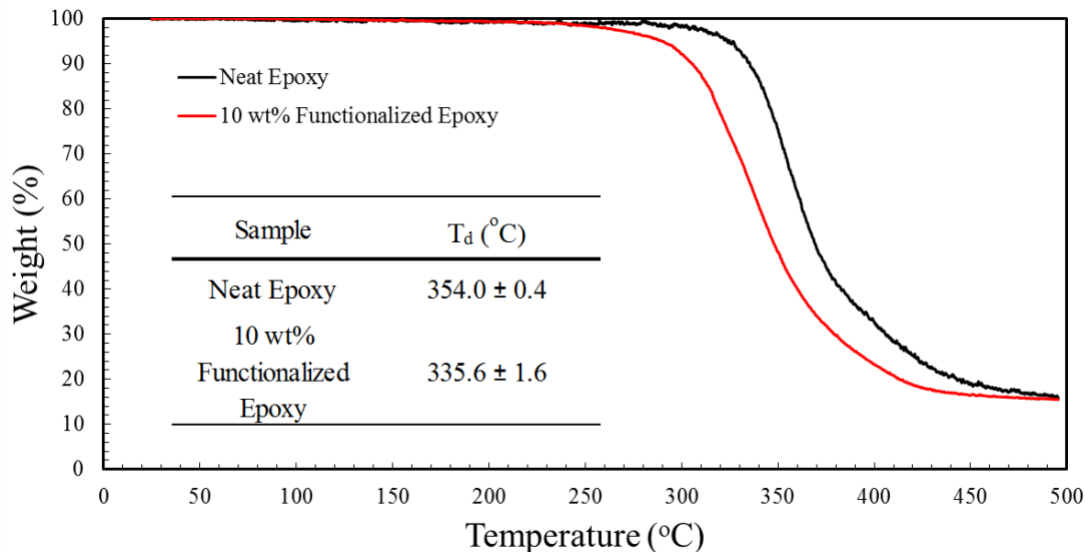


Figure A6. TGA results for neat epoxy and 10 wt% functionalized epoxy showing each respective decomposition curve. Inset table shows calculated decomposition (T_d) temperatures calculated from the derivative weight plots.

DMA was also performed to not only provide a validation for T_g of the materials but also detailed information on their crosslink density. Values measured in Figure 7 were used as a baseline to compare with other experiments performed regarding neat epoxy (Figure A9) and photochemical healing (Figure A11). Crosslink densities were calculated using the theory of rubber elasticity⁴², $\rho_{xl} = \frac{G'}{3RT}$, where ρ_{xl} is the crosslink density in mol cm⁻³, G' is the rubbery plateau storage modulus at a specific temperature T, and R is the gas constant. In this equation, the storage modulus of the tested matrix above the glass transition temperature is the dominant factor in calculating crosslink density. With regards to these calculations, a temperature of 145 °C was chosen as it was significantly past the glass transition temperature of the epoxies as to not include any unwanted glassiness effects.

Systems with high crosslink densities will still maintain a relatively high storage modulus when compared to low crosslink systems with amorphous chains due to high entanglement of their polymer chains. Thus, by calculating crosslink density for these epoxy systems, observations can be made regarding the incorporation of the H2 into matrix. As shown in Figure A7, the results from DMA revealed the improvement from incorporation of H2 on all the measurable properties, with the exception of storage modulus. An increase in both crosslink density and T_g was observed over neat epoxy cured under the same conditions. It is hypothesized that this increase in crosslink is due to the functionalized mechanophore hardener's two highly reactive primary amines, as well as its cyclobutane which can bond to another H2 with two additional primary amines. This is an increase in the number of active sites when compared to neat epoxy's DETA crosslinker, which only contains two primary amines. Glass transition and mechanical property improvements can be explained as a consequence of this increased crosslink density.

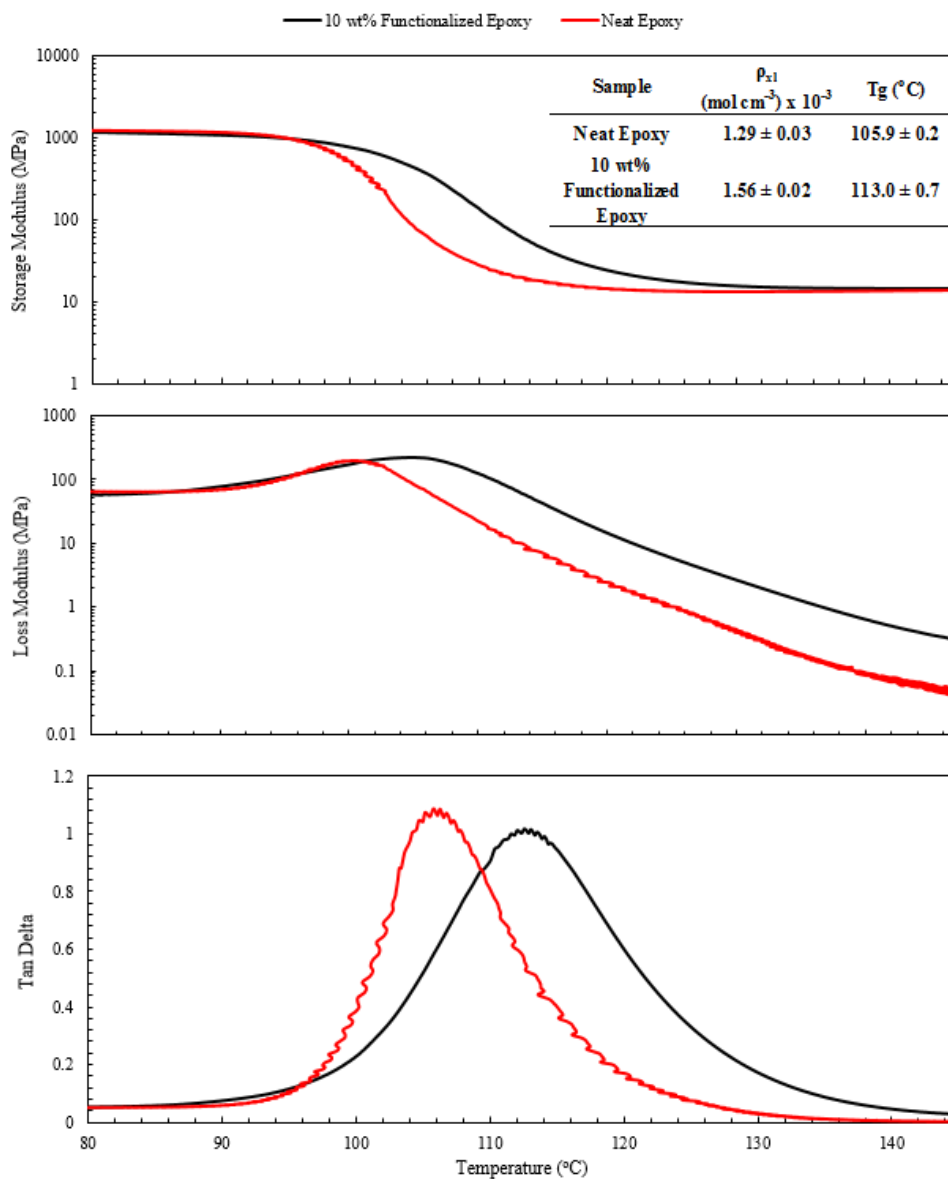


Figure A7. DMA curves for neat epoxy and 10 wt% grafted hardener (H2) epoxy showing storage modulus (G' , top), loss modulus (G'' , middle), and tan delta (bottom). Inset table shows comparison between T_g and crosslink density between samples.

Effect of Self-Sensing via Cinnamoyl-based Functionalized Epoxy

Fluorescent response for H2 based mechanophore grafting improved over particle incorporation and resin grafting approaches. Figure A8 shows a plot of in-situ compression tests with corresponding fluorescent response. Fluorescent signal onset, which is classified as ‘early damage detection’ provided the signal occurs before the yield strain of the material, occurred as early as 6% strain with yield strain at approximately 8% strain. Previous fluorescence detection with cinnamoyl particles and resin-based cinnamoyl grafting methods show mechanophore activation as well as yield at 6% strain. This improvement can be attributed to the drastic change in the hardener structure. It is hypothesized that the disassociation energy for the cyclobutane bond within the mechanophore structure was lowered, creating a more sensitive mechanophore. Some modeling studies have been conducted which investigate the dissociation energy of cyclobutane and cyclooctane mechanophores with various architectures.⁴³ While the mechanism for this decrease in disassociation energy was not conclusive, it can be suggested that the surrounding architecture can affect the load transfer efficiency to the cyclobutane through interactions with the bulk matrix. Further investigation is warranted to determine how these chemical modifications can affect the disassociation energy of the cyclobutane bond, and how this can be tailored to achieve tunable mechanophore sensitivity.

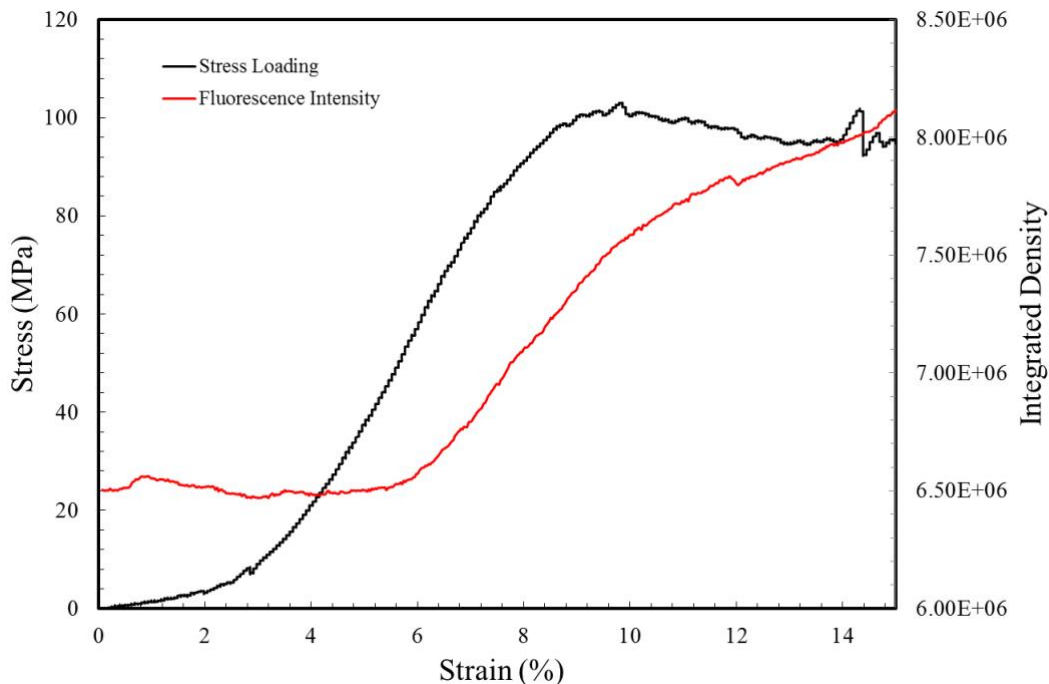


Figure A8. Fluorescence intensity plot and stress-strain curve for branched grafted hardener (H2) epoxy composites. Intensity was captured via a UV lamp/camera, and force was captured via a Test Resources 800L compression system.

Effect of Photochemical Healing via Cinnamoyl-based Functionalized Epoxy

Due to the reversible nature of the cyclobutane bond present in cinnamoyl mechanophores, photochemical healing is a major interest in the mechanophore field. Their feasibility in thermoplastic and gel materials has already been proven but has not been attempted with thermoset materials. Thermosets pose several problems for photochemical healing: inflexibility of thermoset matrix chains inhibits two cinnamoyl monomers from maintaining proximity after breaking and the flexibility of the network can only be varied with crosslink density. Unfortunately, since lower crosslink density generally coincides with weaker mechanical and thermal properties, reducing the crosslink density is not an

option for thermosets with structural applications. It was proposed to examine the potential for healing with 10 wt% H2 epoxy systems, which has not been previously studied. To examine the ‘healing’ mechanism present in the epoxy material, DMA was used to examine crosslink density changes after healing. Samples were prepared in the same manner as outlined previously, with the exception of being molded into 3 x 12 x 30 mm samples designed for tensile loading in DMA. After being synthesized, two experiments were performed. First, a 20 wt% sample with no UV crosslinking was irradiated for 48 hours to observe any changes in the solid state. This increase in weight loading was justified to make the maximum crosslinking potential of the cinnamoyl mechanophore, or ‘healing factor’ as significant as possible. It is important to note that while the ‘healing factor’ is being measured. Mechanical properties were not a concern for the 20 wt% samples because only the ‘healing factor’ was desired. Additionally, a control batch of neat epoxy before and after UV irradiation was examined to be sure that the procedure did not induce any crosslink density or T_g changes. Figure A9 shows a plot of the neat epoxy comparison, while Figure A10 shows the results of the 20 wt% photochemical healing experiments. While there was a slight increase in crosslink density in the control experiments after UV irradiation, there was some overlap with the standard deviation of the samples, leading to believe that no significant change had occurred in the samples.

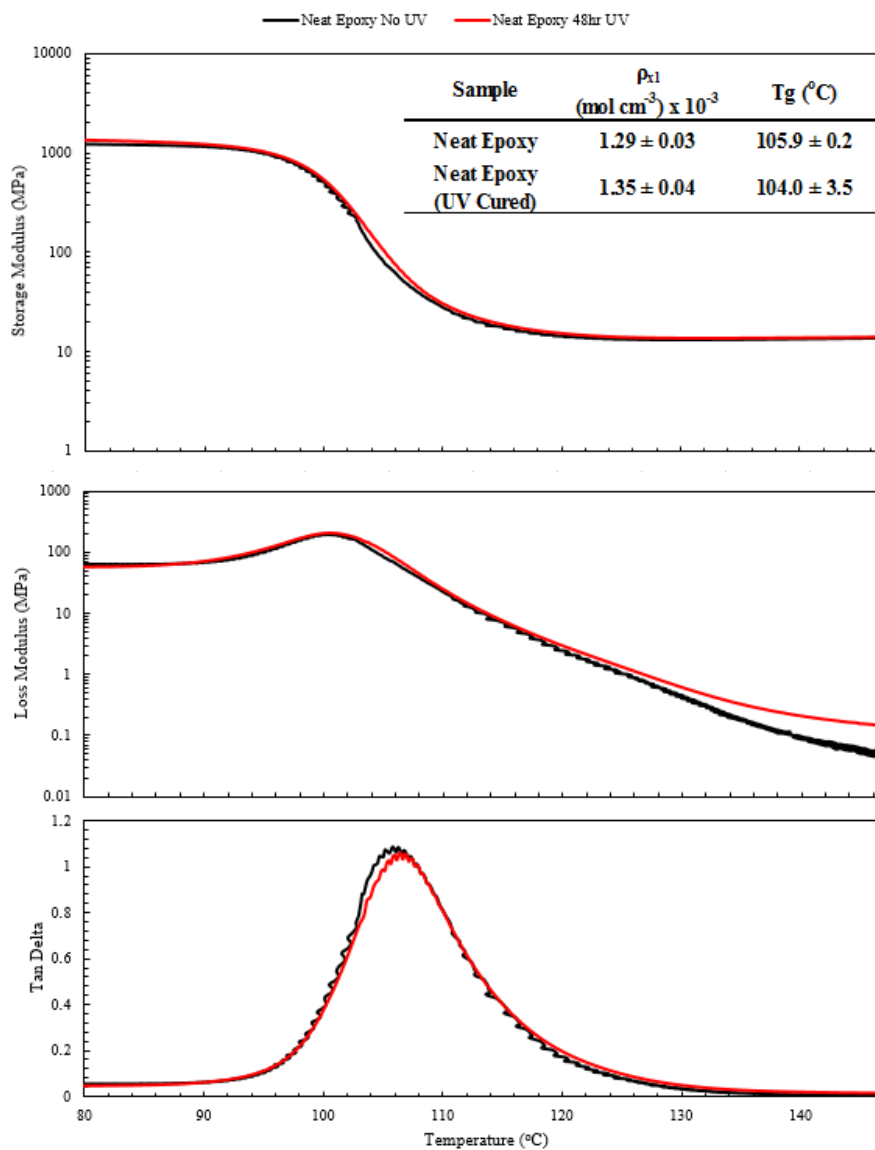


Figure A9. DMA curves for neat epoxy before and after UV irradiation showing storage modulus (G' , top), loss modulus (G'' , middle), and tan delta (bottom). Inset table shows comparison between T_g and crosslink density between samples.

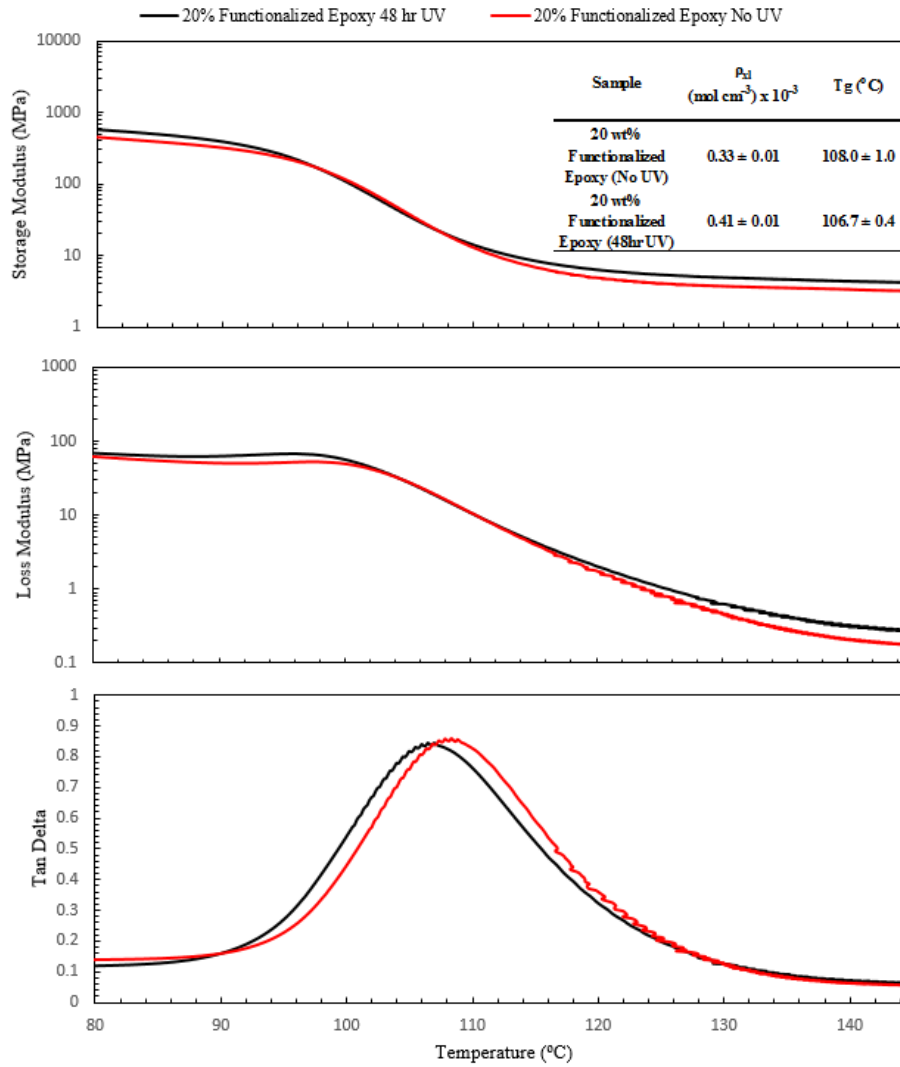


Figure A10. DMA curves for 20 wt% grafted hardener (H2) epoxy before and after UV irradiation showing storage modulus (G' , top), loss modulus (G'' , middle), and tan delta (bottom). Inset table shows comparison between T_g and crosslink density between samples.

The most significant changes occur when UV irradiating a solid mechanophore grafted epoxy system for the first time. Crosslink density increases from 3.27×10^{-4} mol cm^{-3} to 4.09×10^{-4} mol cm^{-3} , suggesting that ‘new’ cinnamoyl crosslinks make up 25.1% of the total crosslinks in the thermoset after UV irradiation for this particular sample. It is important to note that the values present in these samples are significantly lower than shown earlier in Figure A7 due to the fact that it is a higher weight loading of H2. It can be inferred too high loading can inhibit crosslinking of the matrix, resulting in poorer mechanical and thermal properties. However, these increases in crosslink density after UV irradiation show that the cinnamoyl mechanophores are capable of dimerizing in the thermoset matrix, indication that photochemical healing for this particular thermoset matrix is indeed feasible. To apply this approach to a more realistic system, the weight loading of H2 will need to be lowered as to provide the mechanical properties expected of an epoxy network. An already irradiated 10 wt% sample was damaged to 3% tensile loading, before the yield point of the material, using a TestResources 800L Tensile system. The goal of this experiment was to observe any healing after one cycle of significant loading, but not to damage the material past failure and make healing difficult to characterize. Figure A11 below shows the results of these experiments.

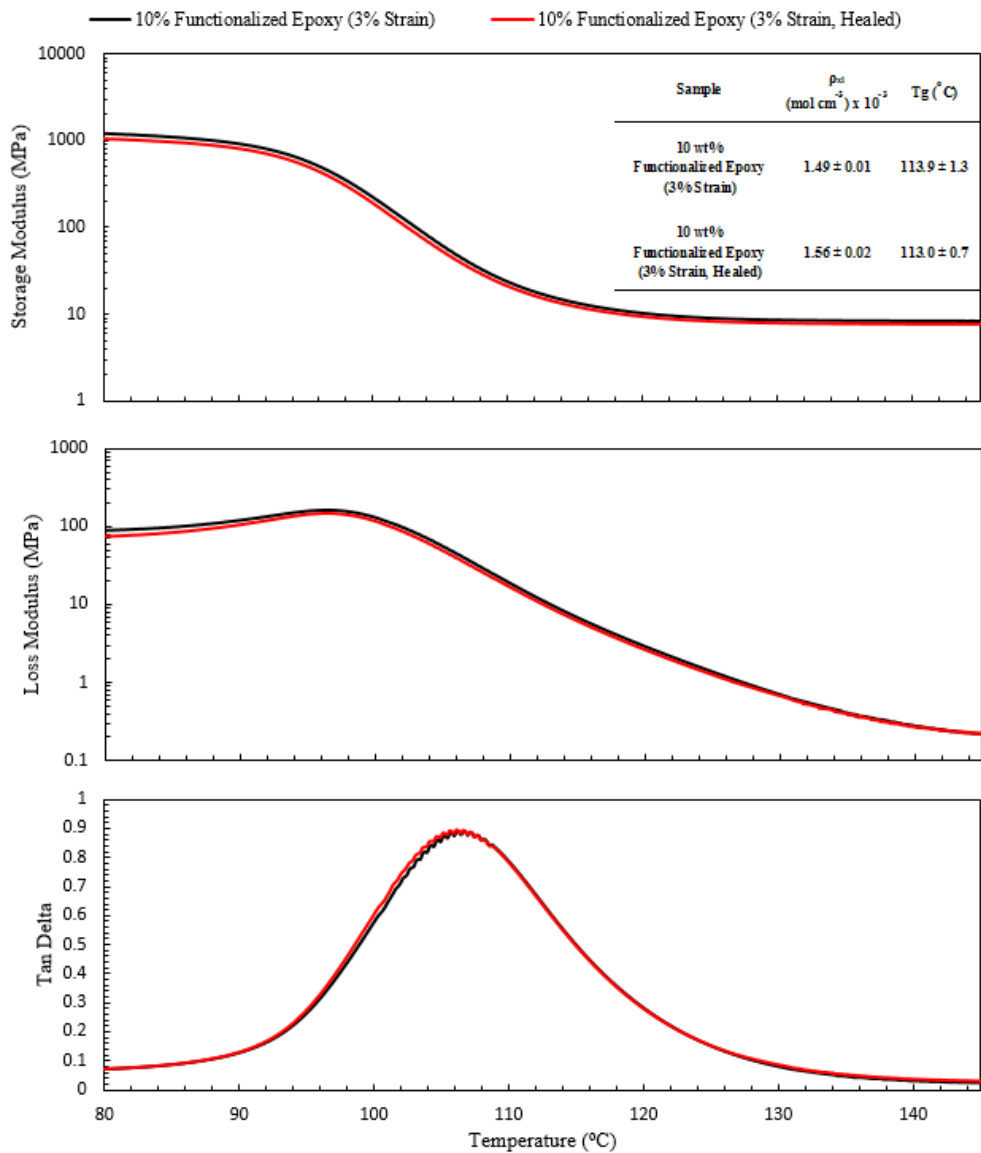


Figure A11. DMA curves for neat epoxy and 10 wt% grafted hardener (H2) epoxy after the first damage cycle showing storage modulus (G' , top), loss modulus (G'' , middle), and tan delta (bottom). Inset table shows comparison between T_g and crosslink density between samples.

Observable changes within 10 wt% samples are not as significant as the previous experiment, in part due to the lower weight loading and the fact that the samples were dimerized before damage. Therefore, only the healing which occurred after damage would be observed. Crosslink density increases from $1.493 \times 10^{-3} \text{ mol cm}^{-3}$ after damage to $1.563 \times 10^{-3} \text{ mol cm}^{-3}$ after healing, an increase of approximately 4%. While it can be noted that the changes from control samples were deemed insignificant due to overlap in standard deviation, samples with 10 wt% H2 did show significant changes in crosslink density. Additionally, storage modulus seems to vary significantly in healed samples. This is hypothesized to be thermal relaxation after thermal cycling during the first experiment. Nonetheless, while not drastically significant after the first cycle of loading, self-healing is indeed occurring in this thermoset system. Higher weight loadings of H2 can be used to increase the healing capability, but at the cost of mechanical properties. Additionally, limitations of this approach are quite apparent due to the brittle failure of epoxy. Only non-critical damage due to low strains such as micro-cracking and micro-fractures are healable with this technique. If strains greater than the yield strain of the material are applied and large fractures occur within the matrix, inflexibility of the matrix becomes a major weakness in this photochemical healing approach. Coope et. al. has shown thermosets that are capable of overcoming this limitation through thermally reversible Diels-Alder based crosslinks, allowing for photochemical healing to take place when heating until the material can become flexible enough to further crosslink.³⁶ A similar approach may be applicable to matrices containing solely cinnamoyl-based hardener components, as the cinnamoyl cyclobutane mechanophore is photoreversible. While further investigation into improvement of this photochemical healing approach to apply to more critical damage is

warranted, we have already shown a promising route to photochemical healing in an epoxy thermoset matrix not previously seen in literature.

Conclusion

In this study, we have demonstrated several key results. First, grafting of amine-based hardener functionality to the cinnamoyl mechanophore was achieved and successfully implemented into an epoxy with robust mechanical and thermal properties. Second, this mechanophore grafted epoxy has shown improved fluorescent response sensitivity over resin-based grafting. Third, preliminary results with healing experiments demonstrate that irradiation of 20 wt% samples allow for as much as 26.5% new crosslinks to form via the cinnamoyl mechanophore. 10 wt% samples show 25.1% recovery when measured with FTIR and a 4% change from their damaged to healed state as measured with DMA and FTIR. Hardener-based grafting allows for improvement in thermal properties (glass transition temperature), mechanical properties (Young's modulus, yield strength), and crosslink density. Additionally, the H2 grafting approach greatly improved on the cinnamoyl moiety's sensitivity to mechanical force by lowering disassociation energy of the cyclobutane bond. While alternative curing conditions and incomplete conversion could limit hardener-based grafting's usefulness, further tests are ongoing to optimize the loading and curing conditions, as well as understand how changing the chemical architecture of the mechanophore can affect the dissociation energy of the cyclobutane group present in the cinnamoyl moiety. This research proves that photochemical healing is indeed feasible for this thermostat system; however, further investigation into various

other methods of incorporation and grafting could continue to improve the stress-sensing sensitivity and the photochemical healing efficiency of the material system.

References for Appendix A

- [A1] J. Li, N. Chikkannagari, J.S. Moore, *Acc. Chem. Res.* 2015, 48, 2181
- [A2] P. Chatterjee, A. Dai, H. Yu, H. Jiang, L.L. Dai, *J. Appl. Polym. Sci.* 2015, 132, 42776
- [A3] Y. Zhao, *Macromol.* 2012, 45, 3647
- [A4] Y. Xu, O. Ghag, M. Reimann, P. Sitterle, P. Chatterjee, E. Nofen, H. Yu, H. Jiang, L.L. Dai, *Soft Matter*, 2018, 14, 151
- [A5] D. Schmaljohann, *Adv. Drug Del. Rev.* 2006, 58, 1655
- [A6] J.Z. Du, X.J. Du, C.Q. Mao, J. Wang, *J. Am. Chem. Soc.* 2011, 133, 17560
- [A7] K.M. Huh, H.C. Kang, Y.J. Lee, Y.H. Bae, *Macromol. Res.* 2012, 20, 224
- [A8] Y.T. Wen, Z.X. Zhang, J. Li, *Adv. Funct. Mat.* 2014, 24, 3874
- [A9] H. Cho, J. Bae, F.K. Garripelli, J.M. Anderson, H.W. Jun, S. Jo, *Chem. Commun.* 2012, 48, 6043
- [A10] J. Sohma, *Prog. Polym. Sci.* 1989, 14, 451-596
- [A11] M.M. Caruso, D.A. Davis, Q. Shen, S.A. Odom, N.R. Sottos, S.R. White, J.S. Moore, *Chem. Rev.* 2009, 109, 5755
- [A12] S.C. Jiang, L.X. Zhang, T.W. Xie, Y.J. Lin, H. Zhang, Y.Z. Xu, W.G. Weng, L.Z. Dai, *ACS Mac. Lett.* 2013, 2, 705
- [A13] K. Ishizuki, H. Oka, D. Aoki, R. Goseki, H. Otsuka, *Chem. Eur. J.* 2018, 24, 3170
- [A14] J. Zou, Y. Liu, B. Shan, A. Chattopadhyay, L.L. Dai, *Smart Mat. Struct.* 2014, 23, 095038
- [A15] A. Black, J.M. Lenhardt, S.L. Craig, *J. Mater. Chem.* 2011, 21, 1655
- [A16] C.R. Hickenboth, J.S. Moore, S.R. White, N.R. Sottos, J. Baudry, S.R. Wilson, *Nat. Lett.* 2007, 446, 423
- [A17] J.N. Brantley, K.M. Wiggins, C.W. Bielawski, *Polym. Int.* 2012, 62, 2
- [A18] G.R. Gossweiler, G.B. Hewage, S. Gerardo, Q. Wang, G.W. Welshofer, X. Zhao, S.L. Craig, *ACS Mac. Lett.* 2014, 3, 216

- [A19] D.A. Davis, A. Hamilton, J. Yang, L.D. Cremar, D. Van Gough, S.L. Potisek, M.T. Ong, P.V. Braun, T.J. Martinez, S.R. White, J.S. Moore, N.R. Sottos, *Nat. Lett.* 2009, 459, 68
- [A20] P. Froimowicz, H. Frey, K. Landfester, *Macromol. Rap. Commun.* 2011, 32, 468
- [A21] M.B. Larsen, A.J. Boydston, *J. Am. Chem. Soc.* 2013, 135, 8189
- [A22] M.N. Silberstein, K. Min, L.D. Cremar, C.M. Degen, T.J. Martinez, N.R. Aluru, S.R. White, N.R. Sottos, *J. Appl. Phys.* 2013, 114, 023504
- [A23] E.M. Nofen, J. Wickham, B. Koo, A. Chattopadhyay, L.L. Dai, *Mat. Res. Express* 2014, 3, 035701
- [A24] E.M. Nofen, N. Zimmer, A. Dasgupta, R. Gunckel, B. Koo, A. Chattopadhyay, L.L. Dai, *Polym. Chem.* 2016, 7, 7249
- [A25] J.P. Wang, I. Piskun, S.L. Craig, *ACS Mac. Lett.* 2015, 4, 834
- [A26] A.L. Black, J.A. Orlicki, S.L. Craig, *J. Mat. Chem.* 2011, 21, 8460
- [A27] J.P. Wang, T.B. Kouznetsova, Z. Niu, M.T. Ong, H.M. Klukovich, A.L. Rheingold, T.J. Martinez, S.L. Craig, *Nat. Chem.* 2015, 7, 323
- [A28] S.Y. Cho, J.G. Kim, C.M. Chung, *J. Nanosci. Nanotech.* 2010, 10, 6872
- [A29] A.H. Ali, K.S.V. Srinivasan, *Polym. Int.* 1997, 43, 310
- [A30] J. Li, T. Shiraki, B. Hu, R.A.E. Write, B. Zhao, J.S. Moore, *J. Am. Chem. Soc.* 2014, 136, 15925
- [A31] J. Li, B. Hu, K. Yang, B. Zhao, J.S. More, *ACS Mac. Lett.* 2016, 5, 819
- [A32] T. Kosuge, K. Imato, R. Goseki, H. Otsuka, *Macromol.* 2016, 49, 5903
- [A33] R. Toivola, P.N. Lai, J. Yang, S.H. Jang, A.K.Y. Jen, B.D. Flinn, *Compos. Sci. Technol.* 2017, 139, 74
- [A34] M.S. Sammon, M. Oncak, M.K. Beyer MK, *Beilstein J. Org. Chem.* 2017, 13, 1710
34
- [A35] B.A. Beiermann, D.A. Davis, S.L. Kramer, J.S. Moore, N.R. Sottos, S.R. White, *J. Mat. Chem.* 2011, 21, 8443
- [A36] S. Radl, M. Kreimer, T. Griesser, A. Oesterreicher, A. Moser, W. Kern, S. Schlogl, *Polym.* 2015, 80, 76

- [A37] B.J. Blaiszik, S.L.B. Kramer, S.C. Olugebefola, J.S. Moore, N.R. Sottos, S.R. White, *Annu. Rev. Mater. Res.* 2010, 40, 179
- [A38] T.S. Coope, D.H. Turkenburg, H.R. Fischer, R. Luterbacher, H. van Bracht, I.P. Bond, *Smart Mat. Struct.* 2016, 25, 1
- [A39] W.J. Choi, J.S. Chung, J.J. Kim, S.H. Cha, M. Park, J.C. Lee, *J. Coat. Technol. Res.* 2014, 11, 455
- [A40] F.G. Garcia, B.G. Soares, V.J.R.R. Pita, R. Sanches, J. Rieumont, *J. Appl. Polym. Sci.* 2007, 106, 2047
- [A41] N. Sbirrazzuoli, S. Vyazovkin, A. Mititelu, C. Sladic, L. Vincent, *Macromol. Chem. Phys.* 2003, 204, 1815
- [A42] L.E. Nielsen, *J. Macromol. Sci., Rev. Macromol. Chem.* 1969, 3, 69
- [A43] B. Koo, A. Chattopadhyay, L. Dai, *Comp. Mat. Sci.* 2016, 120, 135-141
- [A44] R. Gunckel, E. Nofen, J. Hansen-Staggs, S. Babcock, B. Koo, A. Chattopadhyay, L.L. Dai, *Mater. Res. Express* 2016, 7, 7249-7259

APPENDIX B

STRESS-RESPONSIVE REINFORCED POLYMER COMPOSITES VIA FUNCTIONALIZATION OF GLASS FIBERS

Introduction

Fiber reinforced composites are a widespread material in modern structural composites. Much progress has already been made with regards to their applications in aerospace, defense, and wind power [1]. The fiber component is generally much stronger than the matrix component, allowing the force to be transferred away from the weaker matrix and focused on the fibers [2]. Types of reinforcing fibers include glass [3-4], carbon [5-8], aramid [9], and natural fibers [2, 10], and are typically incorporated into a polymer matrix. The mechanical properties of the resulting fiber composites can be effectively controlled by fiber type, volume fraction, length, and fiber orientation relative to loading, among which the load transfer of the ‘interphase’ region between the matrix and the fiber has been considered the most important factor to examine fiber composite properties [11]. If the interphase region has high bond strength, the resulting fibers will exhibit high stiffness and strength [11]. In contrast, a lower bond strength of the interphase region enhances the ability of the fiber to absorb energy under impact conditions while compromising the material strength [1]. Therefore, examining and understanding the relationship between the interphase behavior and the resulting properties can significantly contribute to the design of the fiber reinforced composites. In addition, the separation of the interphase region, which is commonly referred to as ‘delamination’, has been considered as the dominating failure mode in fiber composites. Delamination occurs when stress is accumulated at the interphase between the fiber surface and the matrix, causing the separation of those two components [12-13]. On a macroscopic scale, such a failure is often seen as by detachment of two fiber sheets on a multi-ply composite. In order to mitigate problems associated with internal damage, the early detection of delamination has

become a highly desired goal in the development of advanced fiber reinforced composites. Current techniques for detection of delamination include embedded fiber optic sensors [14-18], infrared thermography [19-20], ultrasonic [21-22], and electrical impedance [23]. While many of these techniques are non-destructive, they have limitations such as requiring coupling liquids, slow inspection speed, and susceptibility to weather. In order to overcome these limitations, a new technique must be developed which offers simplicity and non-invasiveness to increase inspection speed, while also providing enough information to completely characterize the damage. One such approach is achieved through the use of a grafted force-responsive chemical structures within the composite, which utilize an ultraviolet response signal as a means to non-invasively characterize samples quickly and in-situ.

Mechanochemistry is utilized in composites as a means of stress-sensing, utilizing weak force-responsive chemical bonds to activate signals when embedded in a polymer composite material [24-30]. These signals can then be correlated with the amount of stress applied to a polymer composite and subsequent potential damage that has occurred due to the stress. While there are many different types of force responsive moieties, the particular chemistry focused on in this paper is the cinnamoyl molecules. This cinnamoyl group is fluorescent in its initial state and capable of undergoing photocycloaddition in the presence of ultraviolet (UV) light. The [2+2] cycloaddition for the cinnamoyl group cause the initial molecules to lose their fluorescent properties. In the presence of an applied stress, the cyclobutane rings are reverted back to their monomeric state and regain their fluorescent properties. The fluorescent generation in a mechanophore embedded polymer composite is then monitored as a function of strain applied. Signal generation within the elastic region

of the stress-strain curve provides a form of damage precursor detection before real damage occurs in the matrix due to plastic deformation after the yield point of the composite. Damage precursor detection is the main objective of these composites, providing a novel and unique approach to other damage detection methods currently in literature.

As mentioned previously, the fiber-matrix within the interphase region plays a crucial role in delamination effects. One approach for controlling this interphase region is the use of sizing or coating. A typical coating for a glass fiber surface consists of a combination of organosilanes which are splayed on the surface as a monomer and subsequently cured via polycondensation induced by heat [12]. Such porous, crosslinked polysiloxane network at the surface of the fiber can then form an interpenetrating network with the matrix component, increasing adhesion. Carbon fibers are often sized in a similar manner. However, due to the fact that carbon fibers lack natural hydroxyl groups at their surface, they must first be treated using an acid bath to deposit hydroxyl groups on their surface [13]. While this method of increasing adhesion at the interphase region is in fact successful, it does not achieve direct bonding between the matrix and fiber. One such way of achieving direct bonding involves functionalization of the fiber surface with reactive functional groups capable of bonding directly to the matrix. In the instance of an epoxy matrix with a glass fiber reinforcement, fiber surfaces are functionalized via a silanization reaction with (3-aminopropyl)triethoxysilane (APTES) [31]. This reaction produces exposed amine groups of the surface which can readily react with the epoxide groups in the epoxy matrix. If desired, alternative functionalities can be used to bond nanofillers such as CNTs to the surface of the fiber to increase surface roughness, local modulus, and add sensing capabilities [32].

Mechanophores may offer a unique ability to detect onset of delamination and characterize the stress concentration at the fiber surface. To achieve this, mechanophores can be grafted onto the fiber surface via traditional surface-modification methods. In our approach, grafting to glass fibers (rather than carbon fibers) is preferred to avoid excess absorption of ultraviolet light, limiting fluorescent signal emitted. Silanization is a very effective approach to coat fiber surfaces with reactive functional groups and has been used with glass fiber reinforced polymer (GFRP) composites to increase adhesion between the epoxy-fiber interface via reactive amine groups [31]. To expand on this, these amine groups on the surface of the fiber can be reacted to a mechanophore containing an acid chloride group, such as cinnamoyl chloride. Unreacted amine groups at the surface of the composite have the potential of increasing adhesion, a potential positive side effect of the silanization process. Once deposited on the surface, the cinnamoyl groups can easily be dimerized with ultraviolet light and manufactured into composites for testing. It is anticipated that these results will create a glass fiber composite capable of early detection of delamination through a non-destructive approach. In addition, the functionalization of glass fibers with mechanophores may also increase fiber-matrix adhesion and inhibit delamination at lower strains.

Methodology

Materials

Toluene (histological grade) was purchased from Fisher Scientific, tetrahydrofuran (THF, HPLC grade) was purchased from Alfa Aesar, and acetonitrile (HPLC grade) was purchased from Honeywell. APTES (99%), Cinnamoyl chloride (98%) and

trimethylamine (>99%) were used as purchased from Sigma Aldrich. 8HS E-glass fiber was purchased from Fibre Glast. Epoxy resin FS-A23 and epoxy hardener FS-B412 were purchased from Epoxy Systems Inc. and used as received.

Coupling Reaction Between APTES and Cinnamoyl Chloride

Coupling of APTES and cinnamoyl chloride was attempted by dissolving 1 g of cinnamoyl chloride in 12 mL of THF and cooling in an ice bath to 0°C. 1.04 g of potassium carbonate and 1.33 g of APTES were added slowly into the beaker and allowed to react for 1 hour at room temperature. After the reaction was complete, it was quenched with 18 mL of HPLC water and 6 mL of ethyl acetate. The system was washed a second time with 15 mL of HPLC water and the organic phase was decanted. The organic phase was then placed in a vacuum oven overnight at 50°C to remove all solvents.

Preparation of Functionalized Glass Fiber Reinforced Polymer (GFRP) Composites

To prepare an APTES monolayer on the surface of the glass fiber, a 10 mM solution of APTES in toluene was prepared. The cleaned glass fibers were submerged for 4 hours at room temperature. After 4 hours, the fibers were removed and washed twice with toluene, twice with ethanol, and allowed to dry under a nitrogen stream. After drying, the now APTES-coated fibers were then submerged in a 200 mL acetonitrile, 200 mg cinnamoyl chloride, and 1 mL of triethylamine mixture for at least 24 hours. After reacting, the fibers were removed, washed twice with acetonitrile, twice with ethanol, and allowed to dry under a nitrogen purge. Next, composites were prepared using glass fibers functionalized with cinnamoyl mechanophores and a standard epoxy resin (Diglycidyl ether of bisphenol FS-A23) and hardener (diethylenetriamine, FS-B412) as the matrix. For 3-ply grafted fiber composites, 3 separate layers of fibers were combined with epoxy

thermoset. Due to uncertainties of the effect of high temperature on the stability of the mechanophore functionalized glass fibers, the composites were cured while under loading with a simple hydraulic press at room temperature for two days. After the matrix was fully cured, samples were irradiated with 302nm light for several days to ensure that cinnamoyl groups at the surface of the fibers could dimerize. Once UV irradiated on both sides of the composite, the samples were cut into strips and notch was made to accelerate the failure testing.

Instrumentation

Nikon Eclipse TE300 fluorescent microscope was used to examine the cinnamoyl functionalized glass fibers and observe any fluorescence changes between the neat fiber and the functionalized fibers. Ten images were taken across the fiber surface to get an average fluorescent intensity. Images were analyzed in ImageJ and fluorescent intensity was quantified by calculating integrated density. Characterization of branched hardener and glass fiber composites were carried out with a newly designed experimental setup. This setup consisted of a 365 nm UV lamp and UV camera mounted to a load frame. The sample was illuminated by the UV lamp and subsequent emission was captured by the UV camera and plotted against stress-strain information output from a Test Resources 800L Compression/Tensile System. The images/video gathered by the UV camera were analyzed in the same fashion as the fluorescent microscope and ImageJ through integrated density. This setup provides a huge advantage over previously used fluorescent microscope measurements due to its ability to monitor response in-situ and eliminates activation variability from sample to sample due to a clearly defined fluorescent onset strain. Glass transition temperature (T_g) was measured via a Q20 Differential Scanning

Calorimeter (DSC) with aluminum pans, nitrogen purge, and an empty pan as a reference. The DSC procedure followed a standard heat/cool/heat method with initial heating to 70°C, cooling to -20°C, and second heating to 120°C at 10°C min⁻¹. Mechanophore activation in 3-ply GFRP composites was characterized with an MTS servo-hydraulic load frame integrated with a UV lamp/camera. Quasi-static loading test was performed on the specimen and the desired observed wavelength range (500 nm) was achieved via a band pass filter. Characterization of cinnamoyl grafting onto APTES was performed using Fourier Transform Infrared Spectroscopy (FTIR) under vacuum with a Bruker IFS 6v/S FTIR spectrometer and Pike Diamond Attenuated Total Reflectance (ATR) module.

Results and Discussion

Characterization of Fiber Surface Functionalization

A silane-based functionalization was proposed via grafting of the force responsive fluorescent cinnamoyl moiety onto the surface of a glass fiber through APTES silanization and subsequent surface reaction with cinnamoyl chloride. First, a cinnamoyl functionalized triethoxysilane was synthesized to determine the feasibility of the coupling reaction between APTES and cinnamoyl chloride. After the coupling of the cinnamoyl group with the triethoxysilane was confirmed, the next step consisted of silanization of the glass fiber with APTES. Next, a surface reaction between the pendant amine groups on APTES with cinnamoyl chloride was conducted to produce a final product. This product was characterized via attenuated total reflectance Fourier transform infrared spectroscopy (ATR-FTIR) to confirm the chemical structure of the product (Figure B1). It can be seen that the product displayed the characteristic Si-O absorption at 1074 cm⁻¹, as well as an

amide C=O at 1550 cm^{-1} , indicating that the coupling reaction was indeed successful. This is further supported by cinnamoyl C=C absorptions at 1654 and 1618 cm^{-1} indicating both *cis* and *trans* isomers. While the coupling of the cinnamoyl chloride and APTES was successful, the insolubility of the product proved to be problematic when moving forward with silanization onto a glass fiber surface. The product was insoluble in nearly all solvents in which successful silanization was reported (ethanol, methanol, water, toluene, hexanes, dimethylformamide). Therefore, it was concluded that the directly silanization of the functionalized APTES onto a glass fiber surface would not be successful. However, it did provide confidence that the reaction between cinnamoyl chloride and APTES can readily take place after APTES has already been grafted to the fiber surface.

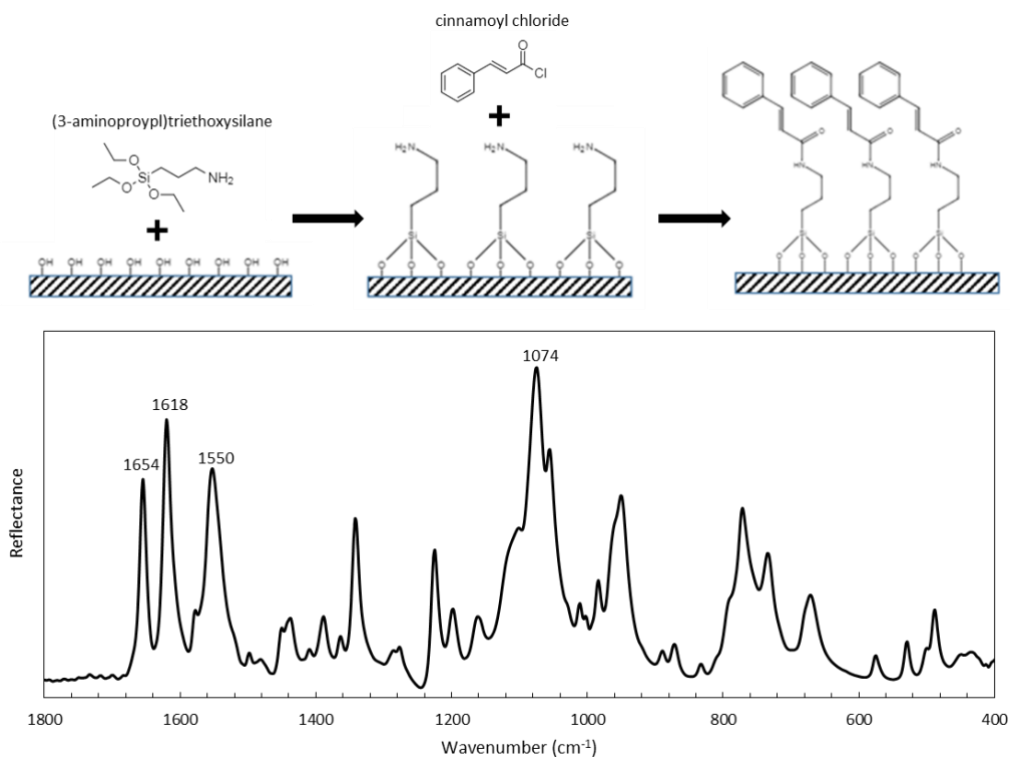


Figure B1. (Top) Schematic of glass fiber surface reaction with APTES and cinnamoyl chloride to produce functionalized fiber surface. (Bottom) FTIR scan of cinnamoyl functionalized triethoxysilane product, N-[3-(triethoxysilyl)propyl]cinnamamide. Absorptions at 1654 and 1618 cm^{-1} are attributed to *cis* and *trans* C=C, 1550 cm^{-1} are attributed to the amide C=O, and 1074 cm^{-1} are attributed to the silane Si-O. Wavenumber values are shown from 1800 to 400 cm^{-1} . Tests were performed under vacuum with a mercury cadmium telluride (MCT) detector.

As described in the experimental section, glass fibers coated with cinnamoyl mechanophore were fabricated. Figure B2 shows sample images of both the neat and grafted fibers, as well as a plot of average integrated density along with standard deviation among the ten images. Grafted fibers do show a significant increase in intensity from neat fibers. However, because of the targeted thin-layer dispersion of cinnamoyl groups, the fluorescence is much lower than other composites previously reported using cinnamoyl functionalities due to lower concentration of fluorescent groups [33-34]. This lower baseline intensity is not necessarily detrimental to the detection capabilities of the cinnamoyl group, provided the concentration of cinnamoyl groups is high enough to yield a detectable signal. Based on the significant increase in fluorescent signal over neat glass fibers, sufficient concentration of cinnamoyl groups were achieved.

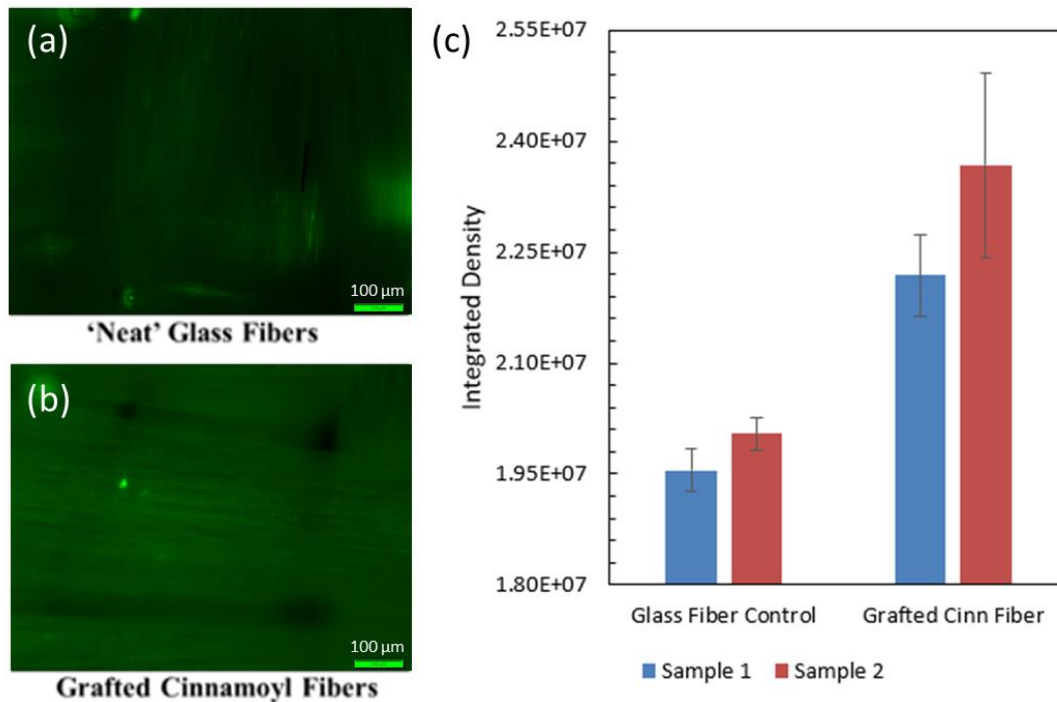


Figure B2. Fluorescent images taken by a Nikon Eclipse TE300 inverted fluorescent microscope for (a) Neat fibers with no coating and (b) fibers grafted with a cinnamoyl silane monolayer. Due to the low intensity values of the images, brightness has been increased by 75% for each image for better visual contrast between the two samples. (c) Unaltered images were processed in ImageJ to produce integrated density information. Both batches of grafted cinnamoyl fibers showed significant improvement in fluorescent properties after the coating process.

Thermal and Mechanical Properties with Surface Characterization

Samples tested in the previous experiments were examined via scanning electron microscope (SEM) imaging to observe potential effects of functionalization on delamination within the GFRP composites. After performing tensile tests on single ply neat

epoxy composites and grafted fiber GFRP composites, the damaged sections of the composite were cut off and imaged using SEM, as seen in Figure B3. Due to the method of functionalizing the surface of the glass fibers, it is hypothesized that unreacted amine groups on the surface of the fibers can bond to the epoxy matrix covalently, helping to prevent potential delamination. While examining SEM images is not necessarily quantitative, it may give a visual representation of the damage occurring within each sample.

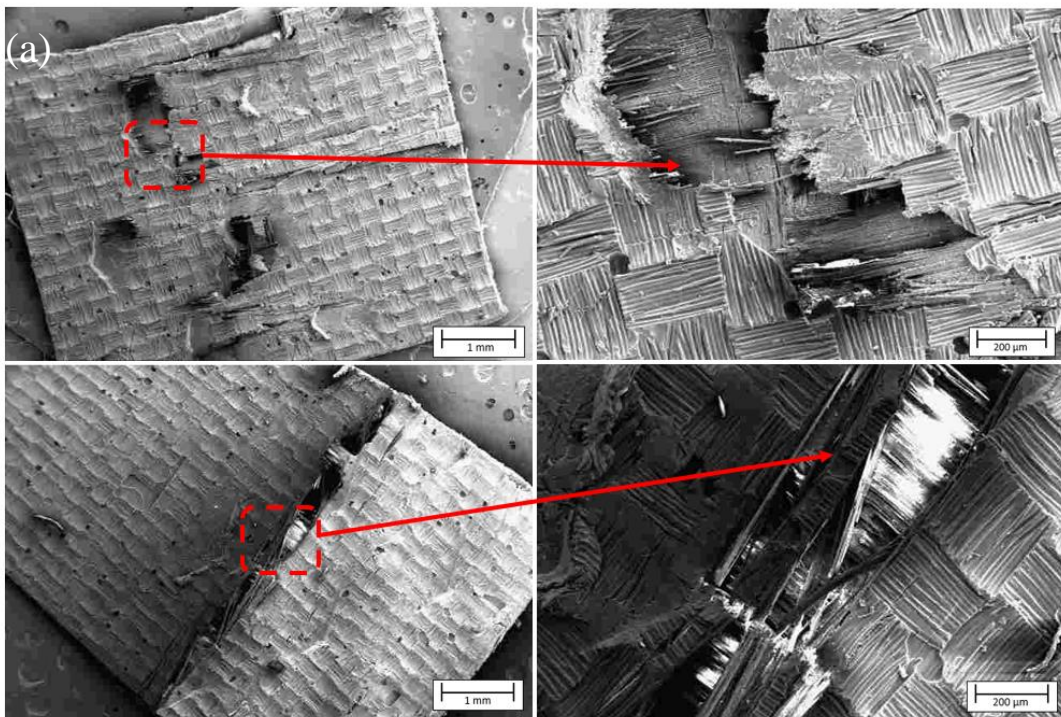


Figure B3. SEM images for (a) overview of neat epoxy GFRP composite with areas of damage highlighted, (b) enlarged image of damage in neat epoxy GFRP composite, (c) overview of grafted GFRP composite with areas of damage highlighted, and (d) enlarged image of damage in grafted GFRP composite.

Although we have reported stress-strain curves previously for our single-ply grafted glass fiber composites, it is important to note that these samples were notched before strain was applied so that the exact location of failure could be characterized via a UV-camera to observe intensity response. In addition to mechanical properties, thermal properties were also examined for a comparison between neat epoxy GFRP composites and grafted GFRP composites via differential scanning calorimetry (DSC). The heat flow profiles for each sample are shown in Figure B4, where glass transition temperatures for grafted fiber samples are slightly lower than neat epoxy glass fiber composites. This decrease in T_g of the composite can be due to interaction of the epoxy matrix with unreacted amine sites from the APTES monolayer. Reactions between APTES and epoxy have been shown in literature to increase tensile properties and interphase strength of the resulting matrix at the cost of T_g [35]. T_g of neat epoxy GFRP composites was found to be 78.5 ± 0.6 °C, while T_g of grafted GFRP composites to was found to be 76.8 ± 0.2 °C.

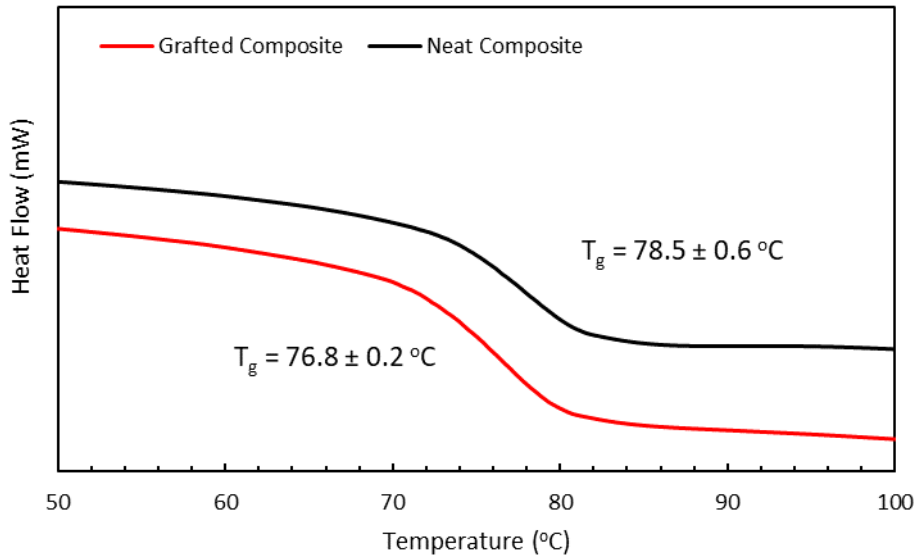


Figure B4. Plot of heat flow for neat epoxy GFRP composites and mechanophore grafted GFRP composites acquired from DSC.

Fluorescent Characterization of Single-Ply and Multi-Ply Mechanophore Functionalized GFRP Composites

Single-ply GFRP composites containing fibers coated with cinnamoyl layer were first tested in order to examine the potential response that could be observed via our experimental system. It can be seen in Figure B3 that for the single-ply system, signal response is observed as early as 1.5% strain, just as failure initiates. It is important to note that there is no mechanophore in the matrix of this material, and so the stress response observed is anticipated at the fiber-matrix interface. Additionally, this response behaves differently from neat epoxy GFRP composites. Both neat and functionalized samples show a sharp decrease in intensity after complete failure due to splitting in the sample and increased void space – areas of image not containing fiber surface due to failure and stretching – in the detection frame. However, functionalized GFRP composites show a sharp increase in signal intensity before this occurs, most likely due to signal response from the activated cinnamoyl groups. It can be noted from these results that the response of single-ply GFRP composites lack the linear increase in fluorescent intensity that is prevalent in mechanophore particle embedded GFRP composites [36]. This difference is hypothesized to be due to damage and stresses at lower strains are mostly applied to the matrix component of the composite causing mechanophore particle activation, while fibers are damaged/undergo delamination at strains closer to the yield point. This effect is captured by mechanophores grafted to the surface of the glass fibers. While these results

are promising, it is still important to characterize any mechanical and thermal property changes that occur due to either process changes or directly grafting to the glass fiber surface.

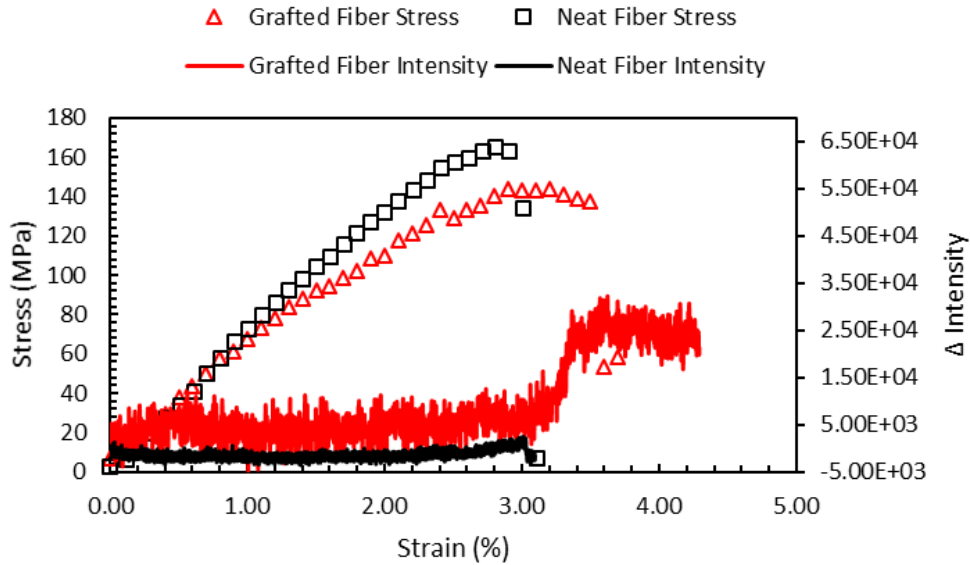


Figure B5. Stress-strain curve and intensity data for composites made with functionalized glass fibers, and neat epoxy GFRP composites.

While force responsive properties of single-ply mechanophore functionalized GFRP composites has been shown, work was also been done regarding multi-ply systems. The main purpose of investigating multi-ply systems is to understand how additional plies affect the sensitivity and detection behavior with mechanophore functionalized GFRP composites. Multi-ply systems provide advantages such as increased mechanical properties, but there are some concerns with the detection abilities of mechanophore grafted fiber systems in thicker samples. First, samples detection is limited by the amount of dimerized mechanophore at the surface of the fibers. If too few mechanophore units are dimerized at

a given area, detection in that area is not achievable. This limitation can be overcome by either limiting the thickness of the sample so that UV-curing can penetrate the entire thickness of the sample or UV-curing each functionalized layer separate before being incorporated into a multi-ply composite. Because the desired thickness of the composite was only 3-ply (approximately 0.65 mm), thickness was not a concern for this experiment, as UV has been shown to penetrate epoxy polymer networks of up to 2 mm in thickness [37]. However, in future composites with a greater number of plies, it may be worth investigation.

After being made into 3-ply GFRP composites, samples were characterized for fluorescence response and the results can be seen in Figure B6. From the figure, it is clear that there is a difference between 3-ply and 1-ply mechanophore functionalized GFRPs. Firstly, there is a noticeable increase in fluorescence intensity before failure. Additionally, the intensity trend observed in these samples follows an exponential behavior, rather than a linear as seen in alternative embedded systems utilizing mechanophores such as dimeric anthracene 9-carboxylic acid (Di-AC) [33]. Large increases or decreases in fluorescence intensity right after failure was a function of the direction the crack propagates.

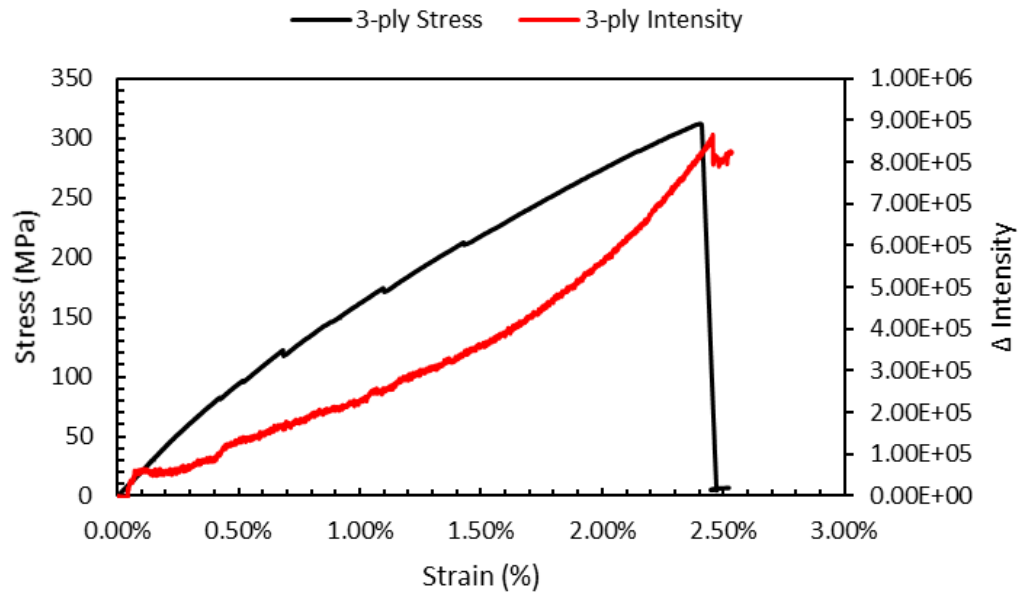


Figure B6. Stress-strain curve versus fluorescent intensity for 3-ply mechanophore functionalized glass fiber reinforced polymer composites.

Conclusion

In conclusion, mechanochemistry has been successfully applied in a GFRP composite system through surface modification, where cinnamoyl based mechanophores were used to examine force concentration at the fiber surface. By detecting the force distributed at the surface of the fiber, targeted precursors to delamination can be characterized *in-situ* with composite deformation. In single-ply grafted glass fiber experiments, signal was detected near the yield point of the material. However, in 3-ply grafted glass fiber composites, onset of signal response began at a much earlier strain and continuously increased until failure. Due to the incorporation of mechanophores at the surface of the fibers, this produced signal was a function of only the deformation occurring at the surface of the fiber instead of a response of overall matrix strain. Results from this study offer a unique outlook for the fundamental understanding of structural health and

monitoring processes and can serve as a promising approach to use mechanophore via chemical modification for alternative applications including equipment and vehicles.

References for Appendix B

- [B1] Soutis C, "Fiber reinforced composites in aircraft construction," 2005, *Progress in Aerospace Sciences*, vol. 41 pp. 143-151
- [B2] Nurazzi NM, Khalina A, Sapuan SM, Laila AHAMD, Rahmah M, Hanafee Z, "A review: fibres, polymer matrices and composites," 2017, *Pertanika Journal of Science and Technology*, vol. 25 pp. 1085-1102
- [B3] Singh J, Kumar M, Kumar S, Mohapatra SK, "Properties of glass-fiber hybrid composites: a review," 2016, *Polymer-Plastics Technology and Engineering*, vol. 56 pp. 455-469
- [B4] Li H, Richards C, Watson J, "High-performance glass fiber development for composite applications," 2014, *International Journal of Applied Glass Science*, vol. 5 pp. 64-81
- [B5] Jin FL, Park SJ, "Preparation and characterization of carbon fiber-reinforced thermosetting composites: a review," 2015, *Carbon Letters*, vol. 16 pp. 67-77
- [B6] Newcomb BA, "Processing, structure, and properties of carbon fibers," 2016, *Composites Part A-Applied Science and Manufacturing*, vol. 91 pp. 262-282
- [B7] Schulte, K, "Sensing with carbon fibres in polymer composites," 2002, *Materials Science Research International*, vol. 8 pp. 43-52
- [B8] Njuguna J, Pielichowski K, Alcock JR, "Epoxy-based fibre reinforced nanocomposites," 2007, *Advances Engineering Materials*, vol. 9 pp. 835-847
- [B9] Afshari M, Sikkema DJ, Lee K, Bogle M, "High performance fibers based on rigid and flexible polymers," 2008, *Polymer Reviews*, vol. 48 pp. 230-274
- [B10] Jawaid M, Khalil HPSA, "Cellulosic/synthetic fibre reinforced polymer hybrid composites: a review," 2011, *Carbohydrate Polymers*, vol. 86 pp. 1-18
- [B11] Karger-Kocsis J, Mahmood H, Pegoretti A, "Recent advances in fiber/matrix interphase engineering for polymer composites," 2015, *Progress in Materials Science*, vol. 73 pp. 1-43
- [B12] Liu XM, Thomason JL, Jones FR, "XPS and AFM study of interaction of organosilane and sizing with e-glass fibre surface," 2008, *Journal of Adhesion*, vol. 84 pp. 322-338
- [B13] Worsley KA, Kalinina I, Bekyarova E, Haddon RC, "Functionalization and dissolution of nitric acid treated single-walled carbon nanotubes," 2009, *Journal of the American Chemical Society*, vol. 131 pp. 18153-18158

- [B14] Kitade S, Fukuda T, Osaka K, "Fiber optic method for detection of impact induced damage in composite laminates," 1995, *Journal of the Society of Materials Science, Japan*, vol. 44 pp. 1196 – 1200
- [B15] Bhatia V, Schmid CA, Murphy KA, Claus RO, Tran TA, Greene JA, Miller MS. "Optical fiber sensing technique for edge-induced and internal delamination detection in composites," 1995, *Smart Materials and Structures*, vol. 4 pp. 164 – 169
- [B16] Chang CC, Sirkis J. "Impact-induced damage of laminated graphite/epoxy composites monitored using embedded in-line fiber etalon optic sensors," 1997, *Journal of Intelligent Material Systems and Structures*, vol. 8 pp. 829 – 841
- [B17] Elvin N, Leung C. "A novel fiber optic delamination detection scheme: theoretical and experimental feasibility studies," 1999, *Journal of Intelligent Material Systems and Structures*, vol. 10 pp. 314 – 321
- [B18] Takeda S, Okabe Y, Takeda N, "Delamination detection in CFRP laminates with embedded small-diameter fiber Bragg grating sensors," 2002, *Composites: Part A*, 2002, vol. 33 pp. 971-980
- [B19] Cheng L, Tian GY, "Comparison of nondestructive testing methods on detection of delaminations in composites," 2012, *Journal of Sensors*, 408437
- [B20] Meyendorf NGH, Nagy PB, Rokhlin S, "Nondestructive materials characterization: with applications to aerospace materials," Springer, Berlin, Heidelberg
- [B21] Dong J, Kim B, Locquet A, McKeon P, Declercq N, Citrin DS, "Nondestructive evaluation of forced delamination in glass fiber-reinforced composites by terahertz and ultrasonic waves," 2015, *Composites Part B*, vol. 79 pp. 667-675
- [B22] Lam PM, Lau KT, Ling HY, Su Z, Tam HY, "Acousto-ultrasonic sensing for delaminated GFRP composites using an embedded FBG sensor," 2009, *Optics and Lasers in Engineering*, vol. 47 pp. 1049-1055
- [B23] Abot JL, Song Y, Vatsavaya MS, Medikonda S, Kier Z, Jayasinghe C, Rooy N, Shanov VN, Schulz MJ, "Delamination detection with carbon nanotube thread in self-sensing composite materials," 2010, *Composites Science and Technology*, vol. 70 pp. 1113-1119
- [B24] Sohma J, "Mechanochemistry of polymers," 1989, *Progress in Polymer Science*, vol. 14 pp. 451-596

- [B25] Ishizuki K, Oka H, Aoki D, Goseki R, Otsuka H, "Mechanochromic polymers that turn green upon the dissociation of diarylbibenzothiophenonyl: the missing piece toward rainbow mechanochromism," 2018, *Chemistry-A European Journal*, vol. 24 pp. 3170-3173
- [B26] Li J, Shiraki T, Hu B, Write RAE, Zhao B, Moore JS, "Mechanophore activation at heterointerfaces," 2014, *Journal of the American Chemical Society*, vol. 136 pp. 15925-15928
- [B27] Li J, Hu B, Yang K, Zhao B, More JS, "Effect of polymer grafting density on mechanophore activation at heterointerfaces," 2016, *ACS Macro Letters*, vol. 5 pp. 819-822
- [B28] Kosuge T, Imato K, Goseki R, Otsuka H, "Polymer-inorganic composites with dynamic covalent mechanochromophore," 2016, *Macromolecules*, vol. 49 pp. 5903-5911
- [B29] Toivola R, Lai PN, Yang J, Jang SH, Jen AKY, Flinn BD, "Mechanochromic fluorescence in epoxy as a detection method for barely visible impact damage in CFRP composites," 2017, *Composites Science and Technology*, vol. 139 pp. 74-82
- [B30] Sammon MS, Oncak M, Beyer MK, "Theoretical simulation of the infrared signature of mechanically stressed polymer solids," 2017, *Beilstein Journal of Organic Chemistry*, vol. 13 pp. 1710-1716
- [B31] Flink S, van Veggel FCJM, Reinhoudt DN, "Functionalization of self-assembled monolayers on glass and oxidized silicon wafers by surface reactions," 2001. *Journal of Physical Organic Chemistry*, vol. 14 pp. 407-415
- [B32] Prolongo SG, Gude MR, Urena A, "Rheological behavior of nanoreinforced epoxy adhesives of low electrical resistivity for joining carbon fiber/epoxy laminates," 2010, *Journal of Adhesion Science and Technology*, vol. 24 pp. 1097-1112
- [B33] Zou J, Liu y, Shan B, Chattoapdhyay A, Dai LL, "Early damage detection in epoxy matrix using cyclobutane-based polymers," 2014, *Smart Materials and Structures*, vol. 23 no. 095038
- [B34] Nofen EM, Zimmer N, Dasgupta A, Gunckel R, Koo B, Chattopadhyay A, Dai LL, "Stress-sensing thermoset polymer networks via grafted cinnamoyl/cyclobutane mechanophore units in epoxy," 2016, *Polymer Chemistry*, vol. 7 pp. 7249-7259
- [B35] Wu Q, Zhao R, Liu Q, Jiao T, Zhu J, Wang F, "Simultaneous improvement of interfacial strength and toughness between carbon fiber and epoxy by introducing amino functionalized ZrO₂ on fiber surface," 2018, *Materials and Design*, vol. 149 pp. 15-24

- [B36] Nofen EM, Wickham J, Koo B, Chattopadhyay A, Dai LL, "Dimeric anthracene-based mechanophore particles for damage precursor detection in reinforced epoxy matrix composites," 2016, *Materials Research Express*, vol. 3 035701
- [B37] Decker C, Keller L, Zahouily K, Said Benfarhi, "Synthesis of nanocomposite polymers by UV-radiation curing," 2005, *Polymer*, vol. 46 pp. 6640-6648